ABSTRACT

Title of Dissertation: DESIGN OF A LARGE BANDWIDTH SCANNING SQUID MICROSCOPE USING A CRYOCOOLED HYSTERETIC DC SQUID

Soun Pil Kwon, Doctor of Philosophy, 2006

Dissertation directed by: Professor Frederick C. Wellstood

Department of Physics

I present the design and analysis of a large bandwidth scanning Superconducting Quantum Interference Device (SQUID) microscope. Currently available SQUID microscopes are limited to detecting magnetic fields with frequencies less than 1 MHz. However, for observing nanosecond time scale phenomena such as logic operations in today's computer chips, SQUID microscopes with 1 GHz bandwidth and larger are required. The major limitation in SQUID microscope bandwidth is not the SQUID itself but the electronics and readout technique. To increase bandwidth, the fast transition of a hysteretic dc SQUID from the zero voltage state to the resistive state can be used as the detection element in a new SQUID readout technique, referred to as pulsed SQUID sampling. The technique involves pulsing the bias current to the dc SQUID while monitoring the

voltage across it. As the pulse length shortens, the SQUID measures the applied external magnetic flux with shorter sampling time, which increases the bandwidth. Experimental tests of the technique have demonstrated the possibility of following signals with frequencies up to 1 GHz using a dc SQUID with Nb-AlO_x-Nb Josephson junctions at around 4 K. Ringing in the pulse profile permitted the effective bandwidth of the sampling technique to be much greater than the nominal value suggested by the pulse length setting on the generator. I identify additional means of increasing bandwidth: redesigning the dc SQUID, implementing transmission line wiring, adding high speed superconducting circuits, etc. which should allow bandwidths to reach 40 GHz and higher. Towards creating a large bandwidth SQUID microscope, I also assembled and tested with collaborators a fully functional 4 K scanning SQUID microscope. With the microscope, which used a nonhysteretic niobium dc SQUID with conventional flux-locked-loop SQUID electronics, I was able to obtain the magnetic field image of a current carrying circuit.

DESIGN OF A LARGE BANDWIDTH SCANNING SQUID MICROSCOPE USING A CRYOCOOLED HYSTERETIC DC SQUID

by

Soun Pil Kwon

Dissertation submitted to the Faculty of the Graduate School of the
University of Maryland, College Park in partial fulfillment
of the requirements for the degree of
Doctor of Philosophy
2006

Advisory Commitee:

Professor Frederick C. Wellstood, Chair
Professor Howard Dennis Drew
Professor Bryan W. Eichhorn
Professor Richard L. Greene
Professor Christopher J. Lobb

PREFACE

I have sometimes wondered whether doctoral dissertations have any significance to people other than its author. It seemed to me that most dissertations end up in library or office shelves just accumulating dust with the passage of time. Only sparingly were these works, books in their own right, taken out of hibernation and read, not cover to cover but for a single chapter at most. Did the reader find what he or she was looking for? Was the information useful? Does the reader recognize that a lot of time and effort went into the document's preparation? As I prepared to write my own dissertation, I thought about my own relationship with dissertations prepared by former students and others. A dissertation should foremost represent the author's original scholarly work while working toward a degree. But beyond that, given the effort put into preparing it, should it not also be useful to others? Often while looking up dissertations of former students, I found the best works to be those which contained information that directly helped my own research. To this end, I decided to make a conscious effort to prepare a dissertation that would be helpful to those interested in constructing and maintaining a scanning SQUID microscope as well as continuing this line of research. As a result, this document is part operation manual, collection of experimental notes, blueprint, and detailed review of basic theory. It is hoped that those who read this document find it useful as reference material, frequently looked up to address problems occurring day to day.

Soun Pil Kwon

DEDICATION

To my parents who provided me opportunities

and

to my children who are my future

ACKNOWLEDGEMENTS

The work presented in this dissertation covers a period of almost four and a half years. During that time I often was alone, working in the sub-subbasement, literally the lowest place in the entire physics building, and then walking back to an off campus apartment in the wee hours of a chilly dark morning. But if it were not for the help and support of numerous individuals, it may not have been just four and a half years. And, it could have been much lonelier.

I would like to thank the physics faculty, especially my advisor Professor Wellstood and onetime co-advisor Professor Lobb. Guidance and direction are good, but it was the financial support they provided through the Center for Superconductivity Research that allowed me to proceed with the work resulting in this dissertation. Considering the delays during the past eighteen months while this dissertation was being prepared, I owe a large debt to Professor Wellstood for his patience and continued financial support. Without funding, I could not have sustained myself and my family, and for that I am grateful.

I would also like to thank my dissertation committee members for their patience. The delivery of this document for their review has been long over due. I hope their patience was not severely tested and that this work is up to their expectations.

I would like to thank the technical staff of the Physics Department as well as that of the Center for Superconductivity Research. In particular, Russell Wood who took over the student shop was vital in providing and setting up equipment needed to

efficiently construct the apparatus for my experiments. His knowledge of tools and materials was much appreciated, and students are fortunate to have him as a resource. I hope he feels that he is well appreciated as well.

I would like to thank colleagues and collaborators at Neocera, Inc., who greatly contributed to the 4 K SQUID microscope project. Most of all, the prototype SQUID microscope would not have been possible if not for Nesco Lettsome, formerly of Neocera, Inc. At least two people are required to safely assemble and maintain the microscope. It was Mr. Lettsome who set up the table top infrastructure, designed and redesigned the majority of the components, and ordered and assembled nearly all of the microscope parts. In fact, he performed most of the initial mechanical work on the project and laid down the foundation on which work continues to date. I hope that he is successful in whatever endeavor he has now moved onto. I would also like to thank Dr. L. A. Knauss and the people at Neocera for being gracious hosts during my time on site working on the microscope.

At the Center for Superconductivity Research, I would like to thank former students and colleagues who assisted in training me and allowed use of their equipment. Dr. Aaron Nielsen first initiated me to the available equipment and facilities at the Center and trained me to prepare SQUID tips, a skill which was vital to the success of the project. I thank Dr. Bin Ming, Dr. Samir Garzon, and Dr. Yuanzhen Chen for help with equipment in Professor Richard Webb's former laboratory. The departure of Professor Webb has left a gap in available facilities that will be missed and will require much time, money, and effort to recuperate. I also

thank Mr. David Tobias and others who helped me in the use and operation of our wire bonding machine.

Other former students at the Center also helped with important advice and discussion. Dr. Andrew Berkley gave observations and suggested changes in experimental setup, and along with Dr. Huizhong Xu, Mr. Mark Gubrud, Ms. Hanhee Paik, and Dr. Matthew Sullivan commented on their experiences with devices and equipment that influenced some of my choices in designing apparatus for my experiments and the prototype SQUID microscope. I also thank my colleague Mr. Constantine Vlahacos and Dr. John Matthews who now continue work on modifying the prototype microscope and investigating the Pulsed SQUID Sampling technique discussed in this dissertation.

On a general level, I would like to thank the support staff of the Physics Department and Center for Superconductivity Research who assisted with preparing and processing the paperwork required by university policy. Processing the dissertation and making sure that I satisfied all the registration requirements was made bountifully easier with the kind assistance of Ms. Jane Hessing. Purchasing of equipment would have been very cumbersome if not for Mr. Robert Dahms, Mr. Jesse Anderson, and others. Financial paperwork for my support and reimbursements for work travel were handled by Ms. Pauline Rirskopa, Ms. Grace Swelall, Mr. Brian Barnaby, and numerous others over the years I have been at the university.

I would also like to thank past and present colleagues who helped me and contributed to the organizing of social events at the Center for Superconductivity Research, the Physics Department, and elsewhere. These social events provided a

sometimes much welcome diversion from everyday routines and helped lubricate the otherwise grinding gears amongst students, faculty, and staff. It is unfortunate that there has been no one to continue this effort as these events were appreciated and enjoyed by all. Along these lines, many thanks go to the staff of the Physics Department, especially the Office of Student Services including Ms. Bernadine Kozlowski and Ms. Linda O'Hara, who helped with communication and provided space for these events.

Lastly, I thank my family. My parents have provided support in every sense of the word and more. My wife has taken on the majority of the burden in physically raising our young children during this time. My parents in-law have provided support for my wife when her burden became too great. And, my children whose smiles relieved some of the stresses associated with both parenthood and graduate school, were a burden that I have gladly carried. They have given me great joy. I hope when they grow up they look back at this time with fonder memories than I.

TABLE OF CONTENTS

LIST OF TABLES

LIST OF FIGURES

CHAPTER 1 Introduction

1.1 SQUID Microscopy

1.1.1 Overview

Since its conception in 1964 by R. C. Jaklevic *et al*., the Superconducting Quantum Interference Device or SQUID has firmly established itself as a reliable tool in physics, electronics, materials research, and other fields [1-7]. In particular, in the last decade, SQUID microscopes have made it possible to image extremely weak magnetic fields generated by electric currents in circuits at microscopic scales [8-14]. The basic technique is to scan and image a component of the magnetic field near the surface of the source using a SQUID and then convert the field image into an image of the source currents [14,15]. The microscope detects the magnetic field component by direct measurement of the field at a large number of points, i.e. as a near field microscope.

An example of the technique is shown in Fig. 1.1, where a SQUID is scanned over a surface containing a current carrying wire. As the SQUID passes over the wire, the magnetic field and consequently the magnetic flux through the SQUID loop changes with a characteristic signature which can be used to identify the current. By comparing the current image to the intended circuit design, the location of problems or faults in the circuit can be found. Today, fault detection or diagnostics of microcircuits is the main commercial application of SQUIDs in the electronics

(a)

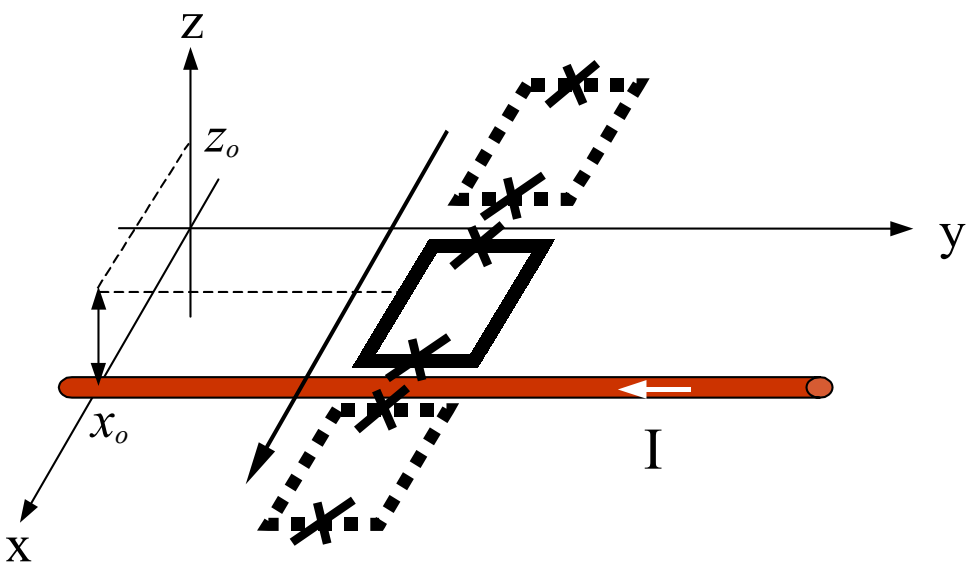

(b)

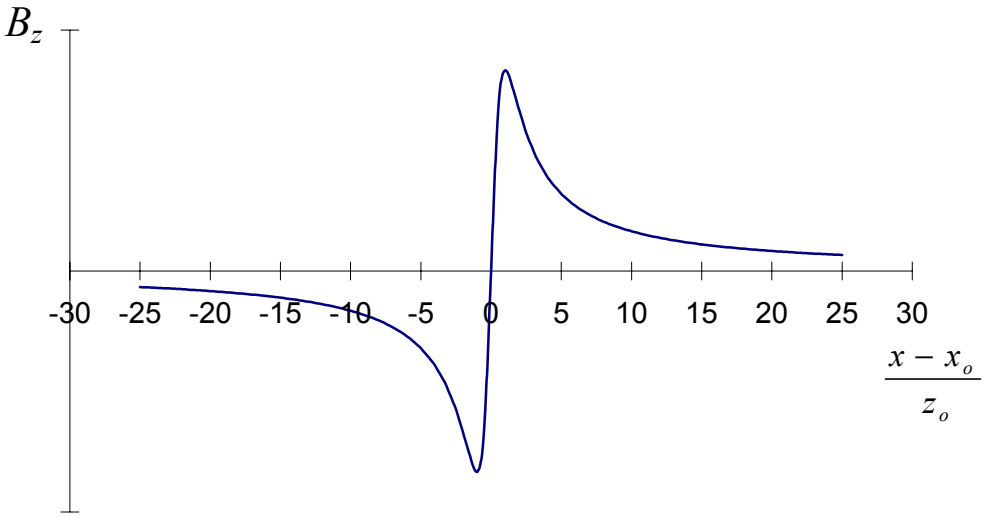

FIG. 1.1. (a) A z-SQUID scanning over a straight wire in the x-y plane at a height z_o. The wire carries current in the y direction and produces a magnetic field around it. If the size of the SQUID loop is sufficiently small, the SQUID will detect the z component of the magnetic field due to the wire. (b) Z-component of the magnetic field due to an infinitely long line current in the x-y plane as observed above the plane at a height z_o. The current is along the y direction and is centered at $x = x_o$. The distance along x is given in units of the height z_o above the plane, and the field scale is arbitrary.

industry [16]. Full scanning SQUID microscopes with diagnostic software for planar electrical circuits are commercially available, and this application is expected to continue as circuits in microchips and supporting systems become more complex [17].

As with any near-field technique, the sensor (SQUID) must be brought nearly in contact with the field generating object in order to have the field measured at maximum strength and with the best spatial resolution. Although the total magnetic field at any point is a sum of all sources, the field at any location can often be regarded as primarily due to local sources, as long as the distances between sources are much larger than the size of the SQUID and the distance between the SQUID and the object surface. As the distance between the object and SQUID increases, the relative importance of more distant field generating sources increases.

For example, Fig. 1.2 shows the combined field of two parallel line current sources with different separations; they can be regarded as the combination of two curves shown in Fig. 1.1(b) centered at different positions. As the relative separation between the sources decreases, the combined field takes on a different characteristic [compare Fig. 1.2(a) with 1.2(b)]. If the measured field cannot be regarded as only being due to local sources, a technique to derive the sources from the field image is required. Such a technique was first developed by Wikswo's group at Vanderbilt and is now available commercially [14-17].

Bringing the SQUID as close as possible to the field source is also important for other reasons. Maximizing the measured field strength also maximizes the signal to noise ratio (SNR). A larger SNR provides a more precise field measurement with

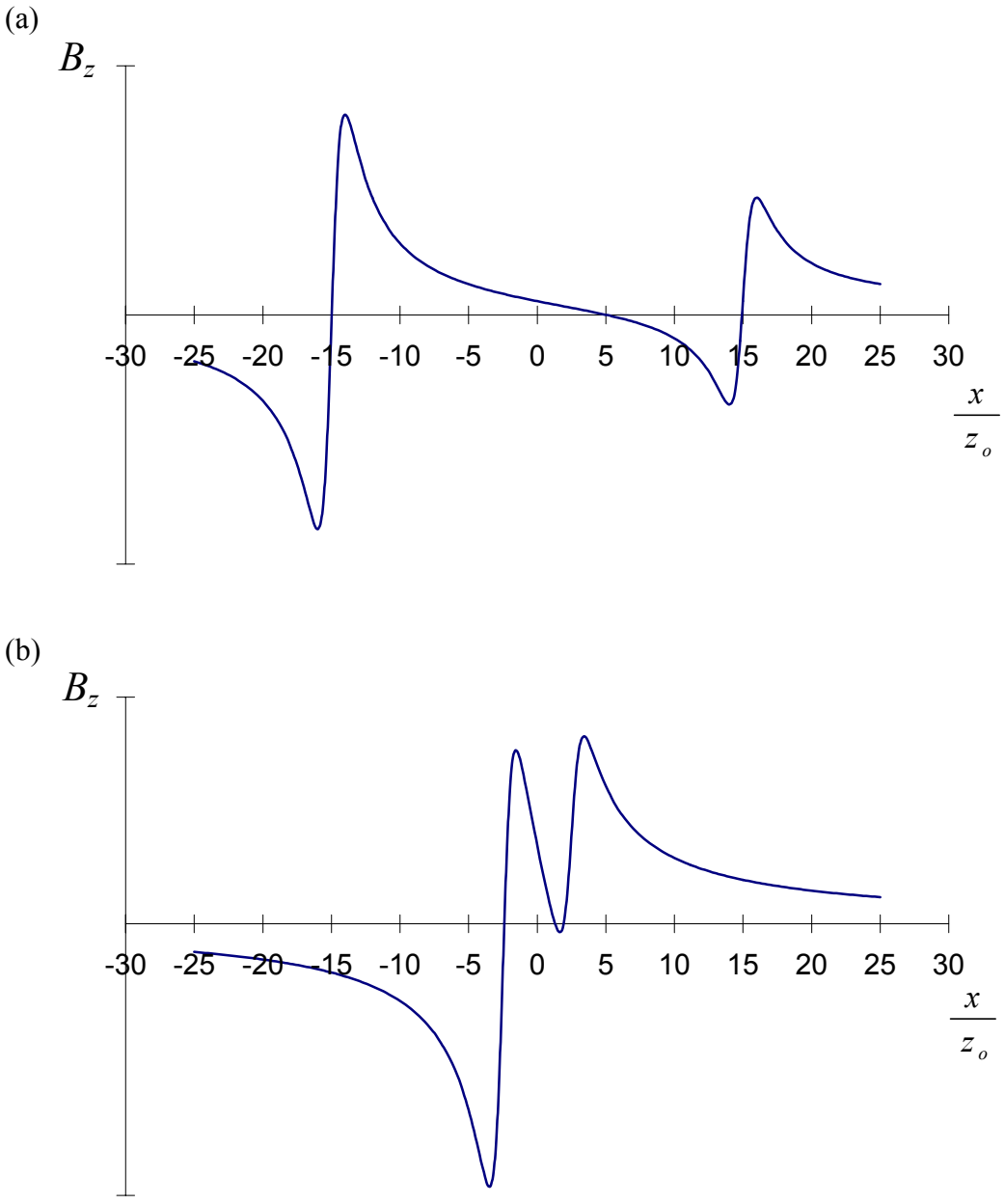

FIG. 1.2. B_z (z-component of magnetic field) due to two infinitely long parallel wires carrying current in the x-y plane as observed above the plane at a height z_o. Both currents flow along the y direction, but the wire to the left has twice the current of the wire to the right. The distance along x is given in units of the height z_o above the plane, and the field scale is arbitrary. The two wires are centered at $x/z_o = \pm 15$ resulting in a separation of 30 in graph (a) and at $x/z_o = \pm 2.5$ with a separation of 5 in graph (b).

less scan time. If the field image is used to derive the source image, the uncertainty in the resulting current density will also be smaller for larger SNR. Noise in the SQUID microscope system ultimately limits the microscope's capability to measure magnetic fields.

1.1.2 Motivation

Advances in microelectronics have made diagnosing some circuit problems more and more difficult. Very high spatial and temporal resolution is now needed to detect all types of possible failures. In microchips, submicron line widths are now common and circuit clock speeds are in the 2 GHz to 3 GHz range. Detecting and analyzing magnetic fields from such circuits is challenging even with SQUID microscopes. Where possible, single circuit leads are activated individually to help differentiate between closely packed circuit elements. Also, if possible, circuit speeds are slowed down so that the electronics in a SQUID microscope can follow the changing field. Without the decrease in speed, present SQUID microscopes are unable to faithfully monitor the rapidly changing ac components of fields.

Despite such tricks and various other techniques to measure high frequency signals in densely packed complex circuits, it would be best if the circuits could be analyzed while working under normal operating conditions. In fact, some dynamic problems do not occur otherwise. This however is not possible with currently available SQUID microscopes. The main limitations lie in the SQUID microscope's readout electronics, rather than in the SQUID itself. The most common dc SQUID electronics are based on the ac modulated Flux-Locked-Loop (FLL) technique. The

electronics relies on a low noise amplifier, an oscillator, a demodulator, an integrator, and negative feedback to produce a linear output proportional to the flux applied to the SQUID [4,5,18-20]. The range of frequencies the microscope can measure is specified by its bandwidth. To increase the bandwidth of the microscope, the bandwidth of the feedback system circuitry has to increase. Unfortunately, the complexity and difficulty of building and optimizing large (gigahertz) bandwidth feedback circuitry has limited the bandwidth of SQUID feedback electronics to a maximum range of about 1 MHz to 2 MHz with typical bandwidths between 10 kHz and 200 kHz [19,20]. Therefore, in order to improve bandwidth to meet diagnostic performance requirements, SQUID readout electronics based on a different approach is needed.

1.2 Preview of Work

Research on hysteretic Josephson junctions has shown that the fast transition from the zero voltage state to the resistive state could be used for high speed measurement. Besides work performed at IBM until 1983, the best known measuring instrument using this technology was perhaps the HYPRES PSP-1000 sampling oscilloscope which used Josephson junctions as fast switches [21-24]. Experiments have shown that the voltage transition times of Josephson junctions are dependent on the junction critical current and can be made much shorter than a nanosecond [25,26]. If the time scale associated with variations in bias current or SQUID critical current is much larger than a nanosecond, the voltage state transition could be regarded as instantaneous.

The basic idea of the HYPRES sampling oscilloscope was to exploit the instantaneous voltage transition of the Josephson junction as a time resolved precision switch. Timing measurements and pulse generation can be performed relatively easily with high precision using modern electronics and do not have the same bandwidth issues as does negative feedback FLL electronics. If this technique can be applied to a dc SQUID, instead of a single Josephson junction, the SQUID could be used to retrieve magnetic field information on very short time scales.

In this thesis, I describe experiments I performed to explore the feasibility of using hysteretic dc SQUIDs for a large bandwidth microscope that can follow magnetic signals with frequencies on the order of 1 GHz and higher. For this, I designed and prepared hysteretic SQUIDs and tested them by observing what happens when they are subjected to short current pulses.

In addition, a tabletop cryogenic system for use in a prototype SQUID microscope was assembled. The cryogenics was based on a low temperature cryocooler with a base temperature below 4 K [27]. Once assembled, the prototype microscope would be a fully functional Scanning SQUID Microscope and was tested with a resistively shunted nonhysteretic dc SQUID [28]. Commercially available FLL electronics with a 250 kHz oscillator were used for driving the SQUID and initially operating the microscope [29]. After initial tests, I was able to produce a magnetic field image of a test electrical circuit, therefore, verifying the feasibility of a 4 K cryocooled scanning SQUID microscope. The idea is to eventually replace the FLL electronics and nonhysteretic SQUID with new electronics and a hysteretic

SQUID to turn the prototype microscope into a fully functional large bandwidth scanning SQUID microscope.

Although the microscope cryocooler was available for experiments, I decided to perform experiments on hysteretic SQUIDs in liquid helium for convenience. These experiments mainly consisted of monitoring the response of the SQUIDs to short bias current pulses and microwave frequency magnetic field signals. Reliable detection of signals with frequencies up to 100 MHz was observed [30]. My review of the results suggested that with better electronics, detection of magnetic fields with frequencies 1 GHz and higher could be achieved, and subsequent experiments performed shortly thereafter did, in fact, demonstrate 1 GHz detection [31]. Finally, from my experiments, I devised new SQUID readout electronics using an approach based on signal sampling with short bias current pulses.

1.3 Outline of Thesis

The organization of this dissertation is as follows. Chapter 2 provides a general introduction to Josephson junctions and dc SQUIDs and ends with a discussion of some specific characteristics. I discuss both hysteretic and nonhysteretic Josephson Junctions and the equations describing them. Chapter 3 describes dc SQUID design criteria, the nonhysteretic dc SQUIDs that were used in the prototype SQUID microscope and the hysteretic dc SQUIDs used in the fast switching experiments. Chapter 4 describes the prototype 4 K cryocooled Scanning SQUID Microscope. I discuss the various subsystem components, from the cold finger which holds the SQUID to the translation system which performs the scanning,

to the conventional FLL SQUID readout electronics. The chapter ends with descriptions of and comments on the SQUID microscope operating procedures. Chapter 5 presents the work performed in producing a magnetic field image using the prototype SQUID microscope. In Chapter 6, I propose my new SQUID readout electronics, which makes use of a hysteretic dc SQUID. The limitations of the ac modulated FLL technique, and how they are overcome by the new technique, are discussed in this chapter. Chapter 7 describes my experiments on current pulsed hysteretic dc SQUIDs and compares the results with calculations made from a model of the SQUID circuit. This chapter includes a section on the large bandwidth dip probe constructed for the experiments and what were considered in its design. Finally, the dissertation concludes with a chapter summarizing the results of my research with comments and suggestions for future work.

CHAPTER 2 Introduction to Josephson Junctions and dc SQUIDs

2.1 Superconductivity and Josephson Junctions

The phenomena of superconductivity in the form of complete loss of electrical resistance in a material was discovered in 1911 by Kamerlingh Onnes [32]. Since then, much has been learned about the phenomenon and the study of superconductivity has contributed to the understanding of many properties of solids. The phenomenon was eventually explained at the microscopic level by Bardeen, Cooper, and Schrieffer (BCS) in 1957 [33,34]. Significant questions still remain, however, principally the microscopic mechanism causing superconductivity in the high transition temperature (T_c) cuprates such as $YBa_2Cu_3O_{7-x}$.

Nevertheless, the basic theory of superconductivity in conventional low-T_c materials first developed in BCS theory is now well established. BCS theory is a quantum mechanical many-body theory in which electrons attract each other through phonons to form Cooper pairs in a coherent collective state. This state can also be described by a complex order parameter which was introduced earlier (1950) by Ginzburg and Landau [35]. The order parameter effectively represents the macroscopic wave function of the superconducting electrons or Cooper pairs [36,37]. Although the description of superconductivity by Ginzburg and Landau using the order parameter is only strictly valid near the transition temperature T_c of the material, it has been successful in describing many phenomena outside of this range.

Since the discovery and explanation of superconductivity, many applications have been proposed and exploited. Some of the more interesting applications have made use of quantum mechanical effects in superconductivity. One such example is the Josephson junction which was proposed by Josephson and fully explained in 1963 [38-41]. A Josephson junction consists of two superconductors that are separated by a very thin electrically insulating barrier. Josephson predicted that if the barrier is sufficiently thin, Cooper pairs would tunnel through the barrier keeping the quantum mechanical phase information intact and producing no voltage drop across the barrier. Resistive currents, though possible, would give rise to a voltage across the barrier unlike a supercurrent and consequently would not be present under zero voltage bias. Shortly after the prediction, experimental verification of supercurrent tunneling was performed by Anderson and Rowell using a tin-tin oxide-lead junction [42].

Many other phenomena associated with Josephson junctions have also been observed. Perhaps the most important of these concern the ac Josephson effect in which a dc voltage drop across the barrier gives rise to an ac supercurrent [38,39]. In addition, macroscopic quantum effects have been discovered in Josephson junctions including macroscopic quantum tunneling, quantum energy levels, stimulated tunneling, and quantum coherence [43-51].

2.2 Josephson Equations

2.2.1 dc Josephson Effect

Equations analogous to the Josephson effects can be derived from a simple one dimensional model [52,53]. Consider the square barrier of length *2d* and height

U centered at the origin (see Fig. 2.1). The energy associated with the macroscopic wave function is E with the condition $E < U$. Outside the barrier, the energy E corresponds to the kinetic energy of the carriers of supercurrent.

$$E = \sum \frac{1}{2} m^* v_s^{\,2} \tag{2.1}$$

where m^* is the mass of a charge carrier, and v_s is its velocity. This model breaks down if $E \geq U$ as in this case the barrier no longer acts as an insulator but as a different superconductor. It should be recalled that the carriers of supercurrent are Cooper pairs, and so the effective charge and mass of these carriers are $-2e$ and $2m_e$, respectively.

The macroscopic wave function of the superconductor can be expressed by the complex order parameter ψ, having the following form on each side of the barrier.

$$\psi = n_i^{\frac{1}{2}} e^{ikx} \tag{2.2}$$

with

$$k = \sqrt{\frac{4 m_e E}{\hbar^2}} \tag{2.3}$$

where $n_i^{\frac{1}{2}}$ is constant and represents the density of Cooper pairs. Assuming zero voltage across the barrier and identical superconductors on each side, $n_1^{\frac{1}{2}} = n_2^{\frac{1}{2}} \equiv n^{\frac{1}{2}}$. Then, the only difference in the value of ψ on each side of the barrier is due to the phase. Inside the barrier, the wave function has the form

$$\psi = C_1 \cosh \kappa x + C_2 \sinh \kappa x \tag{2.4}$$

with

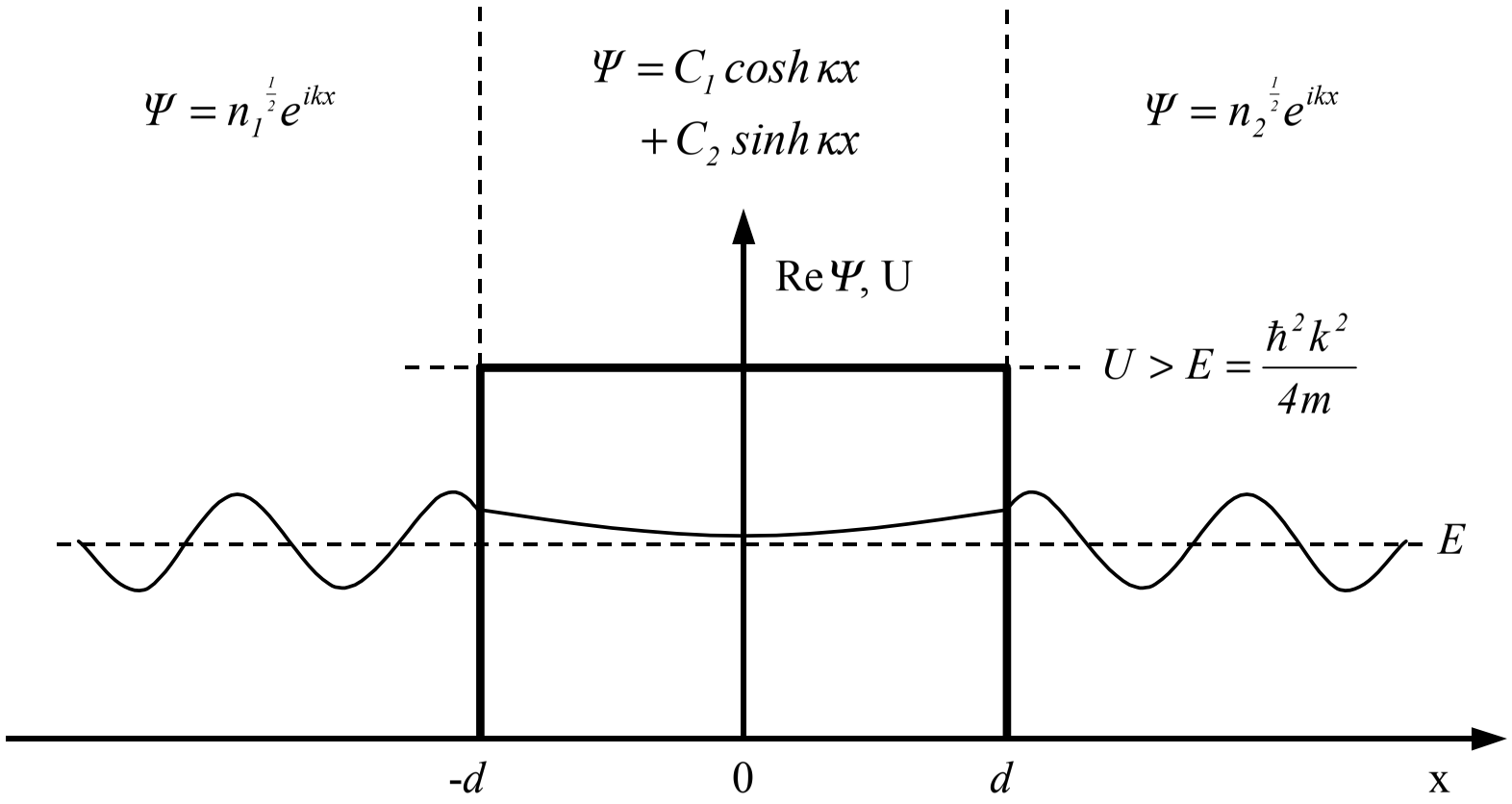

FIG. 2.1. Model of a superconductor-insulator-superconductor Josephson junction. Current carrying particles of energy E and mass $2m_e$ quantum mechanically tunnel through an insulating square potential barrier of thickness $2d$ and height U.

$$\kappa = \sqrt{\frac{4m_e(U-E)}{\hbar^2}}. \tag{2.5}$$

Matching boundary conditions at the edge of the barrier, one finds that the values of C_1 and C_2 are given by

$$\begin{aligned} C_1 &= n^{\frac{1}{2}} \frac{\cos\ kd}{\cosh \kappa d} \\ C_2 &= i\, n^{\frac{1}{2}} \frac{\sin\ kd}{\sinh \kappa d} \end{aligned}. \tag{2.6}$$

From elementary quantum mechanics, the current density can be written as

$$\boldsymbol{J} = -2e\ R_e\left\{\frac{\hbar}{i2m_e}\psi^*\nabla\psi\right\} = -e\frac{\hbar}{m_e} I_m\left\{\psi^*\nabla\psi\right\} \tag{2.7}$$

where $\boldsymbol{J}$ represents the current density, and $-e$ is the charge of an electron. Applying Eqs. (2.2), (2.4), and (2.6) to Eq. (2.7),

$$J = -e|n|\frac{\hbar k}{m_e} \tag{2.8}$$

outside the barrier, and

$$J = -e\frac{\hbar\kappa}{m_e} I_m\left\{C_1^{\ *} C_2\right\} = -e|n|\frac{\hbar\kappa}{m_e}\frac{\cos kd \sin kd}{\cosh \kappa d \sinh \kappa d} \tag{2.9}$$

inside the barrier.

As expected, the current density both inside and outside the barrier is constant with respect to the space coordinate. Applying trigonometric and hyperbolic identities, the magnitude of $\boldsymbol{J}$ inside the barrier can be written as

$$J = J_c \sin(\theta_2 - \theta_1) \tag{2.10}$$

where

$$J_c = -\frac{e|n|\hbar\kappa}{m_e \sinh\ 2\kappa d}, \tag{2.11}$$

$\theta_1 = -kd$,

and (2.12)

$\theta_2 = kd$.

The quantity J_c is known as the critical current density. It depends on the nature and thickness of the insulating barrier, the superconducting material, and environmental factors like temperature. In this model, J_c is dependent on the supercurrent energy and has a limiting value of $e|n|\hbar/2m_e d$ as the energy E approaches the barrier height U. However, J_c will be considered a constant in the rest of this treatment for simplicity.

Note also that $\theta_2 - \theta_1$ is the difference in phase of the wave function on either side of the barrier. Given that the calculations remain unchanged if a constant phase is added to the phase of the wave function, only the phase difference across the barrier is significant. On the other hand, if gauge invariance is imposed on the system, an additional term appears in the expression for the phase difference. The gauge invariant phase difference is given by

$$\gamma = \theta_2 - \theta_1 + \frac{2e}{\hbar}\int_1^2 \boldsymbol{A}\cdot d\boldsymbol{l} \tag{2.13}$$

where $\boldsymbol{A}$ is the vector potential and the integration is performed over the region corresponding to the change of phase from θ_1 to θ_2, which is across the barrier [52].

The additional term comes from a modification of the probability current due to the presence of an electromagnetic field. Instead of Eq. (2.7), the current density becomes

$$\boldsymbol{J} = -2e\, R_e\left\{\psi^*\left(\frac{\hbar}{i2m_e}\nabla + \frac{2e}{2m_e}\boldsymbol{A}\right)\psi\right\} \tag{2.14}$$

$$= -e|n|\frac{\hbar}{m_e}\left(\nabla\theta + \frac{2e}{\hbar}\boldsymbol{A}\right) \tag{2.15}$$

where in this last equation, ψ outside the barrier is expressed in the more general form of Eq. (2.2)

$$\psi = n^{\frac{1}{2}} e^{i\theta}. \tag{2.16}$$

The generalization of Eq. (2.10), for the supercurrent through the barrier, in the presence of an electromagnetic field is then

$$J = J_c \sin\gamma \tag{2.17}$$

which is just the dc Josephson effect [38-41]. The supercurrent is observed to depend on the gauge invariant phase difference γ of the macroscopic wave function across the insulating barrier. The dependence of the phase difference on the vector potential $\boldsymbol{A}$ means that the phase difference can be varied by applying a magnetic field to the junction. This will result in suppression of the dc supercurrent with respect to its maximum possible value. For example, if magnetic flux gets trapped within the junction, this would effectively result in a decrease in the maximum dc supercurrent [54-57].

2.2.2 ac Josephson Effect

The dynamic behavior of the supercurrent can be obtained from the time dependent Schrödinger equation,

$$i\hbar\frac{\partial\psi}{\partial t}=\frac{1}{4m_e}\left(\frac{\hbar}{i}\nabla+2e\boldsymbol{A}\right)^2\psi-2e\phi\psi \tag{2.18}$$

where ϕ is the electric potential. Substituting Eq. (2.16) for the macroscopic wave function gives

$$-\hbar\frac{\partial\theta}{\partial t}=\frac{\hbar^2}{4m_e}(\nabla\theta)^2+\frac{\hbar e}{m_e}\boldsymbol{A}\cdot\nabla\theta+\frac{\hbar^2}{4m_e i}\nabla^2\theta+\frac{\hbar e}{2m_e i}\nabla\cdot\boldsymbol{A}+\frac{e^2A^2}{m_e}-2e\phi \tag{2.19}$$

Separating the real and imaginary parts and solving for $\partial\theta/\partial t$ gives

$$\begin{aligned}\frac{\partial\theta}{\partial t}&=-\frac{\hbar}{4m_e}(\nabla\theta)^2-\frac{e\boldsymbol{A}}{m_e}\cdot\nabla\theta-\frac{e^2A^2}{m_e\hbar}+\frac{2e}{\hbar}\phi\\&=-\frac{\hbar}{4m_e}\left(\nabla\theta+\frac{2e\boldsymbol{A}}{\hbar}\right)^2+\frac{2e}{\hbar}\phi\end{aligned} \tag{2.20}$$

and expressing this in terms of the current density $\boldsymbol{J}$ gives

$$\frac{\partial\theta}{\partial t}=-\frac{m_e}{4e^2|n|^2\hbar}J^2+\frac{2e}{\hbar}\phi \tag{2.21}$$

Now, applying this equation to Eq. (2.13) for the gauge invariant phase γ gives

$$\frac{\partial\gamma}{\partial t}=\frac{\partial\theta_2}{\partial t}-\frac{\partial\theta_1}{\partial t}+\frac{2e}{\hbar}\frac{\partial}{\partial t}\int_1^2\boldsymbol{A}\cdot d\boldsymbol{l} \tag{2.22}$$

$$=-\frac{m_e}{4e^2|n|^2\hbar}\left(J_2{}^2-J_1{}^2\right)+\frac{2e}{\hbar}\int_1^2\left(\nabla\phi+\frac{\partial\boldsymbol{A}}{\partial t}\right)\cdot d\boldsymbol{l} \tag{2.23}$$

Recognizing that the electric field is given by

$$\boldsymbol{E}=-\nabla\phi-\frac{\partial\boldsymbol{A}}{\partial t}, \tag{2.24}$$

Eq. (2.23) reduces to

$$\frac{\partial \gamma}{\partial t} = -\frac{m_e}{4e^2|n|^2\hbar}\Delta J^2 - \frac{2e}{\hbar}\int_1^2 \boldsymbol{E}\cdot d\boldsymbol{l} \tag{2.25}$$

$$= -\frac{m_e}{4e^2|n|^2\hbar}\Delta J^2 + \frac{2e}{\hbar}V \tag{2.26}$$

where the integration is performed through the insulating barrier from the region corresponding to phase θ_1 to the region with phase θ_2. Consequently, V is the voltage drop across the junction. Here, $\Delta \boldsymbol{J}^2$ is the difference in current density squared between one side of the junction and the other.

Assuming current conservation and a lumped circuit or $l << \lambda$ where, l is a characteristic length of the junction and λ is the wave length of electrical signals across the junction, $\boldsymbol{J}_1 = \boldsymbol{J}_2$. So,

$$\Delta J^2 = 0 \tag{2.27}$$

and thus,

$$\frac{\partial \gamma}{\partial t} = \frac{2\pi}{\Phi_o}V \tag{2.28}$$

where

$$\Phi_o \equiv \frac{h}{2e} \cong 2.068\times 10^{-15}\, T\cdot m^2 \tag{2.29}$$

is the definition of the flux quantum.

Equation (2.28) states that the gauge invariant phase across the insulating barrier evolves in time at a rate proportional to the voltage across the barrier. Combining this result with Eq. (2.17) brings about the conclusion that a dc voltage across the Josephson junction will give rise to an ac current through the junction. This is known as the ac Josephson effect [38,39].

Using Eqs. (2.17) and (2.28), a simple expression for the electrical energy density per unit area within the barrier can be derived [58,59]. Noting that γ is only a function of time in this case, one can write the energy density in the barrier as

$$\begin{aligned} \mathcal{E}_j &= \int_1^2 JV dt \\ &= \int_1^2 J_c \sin\gamma' \frac{\Phi_o}{2\pi} d\gamma' \end{aligned} \tag{2.30}$$

$$= \frac{J_c \Phi_o}{2\pi}(1 - \cos\gamma) \tag{2.31}$$

where the integration is performed through the barrier from the region with phase θ_1 to the region with phase θ_2. The total energy in the barrier then scales with

$$E_j = \frac{I_c \Phi_o}{2\pi} \tag{2.32}$$

where I_c is the total critical current through the junction.

From Eq. (2.31), note that the phase difference across the junction is associated with the total energy. If additional energy is supplied from a thermal reservoir, the phase difference will become unstable. This places an upper bound on the temperature for which the phase difference will be able to assume a well defined value. Therefore, a stable phase would be guaranteed by

$$E_j >> k_B T \tag{2.33}$$

or

$$I_c >> \frac{2ek_B T}{\hbar} \tag{2.34}$$

for a temperature T. In practice, the value of I_c can be adjusted by changing the size of the junction or by reducing the thickness of the barrier which increases the critical current density.

2.3 dc SQUID

2.3.1 Critical Current Modulation

The dc Superconducting Quantum Interference Device or SQUID is a highly sensitive detector of magnetic flux. The working principle of the SQUID can be explained using the macroscopic wave function model used to describe the Josephson junction [1-4,6-9,11,12,60]. The dc SQUID (see Fig. 2.2) consists of a superconducting path which splits into two branches that reconnect to form a hole in the middle. Each branch contains a Josephson junction. Only the ideal dc SQUID which contains no other elements other than the Josephson junctions is considered here. What happens when other elements such as loop inductance are included is treated later.

The dc SQUID is usually current biased and can be thought of as an interferometer of the macroscopic supercurrent wave function that splits and reconnects around the hole. The wave function must be single valued, or in other words the integrated phase gradient around the hole must be a multiple of 2π. To appreciate the significance of the Josephson junctions and the consequences of the single valued wave function, first consider the situation if there were no junctions around the loop. In this case, the superconductor forms a continuous ring [see Fig. 2.3(a)]. If the superconductor is thick enough, most of the supercurrent will flow near

(a)

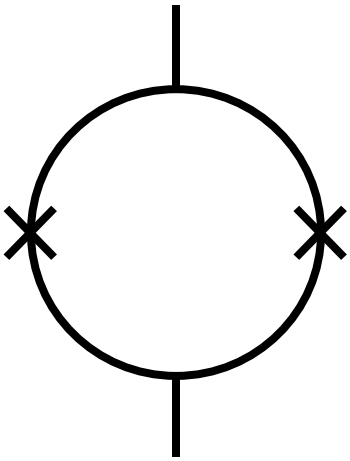

(b)

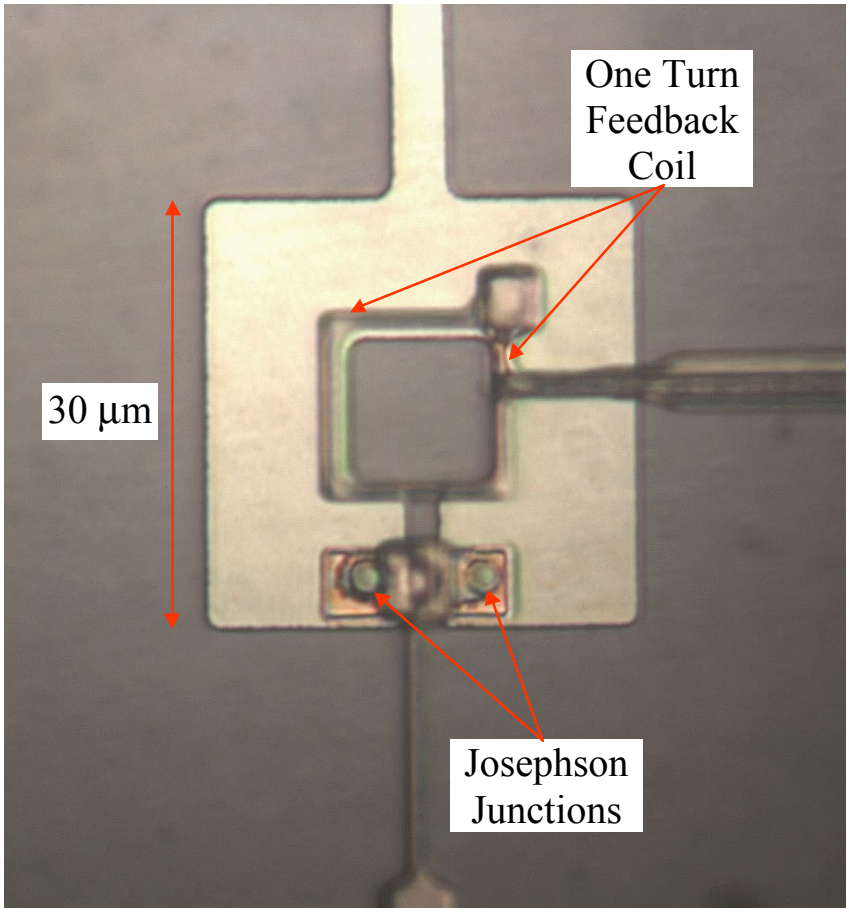

FIG. 2.2. (a) Circuit diagram of an ideal dc SQUID. Crosses indicate Josephson junctions. (b) Photograph of a 30 μm Nb dc SQUID with Nb-AlO_x-Nb Josephson junctions, fabricated by Hypres, Inc. The SQUID includes a one turn magnetic feedback coil.

(a)

(b)

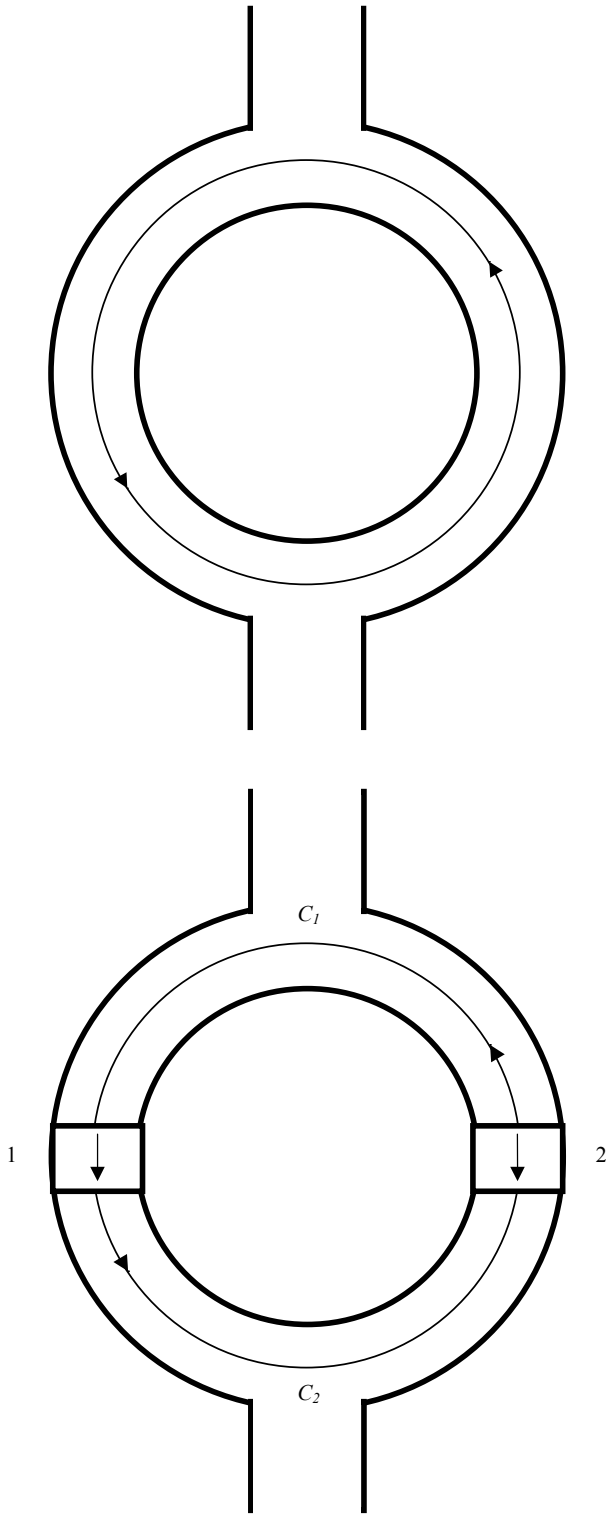

FIG. 2.3. (a) Diagram showing path of line integral around a superconducting loop deep inside the superconductor. (b) Diagram showing paths of line integrals around dc SQUID loop, deep inside the superconductor and through the Josephson junctions.

the surface, within the London penetration depth [61,62]. If so, there will be a continuous region deep inside the superconductor where $\boldsymbol{J} = 0$. A line integral of $\boldsymbol{J}$ around the hole inside this region results in

$$\oint \boldsymbol{J} \cdot d\boldsymbol{l} = 0 \,. \tag{2.35}$$

From Eq. (2.15), this gives

$$\oint \left(\nabla\theta + \frac{2e}{\hbar} \boldsymbol{A} \right) \cdot d\boldsymbol{l} = 0 \,. \tag{2.36}$$

Now, recognize that

$$\oint \boldsymbol{A} \cdot d\boldsymbol{l} = \int \nabla \times \boldsymbol{A} \cdot d\boldsymbol{S} = \int \boldsymbol{B} \cdot d\boldsymbol{S} = \Phi \tag{2.37}$$

where Φ is the total magnetic flux through the hole. Thus, Eq. (2.36) gives

$$\oint \nabla\theta \cdot d\boldsymbol{l} = 2\pi n = -\frac{2e}{\hbar}\Phi = -2\pi \frac{\Phi}{\Phi_o} \tag{2.38}$$

where n is any integer value. This result reveals that the total magnetic flux through the hole is quantized and is an integer multiple of a flux quantum.

$$\Phi = n\Phi_o \tag{2.39}$$

The quantization of flux implies that with a constant applied magnetic field, the value of circulating supercurrent around the hole is also quantized.

Now, consider the situation where a Josephson junction is present on each branch of the SQUID loop. First, the supercurrent through a junction is limited by Eq. (2.17). Second, the line integral of the current density $\boldsymbol{J}$ around the loop need not vanish, as $\boldsymbol{J} \neq 0$ in the junction barriers. To see how this effects the current through both junctions, note that the total quasi static current through the dc SQUID is constant and is given by

$$I = I_{c1} \sin \gamma_1 + I_{c2} \sin \gamma_2 \tag{2.40}$$

$$= I_c \left(\sin \gamma_1 + \sin \gamma_2 \right) \tag{2.41}$$

where in the last equation, I assumed that the critical currents of the Josephson junctions are equal. Using a trigonometric identity, Eq. (2.41) becomes

$$\begin{aligned} I &= 2 I_c \cos \frac{\gamma_1 - \gamma_2}{2} \sin \frac{\gamma_1 + \gamma_2}{2} \\ &= 2 I_c \cos \frac{\Delta\gamma}{2} \sin \gamma_{av} \end{aligned} \tag{2.42}$$

where

$$\begin{aligned} \Delta\gamma &= \gamma_1 - \gamma_2 \\ \gamma_{av} &= \frac{\gamma_1 + \gamma_2}{2} \cdot \end{aligned} \tag{2.43}$$

From Eq. (2.28), one can write

$$\frac{\partial \gamma_{av}}{\partial t} = \frac{2\pi}{\Phi_o} V \tag{2.44}$$

but that

$$\frac{\partial \Delta\gamma}{\partial t} = 0 \tag{2.45}$$

for the ideal symmetric dc SQUID, which ignores the effects of the loop inductance. When the contribution of the SQUID loop inductance is taken into account, Eq. (2.45) no longer holds when $V \neq 0$, due to a time varying circular current around the loop [63,64]. Nevertheless, Eqs. (2.44) shows that the dynamic behavior of γ_{av} is the same as that of the gauge invariant phase difference of a single Josephson junction.

Further analysis shows that $\Delta\gamma$ can be expressed in terms of the total magnetic flux through the SQUID hole [60]. Consider the line integral of the current density

shown in Fig. 2.3(b). The path of integration goes around the loop inside the superconductor and across the junctions through the insulating barriers. From Eq. (2.15),

$$\int_{C_1+C_2} \boldsymbol{J} \cdot d\boldsymbol{l} = -e|n|\frac{\hbar}{m_e}\int_{C_1+C_2}\left(\nabla\theta + \frac{2e}{\hbar}\boldsymbol{A}\right)\cdot d\boldsymbol{l} \ . \tag{2.46}$$

The line integral of $\nabla\theta$ can be expressed as

$$\int_{C_1+C_2}\nabla\theta\cdot d\boldsymbol{l} = \oint\nabla\theta\cdot d\boldsymbol{l} - \int_1\nabla\theta\cdot d\boldsymbol{l} + \int_2\nabla\theta\cdot d\boldsymbol{l} \tag{2.47}$$

where paths C_1 and C_2 are deep inside the superconductor excluding the barriers, and paths *1* and *2* are through the insulating barriers. Note that the circular direction of path *1* around the hole is in the same direction as paths C_1 and C_2 but that path *2* is in the opposite direction. The phase changes across the junction barriers are given by Eq. (2.13). So,

$$\int_i\nabla\theta\cdot d\boldsymbol{l} = \gamma_i - \frac{2e}{\hbar}\int_i\boldsymbol{A}\cdot d\boldsymbol{l} \ . \tag{2.48}$$

With a supercurrent flowing through the SQUID loop, the line integral of $\nabla\theta$ around the loop must be a multiple of 2π. Thus,

$$\int_{C_1+C_2}\nabla\theta\cdot d\boldsymbol{l} = 2\pi n - \gamma_1 + \frac{2e}{\hbar}\int_1\boldsymbol{A}\cdot d\boldsymbol{l} + \gamma_2 - \frac{2e}{\hbar}\int_2\boldsymbol{A}\cdot d\boldsymbol{l} \tag{2.49}$$

Combining Eq. (2.49) with the line integral of the vector potential $\boldsymbol{A}$,

$$\int_{C_1+C_2}\left(\nabla\theta + \frac{2e}{\hbar}\boldsymbol{A}\right)\cdot d\boldsymbol{l} = 2\pi n - \Delta\gamma + \frac{2e}{\hbar}\oint\boldsymbol{A}\cdot d\boldsymbol{l} \ . \tag{2.50}$$

As in the former case of a continuous superconducting ring, if the superconductor is thick enough, the integration can be performed deep inside the

superconductor where $\boldsymbol{J} = 0$. In this case, the left hand side of Eq. (2.50) vanishes resulting in

$$\Delta\gamma = 2\pi n + \frac{2e}{\hbar}\oint \boldsymbol{A}\cdot d\boldsymbol{l} = 2\pi n + 2\pi\,\frac{\Phi}{\Phi_o}. \tag{2.51}$$

Substituting this result into Eq. (2.42) yields

$$I = 2I_c\,cos\left(\pi n + \pi\,\frac{\Phi}{\Phi_o}\right)sin\,\gamma_{av} = (-1)^n\,2I_c\,cos\,\pi\,\frac{\Phi}{\Phi_o}\,sin\,\gamma_{av}\,. \tag{2.52}$$

Equation (2.52) shows that the current through a dc SQUID is similar to that of a single Josephson junction except that its critical current is modulated by the total magnetic flux through the hole. The magnitude of the modulated critical current is given by

$$I_c(\Phi) = 2I_c\left|\,cos\,\pi\,\frac{\Phi}{\Phi_o}\right| \tag{2.53}$$

and is periodic with period Φ_o [see Fig. 2.4(a)].

I note that in Eq. (2.40), if the critical currents of the two junctions are not identical, the supercurrent through the dc SQUID is given by

$$I = \left[(\Delta I_c)^2 + 4I_{c1}I_{c2}\,cos^2\,\pi\frac{\Phi}{\Phi_o}\right]^{\frac{1}{2}} sin(\gamma_{av} + \delta) \tag{2.54}$$

where

$$tan\,\delta = \frac{\Delta I_c}{I_{c1} + I_{c2}}\,tan\,\pi\frac{\Phi}{\Phi_o} \tag{2.55}$$

and $\Delta I_c = I_{c1} - I_{c2}$. Again, this result is only valid for the ideal dc SQUID, which ignores effects due to elements other than the Josephson junctions such as the loop inductance. Equations (2.54) and (2.55) are derived by recognizing that the

(a)

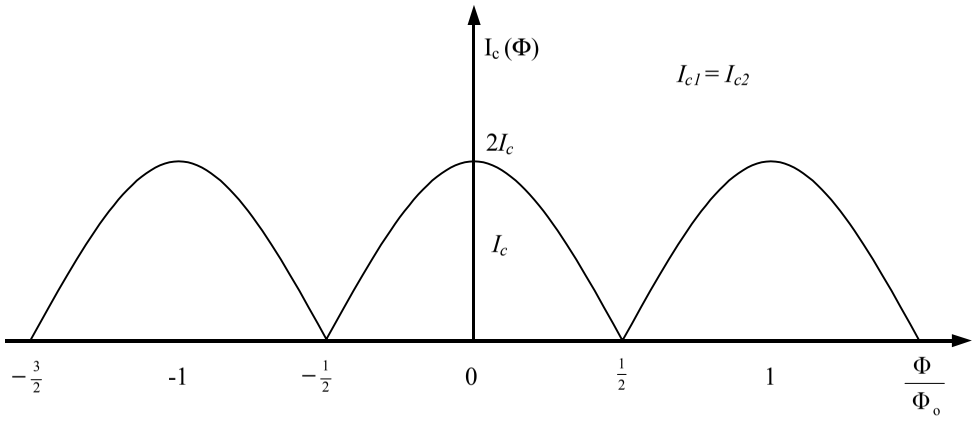

(b)

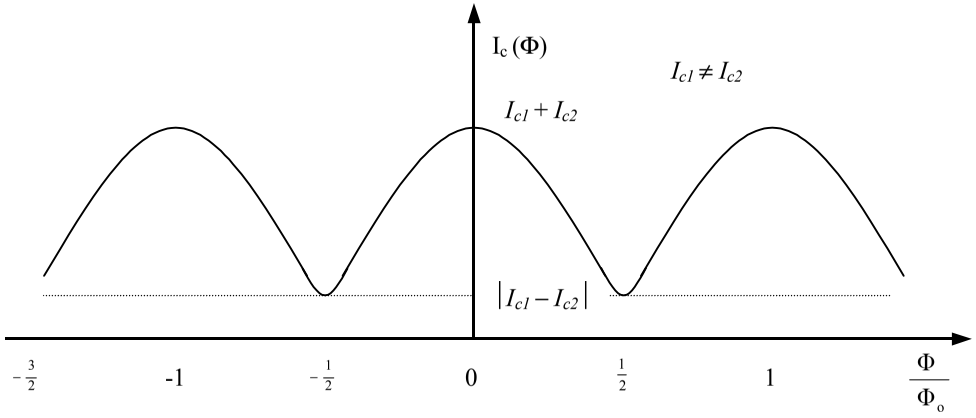

FIG. 2.4. (a) Graph of the magnitude of the supercurrent through an ideal symmetric dc SQUID with identical Josephson junctions and zero inductance plotted as a function of the total magnetic flux through the SQUID hole. (b) Graph of the maximum magnitude of the supercurrent through an ideal dc SQUID plotted as a function of the total magnetic flux through the SQUID hole when the critical currents of the Josephson junctions are different.

summation in Eq. (2.40) can be expressed as the imaginary part of a sum of two complex numbers or phasors [60]. It is also seen that the dynamic behavior of Eq. (2.54) is the same as Eq. (2.52), except that there is a magnetic flux dependent phase shift. The maximum magnitude or envelope of the critical current, which is graphed in Fig. 2.4(b), also depends on the flux and varies between ΔI_c and $I_{c1} + I_{c2}$. Both the magnitude and phase shift are periodic with period Φ_o.

The dependence of the total critical current on the magnetic flux through the SQUID hole is what makes SQUIDs very sensitive detectors. A small change in Φ, even if just a fraction of a flux quantum Φ_o, will significantly modulate the critical current. For example, an optimized 4 K dc SQUID that is 1 mm on a side is able to distinguish changes in magnetic field that are a fraction of a picotesla in one second.

2.3.2 Circulating Screening Current

In many experiments, it is the externally applied magnetic flux through the SQUID loop, not the total magnetic flux through the hole, that is the quantity of interest. The relation between the total magnetic flux Φ and the externally applied flux Φ_A is

$$\Phi = \Phi_A + LI_s \tag{2.56}$$

where L is the self inductance of the SQUID loop, and I_s is the circulating current or screening current around the hole [60,65]. Applying Eqs. (2.43) and (2.51) to an ideal dc SQUID with identical Josephson junctions,

$$I_s = \frac{I_1 - I_2}{2} = \frac{I_c}{2}\left(\sin\gamma_1 - \sin\gamma_2\right) = I_c \sin\frac{\gamma_1 - \gamma_2}{2}\cos\frac{\gamma_1 + \gamma_2}{2}$$
$$= I_c \sin\frac{\Delta\gamma}{2}\cos\gamma_{av} = I_c \sin\left(\pi n + \pi\frac{\Phi}{\Phi_o}\right)\cos\gamma_{av} \quad . \tag{2.57}$$
$$= (-1)^n I_c \sin\pi\frac{\Phi}{\Phi_o}\cos\gamma_{av}$$

Therefore, the externally applied flux is given by

$$\Phi_A = \Phi - (-1)^n L I_c \sin\pi\frac{\Phi}{\Phi_o}\cos\gamma_{av} . \tag{2.58}$$

From Eq. (2.58), one can see that in order to determine the critical current of the SQUID as a function of applied magnetic flux, i.e. $I_c(\Phi_A)$, the total magnetic flux Φ must be solved by inverting Eq. (2.53) and plugging that result into Eq. (2.58). In the limiting case when $\Phi_o >> LI_c$, Eq. (2.58) reduces to

$$\Phi_A \approx \Phi , \tag{2.59}$$

and so

$$I_c(\Phi_A) \approx 2I_c\left|\cos\pi\frac{\Phi_A}{\Phi_o}\right| . \tag{2.60}$$

Note that the inversions of both Eqs. (2.53) and (2.60) are multivalued and can only be solved modulo $\frac{1}{2}\Phi_o$. In addition, it may not be clear in Eq. (2.58) whether the flux due to the circulating current should add or subtract from the total flux. These ambiguities can be resolved by introducing constraints such as energy minimization and by keeping track of the flux, phase differences, and currents [60,63].

Equations (2.57) and (2.58) demonstrate how a SQUID loop differs from a complete superconducting loop. For a given applied magnetic flux, the allowed

values of the circulating current are discrete and constant in the case of the continuous loop regardless of changes in the bias current. For a SQUID loop, the value of γ_{av} varies continuously with the bias current through the SQUID. So, the circulating current can also change continuously with the bias current up to a maximum value within the limits set by Eqs. (2.17) and (2.58). Correspondingly, the allowed values of the total magnetic flux through the SQUID hole are not discrete but have segments in which they can vary continuously.

2.4 Hysteresis in Josephson Junctions and SQUIDs

2.4.1 RCSJ Model

Equations (2.17) and (2.28) alone do not fully describe the characteristics present in a real Josephson junction. Real junctions show more complex behavior that require circuit elements in addition to the ideal junction. The Resistively and Capacitively Shunted Junction (RCSJ) model (see Fig. 2.5) has been widely used to explain the behavior of real junctions and SQUIDs, both qualitatively and quantitatively [66-71]. The RCSJ model consists of an ideal Josephson junction in parallel with a capacitor and a resistor. The capacitor represents the physical fact that a real Josephson junction has finite size and capacitance between the two superconducting electrodes that are separated by the insulating barrier. The resistive channel reflects dissipative losses across the junction. These losses can arise from quasiparticle tunneling, inductive losses at nonzero frequencies, flux flow of vortices, flux pinning near the surface, the tunneling of normal electrons from the breakup of

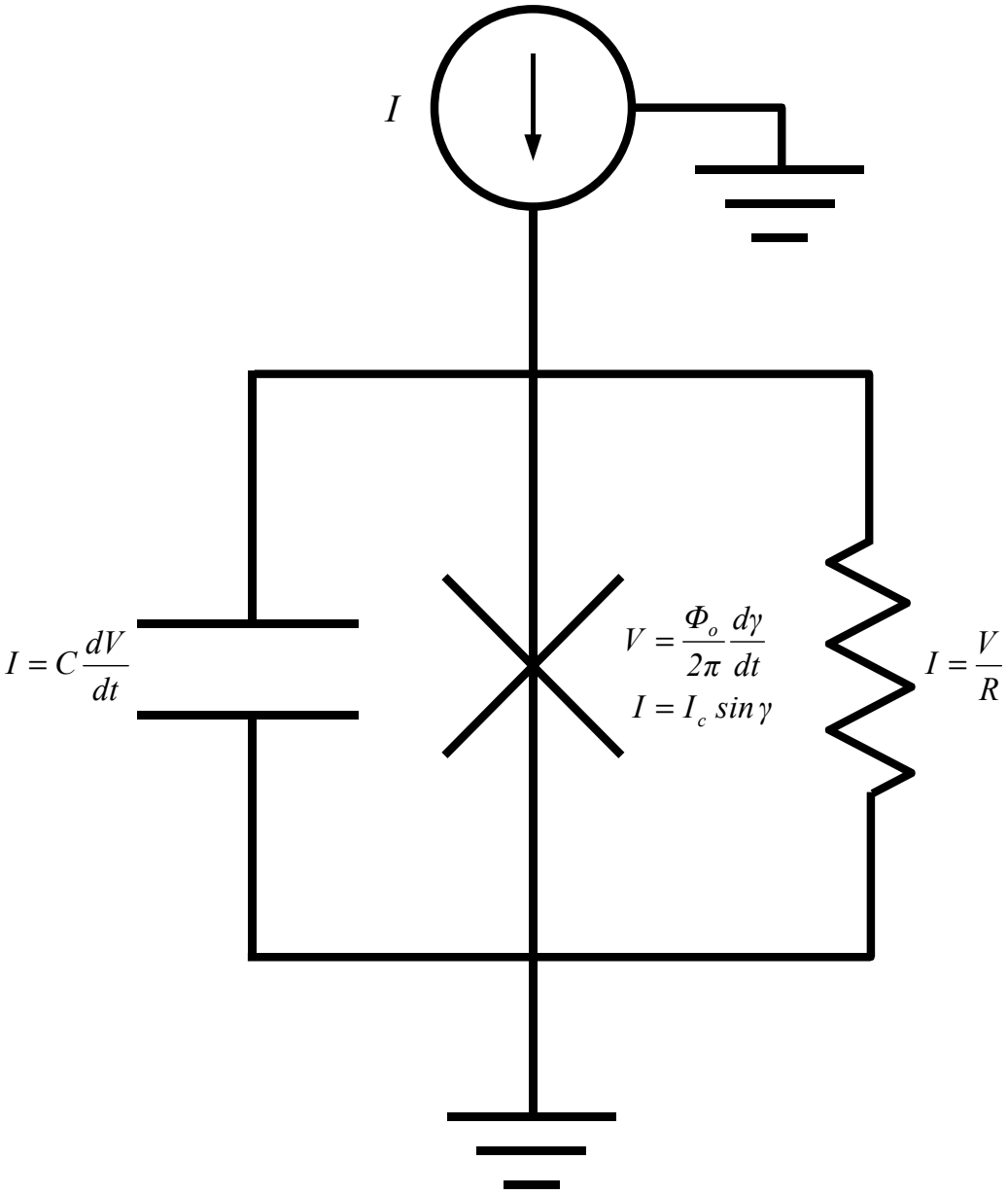

FIG. 2.5. Equivalent electronic circuit of a real Josephson junction described by the Resistively and Capacitively Shunted junction model. A current source which provides the bias current to the junction and ground are also shown.

Cooper pairs or from an extrinsic resistive path deliberately connected across the junction [72-79].

The value of the effective shunt capacitance is assumed to be independent of the bias voltage, bias current, frequency or temperature, as it is mainly set by the geometric configuration of the junction and the choice of insulating material. However, the junction critical current is influenced by temperature, the superconducting material, and geometry [40,41,80]. Furthermore, the effective shunt resistance due to quasiparticles is strongly dependent on temperature and bias voltage [74,79]. For simplicity, I will treat the resistance as piecewise linear. Given this equivalent circuit, the RCSJ model for a Josephson junction can be analyzed without further need to resort to first principles.

Assuming a lumped circuit, the current through the ideal Josephson junction is given by integrating Eq. (2.17) over the junction area resulting in

$$I = I_c \sin \gamma . \tag{2.61}$$

In Eq. (2.61), I_c is the total critical current and is considered constant for constant environmental factors. At zero temperature, it is the maximum dc supercurrent allowed through the junction. The current through the capacitive channel is given by

$$I = C \frac{dV}{dt} \tag{2.62}$$

where V is the voltage across the junction, and C is the effective junction capacitance. The current through the resistive channel is given by Ohm's law,

$$I = \frac{V}{R} \tag{2.63}$$

where R is the effective shunt resistance and is assumed to be constant. Thus, the total current through the RCSJ model junction is the sum

$$I = C\frac{dV}{dt} + \frac{V}{R} + I_c \sin\gamma . \tag{2.64}$$

Recognizing that the gauge invariant phase difference γ is only a function of time, Eq. (2.28) provides a relation between γ and V:

$$\frac{d\gamma}{dt} = \frac{2\pi}{\Phi_o}V . \tag{2.65}$$

Substituting this into Eq. (2.64) gives

$$I = \frac{C\Phi_o}{2\pi}\frac{d^2\gamma}{dt^2} + \frac{\Phi_o}{2\pi R}\frac{d\gamma}{dt} + I_c \sin\gamma . \tag{2.66}$$

Equation (2.66) can be transformed into dimensionless form by using the substitutions

$$y = \frac{I}{I_c} \tag{2.67}$$

and

$$x = \frac{2\pi I_c R}{\Phi_o}t \equiv \frac{t}{\tau_J} \tag{2.68}$$

where $\tau_J = \Phi_o/2\pi I_c R$, which results in

$$y = \frac{RC}{\tau_J}\frac{d^2\gamma}{dx^2} + \frac{d\gamma}{dx} + \sin\gamma \equiv \beta_c\frac{d^2\gamma}{dx^2} + \frac{d\gamma}{dx} + \sin\gamma . \tag{2.69}$$

where $\beta_c = \tau_{RC}/\tau_J = 2\pi I_c R^2 C/\Phi_o$ and $\tau_{RC} = RC$.

From Eq. (2.69), τ_J is seen to be the time it takes for the gauge invariant phase difference γ of the Josephson junction to go through a rotation of 1 radian at the bias voltage I_cR. The constant τ_{RC} is recognized as the time constant in an RC circuit. It

corresponds to the time for a charged capacitor C to discharges through a resistor R to a level that is $1/e$ of the original voltage, where e is the base of the natural logarithm. The constant β_c is the ratio between τ_{RC} and τ_J and is commonly referred to as the Stewart-McCumber parameter [66,67]. If $\beta_c >> 1$, the dynamics of γ is dominated by the ac Josephson effect. If $\beta_c << 1$, the dynamics is dominated by the "damping effect" or discharging of the RC circuit elements, and Eq. (2.69) simplifies to

$$y \approx \frac{d\gamma}{dx} + \sin\gamma \,. \tag{2.70}$$

2.4.2 Nonhysteretic Junctions

Equation (2.69) can be shown to be analogous to the equation for a damped pendulum driven with constant torque in a gravitational field. The behavior of the damped driven pendulum is nonlinear and is treated in many standard texts on nonlinear dynamics [81-85]. The treatment here will follow the geometric approach of Strogatz.

First, it can be seen from Eq. (2.69) that analysis can be limited to values of γ between $-\pi$ and π due to periodicity, and that the solutions for γ with $y < 0$, can be expressed in terms of the solutions with $y > 0$ due to inversion symmetry. Thus, analysis can be restricted to the range $0 \le y \le \pi$. Next, Eq. (2.69) can be written in terms of two coupled first order nonlinear differential equations.

$$\frac{d\gamma}{dx} = v \tag{2.71}$$

$$\frac{dv}{dx} = \frac{1}{\beta_c}\left(y - v - \sin\gamma \right). \tag{2.72}$$

Now, consider the behavior of Eqs. (2.71) and (2.72) as $\beta_c \to 0$, sometimes referred to as the over damped case following the pendulum analogy. This is the case described by Eq. (2.70). The term $\beta_c \frac{dv}{dx} \to 0$. So,

$$y - v - \sin\gamma = 0 \quad \text{or} \quad v = y - \sin\gamma \,. \tag{2.73}$$

All points in the phase space (γ, v) lie on the curve described by Eq. (2.73) which is graphed in Fig. 2.6. The evolution of these points with respect to x is determined by Eq. (2.71).

Consider the case when $y < 1$. For points on the curve where $v > 0$, the value of γ increases. For points where $v < 0$, γ decreases. Therefore, all points on the curve eventually go to the point where

$$v = 0 \quad \text{and} \quad y = \sin\gamma \tag{2.74}$$

which gives

$$\gamma = \arcsin\ y \tag{2.75}$$

except for the point given by

$$\gamma = \pi - \arcsin\ y \quad \text{with} \quad v = 0 \tag{2.76}$$

which can be shown to be unstable.

Equations (2.75) and (2.76) thus have fixed points that are defined by the condition $d\gamma/dx = dv/dx = 0$. It can be seen that when $y = 0$, $\gamma = 0$, and as y increases, γ goes through a succession of fixed points until $y = 1$ when $\gamma = \pi/2$. Also, recall that $d\gamma/dt$ is proportional to the voltage V by Eq. (2.65). Then, from $v = d\gamma/dx = \tau_J\, d\gamma/dt$, the voltage $V = 0$ because $v = 0$ for the fixed points. By inspection, this is just the result expected for the junction supercurrent which is present when $y = I / I_c < 1$.

(a)

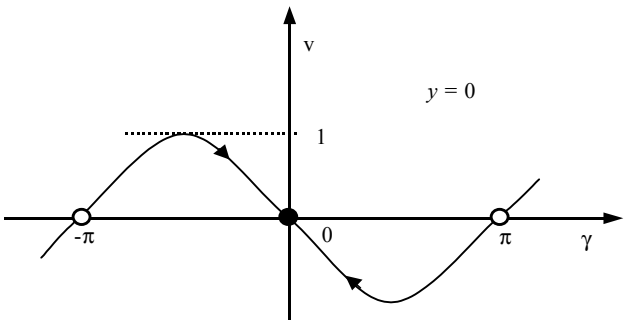

(b)

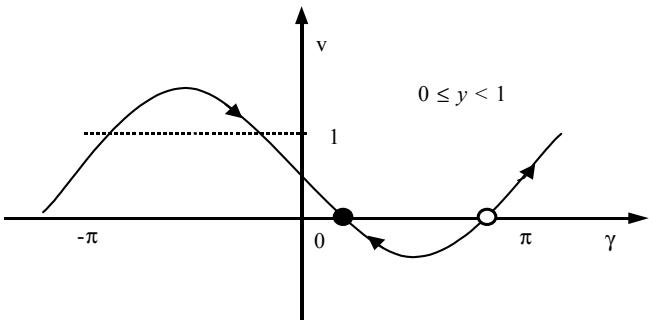

(c)

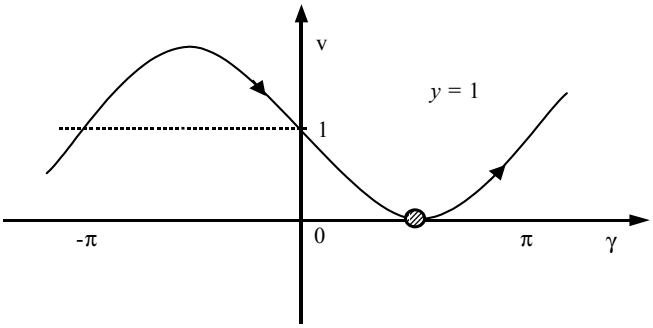

(d)

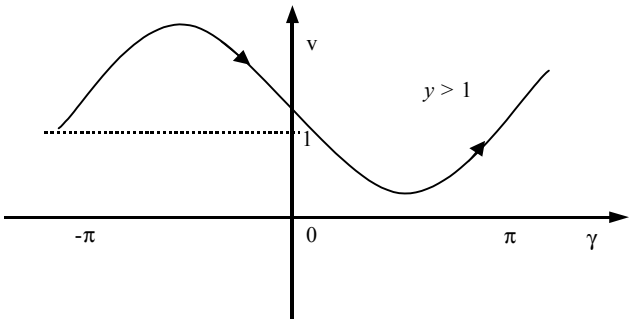

FIG. 2.6. Series of graphs showing the evolution of the phase space (γ, v) of the over damped Josephson junction ($\beta_c << 1$) as the bias current $y = I/I_c$ rises from (a) $y = 0$ to (b) $0 \le y < 1$ to (c) $y = 1$ and finally (d) $y > 1$, at which point a voltage appears across the junction. Filled in dots, outlined dots, and striped dots signify stable fixed points, unstable fixed points, and half stable points, respectively. Arrows signify the direction of evolution of the points.

For $y > 1$, there are no fixed points and the value of γ continually increases. This results in a voltage across the junction [68,69]. Also, note that as $d\gamma/dx$ is not constant for a given value of y, neither is the voltage. Typically, in experiments only the average voltage is detected for measurement time scales much longer than τ_J. Using Eqs. (2.65) and (2.68), the average voltage is given by

$$\langle V \rangle = \frac{\Phi_o}{2\pi\tau_J}\langle v \rangle = \frac{\Phi_o}{2\pi\tau_J}\cdot\frac{1}{T}\int_0^T v dt = \frac{\Phi_o}{2\pi}\cdot\frac{1}{T}\int_0^{2\pi} d\gamma = \frac{\Phi_o}{T} \tag{2.77}$$

where T is the period of v. T can be obtained by solving for γ using Eqs. (2.71) and (2.73). For $y > 1$, the solution is given by

$$x = -\frac{2}{\sqrt{y^2-1}}\arctan\left(\frac{1-y\tan\frac{\gamma}{2}}{\sqrt{y^2-1}}\right), \tag{2.78}$$

and so

$$\gamma = 2\arctan\left(\frac{1}{y}+\sqrt{1-\frac{1}{y^2}}\tan\frac{\sqrt{y^2-1}}{2}x\right). \tag{2.79}$$

And thus,

$$v = \frac{d\gamma}{dx} = \frac{\left(y-\frac{1}{y}\right)\sec^2\frac{\sqrt{y^2-1}}{2}x}{1+\left(\frac{1}{y}+\sqrt{1-\frac{1}{y^2}}\tan\frac{\sqrt{y^2-1}}{2}x\right)^2}. \tag{2.80}$$

Both γ and v can be shown to be periodic in time as expected. Using Eqs. (2.67) and (2.68), the period is given by

$$T = \frac{2\pi\tau_J}{\sqrt{y^2-1}} = \frac{\Phi_o}{I_c R}\left[\left(\frac{I}{I_c}\right)^2-1\right]^{-\frac{1}{2}}. \tag{2.81}$$

Therefore, the average voltage across the junction is given by

$$\langle V \rangle = \frac{\Phi_o}{T} = I_c R \left[\left(\frac{I}{I_c} \right)^2 - 1 \right]^{\frac{1}{2}} \tag{2.82}$$

and is graphed in Fig. 2.7. Equation (2.82) shows that a finite voltage across the junction gradually appears as I increases past I_c and asymptotically approaches Ohmic behavior with increasing current.

2.4.3 Hysteretic Junctions

As $\beta_c \rightarrow \infty$, the behavior of Eqs. (2.71) and (2.72) can be treated in the following way. When $dv/dx = 0$, Eq. (2.73) which was derived for $\beta_c = 0$ is recovered and the same arguments can be made resulting in the conclusion that a supercurrent with $V = 0$ will flow through the junction up to the point $I = I_c$ or $y = 1$. This result required the existence of fixed points and was only possible for $y < 1$. If $dv/dx \neq 0$, then in the limit $\beta_c \rightarrow \infty$, Eq. (2.72) reduces to

$$y = \beta_c \frac{dv}{dx} + v + sin\ \gamma \approx \beta_c \frac{dv}{dx}. \tag{2.83}$$

Solving for v gives

$$v = \frac{y}{\beta_c} x + v_o \approx v_o \tag{2.84}$$

again in the limit $\beta_c \rightarrow \infty$. Thus, γ is given by

$$\gamma = v_o x \tag{2.85}$$

from Eq. (2.71).

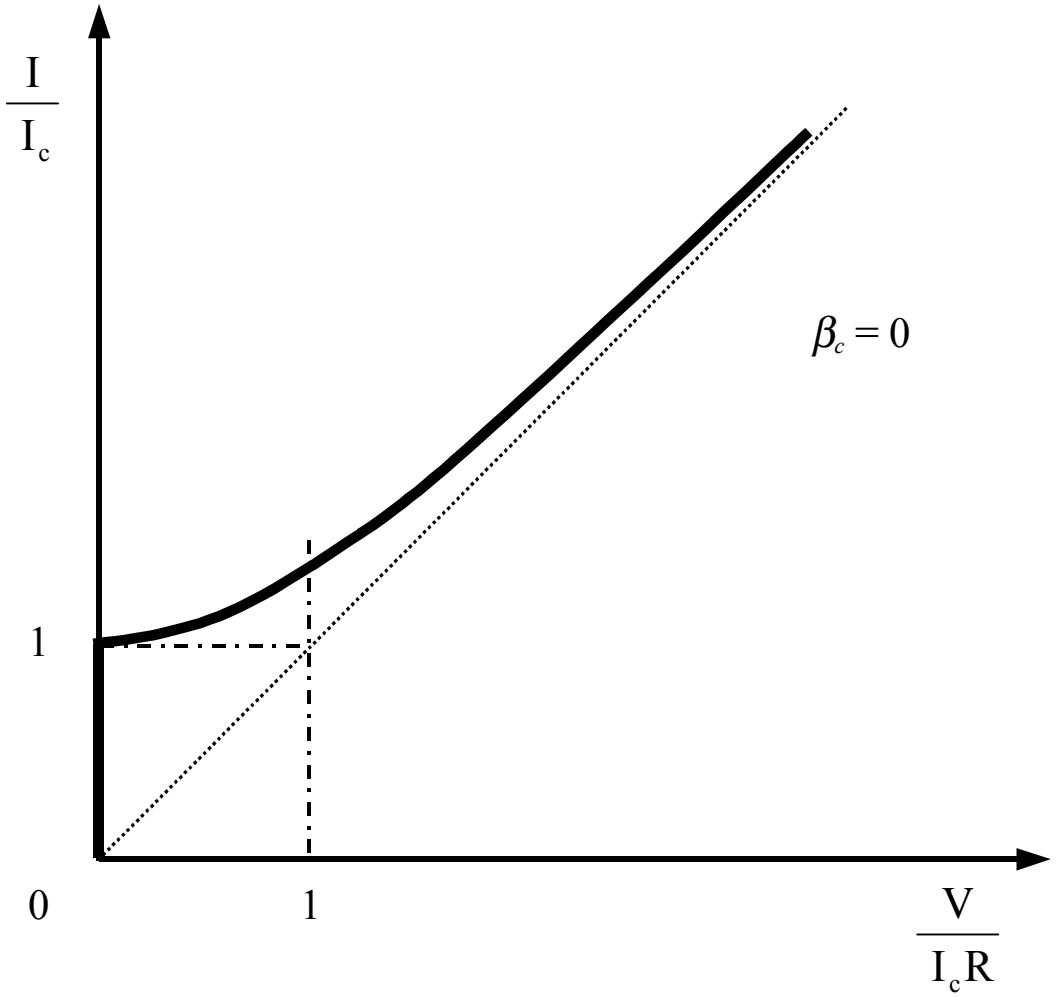

FIG. 2.7. I-V characteristics of an over damped ($\beta_c << 1$) Josephson junction at zero temperature. Dotted curve shows $I = V/R$.

Note that this result implies that a voltage is observed across the junction consistent with the ac Josephson effect, and using Eqs. (2.65) and (2.68), one finds

$$V = \frac{\Phi_o}{2\pi\tau_J} v = \frac{\Phi_o}{2\pi\tau_J} v_o \,. \tag{2.86}$$

With the rough approximation made in Eq. (2.83), the value of v_o and consequently V are independent of y. As will be seen later, this will not be the case with better approximations.

Next, let us assume the quasiparticle tunneling through the insulating barrier is Ohmic [69]. Then, the voltage across the junction can be given by

$$V = IR \,. \tag{2.87}$$

If no quasiparticles are initially present to give rise to resistive tunneling, the gap energy 2Δ must be supplied to break up Cooper pairs. At zero temperature with no other current path present, resistive currents will only occur after the voltage across the junction reaches the gap voltage $2\Delta/e$. Therefore, if a supercurrent can no longer be sustained through the junction, a voltage will appear such that

$$V = \begin{cases} IR & \text{for } V \geq \dfrac{2\Delta}{e} \\ \dfrac{2\Delta}{e} & \text{otherwise} \end{cases} \,. \tag{2.88}$$

The two different cases for $I_cR < 2\Delta/e$ and $I_cR > 2\Delta/e$ are presented in Fig. 2.8(a) and 2.8(b), respectively. I note that Ambegaokar and Baratoff have shown that

$$I_c R = \frac{\pi\Delta(T)}{2e} \tanh \frac{\Delta(T)}{2kT} \tag{2.89}$$

which at zero temperature reduces to

$$I_c R = \frac{\pi}{4} \cdot \frac{2\Delta(0)}{e} \approx 0.79 \cdot \frac{2\Delta(0)}{e} \tag{2.90}$$

(a)

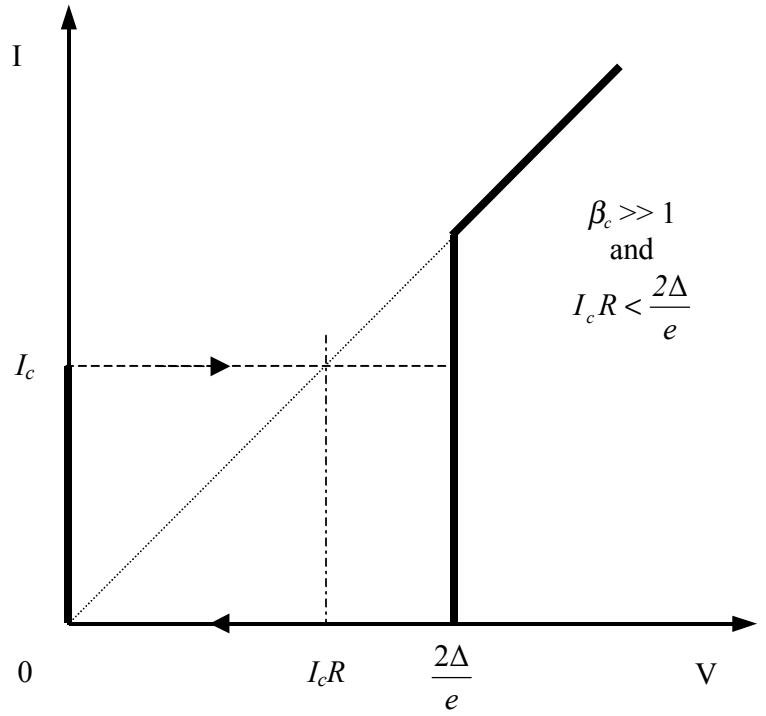

(b)

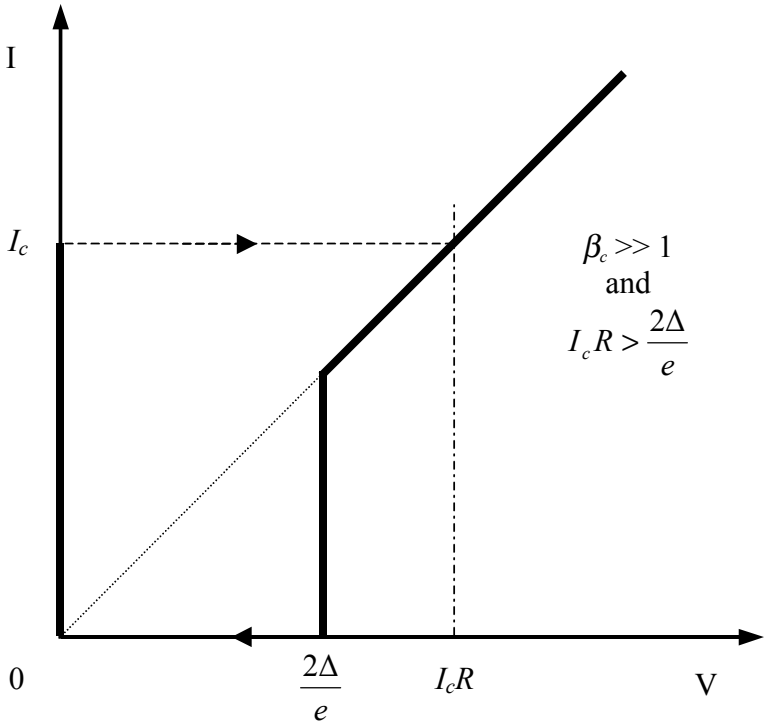

FIG. 2.8. I-V characteristics of an under damped ($\beta_c >> 1$) Josephson junction at zero temperature when (a) $I_cR < 2\Delta/e$ and (b) $I_cR > 2\Delta/e$. Arrows indicate the direction of jumps during transitions between the zero voltage state and the resistive state. Under ordinary circumstances, case (b) $I_cR > 2\Delta/e$ is not expected to occur.

using the BCS theory [41,80]. Consequently, as $tanh(\Delta/2kT) < 1$, the latter case of $I_cR > 2\Delta/e$ is not expected to occur.

Recall that Eq. (2.85) is independent of y, but does require that $dv/dx \neq 0$. In fact, a voltage can be sustained for $y < 1$ as long as $dv/dx \neq 0$. In this case, the voltage continues to follow Eq. (2.88) until the bias current reaches zero or $y = 0$. When that happens, dv/dx is required to equal zero by Eq. (2.83). Thus, the I-V characteristics for the junction with $\beta_c >> 1$ can be seen to be qualitatively different from the previous case of $\beta_c << 1$. As y increases from $y = 0$ and surpasses the point $y = 1$, v is seen to jump from $v = 0$ to $v = (2\pi\tau_J/\Phi_o)V = V / I_cR$ with further increases in y resulting in V following Eq. (2.88). If y is decreased, v does not drop back to $v = 0$ at $y = 1$, but continues to follow $v = V / I_cR$ where V is given by Eq. (2.88) until $y = 0$. This I-V curve for $\beta_c \rightarrow \infty$, graphed in Fig. 2.8, is known to be valid when the Josephson junction is at zero temperature. Such irreversible behavior of v with respect to y, the controlling parameter, is an example of hysteresis. Hysteresis occurs when $\beta_c \approx 1$ [66,67,81].

At finite temperatures, the I-V characteristics deviate from those shown in Fig. 2.8. Some of these deviations can be explained with the inclusion of an additional term in Eq. (2.83). For very large β_c, γ can still be approximated by Eq. (2.85), in which case $sin\ \gamma$ varies so rapidly that its average effect is zero. Then, instead of Eq. (2.83), the governing equation becomes

$$y = \beta_c \frac{dv}{dx} + v \tag{2.91}$$

which can be solved to give

$$v = y + y_o\, e^{-\frac{x}{\beta_c}} \approx y \tag{2.92}$$

as $x \to \infty$, where y_o is the starting value of y in the phase space of (v, dv/dx). In other words, all points in this phase space merge exponentially fast toward the point given by $v = y$.

The exception to this result is when $dv/dx = 0$ in the original equation of state, Eq. (2.72). In this exception, the result leads to the existence of the supercurrent with $v = 0$. The relation $v = y$ is just Ohm's law stated in normalized units, which is incorporated in Eq. (2.88). However, Eq. (2.92) also implies that Ohm's law continues to apply for $V < 2\Delta/e$. An additional factor to consider is that the effective resistance of the junction is different above and below $V = 2\Delta/e$ [69,70,79]. Above $2\Delta/e$, the dominant loss mechanism is single electron tunneling through the break up of Cooper pairs. Below $2\Delta/e$, tunneling is by quasiparticles that are excited thermally. In type I superconductors, the conductance associated with quasiparticle tunneling at low temperatures and low voltage is very small because few quasiparticles are present [34,86]. Consequently, the resulting subgap resistance R_{sg} is greater than the normal resistance R above $2\Delta/e$. In type II superconductors, however, quasiparticle tunneling mechanisms are more easily allowed when magnetic flux penetrates into the superconductor, as this causes regions where the gap vanishes. This results in a smooth transition of the resistance from the subgap value to the normal value in fields above H_{c1} [87].

The effect of a large subgap resistance can be treated through a scaling of the normalized units. If the subgap resistance is given by

$$R_{sg} = \alpha R \quad \text{where} \quad \alpha >> 1 \tag{2.93}$$

then, in terms of the normal resistance R, Eqs. (2.69) and (2.91) transform into

$$y = \beta_c \frac{d^2\gamma}{dx^2} + \frac{1}{\alpha}\frac{d\gamma}{dx} + \sin\gamma \tag{2.94}$$

and

$$y = \beta_c \frac{dv}{dx} + \frac{v}{\alpha}. \tag{2.95}$$

The solution of Eq. (2.95) is given by

$$v = \alpha y + y_o\, e^{-\frac{x}{\alpha\beta_c}} \approx \alpha y \tag{2.96}$$

as $x \rightarrow \infty$ giving the expected result $v / y = \alpha >> 1$.

Figure 2.9 shows the resulting I-V characteristics of the hysteretic junction at finite temperature. As y increases from $y = 0$, v remains at $v = 0$ until $y = 1$ at which point v jumps to the curve $v = V / I_cR$, where here V is given by Eq. (2.88), and follows this curve with further increases in y. If y decreases, v retraces the curve $v = y$ until $v = 2\Delta / eI_cR$. Then, despite further decreases in y, v remains at $v = 2\Delta / eI_cR$ until $y = v/\alpha$ where $\alpha = R_{sg}/R$. From that point on, v follows the curve $v = \alpha y$ as y decreases to $y = 0$.

Full analysis of Eq. (2.69) reveals additional features due to the $\sin\gamma$ term left out in Eqs. (2.91) and (2.95) [70,81]. As the voltage decreases below $2\Delta/e$, Eq. (2.85) no longer holds and γ begins to evolve non-uniformly and more slowly. This is similar to the situation with $\beta_c = 0$ at small v. There, the result was a decrease in v that was more rapid than $v = y$. Here, a decrease occurs that is more rapid than $v = \alpha y$ and implies that the voltage returns to zero before $y = 0$. This is referred to as retrapping and its onset is determined by the value of β_c.

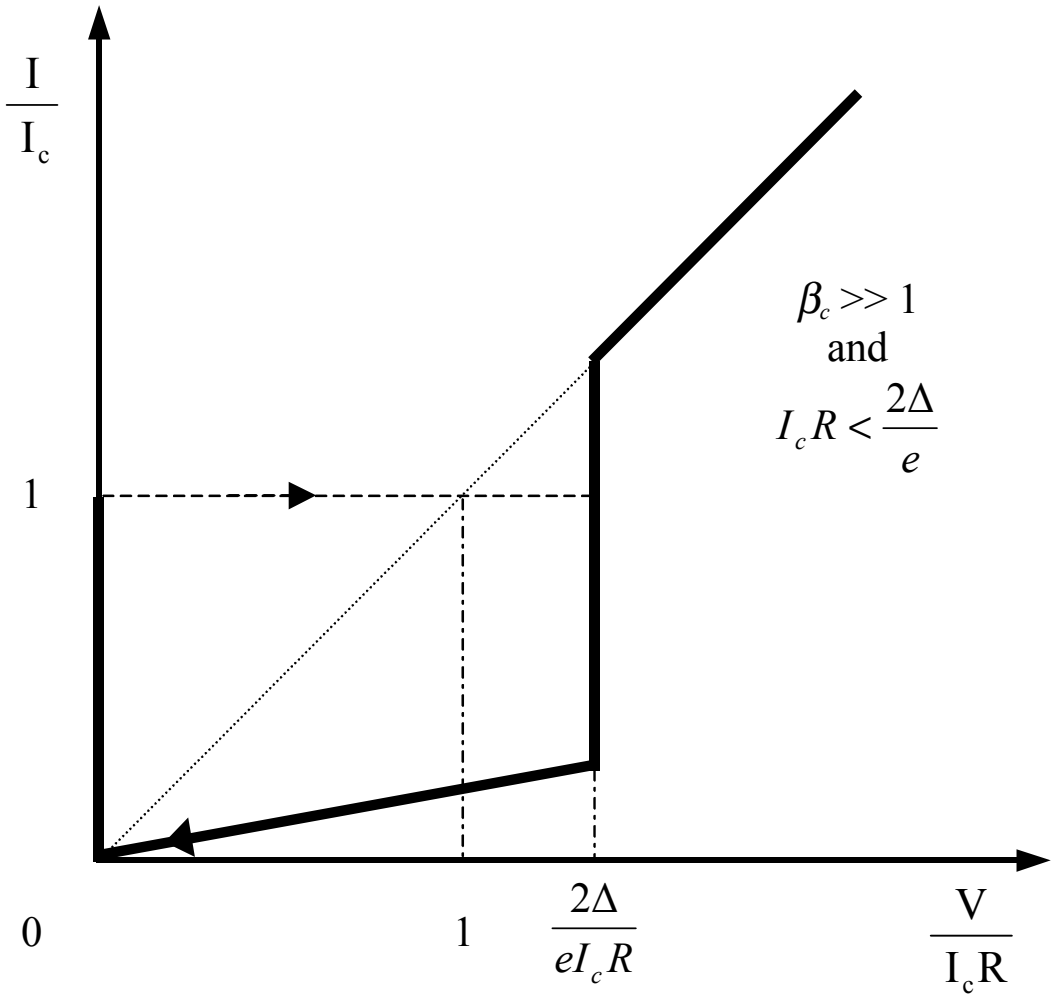

FIG. 2.9. Approximate I-V characteristics of an under damped ($\beta_c >> 1$) Josephson junction with $I_cR < 2\Delta/e$ at finite temperature in the RCSJ model. A piecewise linear approximation of the RCSJ resistor is used.

Analysis by Guckenheimer and Holmes, as cited by Strogatz, shows that the onset of retrapping occurs near $y_r = 4 / \pi\sqrt{\beta_c}$, as $\beta_c \rightarrow \infty$ [81]. An alternate derivation is given in Ref. [70]. Unlike the jump at $y = 1$, retrapping is continuous. Nevertheless, retrapping is experimentally seen as a sudden jump due to the rapid approach of v to $v = 0$; v behaves like $[\ ln|\ y - y_r\ |\ ]^{-1}$ near $y = y_r$. The resulting complete I-V curve of the Josephson junction at finite temperature is presented in Fig. 2.10. As expected, retrapping will not occur unless there is hysteresis. Studies of the parameter space (β_c, y) as presented in Ref. [81] show that at zero temperature hysteresis will not happen until β_c is greater than 0.69, i.e. of order unity. Similar results are reported by Stewart and de Waal *et al*. [64,66]. Levi *et al*. and other references on nonlinear equations, as suggested in Ref. [81], provide a more rigorous analysis. Finally, some of the sharp edges and well-defined limits of I-V curves are rounded off or smeared by noise due to thermal and nonlinear effects. Such effects have been described by Tinkham and others [70,71,88-93].

2.4.4 From Junctions to dc SQUIDs

Earlier, I described dc SQUIDs as being like Josephson junctions with critical currents that are modulated by the magnetic flux through their holes. Using this idea, it follows that dc SQUIDs will also manifest hysteresis and other characteristics described by the RCSJ model. All of the results for the RCSJ model can be crudely used to model a dc SQUID by substituting I_c with $I_c(\Phi)$, where Φ is the magnetic flux through the SQUID hole. However in my treatment of the Josephson junction, I_c was assumed to be constant. So, the RCSJ model results will only be valid for dc

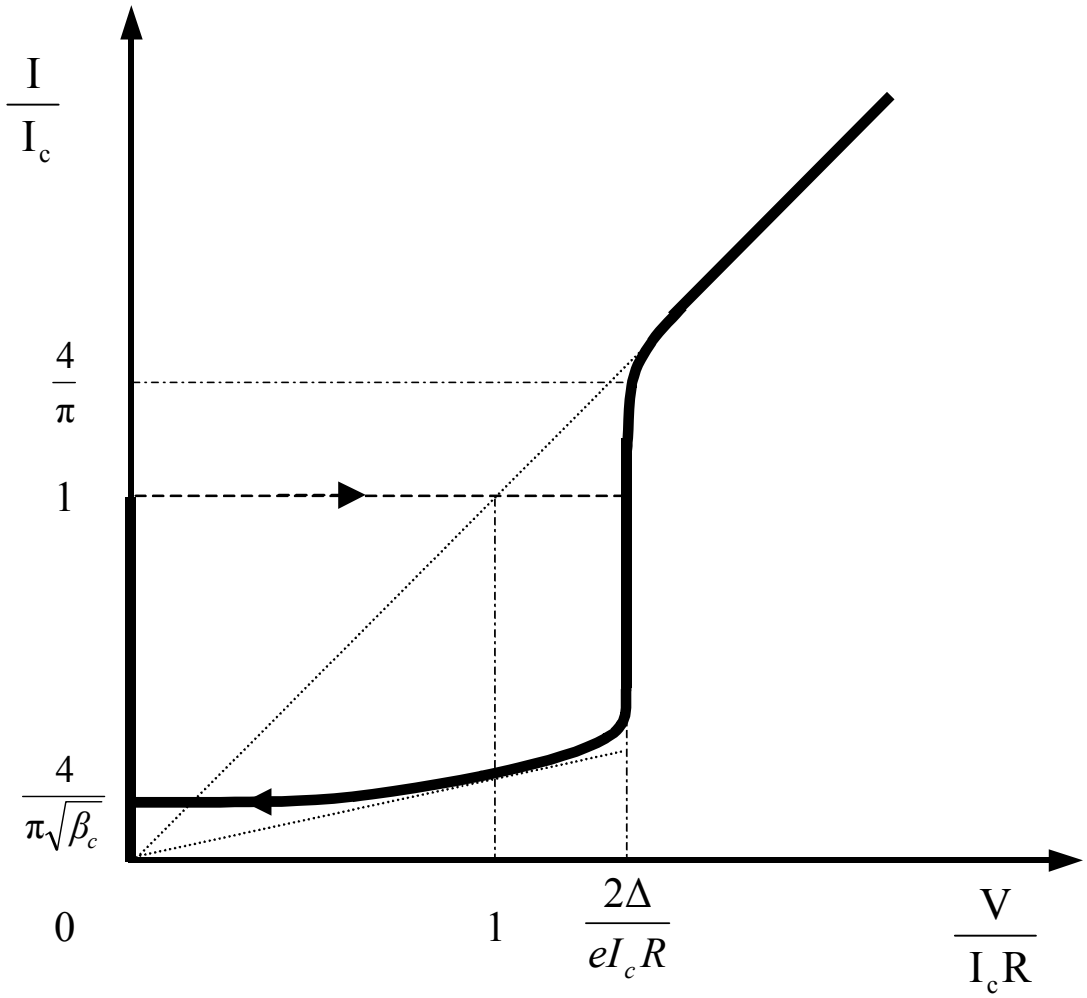

FIG. 2.10. I-V characteristics of an under damped ($\beta_c >> 1$) Josephson junction with $I_cR < 2\Delta/e$ at finite temperature including retrapping. Arrows on graph indicate direction of jumps during transitions between the zero voltage state and the resistive state. The vertical reference currents for retrapping and the gap voltage are the values at zero temperature.

SQUIDs if the characteristic time of $I_c(\Phi)$ and consequently Φ is very long compared to the characteristic time of the junction.

The characteristic time of a Josephson junction is the greater of τ_{RC} and τ_J. The characteristic time of the magnetic flux Φ through the SQUID hole is the period of the maximum frequency Fourier component of Φ. If the range of frequencies starts from dc, the characteristic time is the inverse bandwidth. Thus, the analysis in this section should roughly be valid for dc SQUIDs given the condition

$$\begin{aligned} &\text{for} \quad \beta_c > 1, \quad \tau_{RC} << \frac{1}{\Delta f} \\ &\text{for} \quad \beta_c < 1, \quad \tau_J << \frac{1}{\Delta f} \end{aligned} \tag{2.97}$$

where Δf is the bandwidth of the externally applied magnetic flux signal. Thus, I note that the time constants τ_{RC} and τ_J are of fundamental importance in determining the dc SQUID bandwidth for high speed magnetic flux sampling.

CHAPTER 3 SQUID Design Considerations

3.1 SQUID Parameter Optimization

3.1.1 SQUID Loop Inductance and Spatial Resolution

I begin this chapter by discussing practical concerns in designing dc SQUIDs for SQUID microscopy. The main points of discussion are the spatial, temporal, and magnetic flux resolution. The spatial resolution of a SQUID is mainly determined by the dimensions of the SQUID and its distance from the magnetic source. A SQUID is sensitive to the total magnetic flux through its hole. Information pertaining to field variations or gradients at scales less than the dimensions of the hole tend to be lost. Consequently, the average magnetic field over the area of the hole is what is measured.

SQUID dimensions can effect spatial resolution in the following way. For wide SQUID loops, where the widths of the loop are comparable or larger than the diameter of the hole, some of the flux incident outside the hole can be channeled through the hole by the Meissner effect [4,13,94]. This is referred to as "flux-focussing". Thus, spatial resolution tends to worsen and increase beyond the hole size for loops with wide line widths. On the other hand, the larger line widths increase the effective area, which in turn increases field sensitivity by enhancing the field through the hole. An optimal balance can be reached by first determining the

maximum spatial resolution required and then adjusting the width and hole size until the desired field sensitivity is reached.

The dimensions of the SQUID loop also determine the self inductance of the loop, which influences field sensitivity, as will be seen later. The inductance is primarily dependent on the size and shape of the loop but could also depend on the position and sizes of the Josephson junctions and any leads connecting them due to their influence on current flow [95-97]. Numerical methods have been developed to calculate the inductances, but some general conclusions on the inductance with respect to dimension can be drawn from basic ideas.

First, due to the superconducting nature of the loop, most of the current will flow along the inner edge of the hole. This leads to the conclusion that the width of a loop has less influence on the inductance than the size of the hole. In fact, Jaycox and Ketchen have shown by numerical simulation that the inductance of a square loop is almost independent of the line width of the loop when the line width surpasses the width of the hole [97]. They further show that the limiting value of the self inductance L for a square hole is given approximately by

$$L = 1.25\,\mu_o d \tag{3.1}$$

where d is the inner side length of the square hole. Therefore, for a given effective SQUID area, the inductance of a SQUID loop can be reduced to $1.25\mu_o d$ by increasing the line width of the loop, which in turn reduces the hole size.

I note that Eq. (3.1) is qualitatively consistent with the inductance of a planar loop with circular cross section, where the self inductance L goes as

$$L \approx \frac{\mu_o}{4\pi} C_{ir} \, ln \frac{A_{rea}}{a^2} \tag{3.2}$$

where C_{ir} is the circumference of the loop, A_{rea} is the area enclosed by the loop, and a is the width of the conductor forming the loop [98]. If $C_{ir} = 4d$ and $A_{rea} = d^2$, it can be seen that $L \propto d$ as long as $ln(d/a)$ does not vary very much. In Eq. (3.2), it is assumed that $d >> a$, so $ln(d/a)$ always comes out positive.

3.1.2 SQUID Bandwidth

For a SQUID to have high temporal resolution, its bandwidth must be large. An upper limit on the bandwidth can be inferred from the analysis presented in section 2.4. The bandwidth limits are summarized in Eq. (2.97):

$$\text{for} \quad \beta_c > 1 \quad \text{or} \quad \tau_{RC} > \tau_J, \quad \Delta f < \frac{1}{\tau_{RC}} = \frac{1}{RC}, \tag{3.3}$$

$$\text{for} \quad \beta_c < 1 \quad \text{or} \quad \tau_{RC} < \tau_J, \quad \Delta f < \frac{1}{\tau_J} = \frac{2\pi I_c R}{\Phi_o}, \tag{3.4}$$

where Δf is the SQUID bandwidth. In other words, the bandwidth is limited by the longer of the two time constants τ_{RC} and τ_J.

If the geometric mean of τ_{RC} and τ_J is calculated, it gives

$$\Delta f < \frac{1}{\sqrt{\tau_{RC}\tau_J}} = \sqrt{\frac{2eI_c}{\hbar C}} \equiv \omega_p \tag{3.5}$$

where $\omega_p = 2\pi f_p$ is known as the "plasma frequency" of the junction. Although f_p is only an upper limit for Δf, it is a convenient parameter since it does not require knowledge of the effective shunt resistance of the Josephson junctions. Furthermore, the capacitance and critical current are both approximately proportional to the

junction area. Thus, the ratio I_c/C and consequently some limitations on the bandwidth are determined by the intrinsic junction characteristics. For the niobium SQUIDs used in this study, I_c/C is approximately 2×10^8 A/F resulting in $f_p \approx 124$ GHz as the upper limit of the bandwidth. If the value of β_c is known, then a better estimate for the SQUID bandwidth is given by multiplying or dividing f_p by $\sqrt{\beta_c}$ depending on whether β_c is respectively less than or greater than one. Thus, $\Delta f \approx f_p / \sqrt{\beta_c}$ for a hysteretic SQUID.

Equations (3.3) and (3.4) are limitations that arise from the dynamical behavior of the Josephson junctions. It turns out there are other dynamical limitations that can restrict the bandwidth of a dc SQUID. For example, consider the voltage rise time across the junction. The analysis in Chapter 2 assumed that the transition from the zero voltage state to the resistive state was instantaneous. In fact, the time needed to make this transition is finite. Although the ultimate origin of the transitions are quantum mechanical, an estimate for the voltage rise time can be derived from the following classical considerations using the RCSJ model [43-51,99].

Assume that the SQUID junctions are initially in the zero voltage state. Then, while the current through a junction is fixed and smaller than the critical current, the voltage across the junction remains at zero. However, once the current exceeds the critical current, an average voltage appears across the junction. This voltage is a consequence of the charge accumulated across the insulating barrier and normal current tunneling through the break up of Cooper pairs. In determining this average voltage, consider only the shunt capacitor and resistor in the RCSJ model in parallel with the current source as shown in Fig. 3.1(a). In hysteretic junctions, I can assume

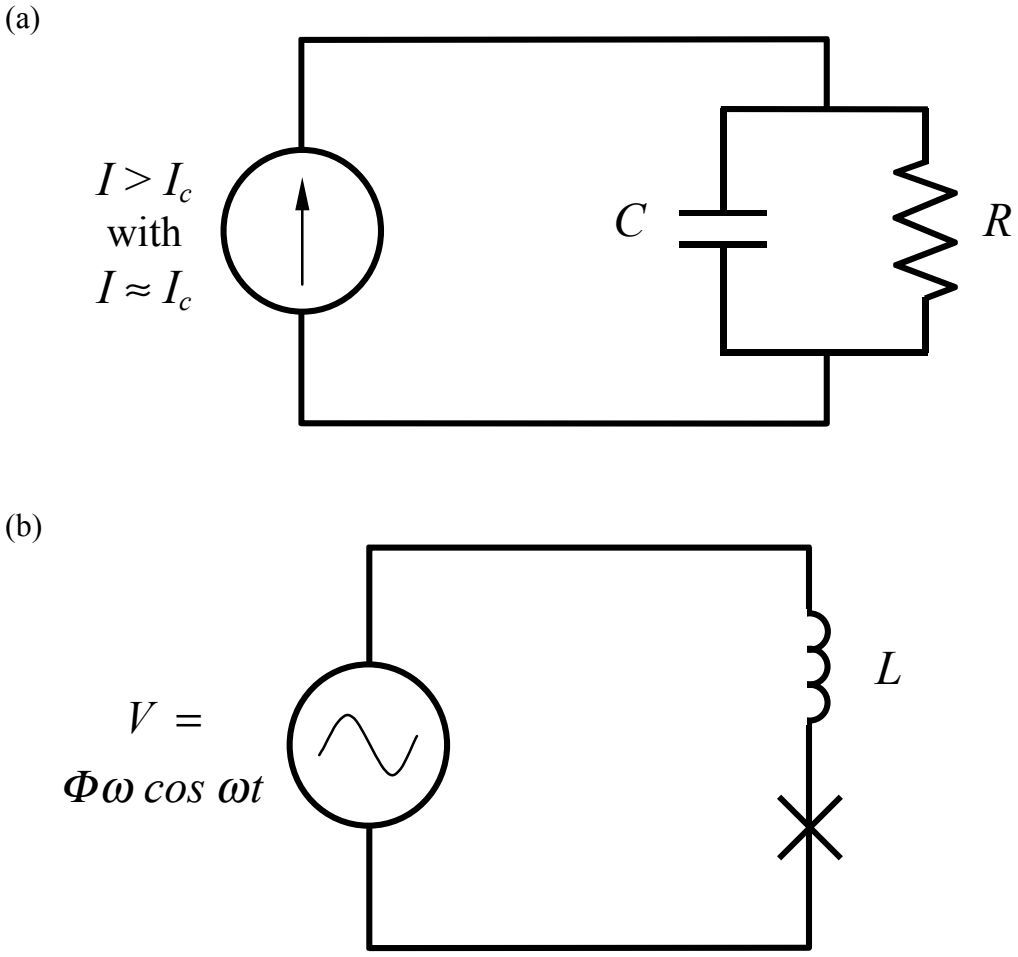

FIG. 3.1. (a) Simplified circuit model of a current biased Josephson junction with static bias current where the current is just a little greater than the junction critical current. The current path through the ideal Josephson junction in the RCSJ model is ignored for simplicity. (b) Simple circuit model of a SQUID loop with an externally applied ac magnetic field. The induced emf is modeled by an ac voltage supply. The total magnetic flux through the loop is Φ, and its frequency is $\omega /2\pi$. The self inductance of the SQUID loop is L.

that the ac current through the ideal Josephson junction channel varies too quickly for it to influence the accumulated charge. In nonhysteretic junctions, the dynamics are dominated by the RC components. The current through the shunt capacitor and resistor is then given by

$$I = C\frac{dV}{dt} + \frac{V}{R} \tag{3.6}$$

where C and R are the shunt capacitance and resistance, respectively. The voltage V across the junction appears when the current I just exceeds the critical current I_c. Then, replacing I with I_c, the solution to Eq. (3.6) is given by

$$V = I_c R\left(1 - e^{-\frac{t}{RC}}\right). \tag{3.7}$$

As the voltage increases from zero, R corresponds to the subgap value R_{sg}. For small $\tau_{RC} = RC$, as in the nonhysteretic case of $\beta_c << 1$, the voltage quickly approaches the limiting value. However, in this limit, Eq. (3.4) yields a more stringent condition on the bandwidth, and the voltage rise time does not limit the response. For large τ_{RC}, i.e. the hysteretic case of $\beta_c >> 1$, where R takes on the value of the subgap resistance R_{sg}, the value of $I_c R_{sg}$ is much greater than the gap voltage $2\Delta/e$, and so the time required to reach $2\Delta/e$ is relatively small. Approximating the exponential in Eq. (3.7) by its linear expansion for small values of the exponent with $V = 2\Delta/e$, one finds

$$\frac{2\Delta}{e} = I_c R_{sg}\left(1 - e^{-\frac{\tau}{R_{sg}C}}\right) \approx I_c R_{sg}\left(1 - 1 + \frac{\tau}{R_{sg}C}\right) = \frac{I_c}{C}\tau\,. \tag{3.8}$$

Thus, the voltage rise time is

$$\tau_{rise} = \frac{2\Delta C}{eI_c} \tag{3.9}$$

which has been verified experimentally [25]. Depending on the specific junction characteristics, either τ_{RC} or τ_{rise} will determine the maximum bandwidth.

For the hysteretic niobium dc SQUIDs with $I_c/C \approx 2\times10^8$ A/F mentioned earlier, Eq. (3.9) gives a rise time of about 12 ps. When pulsing the bias current, one should use pulses with durations that are at least twice as long as the rise time. Thus, the maximum bandwidth corresponds to the inverse of $2\tau_{rise}$ or around 40 GHz. This value is smaller than the SQUID bandwidth limit given by Eq. (3.5) by an order of magnitude.

Comparing the two time constants τ_{RC} and τ_{rise},

$$\frac{\tau_{rise}}{\tau_{RC}} = \frac{2\Delta C}{eI_c R_{sg} C} = \frac{2\Delta}{eI_c R_{sg}} < 1 \tag{3.10}$$

from arguments given earlier. This suggests that Eq. (3.3) still provides a more stringent condition on the SQUID bandwidth than Eq. (3.9). Nonetheless, Eq. (3.9) can be used as an upper limit for the bandwidth for large β_c and is particularly useful when the subgap resistance R_{sg} is not known. So, instead of Eqs. (3.3) and (3.4), Eqs. (3.5) and (3.9) can approximate the bandwidths for nonhysteretic and hysteretic SQUIDs respectively.

It is also interesting to note that for $\beta_c << 1$, I_cR in Eq. (3.7) can be made smaller than $2\Delta/e$ by a sufficiently small R. In other words, the voltage rise time of a nonhysteretic SQUID can be made smaller than a hysteretic SQUID with the same I_c and C. This suggests that nonhysteretic SQUIDs have the potential to have larger

bandwidths than hysteretic SQUIDs. In fact, recalling the earlier result of Eq. (3.5) with $I_c/C = 2\times10^8$ A/F, $f_p \approx 124$ GHz whereas Eq. (3.9) gives 40 GHz. This result points to why development of superconducting circuits have mostly involved nonhysteretic Josephson junctions and SQUIDs, as will be discussed in a later chapter.

In any case, I note that these results all predict relatively large bandwidths and imply that the intrinsic bandwidth of a SQUID is unlikely to be the main factor limiting the bandwidth of real SQUID microscopes.

3.1.3 Magnetic Hysteresis and Critical Current Modulation

A SQUID acts as a detector of magnetic field because the field modulates the SQUID's critical current. In order to maximize the sensitivity to field, the range of critical current values needs to be maximized. From section 2.3, this involves increasing I_c while reducing L and matching the two Josephson junction critical currents. It was also observed in section 2.3 that if $\Phi_o >> LI_c$, then the fractional modulation $\Delta I / 2I_c$ would be maximal. Maximum modulation can also be achieved if $\Phi_A >> LI_c$. Neither of these conditions, however, are always attained or satisfied.

In general, Eq. (2.58) can be used to determine the modulation amplitude. To proceed, Eq. (2.58) can be graphically solved by finding the intersection of the two curves

$$\begin{cases} y_1 = \dfrac{\Phi_o}{LI_c'}\left(\dfrac{\Phi}{\Phi_o}\right) - \dfrac{\Phi_A}{LI_c'} \\ y_2 = (-1)^n \sin\pi\dfrac{\Phi}{\Phi_o} = \sin\pi\dfrac{\Phi}{\Phi_o} \end{cases} \tag{3.11}$$

where $I_c' = I_c \cos \gamma_{av}$ and n is an even integer. If n is odd, the conclusions of the analysis do not change as this only corresponds to a phase shift of the curve y_2. The line y_1 intersects the horizontal axis when $\Phi = \Phi_A$. Analysis of Eq. (3.11) can be limited to a region where the value of Φ / Φ_o ranges from $2n - 1$ to $2n + 1$, or equivalently from -1 to 1, with the points of intersection within this domain.

For $\Phi_A = 0$, the graph of Eq. (3.11) is given in Fig. 3.2 for different values of a given by

$$a = \frac{\Phi_o}{LI_c'} = \frac{\Phi_o}{LI_c \cos \gamma_{av}} . \tag{3.12}$$

For $a < \pi$, it can be seen that there are multiple intersections between -1 and 1, and there will be an increasing number of intersections as $a \to 0$. Now, the value of I_c' ranges from I_c to 0 as γ_{av} changes from 0 to $\pi/2$. Correspondingly, the slope a changes from Φ_o / LI_c to ∞ as the bias current goes from 0 to I_c.

For fixed bias current, the value of a remains constant. However, if there is an applied magnetic flux, this will cause line y_1 to be vertically translated up or down as the applied flux is decreased or increased respectively. As y_1 is vertically translated, it can be seen that an intersection can suddenly disappear if the slope a is less than π. This is represented in the sequence of graphs shown in Fig. 3.3. So, if the system started out with $\Phi / \Phi_o = 0$ or some multiple of 2π, then as the applied magnetic flux Φ_A increased, Φ / Φ_o would have to make a discontinuous jump to another value. If the applied flux then reversed, Φ / Φ_o would not necessarily return to its original value. This is another example of hysteresis and is problematic in determining Φ / Φ_o from the critical current.

(a)

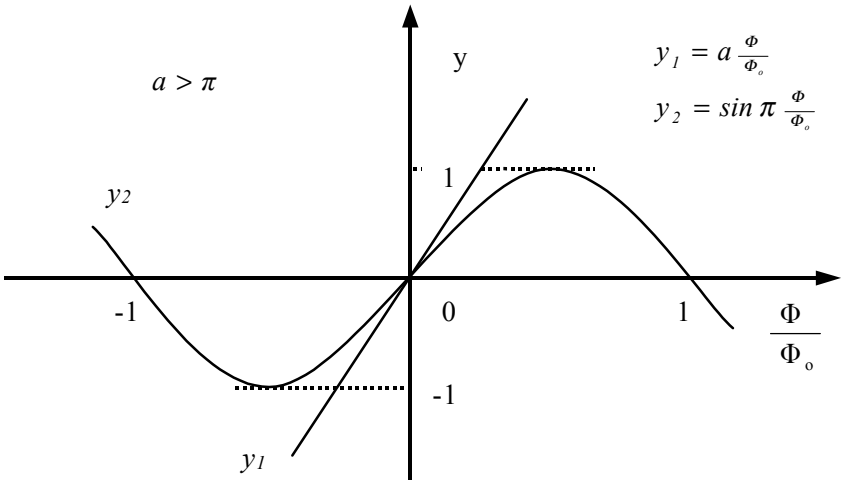

(b)

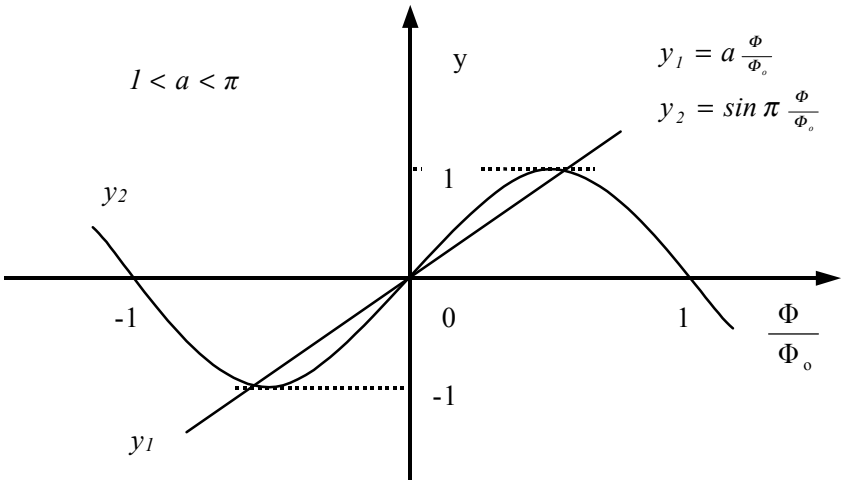

(c)

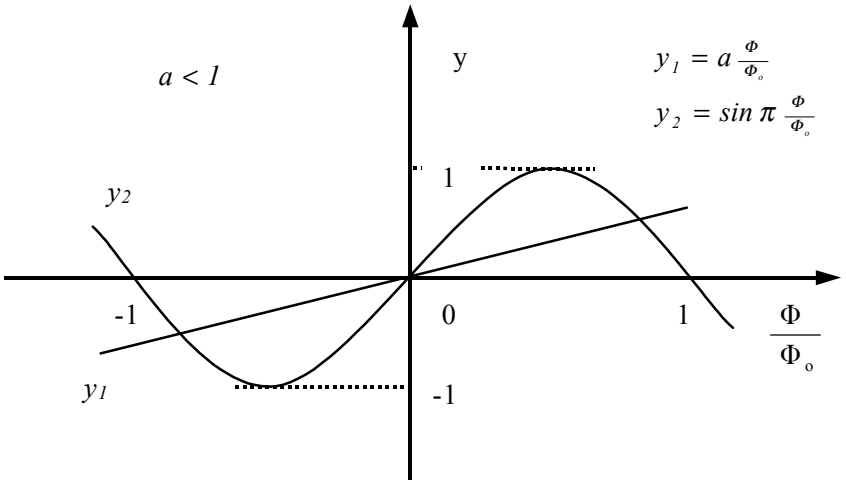

FIG. 3.2. Series of graphs showing the solutions $y_1 = y_2$ for the total magnetic flux through a dc SQUID loop of self inductance L and junction critical current I_c when there is no externally applied flux, for decreasing values of $a = \Phi_o / LI_c \cos \gamma_{av}$.

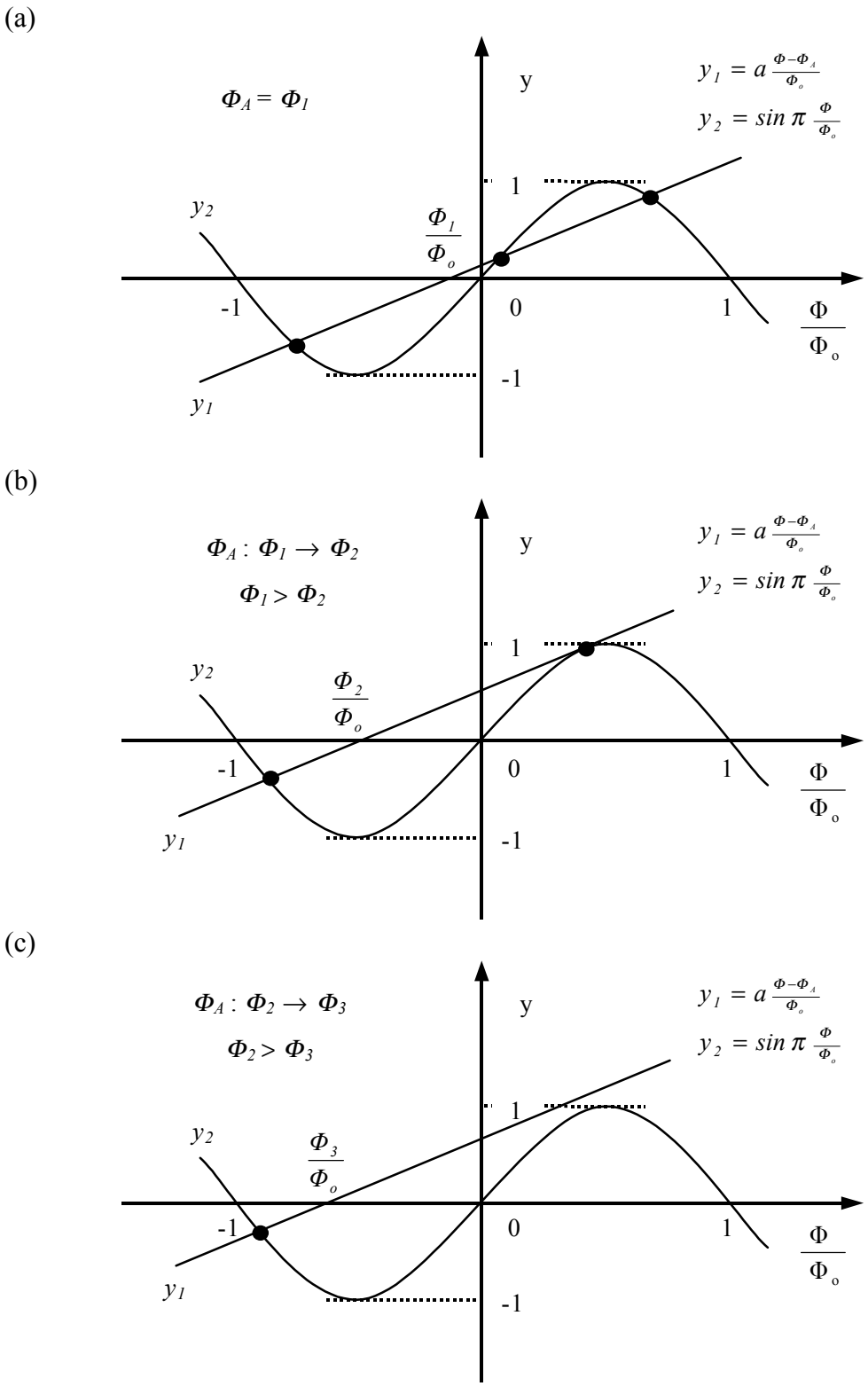

FIG. 3.3. Series of graphs showing the disappearance of intersections between y_1 and y_2 as the line y_1 is translated vertically upward from 0, corresponding to decreasing external magnetic flux Φ_A through the SQUID hole. Slope of y_1 is $a < \pi$.

It can also be seen from Fig. 3.3 that as Φ_A is continually increased or decreased, a range of values in Φ/Φ_o is not attained though $sin(\pi\Phi/\Phi_o)$ is periodic with Φ_A. A discontinuity in Φ/Φ_o and consequently in the critical current is also seen in Fig.3.3. However, the discontinuity in critical current is not seen in numerical simulations when additional circuit elements in the SQUID model are included into Eqs. (2.58) and (3.11) [60,63,100]. Regardless, the result is a decrease in the modulation amplitude of the SQUID critical current.

In order to avoid the hysteresis, the intersection between y_1 and y_2 should be unique, which requires that a satisfy $a > \pi$ for any value of the bias current $I < I_c$. This places a restriction on the maximum self inductance L in terms of the critical current I_c of a dc SQUID's Josephson junction, which is

$$L \leq \frac{\Phi_o}{\pi I_c}$$

or (3.13)

$$\beta \equiv \frac{2LI_c}{\Phi_o} \leq \frac{2}{\pi}$$

where β is the SQUID screening or modulation parameter [4,6,13,65]. It can also be seen that if Eq. (3.13) is satisfied, the total flux Φ is continuous with Φ_A in Eqs. (2.58) and (3.11), and the relative modulation of the SQUID's critical current $\Delta I/2I_c$ is maximized as well. For $\beta \geq 1$, numerical calculations by Tesche *et al*. and by de Bruyn Ouboter *et al*. show that the fractional modulation $\Delta I/2I_c$ diminishes as $\beta \to \infty$ with the modulation amplitude $\Delta I \approx \Phi_o/L$ [60,63].

Regardless of the elimination of hysteresis by limiting the value of β, the modulated critical current remains a periodic function of the externally applied

magnetic flux Φ_A as well as the total magnetic flux Φ through the SQUID loop. Therefore, without shielding or additional information, only changes in magnetic flux or field are reliably determined using a SQUID alone. On the other hand, determining the value of Φ/Φ_o modulo ½ in Eq. (2.53) can be extended to modulo 1 by identifying whether the critical current increases or decreases with a small increase in the applied external flux.

3.1.4 Flux Noise and Optimization

Summarizing the above results, one finds that to improve spatial resolution, one needs to minimize the size of the SQUID, which also decreases its self inductance L. To increase SQUID bandwidth, one should maximize I_c/C. To improve flux sensitivity, one needs to minimize β while maximizing I_c. If the flux modulated critical current $I_c(\Phi)$ requires a nonzero minimum, one can restrict β so that $\beta > 2/\pi$, though Tesche and Clarke suggest the condition $\beta > 0.1$ for nonhysteretic dc SQUIDs [63]. A similar outcome can be obtained by making the critical currents of the SQUID Josephson junctions unequal. These results suggest that the SQUID self inductance L and junction capacitance C be minimized and the junction critical current I_c be maximized within fabrication limits. If hysteresis in the I-V characteristics is desired, β_c should be maximized, meaning that, consistent with the aforementioned conditions, the junction shunt resistance R should be maximized. If hysteresis needs to be eliminated, the reverse should be true.

These conditions, however, are still not the complete set of requirements a SQUID must fulfill. In particular, SQUIDs should have low noise [4-

6,12,20,63,64,100]. A significant source of noise is Nyquist noise which depends on temperature and the shunt resistance. A general limit on thermal energy was given in Eq. (2.34). Clarke and Koch suggest the constraint

$$I_c > \frac{10ek_BT}{\hbar} \tag{3.14}$$

to be sufficient, based on numerical simulations [6].

The shunt resistance in the Josephson junctions produces a current noise spectral density S_I given by the Johnson noise expression

$$S_I(f) = \frac{4k_BT}{R} \tag{3.15}$$

where S_I has the dimensions of current squared per unit bandwidth [101]. This noise causes fluctuations in the current flowing through the junctions and thus also in measurements of the applied flux. Following Tinkham, Eq. (3.15) can be used to deduce an expression for the flux noise density [65]. The transfer function between critical current and magnetic flux for a symmetric dc SQUID with negligible β is given by Eq. (2.53), and

$$\left|\frac{\partial I_c}{\partial \Phi}\right|_{max} = 2\pi \frac{I_c}{\Phi_o} \leq \frac{2}{L} \tag{3.16}$$

where in the last inequality, the requirement of $\beta \leq 2/\pi$ is used to ensure no magnetic hysteresis. Therefore, the minimum flux noise density becomes

$$\left|S_\Phi(f)\right|_{min} \approx \frac{S_I(f)}{\left|\frac{\partial I_c}{\partial \Phi}\right|^2_{max}} \approx \frac{k_BTL^2}{R_{sg}} \tag{3.17}$$

where the limiting value of $2/L$ was substituted for $|\,\partial I_c/\partial \Phi\,|_{max}$. De Waal *et al.* suggest that the actual flux noise density is closer to

$$S_{\Phi}(f) \approx \frac{14 k_B T L^2}{R_{sg}} \tag{3.18}$$

which was obtained from computer simulations [64]. Other results suggest an even higher proportionality factor in Eq. (3.18) [4,6,63,100]. Equations (3.17) and (3.18) indicate that noise will decrease with decreasing temperature and SQUID hole size. Using Eqs. (3.1) and (3.18), the magnetic flux noise at 5 K over 1 Hz for a SQUID with a 10 μm by 10 μm hole and R_{sg} = 100 Ω is about 5.5×10^{-23} T·m^2 or $2.7\times10^{-8}\Phi_o$. Over a bandwidth of 100 GHz, the flux noise is about 1.8×10^{-17} T·m^2 or $8.5\times10^{-3}\Phi_o$ in 10 ps. In comparison, typical high-T_c SQUID microscopes using nonhysteretic small β_c SQUIDs have bandwidths of about 100 kHz, limited by the readout electronics, and a flux noise density on the order of 10^{-5} $\Phi_o / \sqrt{\text{Hz}}$ giving a magnetic flux resolution of around $10^{-3}\Phi_o$ in 10 μs.

3.1.5 Magnetic Induction and Nonlinear Effects

Besides Johnson noise, other effects may limit the performance of a SQUID. For example, consider the effect of a changing magnetic field. The electromotive force (emf) due to the changing field is given by Maxwell's equations in integral form:

$$\int \nabla \times \boldsymbol{E} \cdot d\boldsymbol{A} = \oint \boldsymbol{E} \cdot d\boldsymbol{l} = -V = -\frac{\partial}{\partial t}\int \boldsymbol{B} \cdot d\boldsymbol{A} \ . \tag{3.19}$$

If the magnetic field is $\boldsymbol{B} = \boldsymbol{B_o} \sin \omega t$, then

$$V = \frac{\partial}{\partial t}\int \boldsymbol{B_o} \sin \omega t \cdot d\boldsymbol{A} = \frac{\partial}{\partial t} \sin \omega t \cdot \int \boldsymbol{B_o} \cdot d\boldsymbol{A} = \Phi_A \omega \cos \omega t \tag{3.20}$$

where Φ_A is the magnitude of the externally applied magnetic flux through the SQUID hole. If $\Phi_A \approx \Phi_o$, at the band limited frequency of 40 GHz for the hysteretic SQUIDs in this study, the induced voltage amplitude is on the order of 10^{-4} V. Although the induced emf may not be enough to overwhelm the dynamics of the SQUID, it could have a perturbing effect that could, for example, increase the voltage noise across the junctions or cause a large transient.

As an example, suppose the SQUID loop is approximated as a simple inductor in series with a Josephson junction [see Fig. 3.1(b)]. The induced current around the ring is given by

$$\begin{aligned} V &= -L\frac{dI}{dt} = \Phi\omega \cos\omega t \\ \frac{dI}{dt} &= -\frac{\Phi}{L}\omega \cos\omega t \end{aligned} \tag{3.21}$$

where the contribution of the Josephson junction impedance has been ignored [102,103]. Solving Eq. (3.21) gives

$$I = I_o - \frac{\Phi}{L}\sin\omega t \tag{3.22}$$

where I_o is the dc current component that is supplied by the static current bias. Inserting Eq. (3.22) into Eq. (2.66) and transforming into dimensionless form yields

$$\beta_c \frac{d^2\gamma}{dx^2} + \frac{d\gamma}{dx} + \sin\gamma = y + y_{ext}\sin\omega' x \tag{3.23}$$

where

$$y_{ext} = -\frac{\Phi}{LI_c}$$

and (3.24)

$$\omega' = \omega\tau_J .$$

Solving for γ in Eq. (3.23) reveals chaotic solutions for certain values of the parameters [88-92,104]. The chaotic solutions cause enhanced voltage noise and may limit sensitivity. In addition, the induced emf around the SQUID loop may also affect the junction in the resistive state, producing enhanced dc current effects from Shapiro steps and similar phenomena [102,105-109]. I have not fully considered the effect of these phenomena. However, as SQUIDs are used to measure high frequency magnetic fields, effects such as these may well become apparent.

3.2 Resistively Shunted SQUIDs

As part of developing a large bandwidth SQUID microscope, I helped build and test a prototype 4 K SQUID microscope. Testing of the microscope was performed using dc SQUIDs with resistively shunted Josephson junctions and conventional Flux-Locked-Loop (FLL) electronics [4,5,18-20]. The electronics require a nonhysteretic SQUID ($\beta_c << 1$) so that changes in flux correspond to changes in voltage in a reversible manner (see Fig. 3.4). When fabricating SQUIDs, the value of β_c is controlled mainly by adjusting the values of the critical current I_c, the shunt resistance R, the barrier thickness, and area of the Josephson junctions. High-T_c superconductor SQUIDs, for example those based on YBCO, have intrinsically small subgap resistance making β_c small. However, niobium SQUIDs have large subgap resistance and the junctions must be externally shunted with low resistive channels in order to eliminate hysteresis.

The selection of the shunt resistance R is determined by a few considerations. The upper limit is determined by the requirement that β_c should be less than 0.69,

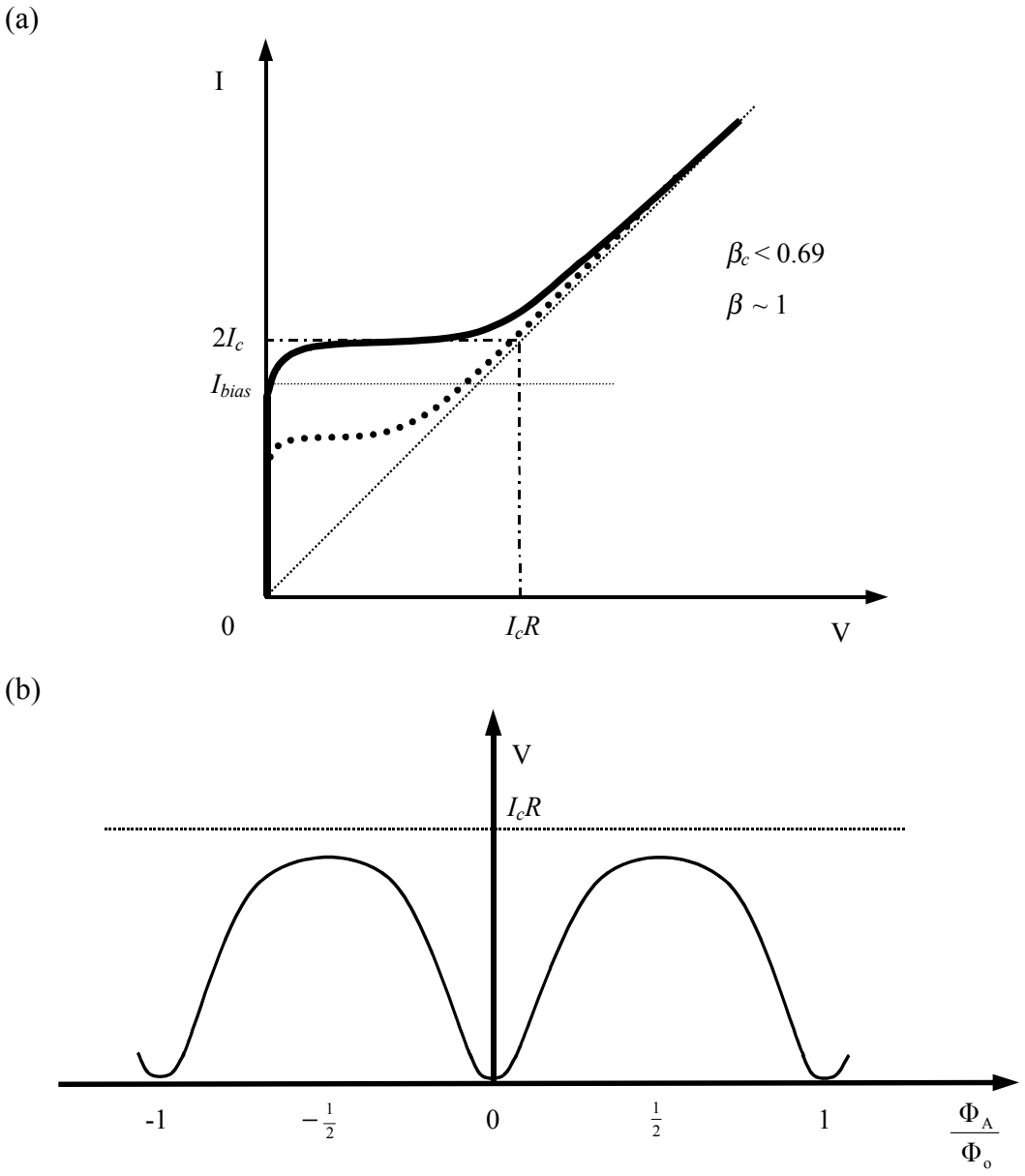

FIG. 3.4. (a) I-V characteristics of a nonhysteretic dc SQUID with $\beta \approx 1$ at finite temperature. The junction critical current is I_c, and the subgap resistance is R. The solid curve corresponds to integer multiples of a flux quantum applied through the SQUID hole. The dotted curve represents the I-V characteristics when the applied flux is a half flux quantum more than the solid curve. (b) Graph of the SQUID voltage versus applied magnetic flux through the SQUID hole when the dc SQUID is current biased at the current I_{bias} shown in (a).

where the onset of hysteresis occurs [81]. The lower limit to R is mostly determined by noise considerations. In FLL electronics, a room temperature amplifier monitors the voltage signal across the SQUID instead of the critical current. The magnitude of this voltage is partly dependent on R and scales with I_cR, where R is assumed to be much smaller than the intrinsic subgap resistance. For a junction with I_c = 100 μA and C = 0.5 pF, the effective shunt resistance has to be less than 2.13 Ω to avoid hysteresis.

If the shunt resistance R is too small, the SQUID voltage signal will also be small and can be overwhelmed by noise from the amplifier. For example, if R = 1 Ω, the maximum voltage signal will be about 100 μV for a critical current of 100 μA. The SQUID must also operate below a temperature given by Eqs. (3.14) and (3.18) to resolve this level of voltage. For a nonhysteretic SQUID with $\beta \approx 1$, the voltage noise spectral density S_V is

$$S_V(f) \approx 16 k_B T R \tag{3.25}$$

where S_V has the dimensions of voltage squared per unit bandwidth [4,110]. Using Eq. (3.25) for a 1 Ω resistor over a bandwidth of 100 GHz, the temperature of the system has to be lower than 4.5 K to decrease thermal noise below 10 μV. This calculation ignores noise from other factors, such as the readout electronics. So, this estimate is only a lower limit to the actual noise that will be present. In conclusion, the shunt resistor value must be selected such that β_c is less than 0.69 and the SQUID voltage signal is large enough to be measurable but small enough to not affect the bias current as the SQUID alternates between the zero voltage state and the resistive state.

When using nonhysteretic dc SQUIDs with FLL electronics, it is common to use a transformer to couple the SQUID output to a low noise preamplifier [4,5,18]. This has a number of advantages. First, standard FLL electronics uses ac flux modulation and detects the SQUID voltage at a particular frequency. The transformer naturally filters out the dc component as well as the very high frequencies. Further, the transformer steps up the voltage signal according to the transformer turns ratio. Also, without a transformer, the voltage measurement leads would go directly up to electronics which is at room temperature and may send noise signals back to the dc SQUID or even damage it. The transformer helps to isolate the SQUID from the environment. Finally, the transformer can be used to match the output impedance of the SQUID signal to the input impedance of the amplifier and transmission line for high frequency applications. This can result in the best signal to noise performance for the SQUID and amplifier combination. The ideal matching condition for lowest noise is obtained when

$$R \cdot N^2 = Z_n \tag{3.26}$$

where Z_n is the noise impedance of the amplifier, N is the turns ratio of the transformer, and R is the dynamic resistance of the nonhysteretic dc SQUID at the operating bias current [4,19,111].

A small problem with using a transformer is that the primary is in parallel with the dc SQUID, and this shunts current away from the SQUID bias. If the effective shunt resistance of the dc SQUID is much larger than the impedance of the transformer primary, the bias current to the SQUID will change considerably when the SQUID goes from the zero voltage state to the resistive state and vice versa. This,

in turn, diminishes the voltage signal and should be prevented. A solution to the transformer problem is to add a small resistance R_x in series with the transformer primary to increase its impedance [19,20]. If the added resistance is too large, the voltage across the transformer will be too small. So, the resistance is chosen to be somewhat less than the impedance of the transformer primary.

When adding shunt resistors to Josephson junctions, the leads of the shunt resistors can contribute an inductive term to the equation of motion given by Eq. (2.69). Specifically, an additional current channel with a resistive and inductive component appears across the junction. Cawthorne showed that this additional channel can give rise to complicated behavior of the SQUID voltage immediately after the bias current exceeds the critical current, though the zero voltage state is not affected [95]. The voltage structures due to inductive effects were seen to broaden and diminish as the value of β_c approached zero.

Even if the magnetic field detecting properties of a SQUID were not adversely affected by the presence of some inductance in the shunt resistors, it would be preferable if the SQUID resistive state characteristics were simple and predictable. For certain values of the parameters, analysis of the junction with the added inductive element shows that the system can be chaotic, as was the case for Eq. (3.23). Therefore when adding shunt resistors, care should be taken to minimize lead lengths and use intrinsically resistive materials to shorten the shunts so as to minimize the total inductance. The difference in the inductance of the SQUID loop between paths through the shunt resistors and those through the Josephson junctions should be

minimal as well. Adherence to these criteria will in general have to be verified by numerical simulation in the absence of analytical techniques [95,96].

3.3 Niobium SQUID Design and Characteristics

3.3.1 Prior SQUID Design

The SQUIDs I used in my work were made with niobium. The reasons for choosing niobium were that it has a superconducting transition temperature $T_c \approx 9.3$ K with a gap voltage $2\Delta/e$ of about 3.05 mV at zero temperature [112-115]. Secondly, commercial facilities for the fabrication of custom Nb-AlO_x-Nb integrated circuits such as those operated by HYPRES, Inc. are readily available. Needless to say, there can be enormous advantages to ordering chips from such facilities compared to fabricating them in-house. Finally, niobium also has large subgap resistance which enables hysteretic Josephson junctions to be prepared, which is critical for my high speed measurement technique.

The dc SQUIDs I tested on the prototype 4 K SQUID microscope had the same design used on a LHe cooled scanning SQUID microscope maintained by Cawthorne and Nielsen [11,95]. Figure 3.5(a) shows a photograph of one of these SQUIDs. The LHe cooled microscope had been used for the study of magnetic properties of microscopic superconducting structures. The Cawthorne and Nielsen microscope incorporated conventional FLL electronics, so the SQUID junctions had to be resistively shunted. The SQUID chips were designed using ICED which is an MS-DOS based integrated circuit editor program [116]. Fabrication of the chips was performed by HYPRES, Inc. using their niobium chip foundry [117]. The LHe

(a)

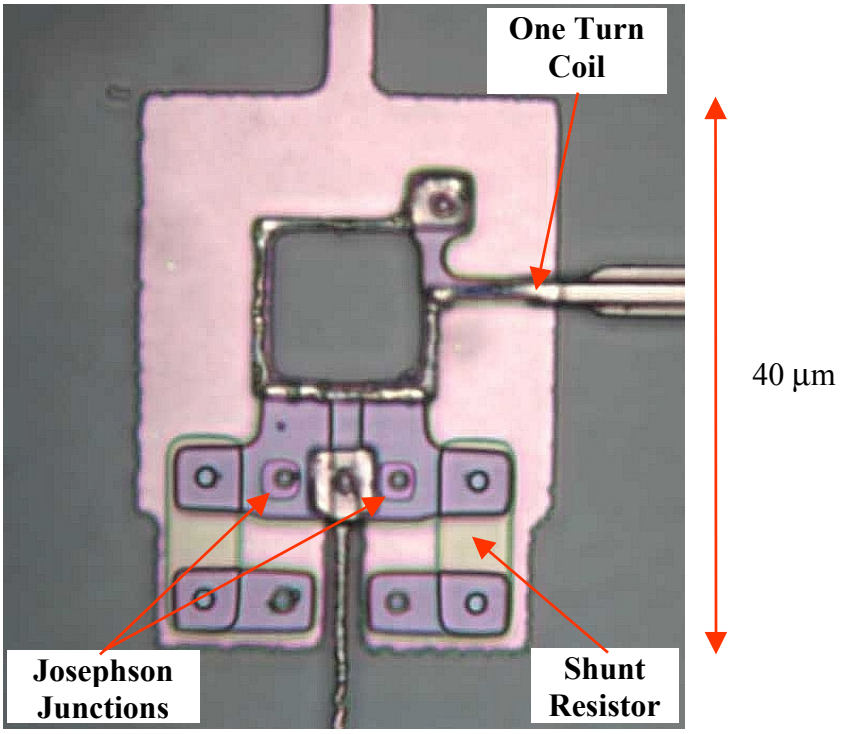

(b)

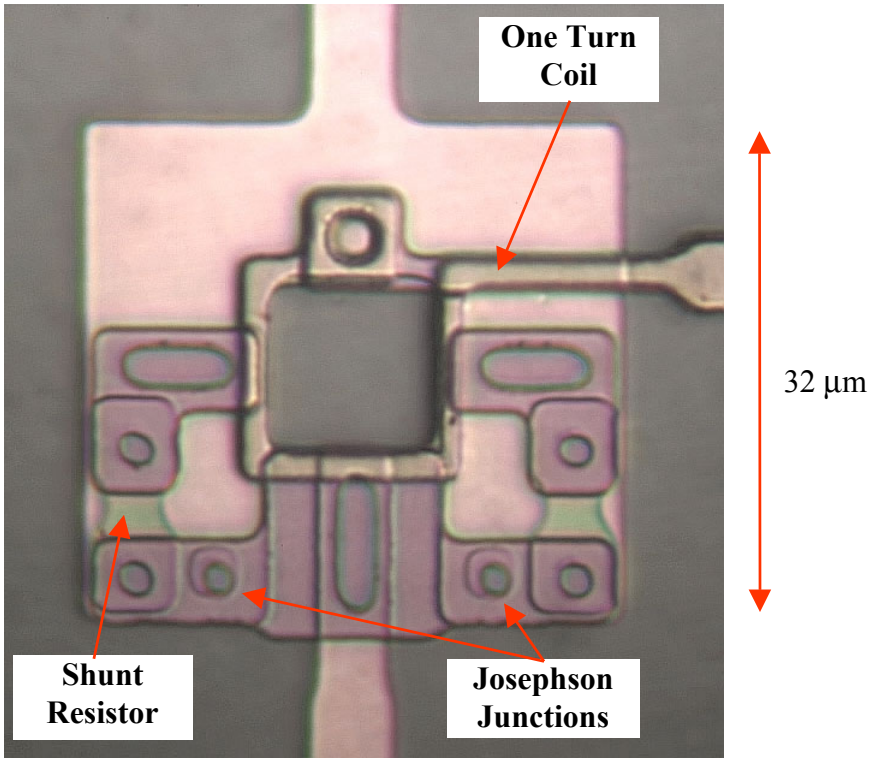

FIG. 3.5. (a) Photograph of the resistively shunted niobium dc SQUID designed by Cawthorne and Nielsen, which was used in a LHe cooled scanning SQUID microscope. (b) Photograph of updated resistively shunted dc SQUID I designed with features compliant with HYPRES design rules.

cooled microscope required micron scale spatial resolution, so the SQUIDs had outer loop dimensions of 30 μm by 40 μm and a 10 μm by 10 μm square hole. The small SQUIDs have an estimated loop inductance $L \approx 16$ pH and, in conjunction with Josephson junctions with critical current $I_c \approx 60$ μA, were designed so that $\beta \approx 1$.

The Josephson junctions of the dc SQUID were designed to be 3 μm by 3 μm squares, the minimum size allowed by HYPRES. However, due to the fabrication process, the junctions came out slightly rounded and smaller than designed. HYPRES reported that the loss in area is statistically about 3.0±0.5 μm^2 [118]. This variation was significant and had to be factored into the design, as will be discussed later.

Each SQUID junction was shunted with a resistor 3 squares long. The resistive material for shunting the junctions was molybdenum with a calibrated resistance of around 1 Ω/square according to HYPRES specifications. The actual resistances were not explicitly determined; interlayer connections to the resistors required significant area near their ends making the effective area smaller by around a half square. As there are two shunts per SQUID, one for each junction, the combined parallel resistance is around 1 Ω.

The dc SQUIDs also have a one turn coil around the inner hole of the SQUID (see Fig. 3.5). The coil is mostly made up of niobium as well. With FLL electronics, the coil is connected to the feedback system and provides a nulling magnetic flux through the SQUID loop. In my experiments, it is connected to a signal generator and sends external high frequency flux to the SQUID. The small size of the coil allows the field to concentrate the magnetic flux through the hole.

Measurements I made of the I-V curve of a resistively shunted dc SQUID (SQUID AN) in LHe showed some problems (see Fig. 3.6). In particular, the SQUID's shunting resistance was much greater than 1 Ω. There was also some subtle structure in the resistive region of the I-V curve. This may have been due to inductive effects or ac biasing, as discussed earlier [95,108,109]. Nevertheless, the observed large normal resistance is an indication of a fabrication problem, most likely poor contact between the resistors and the niobium layer.

The problems with SQUID AN, however, were much less severe than problems with the dc SQUIDs left over from the LHe cooled microscope. Some of those problems were clearly visible under a high power optical microscope. The major problems were with respect to the SQUID leads, their uniformity in particular, and with the via holes between layers. The leads were sometimes too thin or not properly defined. The result was that they did not make a continuous connection or failed easily. As it turned out, this was due to lack of adherence to the manufacturer's design rules, i.e. the designed features did not fully adhere to the fabrication criteria [117,118]. Particularly, some leads were thinner than the minimum requirement, and some via holes did not follow the required size or edge separation.

For example, the minimum allowed lead width for a niobium layer was 2 μm to 2.5 μm depending on the layer. But, this was not followed in some features resulting in excessively narrow sections in the fabricated lead. The one turn coil around the inner hole was a particular area where the design did not meet the HYPRES design rules; the coil width was designed too thin and would sometimes not come out as a continuous loop. For some devices, excessively narrow

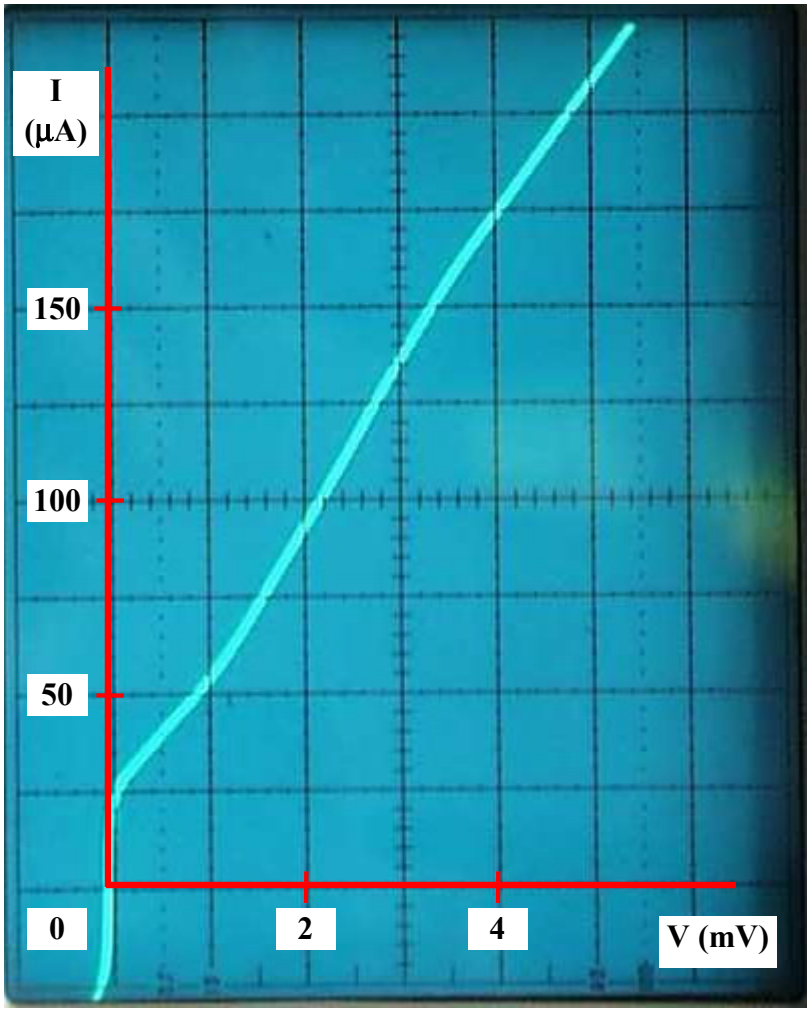

FIG. 3.6. I-V characteristics of SQUID AN which is of the Cawthorne and Nielsen design. Four point measurement made in LHe. Magnet wire leads used to measure signals. SQUID chip attached to a circuit board with wirebonding. Multiple changes in the differential resistance can be seen. Beyond the zero voltage state, the differential resistance dV/dI is approximately 40 Ω between 25 μA and 50 μA. It then decreases to about 23 Ω near 100 μA, after which it increases to around 30 Ω beyond 175 μA. Additional changes can be seen as the current increases further beyond the current values shown here. Modulation of critical current with applied magnetic field is observed between 100 μA and 150 μA. A second current modulating region is observed at higher current but with smaller amplitude.

superconducting leads became resistive under power, producing enough heat to blow out the leads. This was observed to have happened in a few cases, and the damage was visible under an optical microscope.

Regarding via holes, they sometimes lacked clear edges. Electrical connections either did not exist or failed in these cases. Other problems with the SQUIDs included leads and contact pads flaking off during chemical cleaning. And, there were still problems that could not be identified visually that were only detectable during testing.

After realizing the SQUIDs designed by Cawthorne and Nielsen contained these problems, I updated the design to bring it into compliance with the HYPRES design rules [118]. The updated design has resistively shunted SQUID junctions of the same size with similar shunt resistor values compared with the original design. When all the rules were followed, features in the SQUID were much more well defined and uniform, as can be seen in Fig. 3.5(b). Unfortunately, the updated SQUIDs arrived too late for them to be installed on the 4 K SQUID microscope, and I did not have the opportunity to test them after they were made available to me.

Notwithstanding, even when the HYPRES design rules are followed, I found deviations in the parameter values of the SQUIDs. Although HYPRES's process attempts to produce uniformity in the niobium chips, there are variations in the features of the chips, particularly in the critical current densities of the junctions from chip to chip. These variations can be as much as 30% from the stated target value and typically differ between 5% and 15%. Another cause of variations in critical current, particularly for small junctions, is that there is a significant difference in the

areas due to the rounding of the square corners as mentioned earlier. While HYPRES states that these differences are fairly regular, for the smallest junction size, the variations can be significant enough to cause a mismatch between the actual and intended SQUID characteristics.

Besides junction area and critical current density, junction capacitance and external resistor characteristics also vary. Junction capacitance depends on the junction area and thickness of the insulating barrier. The barrier thickness is, in turn, reflective of the critical current density of the junction. Variations in external resistors, however, were not significant as resistor size is larger than the minimum required dimensions. The expected variation in resistivity is typically less than 10%. Furthermore, for our parameters, the dc SQUID's performance is not very sensitive to the actual value of the shunt resistance. Considering that larger areas are less affected by small variations, increasing the junction area by going to a lower critical current density foundry process would tend to improve the match between designed and actual parameter values without drastically affecting SQUID characteristics.

3.3.2 Measured SQUID Characteristics

Figure 3.6 shows the I-V characteristics in LHe of the resistively shunted dc SQUID I used for the prototype 4 K microscope (SQUID AN). This nonhysteretic SQUID shows a zero voltage state with a maximum supercurrent of around 25 μA and a resistive region with $R_d = dV/dI$ changing piecewise from 40 Ω to 23 Ω then to 30 Ω to within 7% uncertainty. This is much higher than the expected value of 1 Ω.

I observed current modulation with respect to magnetic flux, which was small in this device. Figure 3.7 shows the ac component of the SQUID voltage measured at different bias current values while an ac magnetic field is applied to the SQUID. Maximum modulation occurs at a bias current around 130 μA resulting in voltage modulation of around 80 μV peak to peak [see Fig. 3.7(e)]. This result shows that peak modulation is actually occurring well inside the resistive region of the I-V curve. This was not expected and is irregular. Although maximum modulation is occurring near the expected bias current, obtained from calculations of the designed critical current described below, the maximum supercurrent is much smaller than expected. This phenomenon could be explained by a Josephson junction with a critical current of 25 μA and a shunt resistance between 20 Ω and 30 Ω in series with the dc SQUID. Such a junction would be parasitic or accidental and a result of a defect in the fabrication of the SQUID chip.

These features in the dc SQUID were never fully understood and seemed to be common to all SQUID chips in the same batch. Notwithstanding these problems, the dc SQUID could still be used as a magnetic field sensor. For example, Fig. 3.8 shows the voltage across the SQUID as the magnetic flux through its hole is linearly increased then decreased. These measurements show that as the magnetic flux continuously increased or decreased, the ac SQUID voltage oscillated as expected, similar to Fig. 3.4(b).

I found the SQUID parameters for SQUID AN as follows. Using Eq. (3.1) with an inner hole length $d = 10$ μm, the SQUID loop inductance is $L \approx 16$ pH. The maximum expected critical current I_c of each Josephson junction is calculated from

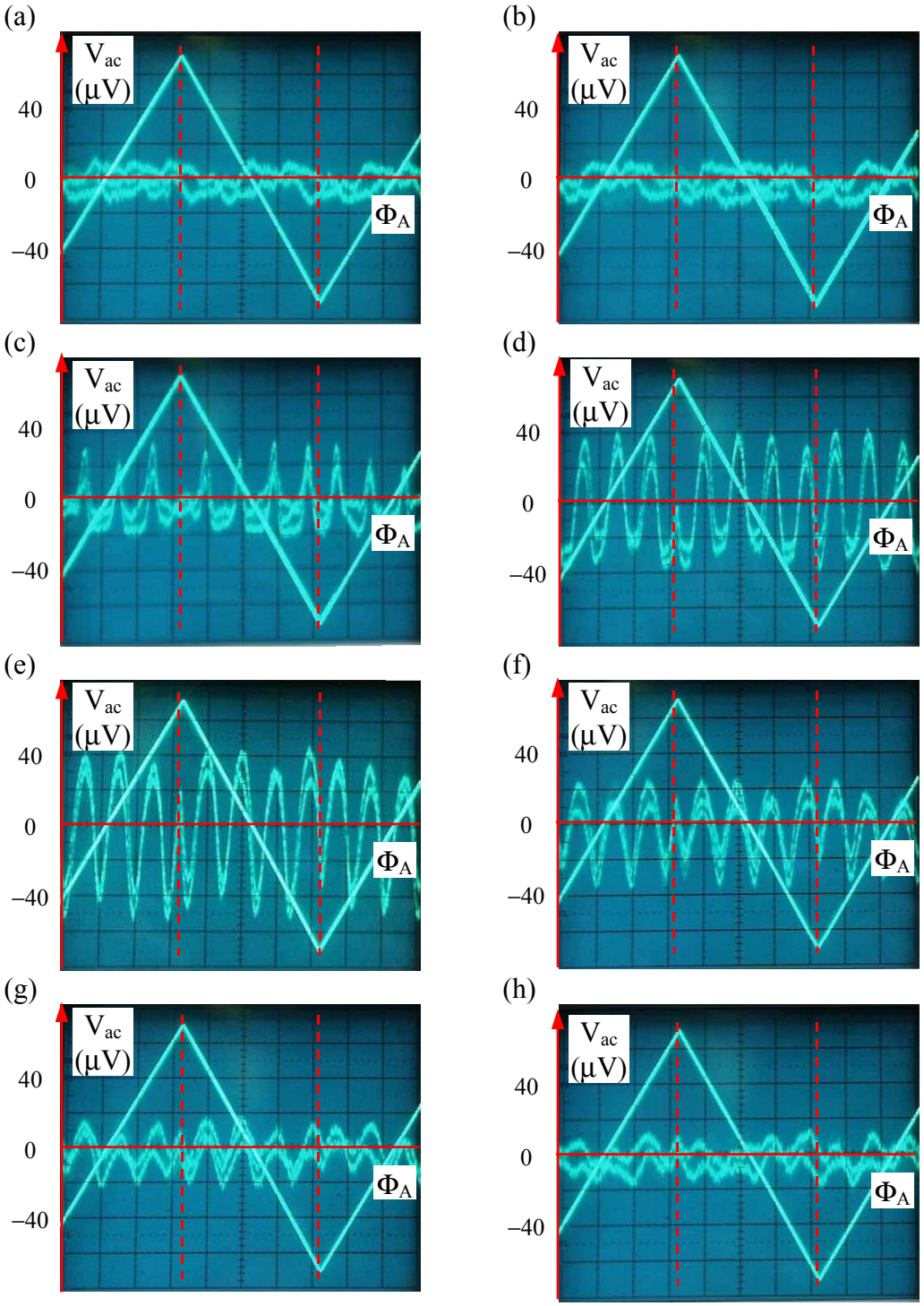

FIG. 3.7. Series of oscilloscope pictures showing ac component of voltage across SQUID AN at different bias currents. Bias current values are (a) 54 μA, (b) 79 μA, (c) 96 μA, (d) 116 μA, (e) 130 μA, (f) 148 μA, (g) 180 μA, and (h) 207 μA. Triangular wave represents current through one turn coil on SQUID chip, with amplitude of 700±5 μA peak-to-peak. No noise filtering was performed on the signals. Maximum modulation amplitude seen with bias current at around 130 μA.

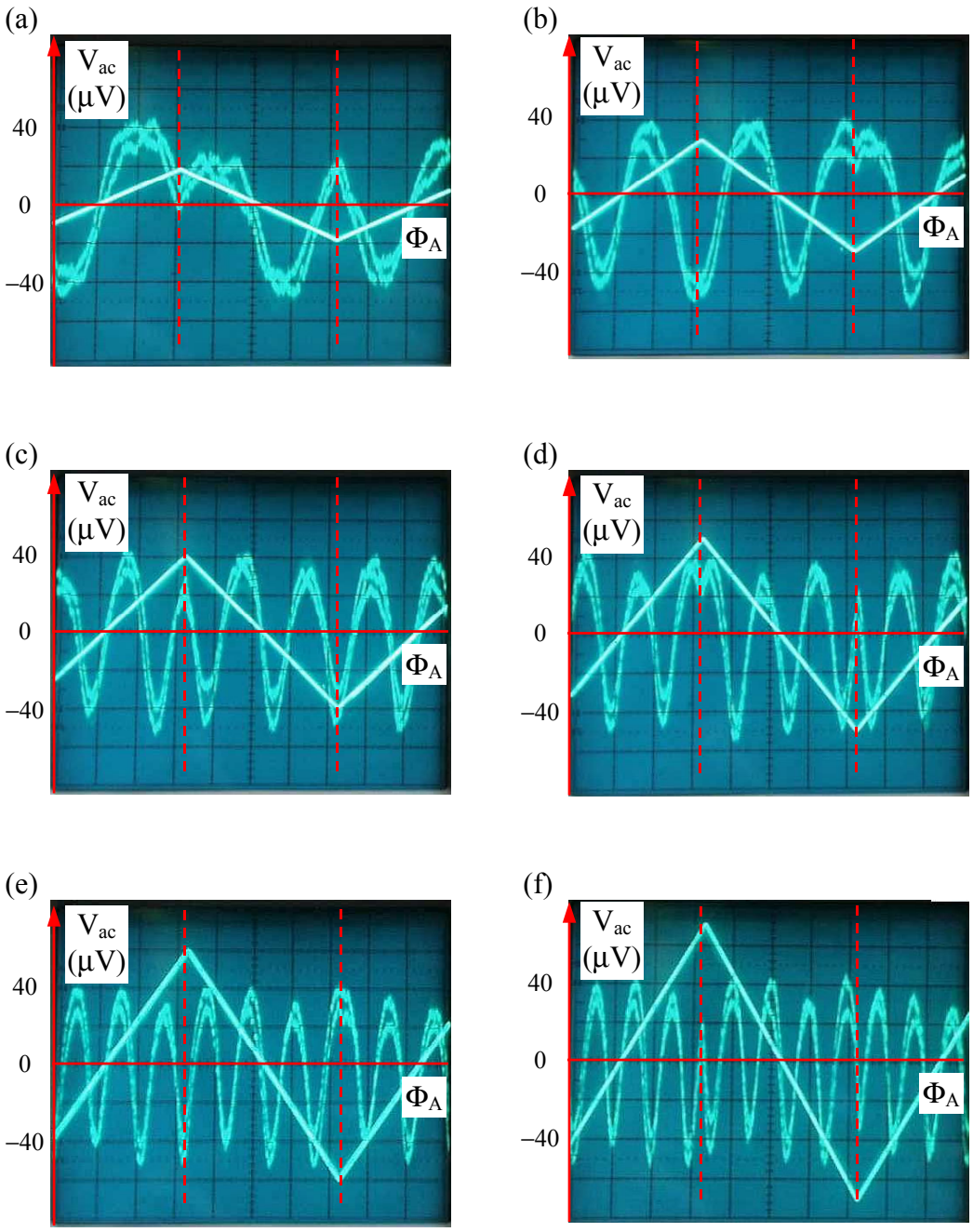

FIG. 3.8. Series of oscilloscope pictures showing ac component of voltage across SQUID AN in LHe, as the amplitude of an externally applied magnetic field is increased. The SQUID bias current was fixed at 130 μA, and the magnetic field was applied to the SQUID using the one turn coil on the SQUID chip. The triangular wave represents the current through the one turn coil, with peak-to-peak amplitudes of (a) 180 μA, (b) 290 μA, (c) 389 μA, (d) 499 μA, (e) 579 μA, and (f) 700 μA. No noise filtering was performed on the signals.

the calibrated value of $J_c \times Area$ = 70±6 μA where, the critical current density J_c of 1168.6 A/cm^2 was provided by HYPRES, and I took $Area$ = 6.0±0.5 μm^2. From Eq. (3.13), this yields $\beta \approx 1.07$ which is greater than $2/\pi$. Next, from Eqs. (2.68) and (2.69), $\beta_c \approx 0.26$ for a single 6 μm^2 junction with a shunt resistance of 2 Ω and a capacitance of 0.30 pF calculated from HYPRES's capacitance formula

$$C = \frac{10.0}{0.20 - 0.043 \log_{10} J_c} \tag{3.26}$$

where C is the capacitance per unit area in fF/μm^2 and the critical current density J_c is in kA/cm^2 [118]. Given the smallness of β_c, the dc SQUID should be nonhysteretic in its I-V characteristic, which is by design and what is observed in Fig. 3.6.

With these parameters, the SQUID's maximum critical current should be 140±12 μA, and the critical current modulation should be about 70 μA corresponding to a voltage modulation of around 70 μV. These expectations are consistent with the characteristics of the dc SQUID, except for the suppressed critical current and large normal resistance mentioned earlier. From Fig. 3.8, I also find that one period of the voltage corresponding to one flux quantum requires a change in current of 169±4 μA in the one turn coil. Thus, the mutual inductance between the one turn coil and SQUID loop is approximately 12 pH.

For comparison, Fig. 3.9 shows the I-V characteristics in LHe of the niobium dc SQUID seen in Fig. 2.2(b), which has no shunt resistors (SQUID BH). Figure 3.9 shows two sets of curves, one where the magnetic field through the SQUID hole results in maximum SQUID critical current and the other where the critical current is minimum. The I-V curve clearly shows hysteresis due to a large β_c value.

(a)

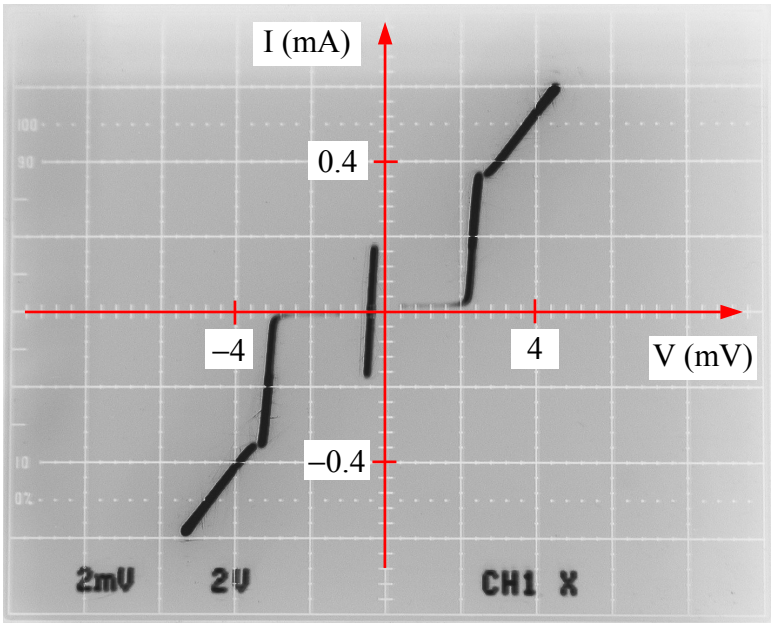

(b)

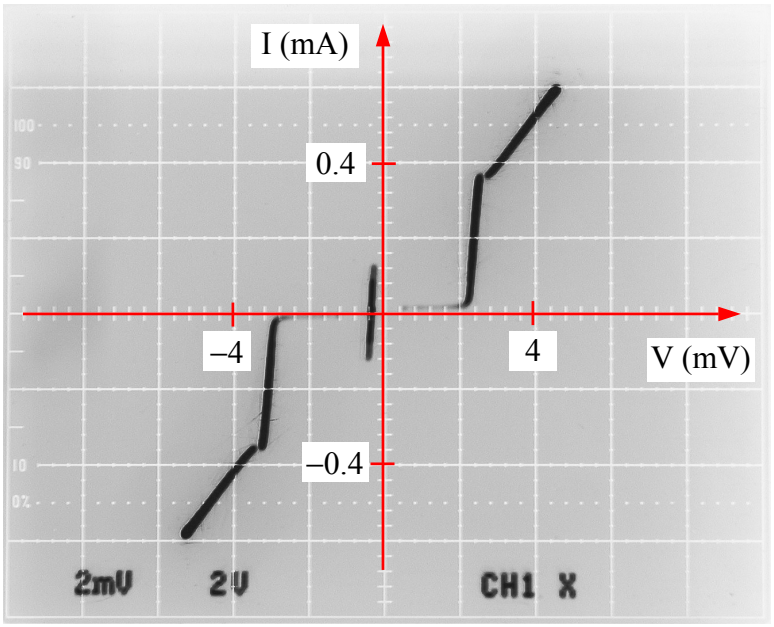

FIG. 3.9. I-V characteristics of SQUID BH obtained from a four point measurement with common ground. Measurements performed in LHe using micro coaxial cable with silver platted copper weld inner conductor and stainless steel outer conductor. Connections to the SQUID performed by wirebonding. Horizontal scale is voltage with 2 mV/div. Vertical scale is current with 0.2 mA/div. Origin centered at middle of picture. An offset voltage of approximately –0.5 mV is seen due to thermal emf. Modulation of critical current between (a) maximum and (b) minimum values is observed. Change in magnetic flux through SQUID hole achieved by rotating dc SQUID in ambient magnetic field.

Using the expression for the retrapping current given by

$$I_r = \frac{4I_c}{\pi\sqrt{\beta_c}}, \tag{3.27}$$

β_c can be estimated to be approximately 480 with $2I_r = 10\pm5$ μA and $2I_c = 172\pm5$ μA [70,81]. However, due to the relatively large uncertainty in I_r and the effects of noise and temperature in raising the apparent retrapping current, β_c could be anywhere between 200 and 2000. Assuming identical junctions and using Eq. (2.68), the subgap resistance of a single SQUID Josephson junction is expected to be in the range between 30 Ω and 100 Ω, dependent on the value of β_c. However, this result conflicts with direct observation of the effective subgap resistance from Fig. 3.9, which gives a lower limit of 340 Ω across each junction. Such a resistance would correspond to a value of β_c that is greater than 2×10^4. On the other hand, this conclusion is based on a simple linear model following the analysis in section 2.4. A more complete analysis of the nonlinear behavior of a Josephson junction based on Eq. (2.94) does not fully explain the experimental observations, as discussed by Prober *et al*. [71]. Consequently, more confidence is given to the former result of β_c between 200 and 2000 but with prejudice toward the higher limit, not only due to the results of direct observation but also due to thermal effects that increase the effective retrapping current [70,83].

Some other notable features in the I-V curves of Fig. 3.9 are the gap voltage $2\Delta/e = 2.7\pm0.1$ mV and the normal resistance above the gap voltage $R = 16.9\pm0.5$ Ω. At the boiling point of LHe, $T = 4.2$ K, so $T / T_c = 0.45$. According to BCS theory, the gap voltage at 4.2 K should be very close to the zero temperature value, differing

by less than 4% [34,86,115]. However, the observed difference of 11.5% from the zero temperature value suggests a higher temperature $T \approx 0.64T_c \approx 6.0$ K. Although a satisfying explanation for the discrepancy has not been determined, there is always the possibility of excess heating due to the current in the measurement leads.

If one assumes that the higher temperature is correct, the estimated critical current at zero temperature should be $I_c(0) \approx I_c(T)/0.7 \approx 120$ μA [41]. Then by Eq. (2.90), the gap voltage at zero temperature should be 2.6 mV. This discrepancy could be a result of critical current suppression or an effective resistance of $R \approx 20$ Ω which lies between the observed normal resistance and the estimated range of the subgap resistance. An alternate explanation for the multiple discrepancies could be that the superconducting material is not pure niobium. Fortunately, whatever the situation, the magnetic field sensing properties and the fast transition from the zero voltage state to the resistive state of the SQUID are not affected.

Using the calibrated critical current density of 1160 A/cm^2 provided by HYPRES for SQUID BH, the expected maximum critical current was 139±12 μA for the two 3 μm × 3 μm SQUID junctions. The measured value of 172±5 μA is somewhat larger than this value and is probably due to a slightly larger junction area than expected. Compensating for the larger area using the new value of I_c, the total SQUID capacitance of the two Josephson junctions is approximately 0.75 pF using Eq. (3.26). I can now use Eq. (3.9) to estimate the voltage rise time τ_{rise} of the junction and find $\tau_{rise} \approx 11$ ps. The maximum SQUID bandwidth is then 44 GHz.

Again using Eqs. (3.1) and (3.13) with $2I_c = 172$ μA, the estimated value of β is 1.3, which means there could be magnetic hysteresis, though no obvious

manifestation of this was observed. This value of β also implies that the modulation amplitude of the critical current will be roughly $0.7I_c \approx 60$ μA [60,63]. The observed modulation seen in Fig. 3.9 is 49±7 μA, suggesting that β is slightly larger than 1.3. To observe the full range of modulation, I rotated the SQUID in the ambient magnetic field, which varied the magnetic flux through the SQUID hole. Multiple oscillations of the critical current were observed as the SQUID rotated through 90°.

Examination of Fig. 3.9 also shows that the supercurrent occurred at around −0.5 mV instead of zero. I have concluded that this effect was due to the Seebeck effect or thermoelectric emf in the leads during I-V measurements. The measurement was performed with micro coaxial cable with an inner conductor made of silver-plated copper-clad steel (SPCW) and an outer conductor of stainless steel. The Seebeck coefficients of copper and iron respectively range from 2 μV/K and 16 μV/K to zero decreasing as $T \rightarrow 0$ [119]. I measured voltages using the inner conductor with the outer conductor connected to a common ground. Given an average difference of −1 μV/K in Seebeck coefficient between the inner and outer conductors for temperatures between 300 K and 4 K, the resulting thermal emf would be around −0.3 mV. This is the magnitude of the observed voltage offset.

I occasionally observed a few other anomalies in the I-V characteristics. Under certain circumstances, the zero voltage state was not symmetrical for positive and negative currents. This can be seen in Fig. 3.10. When this occurred, the modulation of the critical current was such that one polarity seemed to lag the other. For example, if for positive current, the modulated critical current was given by

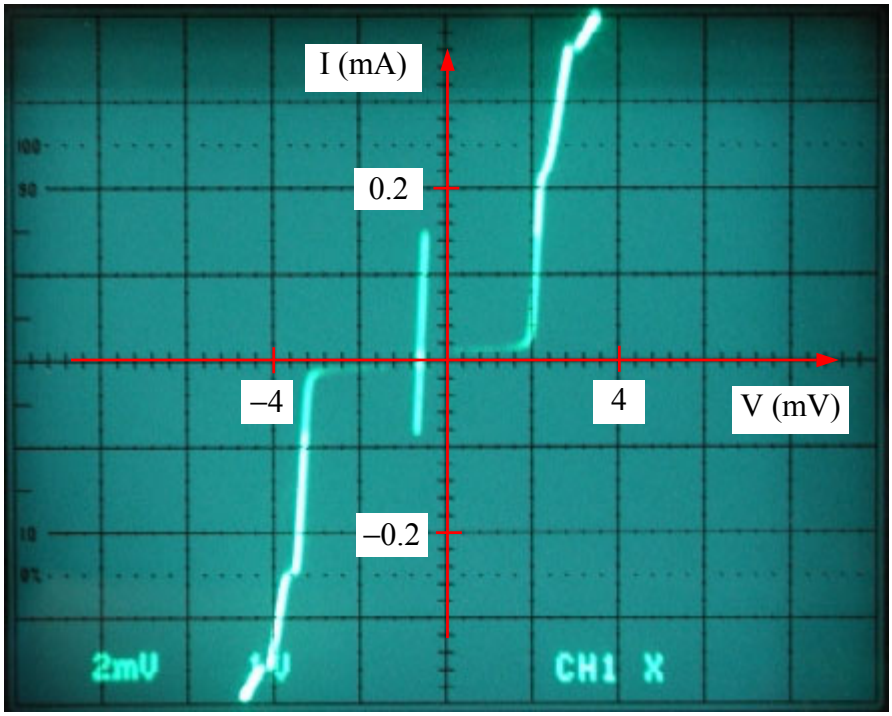

FIG. 3.10. I-V characteristics of a hysteretic dc SQUID showing asymmetry in the positive and negative critical currents. Modulation of critical current in one polarity was found to lag behind modulation of critical current in opposite polarity, as magnetic flux through SQUID hole is increased. Origin centered at middle of picture. An offset voltage of approximately –0.5 mV seen due to thermal emf.

$$I_c(\Phi) = 2I_c \cos \pi \frac{\Phi}{\Phi_o}, \tag{3.28}$$

then for negative current, it was behaving like

$$I_c(\Phi) = -2I_c \sin \pi \frac{\Phi}{\Phi_o}. \tag{3.29}$$

The cause of this behavior was not determined, but the effect sometimes disappeared with thermal cycling, suggesting that the phenomenon was associated with trapped flux.

Finally, in Table I, I summarize the main SQUID parameters for the nonhysteretic SQUID AN and the hysterestic SQUID BH.

3.3.3 SQUID Chip Layout and Leads

In addition to the SQUIDs themselves, SQUID chips require leads, contact pads, and connections to external wiring. Several individual SQUIDs can fit onto a single HYPRES chip which is 5 mm × 5 mm square (see Fig. 3.11). Although the actual SQUIDs are very small, the contact pads are considerably larger, so most of the chip area is taken up by the contact pads. These pads are made from titanium, palladium, and gold with gold constituting most of the pad; this provides a low resistive connection of less than 0.1 Ω/square for the contact pad leads from external wiring to the SQUIDs [118].

In my design, there are two sets of pads, one for use in the SQUID microscope and another for testing the chip. Two sets are included because after testing a chip, wire leads connected to the contact pads needed to be removed, and during this process the pads would be damaged. Thus, with two sets, an auxiliary set would be

TABLE I. SQUID parameters for SQUIDs AN and BH. Values in the Actual column are best estimates determined from data or information provided by HYPRES, Inc.

Parameters	SQUID AN		SQUID BH	
	Designed	Actual	Designed	Actual
Size (outer)	30 μm × 40 μm		30 μm × 30 μm	
Size (hole)	10 μm × 10 μm		10 μm × 10 μm	
L	16 pH		16 pH	
C	0.30 pF	0.30 pF	0.30 pF	0.38 pF
β_c	1	0.26	high	200 to 2000
β	1	1.07	1	1.3
$2I_c$	120 μA	25 μA	120 μA	172 μA
ΔI_c	60 μA	70 μA	60 μA	49 μA
ΔV	60 μV	80 μV	3.0 mV	2.7 mV
R	2 Ω	23 to 30 Ω	low	16.9 Ω
R_{sg}	2 Ω		high	30 to 100 Ω

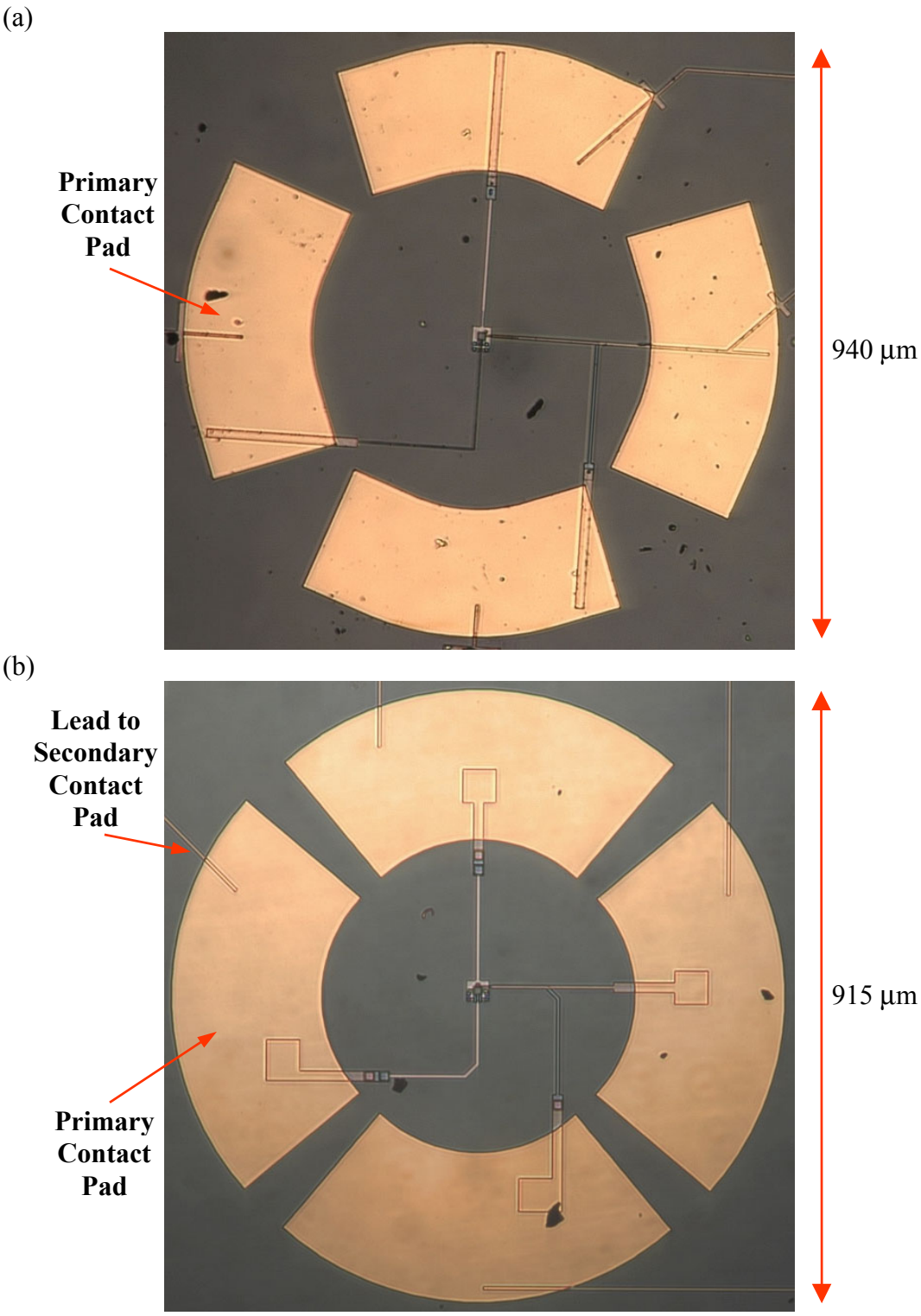

FIG. 3.11. Photographs of niobium dc SQUIDs showing their primary contact pads and leads. (a) Original design by Cawthorne and Nielsen for the LHe cooled scanning SQUID microscope. (b) Updated design with more circular pads and HYPRES design rule compliant lead thicknesses.

used during testing. Then if the SQUID is to be installed into the microscope, it is diced from the chip, and the primary set is used for wiring inside the microscope. The auxiliary contact pads used for testing are located around the rim of the HYPRES chip, and each pad corresponds to and is electrically connected to a primary pad that is located near the SQUID (see Fig. 3.11).

The size of a contact pad is determined by the number of pads needed and the dimensions of the chip. I found the sizes of pads in the original Cawthorne and Nielsen design to be too small. So, I enlarged the pads to allow more connections per pad. In the updated design, shown in Fig. 3.12, the auxiliary contact pads are about $500\ \mu m \times 400\ \mu m$ on average.

For the primary contact pads, I found that increasing the outer dimension of an individual SQUID chip was not the deciding factor in increasing the effective area of the pads. For z-SQUID configurations, seen in Fig. 3.11, the pads surround the SQUID evenly. However, most of the outer edges of the pads are ground off as a diced SQUID must ultimately be placed on a 1 mm by 1 mm sapphire tip for use in a SQUID microscope. In order to maximize the remaining pad area, I found that the pads had to fill as much area around the SQUID as possible, except near the SQUID to avoid interference from stray field. This was achieved by making the pad design more circular than before.

Consideration was also given to making contact pads large enough so that silver paint could be applied by hand to make electrical connections to the chip. I had attempted making such connections with silver paint for testing purposes, and the practice is routine for preparing SQUID chips used in high-T_c SQUID microscopes

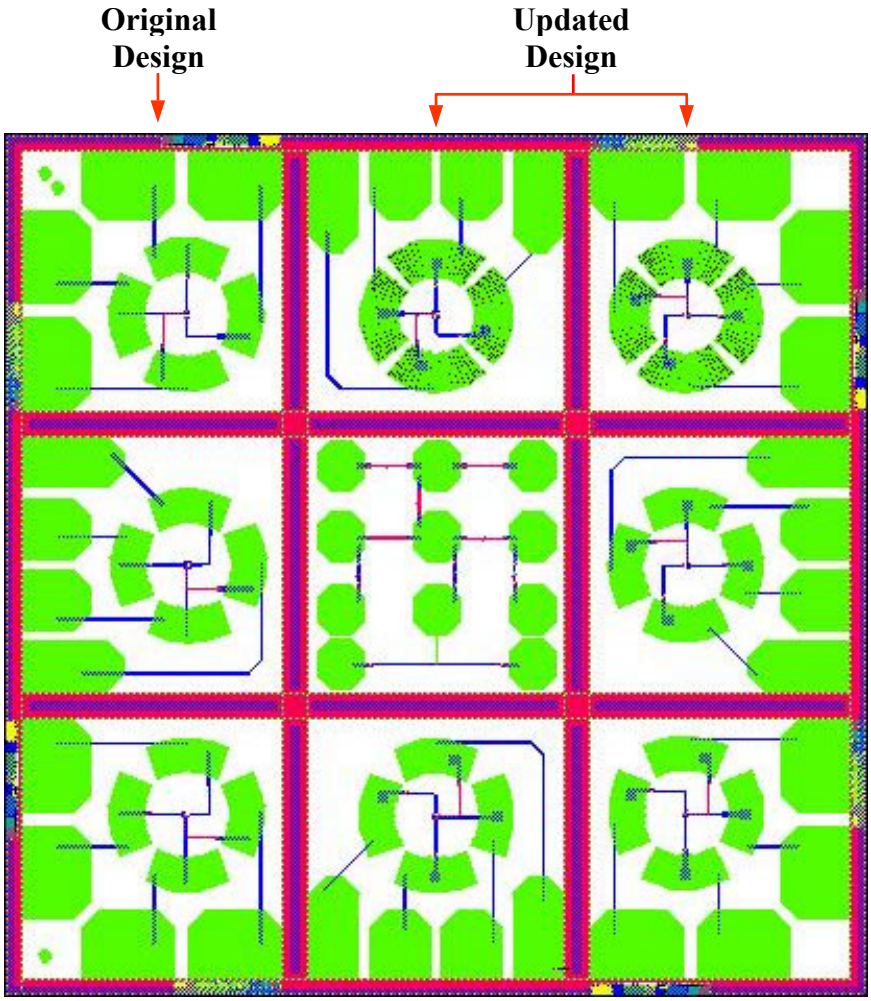

FIG. 3.12. Updated design of HYPRES niobium SQUID chip. Auxiliary contact pads used for testing are located around the rim of 5 mm × 5 mm chip. Vertical and horizontal stripes indicate dicing channels for extracting individual SQUIDs after testing. The dicing channels divide the chip into nine square areas each containing a single SQUID. There are no auxiliary contact pads for the center square which can contain a SQUID or some other test circuit, as shown here. The chip shown in this diagram contains dc SQUIDs with both the original design used in the LHe cooled SQUID microscope and the updated design with HYPRES compliant features, some with more circular primary contact pads.

[17]. However, pad sizes would have to increase further to make this easy to perform. Furthermore, if the quality of either the silver paint or the contact surfaces were poor, these connections would show a lot of noise and fail in a short time. In the end, I found the best electrical connections were produced by wirebonding. Consequently, the updated contact pad design was optimized to easily allow multiple wirebonded connections, particularly for the auxiliary pads.

In both the original Cawthorne and Nielsen design and in my updated design, four pads are used for each SQUID. Two are connected to the dc SQUID while the other two are connected to a one turn coil around the SQUID hole. The SQUID pads are used both to supply the dc SQUID with bias current and to measure its voltage. Leads to the SQUID are connected to the SQUID loop in a symmetrical design, as shown in Figs. 2.2(b) and 3.5. This prevents any asymmetry in the inductances of the two branches of the SQUID loop. Asymmetry may lead to the bias current providing a circulating current around the loop, which in turn would lead to a shift in the critical current versus flux relation. Figures 2.2(b), 3.5, and 3.11 also show how the leads to the one turn coil overlap near the SQUID. This reduces the effect of stray magnetic field near the SQUID due to the coil leads.

The leads were also designed such that the geometrical shape they formed helped identify and differentiate the SQUID leads from the coil leads. For instance, the SQUID leads formed an "L" shape, which is inverted during the chip fabrication process, and the coil leads formed a "T" shape (see Fig. 3.11). This was especially helpful in preventing basic wiring mistakes, such as during wirebonding. Furthermore, in the updated chip, the secondary pads were sequenced such that each

pad in a sequence corresponded to the same lead on an individual SQUID regardless of which SQUID was being tested (see Fig. 3.12). This made it more convenient during testing, as it was easier to identify, verify, and align connections.

The idea behind x-SQUIDs, z-SQUIDs, and how they affect contact pad design is as follows. A SQUID can have two configurations depending on whether the plane of the SQUID loop is parallel with or perpendicular to the plane of the surface it is scanning. In a z-SQUID configuration, the SQUID is oriented to measure the magnetic field that is normal to the surface being scanned, i.e. the SQUID loop is parallel to the sample surface. On the other hand, the x-SQUID configuration has the SQUID loop normal to the sample surface, so the SQUID measures the component of the magnetic field that is parallel with the surface and normal to the loop.

Now, the ability of a SQUID microscope to spatially resolve individual sources of surface currents improves as the distance between the scanned surface and SQUID decreases [14,15]. So, to maximize spatial resolution, the SQUID must not only be small but also brought as close as possible to the scanned surface. In the case of a z-SQUID, the whole loop can be brought close to the surface, and the contact pads can be placed around the SQUID evenly as in Fig. 3.11. In contrast, for an x-SQUID, only one edge of the SQUID loop is brought close to the surface. Therefore, all the contact pads have to be placed on one side of the SQUID loop. This requires positioning the pads as in Fig. 3.13.

Although I did not prepare SQUID chips with primary pads configured as x-SQUIDs, the auxiliary contact pads are in the x-SQUID configuration. In fact,

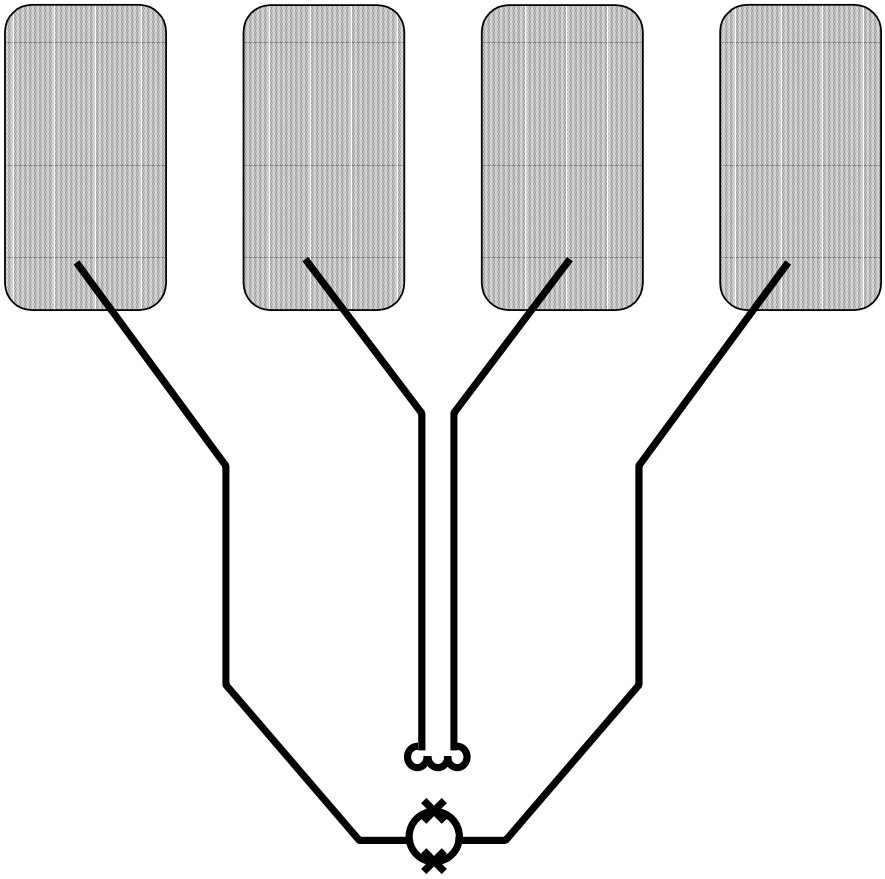

FIG. 3.13. Diagram showing an x-SQUID configuration with all contact pads and leads going to one side of the SQUID loop. The configuration includes leads and pads for a coil to generate a magnetic field through the SQUID hole. The coil can be part of a feedback system or used to test the SQUID.

Vlahacos *et al*. have made use of my SQUIDs in the x-SQUID configuration for the prototype SQUID microscope [120].

CHAPTER 4 The 4 K Cryocooled Scanning SQUID Microscope

4.1 Overview of Microscope

The main components of a scanning SQUID microscope, besides the SQUID itself, are a cryocooler or cryostat, a vacuum chamber, a cold finger, a sample translation mechanism, and electronics for monitoring the SQUID and controlling the microscope. Figure 4.1 shows a conceptual sketch of the prototype 4 K scanning SQUID microscope including the cryocooler, a radiation shield around the cold finger, and a movable sapphire window separating the SQUID from the sample. Figure 4.2 shows a photograph of the entire system. In the prototype microscope, the cryocooler takes up the bulk of the volume and is the most expensive single component. Until room temperature superconductors are discovered, a cryogenic system will be needed for cooling the SQUID to superconducting temperatures.

Several criteria were involved in the design of the SQUID microscope. Foremost, the microscope needed to be able to operate with hysteretic SQUIDs. This lead to the choice of niobium SQUIDs which operate at liquid helium (LHe) temperatures. Also for practical purposes, it is preferable for the microscope to be operable and serviceable by one person. Samples should be easy to mount and change. So, to make the system compact and simple to operate, a large capacity cryocooler is preferred rather than a cryostat which would take up more space and require repeated filling of cryogen. Although cryostats are a mature technology with

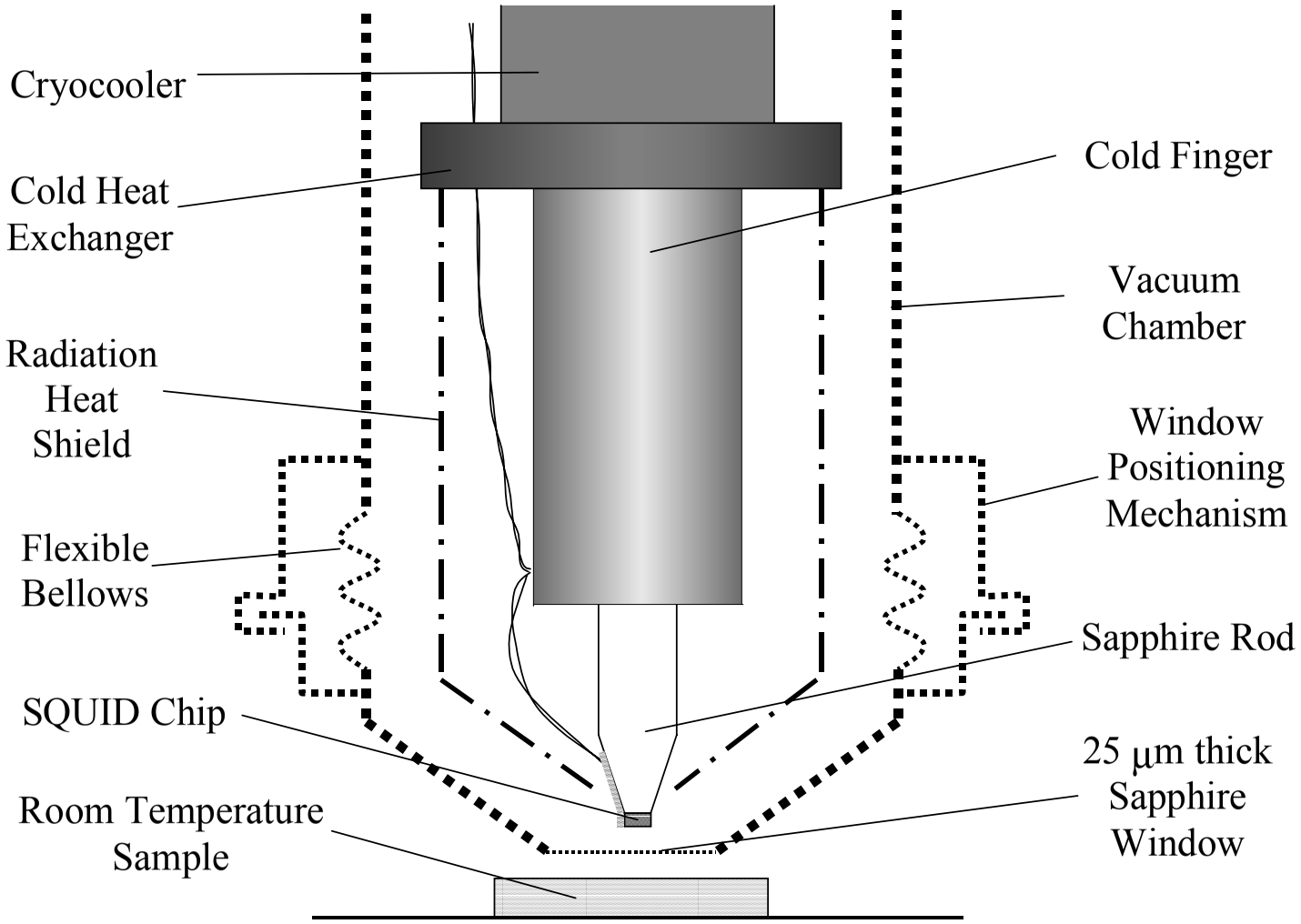

FIG. 4.1. Schematic diagram of the cold region of the prototype 4 K cryocooled Scanning SQUID Microscope.

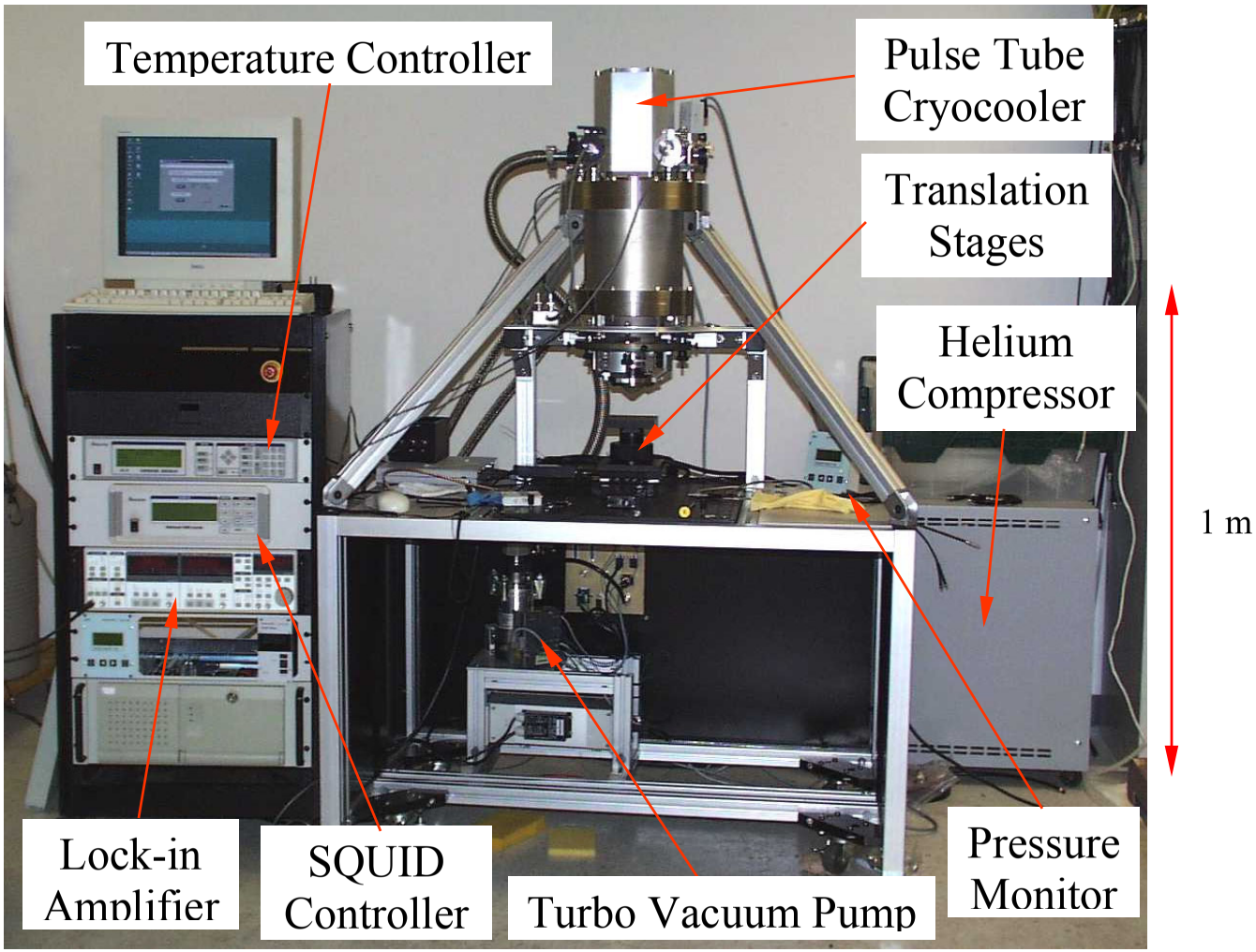

FIG. 4.2. Photograph of prototype Scanning SQUID Microscope with a 4 K pulse tube cryocooler. A diaphragm vacuum pump which supports the turbo pump lies behind the table top chassis and is not seen in the photograph.

fewer mechanical vibration issues than cryocoolers, it is a major advantage to only need electrical power and not have to regularly supply LHe to the system. Closed cycle cryocoolers reaching temperatures below 4 K are currently available and allow low temperature superconducting material such as niobium to be used. Furthermore, the lower temperature allows superconducting material with higher T_c to be used in the future, and the effect of thermal noise is smaller as discussed in section 3.1. It is also advantageous to have samples at room temperature. This is made possible by the moveable sapphire window in the vaccum chamber and permits mounting and changing samples without having to shut down the microscope [8,12,17].

In the following sections, I describe the main microscope components and some issues and that affect performance. The main sources of noise in the prototype microscope are mechanical noise from mechanical oscillations of the SQUID cold finger caused by the pulse tube cryocooler, electrical noise from the SQUID electronics, and intrinsic noise from the SQUID itself and from resistive contacts. Some of these noise sources, such as the mechanical oscillations of the cold finger, are so significant that they will need to be addressed through design changes. The chapter ends with a section on the microscope's operating and servicing procedures, including comments on its performance.

4.2 Cryocooler and Vacuum System

4.2.1 The Pulse Tube Cryocooler

The cryocooler chosen for the prototype SQUID microscope is a PT405 pulse tube cryocooler from Cryomech, Inc. (see Fig. 4.3) [27,121]. The working principle

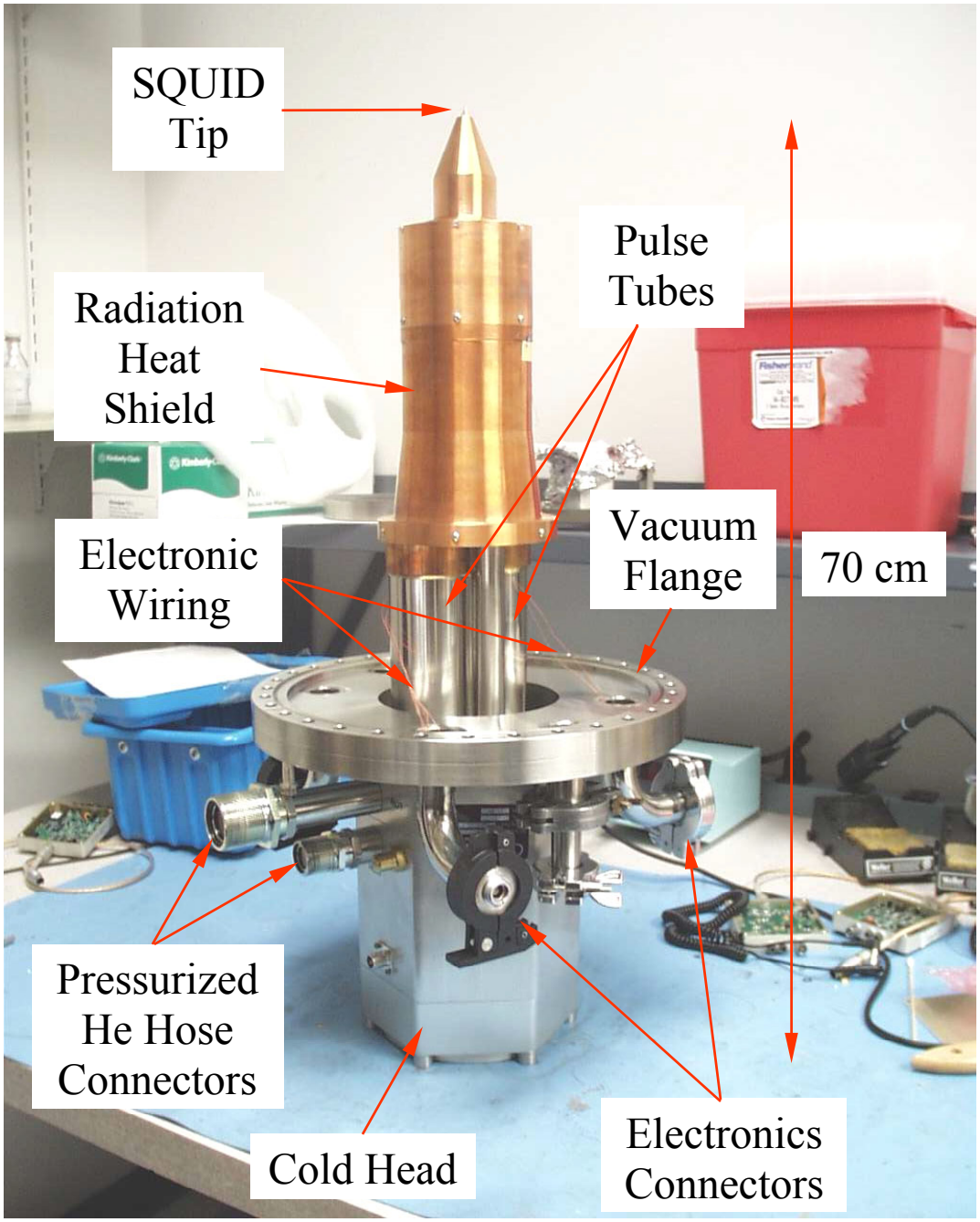

FIG. 4.3. Photograph of the Cryomech PT405 4 K pulse tube cryocooler with the cold finger attached to the second stage heat exchanger. The copper radiation shield is attached to the first stage heat exchanger and covers the cold finger and most of the pulse tubes. When installed, the SQUID tip points downward. Hermetic connectors available on flange for pressure gauge and electronic wiring.

behind the pulse tube is similar to that of Stirling cryocoolers and is summarized in Fig. 4.4 [122-127]. Compressed gas is forced to flow into a tube where it expands and cools the surrounding material. The pulse tube performs this without requiring any moving parts in the cold region. This is made possible by substituting the piston, or displacer, in a Stirling cryocooler with a column of compressed gas or gas density wave in the tube. The expanded cold gas removes heat from the cold region and is then retrieved from the tube. The tube is designed to minimize convection currents which would mix the cold and hot gases in the tube. Before the gas is recompressed and the cycle repeated, the gas goes through a regenerator which is cooled by the cold gas. The role of the regenerator is to pre-cool the warm gas passing through before it enters the pulse tube on the following cycle. The pulse tube system operates in a closed cycle and only needs additional coolant (pure helium) when a sufficient amount is lost due to leaks or when there is significant contamination.

The PT405 cryocooler uses a low frequency (Gifford-McMahon type) pulse tube and operates at a frequency of around 1.3 Hz. Compressed helium gas is supplied to the cryocooler from a separate compressor unit through a flexible metal hose, and the decompressed gas is returned to the compressor where heat from the gas is removed for recompression. Cold water must be supplied to the compressor to keep it from over heating. I recommend some type of filtering to the water supply to remove contaminants which may cause damage to the compressor.

In order to increase the cooling efficiency and reach temperatures below 4 K, an intermediary stage exists between the room temperature components and the cold region second stage. The first stage acts as the high temperature sink to the second

(a)

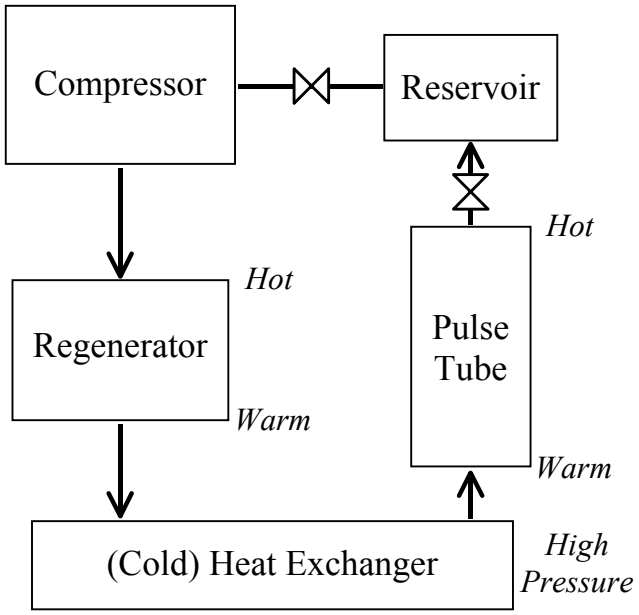

(b)

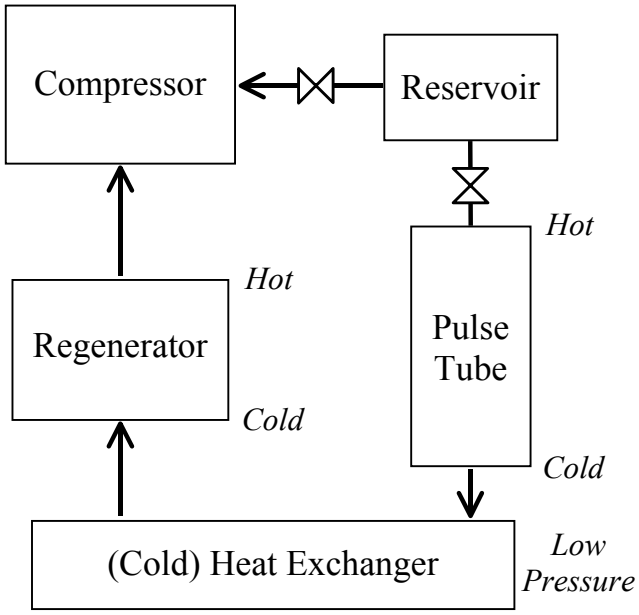

FIG. 4.4. Block diagrams representing the working principle of a basic single stage pulse tube cryocooler. (a) Compression phase: compressed helium gas passes through the regenerator and cold heat exchanger before entering the pulse tube. The cold end of the regenerator is thermally anchored to the heat exchanger and is already cooler than the other end due to the previous cycle. Gas at the warm end of the pulse tube leaks into a reservoir but out of phase with the change in pressure inside the tube. (b) Expansion phase: leakage into the reservoir is cut off, and compressed gas inside the pulse tube expands out through the heat exchanger removing heat in the process. As the gas returns to the compressor through the regenerator, the temperature gradient in the regenerator increases.

stage. This first stage can reach temperatures down to 32 K with the second stage reaching below 4 K. The efficiency of the regenerator for the second stage is maximized for temperatures below that of the first stage. However, overall cooling power of the second stage is less than that of the first stage. The first stage has a rating of 25 W at 65 K compared to 0.5 W at 4.2 K for the second stage. The first stage is used to cool a radiation shield which surrounds the second stage as well as the attached cold finger, reducing radiation heating from the room temperature environment (see Fig. 4.3). Signal wires going to the cold finger are also thermally anchored to the first and second stage heat exchangers to minimize conductive heating of the cold finger and SQUID chip.

4.2.2 The Vacuum Chamber and Pumps

For good thermal insulation, all the cryogenic components are contained within a vacuum chamber. The vacuum environment also prevents air and moisture from condensing on the cold parts of the system, thus reducing damage during thermal cycling. In the microscope, a diaphragm pump is used for rough vacuum and a turbo pump is used to reach the base pressure of about 10^{-4} torr before starting the cryocooler [128]. Both pumps are air cooled. Once the cryocooler is activated, the vacuum level improves as remaining gas molecules stick to cold surfaces inside the chamber.

The vacuum chamber and chassis are made from nonmagnetic stainless steel and aluminium alloy and consist of three main sections. A large cylindrical section surrounds the pulse tubes and is bolted to the top of a brace on the table chassis (see

Fig. 4.2). The bottom of this section, with the cryocooler in place, is seen in Fig. 4.5(a). The cryocooler is inserted from the top and sealed to the vacuum chamber with a rubber o-ring and vacuum grease. The cryocooler has to be oriented with the heat exchangers pointing downward for it to operate efficiently. Attached to the bottom of the cylindrical section is a metal bellows section. Finally, a cone shaped section made from fiberglass with a 25 μm thin sapphire window at the tip attaches to the bottom of the bellows.

The bellows section includes a mechanism to translate the cone shaped section relative to the cylindrical section. A photograph of the lower portion of the assembled chamber is shown in Fig. 4.5(b). The SQUID must be brought as close as possible to the scanned object. The bellows makes this possible by allowing the thin sapphire window to be brought close to the SQUID chip. The scanned object on a translation stage is then brought as close as possible to the sapphire window.

I note that this overall design is based on the 77 K cryocooled high-T_c SQUID microscope by Fleet *et al*. for imaging room temperature objects [10,17].

4.2.3 Leak Problems

Over time, the vacuum inside the chamber was found to slowly deteriorate and the temperature of the cold finger rose. Small leaks through the fiberglass cone are thought to be the main source as the fiberglass was found to be porous. If the base temperature of the cold finger rose too much, the main remedy was to shut down the cryocooler and allow it to warm up while continuously pumping the chamber. Cryocooler operation was resumed when the vacuum level returned to desired levels.

(a)

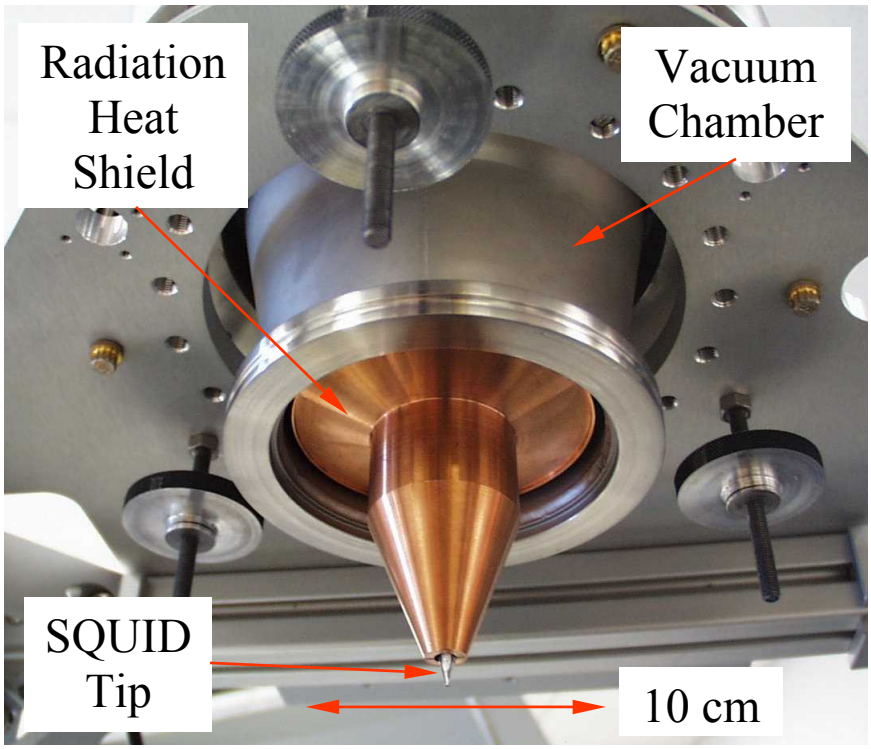

(b)

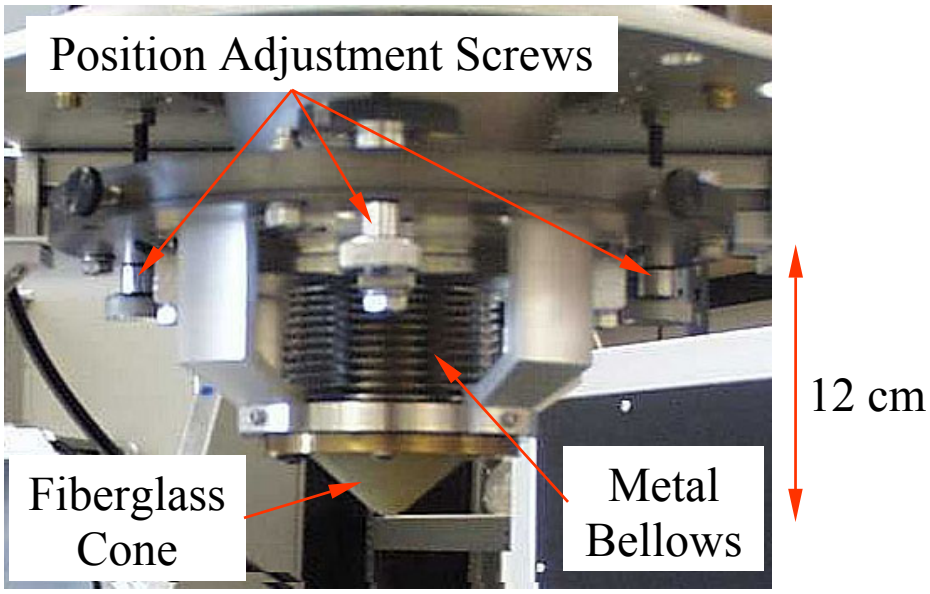

FIG. 4.5. (a) Bottom portion of the cylindrical vacuum chamber with the cryocooler assembly in place. The bellows and fiberglass cone sections are not installed. The SQUID tip can be seen sticking out of the radiation shield. (b) Bottom portion of the assembled vacuum chamber. The thin sapphire window is located at the tip of the cone shaped fiberglass section of the chamber.

A permanent fix would involve replacing the fiberglass cone with a less porous non-conducting and magnetically permeable material such as ceramic. An alternate method would be to treat the fiberglass with a vacuum seal spray as used by Lee on her high-T_c SQUID microscope [12].

Vacuum contamination and thermal cycling also degraded the performance of the SQUID. The degradation appeared to be related to electrical contact problems on or near the SQUID chip. Vacuum contaminants could have seeped into the silver paint used in some electrical connections, and with thermal contractions and expansions, may have caused connections to fail over time. Thus, maintaining a good vacuum with constant temperature was important to the long term performance of the microscope.

4.3 Cold Finger and Thermal Anchoring

4.3.1 Preparing the SQUID Tip and Cold Finger

For a niobium SQUID to work, it must be cooled below $T_c \approx 9.3$ K. However, to scan room temperature samples, the SQUID must also be positioned near the sapphire window inside the narrow cone section of the vacuum chamber. This requires attaching the SQUID to a cold finger (see Fig. 4.6), which is thermally anchored to the cryocooler's second stage.

Attaching the SQUID to the cold finger needs considerable preparation. The SQUID is first attached to the tip of a sapphire rod which has good thermal conducting properties as well as being a nonmagnetic insulator. The width of the tip end where the SQUID chip is mounted is about 1 mm. This allows the SQUID to be

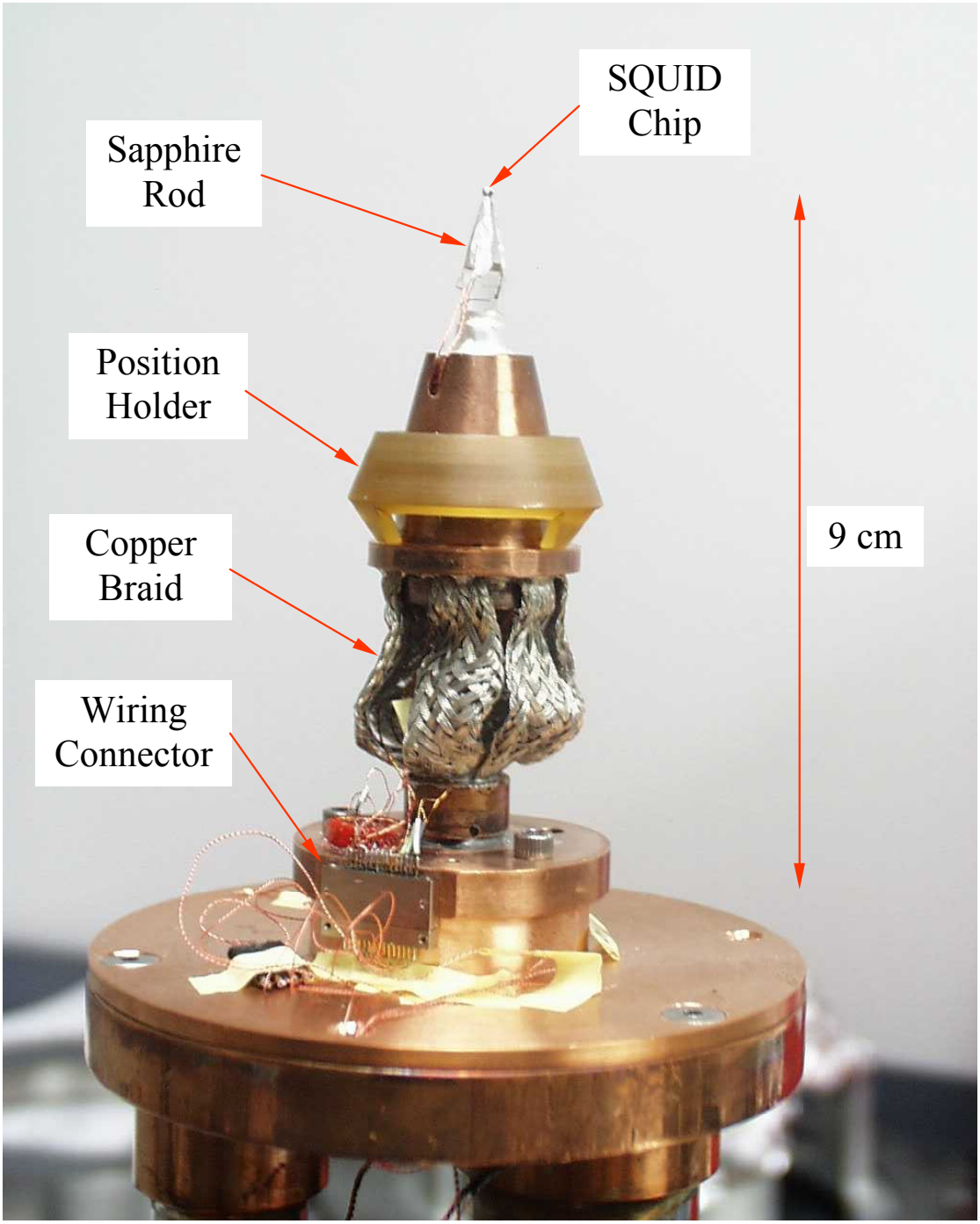

FIG. 4.6. Photograph of cold finger attached to the second stage of the 4 K pulse tube cryocooler. The wiring is configured for FLL electronics with a nonhysteretic dc SQUID.

positioned close to the sapphire window without touching any surfaces. The HYPRES SQUID chips, on the other hand, are on 5 mm × 5 mm substrates, and a single z-SQUID with contact pads and margins takes up about 1.5 mm × 1.5 mm [117,118]. Thus, the first step is to dice out single SQUIDs from a HYPRES chip that will fit on top of the sapphire tip. I diced chips by using an automated chip dicing machine or by hand using a diamond scriber.

The next step is to chemically clean the chip and epoxy it to the sapphire tip. Cleaning is performed in an ultrasonic bath for a few minutes with acetone followed by a methanol rinse. To perform any necessary degreasing, I did an additional cleaning step using TCE at the beginning.

To attach the diced SQUID to the sapphire tip, I used a thin layer of a two part epoxy, STYCAST 2850FT with catalyst 9 from Emerson and Cuming [129]. Although not ideal, the epoxy was the best epoxy readily available for use. I had tested other epoxies, but they either had poor chemical tolerance to solvents like acetone, or their bonds failed under applied force and thermal stress from repeated thermal recycling. Preparation of the epoxy requires good mixing and an accurate ratio of the two parts, especially when preparing small quantities. Small air bubbles form during the mixing process, and these should be avoided to obtain a smooth surface and void-free finish. The manufacturer recommends removing the bubbles by intermittently placing the epoxy in a vacuum chamber during mixing. During the process, the epoxy outgases and expands, possibly contaminating the chamber. Due to a lack of appropriate equipment, the evacuation step was skipped.

For the bond between the SQUID chip and epoxy to reach full strength, the epoxy has to be sufficiently cured. With the layer of epoxy being very thin, the longest curing times were found to produce the strongest bonds. At room temperature, this meant curing the epoxy for 72 hours or more. Higher curing temperatures would shorten the curing time, and a post cure at an elevated temperature is recommended by the manufacturer. However, high temperatures can permanently change the SQUID characteristics or cause damage. So, temperatures above 50°C were avoided.

After curing, I ground the SQUID tip using a turn table grinding machine to remove epoxy and excess parts of the chip around the SQUID. The top surface of the SQUID tip must have some protective layer to prevent damage to the SQUID while grinding. I found that a layer of hardened photoresist on the SQUID chip surface was sufficient for protection. I ground the SQUID tip to a roughly 1 mm × 1 mm square and then chemically cleaned it. The last step remaining in tip fabrication is to make electrical connections, which is discussed in detail later.

Once the sapphire rod with the SQUID tip is prepared, it goes into the cold finger through a tightly fitting hole. In the prototype microscope, silver paint and copper sheet shims were used to create a good strong thermally conducting bond between the sapphire rod and cold finger. Thermal conductance is essential, so the cold finger is made of copper.

When inserting the sapphire rod into the cold finger, the height of the tip needs to be adjusted. The microscope's radiation shield is conically shaped near the tip and has a hole where the SQUID tip protrudes out as seen in Figs. 4.3 and 4.5(a).

The height of the SQUID tip determines how much the tip protrudes outside the hole. If it is too high, the sides of the sapphire rod will touch the radiation shield. If it is too short, the sides of the radiation shield may touch the vacuum chamber when the sapphire window is brought close to the SQUID tip. Both situations should be avoided.

4.3.2 Motion Isolation

For vibration isolation, the cold finger comes in two parts. There is a top part which holds the sapphire rod and a bottom part which attaches to the cryocooler. The two parts are connected to each other with six strips of copper braid for flexibility as seen in Fig. 4.6. A flexible structure is required to provide crude mechanical vibration isolation of the SQUID tip from movement due to cryocooler operation. To hold the SQUID tip fixed inside the prototype microscope, a fiberglass position holder which fits over the cold finger and conforms to the inside surface of the radiation shield is used. The fiberglass holder is designed so that the SQUID tip is positioned at the center of the radiation shield hole. The cold finger itself is kept in contact with the position holder by gravity.

Despite the position holder, low frequency oscillations of the SQUID tip were observed in the prototype SQUID microscope with an amplitude between 15 μm and 30 μm peak-to-peak. Such oscillations are undesirable and need to be suppressed as they cause large imaging noise and lead to acoustic pickup as the SQUID moves in the ambient field. The oscillations occur due to the pulse tube's expansion and

contraction. This results in the second stage heat exchanger deforming as the pressure inside the pulse tubes change [130].

It is still not known whether the problem is only confined to the second stage heat exchanger or prevalent throughout the cryocooler. The remedy to the oscillation problem will depend on the cause. If the whole cryocooler is affected, a completely different SQUID tip holding scheme is required. If the problem is confined to the second stage heat exchanger, the cold finger just needs to be rigidly secured to the radiation shield.

Another motion problem was high frequency vibrations that affected the entire microscope chassis. These vibrations were found to originate from the helium compressor. The compressor generated high frequency vibrations which were mechanically coupled not only via the compressed helium hoses but also through the hard surface of the floor. In fact, I first noticed the significance of the high frequency vibrations while observing the SQUID tip through the sapphire window with an optical microscope placed on the floor. The image did not seem to sharply focus and looked fuzzy due to the vibrations. Fortunately, the relative motion was less noticeable between components on the microscope table top. Therefore, signal distortions due to the high frequency vibrations may be less significant than the low frequency oscillations.

Some vibrational issues had been expected. Kenyon *et al*. used a Gifford-McMahon cryocooler to cool a Single Electron Transistor (SET) to 4 K [131]. There, the use of copper braid and fiberglass position holder to isolate mechanical motion was also found to be insufficient. Better isolation was achieved by using strips of

ultra high purity copper foil (99.999% pure). Such strips have thermal conductivity that is orders of magnitude higher than regular copper but are far more flexible than braid, thus decreasing mechanical coupling [132]. The increased thermal conductivity of the foil allows less material to be used and makes the connection more flexible. Multiple strips can then be added to increase heat flow as needed.

Unfortunately, I did not prepare and implement a copper foil cold finger before testing the cryocooler. This was mainly because the pulse tube cryocooler was expected to have much smaller vibrations than the Gifford-McMahon cryocooler. As it turned out, the prototype microscope would still have significantly benefited from the copper foil design.

4.3.3 Heat Removal

The result of heating and insufficient heat removal by the microscope cold finger is a relatively small temperature difference between the cold finger and the tip of the sapphire rod. Such a temperature difference was observed with the prototype SQUID cold finger. The difference was especially noticeable when the cryocooler was turned off and the SQUID allowed to warm up. I observed the I-V characteristics of the dc SQUID while the temperature increased and noted the temperature at which the superconductor to resistor phase transition occurred. I found that the transition occurred when the temperature of the top part of the cold finger was around 8.3 K. As the transition temperature of niobium is approximately 9.3 K, the temperature difference between the SQUID and cold finger is approximately 1 K.

If the assumption holds that the cold finger is at the same temperature as the second stage heat exchanger, the 1 K temperature difference is likely due to insufficient thermal conductance of the sapphire rod. To diminish the temperature difference, I would have to replace the sapphire with a better thermally conducting electrical insulator, provided I could obtain such material. On the other hand, the thermal coupling between the top and bottom parts of the cold finger may be a limiting factor. More copper braid would be needed to increase heat removal, but this would reduce vibration isolation. Again, the solution may be to use strips of ultra high purity copper foil instead of braid.

4.3.4 Making Electrical Contacts to the SQUID

The prototype SQUID microscope used a dc SQUID in the z-SQUID orientation. This orientation does not leave much space for electrical connections to be made to the chip. For more space, electrical contacts must be extended to the sides of the sapphire rod (see Fig. 4.7). There were two methods I used to make these extensions. One involved a thin layer of silver paint that extended from the gold contact pads on the surface of the SQUID chip, over the chip edge and down the sides of the sapphire rod. Although relatively quick and convenient, the electrical connections made this way were not always reliable and tended to degrade with time due to inconsistent contact between the paint and gold pads or due to the quality of the silver paint itself.

An alternative method, which is more permanent, involved evaporating a thin layer of gold onto the SQUID chip and sapphire rod, effectively extending the gold

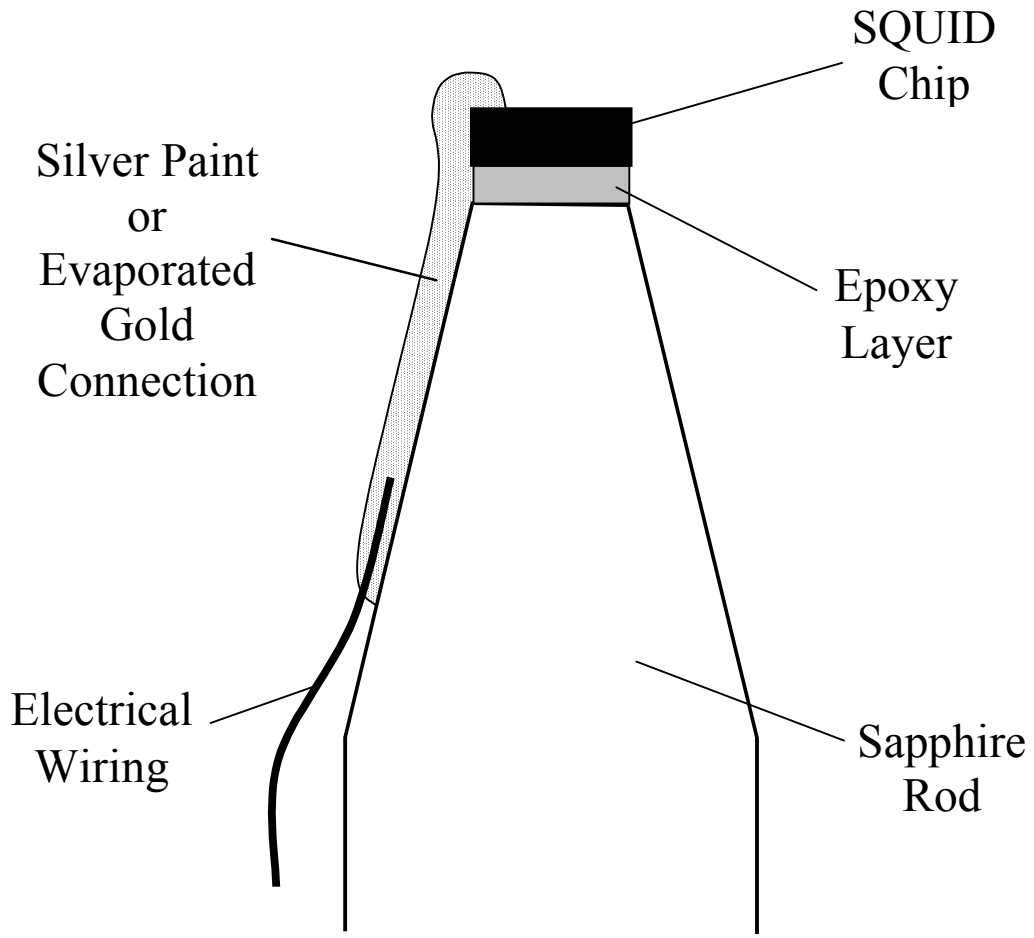

FIG. 4.7. Diagram of SQUID tip used in prototype SQUID microscope. Four electrical connections are present though only one is shown. The thickness of silver paint or evaporated gold is exaggerated to highlight the structure.

contact pads to the sides of the rod. This method required masking areas on the surface of the SQUID chip and on the sides of the sapphire rod, so that the SQUID and leads were protected and short circuits between leads or contact pads were prevented. Areas where gold was to be deposited were left exposed while everywhere else was covered by the mask. For the mask, I used photoresist which I applied by hand following a procedure similar to that of Nielsen [11]. I clamped a short segment of small diameter wire to tweezers and dipped it in wet photoresist. Small photoresist droplets formed on the wire, which I applied to the SQUID tip. Once the application of photoresist was complete, the SQUID tip was baked at 50°C for about 30 min to harden the resist.

Before evaporating gold, I used an argon ion mill on the SQUID tip for about a minute with an accelerating voltage of 79 V to produce a clean surface. I then evaporated a 5 nm to 10 nm layer of chromium which helps the gold adhere to the substrate. Finally, I evaporated a 50 nm to 200 nm layer of gold at a rate of 0.1 nm/s to 0.2 nm/s onto the SQUID tip. I used an in-house cryopumped high vacuum thermal evaporator for all of the evaporations and ion milling. After evaporation, I chemically cleaned the SQUID tip to remove the photoresist mask and then examined the tip for defects.

With the gold evaporation method, I always found a discontinuity problem. The problem was caused by the epoxy layer that held the SQUID chip to the sapphire rod. After the chip grinding process, the epoxy surface was no longer smooth and sometimes deteriorated with time, so that the evaporated gold would not form a

continuous surface over the epoxy. I resolved the problem by applying a small amount of silver paint to bridge the gap.

However, I also investigated another solution in which I sputtered silicon oxide on the epoxy surface to form a thin insulating layer prior to the evaporation of chromium and gold. The results were mixed, as the insulating layer would only occasionally produce a surface good enough for the gold to form a continuous connection. My limited success may well have been due to problems with the sputtering equipment. In particular, the vacuum system for the containment chamber failed to reach recommended pressures before sputtering was initiated. This may have resulted in a poor silicon oxide layer being formed.

After completing the electrical extensions, I visually check them for shorts and discontinuities and then measure the resistances between the leads. For a good SQUID tip, the resistance at room temperature between the dc SQUID leads should be smaller than 1 kΩ. Lower resistance can be expected between the feedback coil leads while much higher resistance should exist between a dc SQUID lead and a feedback coil lead. In LHe, the dc SQUID leads look shorted, as do the feedback coil leads. The connection between the dc SQUID leads and the feedback coil should be an open at 4 K.

When measuring SQUID chip resistances at room temperature with a multimeter, the values were not very precise. This was because I had to set the multimeter to its high resistance range, typically 1 MΩ or greater. This limited the input current to less than 100 μA to prevent damage to the SQUID. At these settings, low resistances all looked like shorts. What was important was that when a high

resistance was expected, it would be orders of magnitude higher and therefore easily discernible.

I finished the SQUID tip wiring by attaching small diameter copper magnet wire to the electrical extensions on the sides of the sapphire rod using silver paint (see Fig. 4.7). The copper wires were formed into twisted pairs and soldered to a multipin connector attached to the bottom of the cold finger (see Fig. 4.6). This scheme was adequate for the prototype microscope using a nonhysteretic dc SQUID with Flux-Locked-Loop (FLL) electronics. However, changes would be required for the large bandwidth electronics described in Chapter 6, which makes use of a hysteretic dc SQUID.

4.4 Sample Scanning Mechanism

4.4.1 Translation System Overview

The purpose of a Scanning SQUID microscope is to measure spatial variations in magnetic field on the surface of an object. In order to accomplish this, a mechanism is required to support and translate the object with respect to the SQUID. The translation system of the prototype microscope can be divided into three main components. First, there is the human interface and data processing unit, which is an IBM PC compatible computer. Second, controller boxes read the position data of the translation stages and convert instructions from the computer into electrical signals for controlling actuators. And third, there are precision x-y translation stages and actuators that support and move the sample. As the stages move the sample, the magnetic field detected by the SQUID is recorded along with the position of the x-y

stages. This data is then used to create a magnetic field image of the object. A block diagram of the scanning system and electronics used in the prototype SQUID microscope is shown in Fig. 4.8.

Data is taken one line at a time, i.e. as the sample is scanned along one axis which I will define as the x-axis. Measurements of the magnetic field are taken at predetermined time intervals according to the scan speed. The scan position is determined by the corresponding time interval. Averaging of measurements is performed by taking multiple successive measurements, then averaging those values before taking measurements for the next pixel. After a line is scanned, the sample is moved one step along the y-axis. The microscope is then ready to perform another line scan and the process is repeated until a specified area is covered.

If a single step along the y-axis is larger than the SQUID size, some areas between steps in the y direction will not be scanned. If the characteristic length scale of variations in magnetic field is smaller, then the step size should be made smaller to avoid missing any field information. However, for directed measurement, step sizes smaller than or comparable to the SQUID size do not render additional information.

I note that in the prototype microscope, as well as in most other scanning SQUID microscopes, the sample is moved about the SQUID instead of the SQUID moved over the sample. There are two main reasons for this. First, the SQUID is attached to a heavy and bulky cryocooler inside a vacuum chamber. The mechanical link between the SQUID and cryocooler does not permit significant movement of the SQUID without moving the cryocooler and vacuum chamber. Precision translation of the cryocooler can be avoided by translating the sample instead. Second, the SQUID

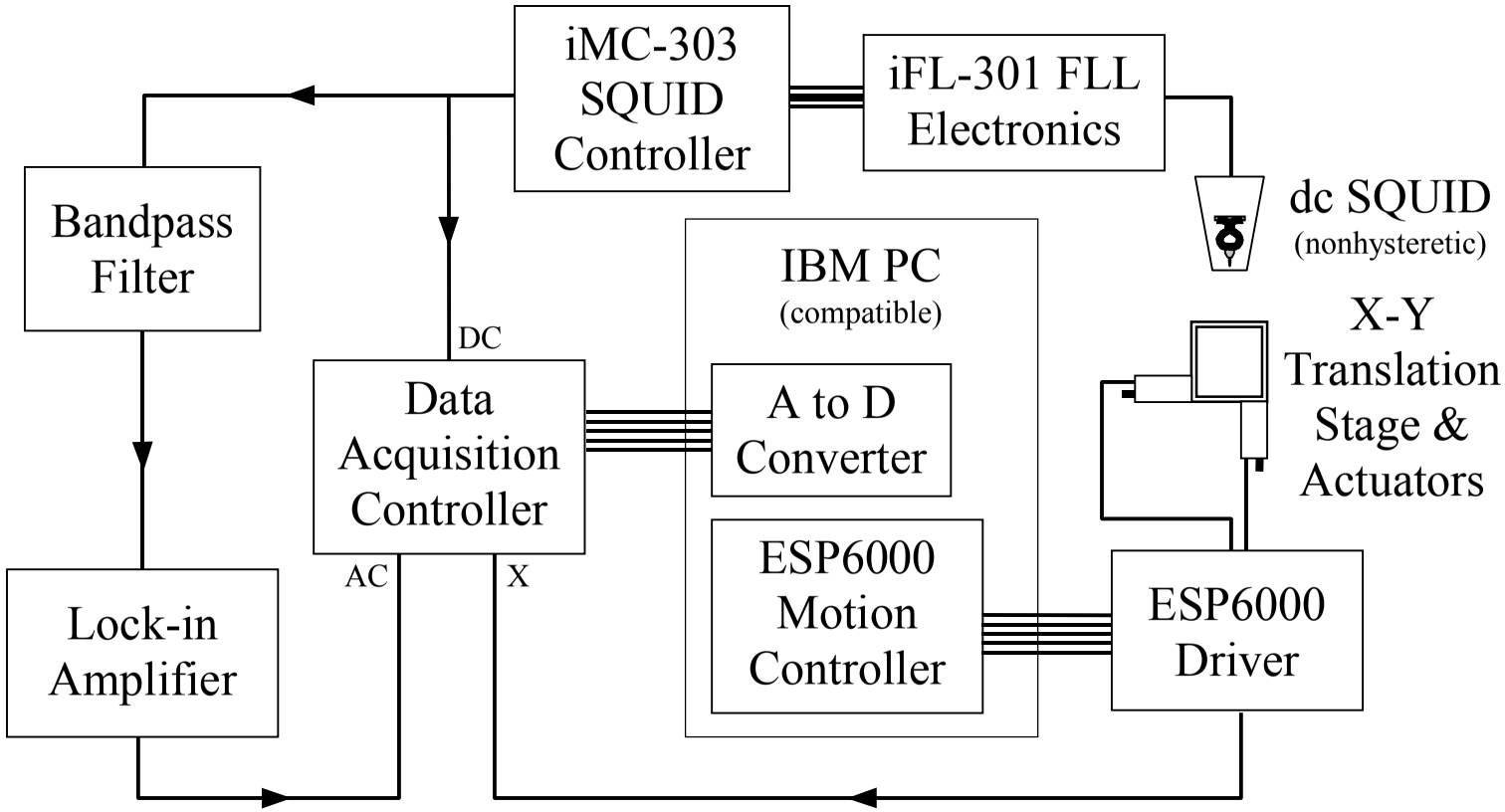

FIG. 4.8. Block diagram of the prototype Scanning SQUID Microscope electronics and scanning system. Arrows indicate direction of data flow on coaxial cable for connections with unidirectional communication. The connection between the iMC-303 SQUID controller and the iFL-301 FLL SQUID electronics includes fiber optic cable as well as coax. The connection between the Data Acquisition Controller and the Analog-to-Digital converter consists of a dedicated multiwire signal cable with bidirectional communication. A similar connection exists between the ESP6000 motion controller and the driver.

is sensitive to minute changes in ambient field. If the SQUID moves, it becomes difficult to differentiate whether measured changes in field are due to changes caused by the sample or due to spatial variations in the ambient field. By keeping the position of the SQUID fixed, the only changes in field should be due to the translation of the sample or due to temporal variations in the field if the object position is fixed.

4.4.2 Hardware

The translation stages, actuators, motion controller, and related computer interface cards in the prototype SQUID microscope were commercial products which were assembled together by Neocera, Inc. Additional electronics were also developed by Neocera for the translation system.

The translation stages must perform three dimensional positioning of the scanned object. Sub-micron precision is desired for translations in the horizontal plane. While typical samples are on the order of a few centimeters, the field variations are on the micron scale, for example integrated circuit chips and modules. Precise translation in the vertical direction is needed to position the sample as close as possible to the sapphire window of the vacuum chamber without crashing into it. Some commercial SQUID microscopes can perform vertical translation electronically and use a feedback system to keep the object at a fixed distance from the window [17]. However, the prototype microscope uses a manual z-stage with 1 μm precision mounted on the x-y stages.

The scanning system incorporated two model 850G actuators with linear horizontal translation stages, all made by Newport, Inc. [133]. One stage was stacked

and bolted on top of the other at a right angle, thus forming the two dimensional x-y horizontal stage. Care was taken to set the angle to 90° as if it were not, the resulting field image would be skewed.

The dc motor actuators had a minimum step increment of about 1 μm with an absolute accuracy of 50 μm over the full range of motion. To obtain faster scanning times, the actuator used for the x direction was a high speed type 850G-HS. The main motion controller and computer interface card was a model ESP6000, also from Newport, Inc. [134,135]. In conjunction with a motor driver box, the system was capable of controlling up to four actuators, though I only used two for x-y motion.

In order to optimize scanning, the driver box was modified to output a dedicated signal indicating the position of the translation stages along the x direction. This signal was sent to the data acquisition controller along with signals from the SQUID electronics. From there, the signals were relayed to the control system computer where the data was correlated and processed into the field image.

Translation in both x and y directions has to be consistent and reproducible. The model 850G actuators and ESP6000 motion controller have some built in features which support these requirements. However, relying on such features alone can be insufficient [12]. There are some remedies to address position error, which are discussed in Chapter 8. In general, problems with the translation system can be due to software that control the actuators and other components. In other cases, the hardware may cause error signals and halt operation. Without detailed analysis, it is difficult to determine the cause of such problems. Indeed, I encountered a very

serious problem in the translation system of the prototype microscope, which is discussed in Chapter 5.

4.4.3 Software and Scanning Parameters

The software I used for the scanning system was a version of the Magma C1 control software developed by Neocera specifically for the Newport 850G actuators and ESP6000DCIB motor driver. The software ran under Microsoft Windows in an IBM PC compatible computer equipped with the ESP6000 motion controller and an analog-to-digital data acquisition card for receiving SQUID data. Besides positioning and translating the scanned object, the software also recorded, graphed, and normalized the SQUID data as it was being received. Separate software utilities were available to analyze magnetic field images and perform calibration and diagnostics of the translation hardware.

To operate the scanning software, I provide values for certain parameters including scan speed S, scan area A, number of measurements averaged N, and grid size $X \times Y$. Not all parameters are independent, so those parameters of more significance determine the others. For example, scan speed S is determined by a number of factors, one being the size of the scanned area A and the other the time T needed to acquire the image. However, the scanned area is divided into separate pixels according to a grid size. The grid size determines how many pixels will be stored for the field image. Very often, there is a desired grid size for a given scanned area, so this also partly determines the scanning speed.

The scanning software was designed so as to let the operator set certain parameters, such as the scanning area and grid size. This determined the spatial resolution R and the x and y step sizes. The number of measurements to average N could also be specified. But, the scan speed S was predetermined from stored profile information set during calibration. Consequently, the scan time T was mostly determined by the grid size and the measurement time per pixel, where the measurement time per pixel was dependent on the number of measurements to average. The approximate relationship between some of the parameters can be summarized by the following equations.

$$\begin{aligned} R &= \frac{L}{X} \\ S &= \frac{L}{T} \\ T &= X \times N \times T_o \end{aligned} \tag{4.1}$$

where L is the scan length in the x direction and T_o is the time for one measurement.

The actual time T_o needed for a single measurement was something that was mostly determined by internal factors and was not readily adjustable. In principle, the time needed for a single measurement must be long enough to compensate for any transitory effects in the electronics. Averaging would then reduce the effect of external noise that is present during the time T_o.

Ultimately, the scan speed was limited by the hardware. If the speed was too high, the dc motors drew a high level of current, which could damage the motor. Also, if the speed were too high or too low, the positioning would not be reliable. Typically, the speed had to be constant over a relatively large distance in order for the position to be accurate. Acceleration also had to be controlled and well determined

for measurements near the starting and ending points. The acceleration profile used in the scanning system for the prototype microscope was a simple constant acceleration profile.

One of the utilities included with the scanning software had the capability to change and specify the acceleration profile and scanning speed for the actuators. Making changes using the utility permanently changed the default settings and could cause the actuators to react differently to signals and ignore predetermined limits. Using the utility, I experimented a little in attempts to optimize and determine the cause of some scanning problems. However, adjusting actuator performance was very involved. Some adjustments resulted in dramatic changes while others seemed to have no effect. Consequently, the default settings were kept.

To reduce scan time, it was possible to perform line scans in both directions along the x-axis, once in the positive x direction and the next line in the negative x direction. However, I only performed unidirectional line scanning to avoid alignment problems due to hysteresis in position or speed. For example, there could be lag in the actuators when the scanning direction is reversed. For accurate alignment, the scanning software returned the x-y stages to a reference point along the x-axis after each line scan. It also performed a similar action during system initialization.

4.5 SQUID Electronics and Instrumentation

4.5.1 Flux-Locked-Loop Feedback Electronics

The prototype Scanning SQUID Microscope uses modulated Flux-Locked-Loop (FLL) electronics, an iMAG SQUID system from TRISTAN Technologies, Inc.

[29]. The system comes in two parts, the iFL-301 FLL electronics which directly connects to a dc SQUID and the iMC-303 multichannel controller. The controller incorporates the user interface, reads and displays the output from the FLL electronics, and adjusts parameters such as the bias current, modulation current amplitude, and amplifier gain. The FLL electronics has a 250 kHz oscillator and a bandwidth of 20 kHz under normal operation.

The TRISTAN electronics has fiber optic and coaxial cable connections between the two separate units. It also features fully automated setup and diagnostics. This is very different from the "Berkeley Box" FLL electronics used in earlier SQUID systems such as those of Black, Nielsen, and others [136]. The main differences are that the "Berkeley" boxes were entirely based on analog electronics and required manual adjustments with dials and switches to control various parameters. Nevertheless, despite the differences in physical implementation, the working principle is the same in both electronic systems.

The FLL requires a nonhysteretic dc SQUID which is current biased with a static dc current. When the bias current level is optimum, the voltage across the SQUID will be periodic in the magnetic flux through the SQUID hole with maximum amplitude [4,5,18-20]. Ideally, the bias current $I_{bias} \approx I_c$, i.e. I_{bias} should be near the transition between the zero voltage state and the resistive state (see Fig. 3.4). However, this was not always the case, as for example with SQUID AN which I used in the prototype microscope. For SQUID AN, I had to adjust the bias current until the maximum signal response, described next, was obtained.

In normal operation, the FLL electronics supplies an ac flux around $\Phi_o/4$ to an optimally biased dc SQUID at the oscillator frequency f = 250 kHz. If there is no external quasi static flux through the SQUID hole, then the ac voltage across the SQUID will only have components with frequencies that are a multiple of 2f. This comes from the symmetric nonlinear relationship between the SQUID voltage and the external magnetic flux. On the other hand, if there is a small externally applied quasi static flux, then the ac voltage across the SQUID will have a component at frequency f (see Fig. 4.9). The detection of this signal is the key to the modulated FLL technique.

To isolate the ac SQUID voltage at frequency f, the voltage from the SQUID is amplified and fed to a phase detector. The phase detector mixes the voltage signal with a reference signal from the FLL oscillator and produces a new signal that has a pseudo dc component which is proportional to the amplitude of the input component at frequency f. Whether the external magnetic flux increased or decreased the total flux through the SQUID can be determined from the relative phase between the oscillator and the voltage signals. If the ac component of the voltage signal at f is in phase with the oscillator, the external flux increased the total flux. If the ac component is out of phase by 180°, the external flux decreased the total flux (see Fig. 4.9). However, it should be noted that there will be phase shifts between the SQUID voltage and the signal detected by the FLL electronics. So, instead of looking for the 0° and 180° phase shift in the ac component, in practice the FLL electronics adjusts a phase shift setting that maximizes the signal response at frequency f during calibration or initialization.

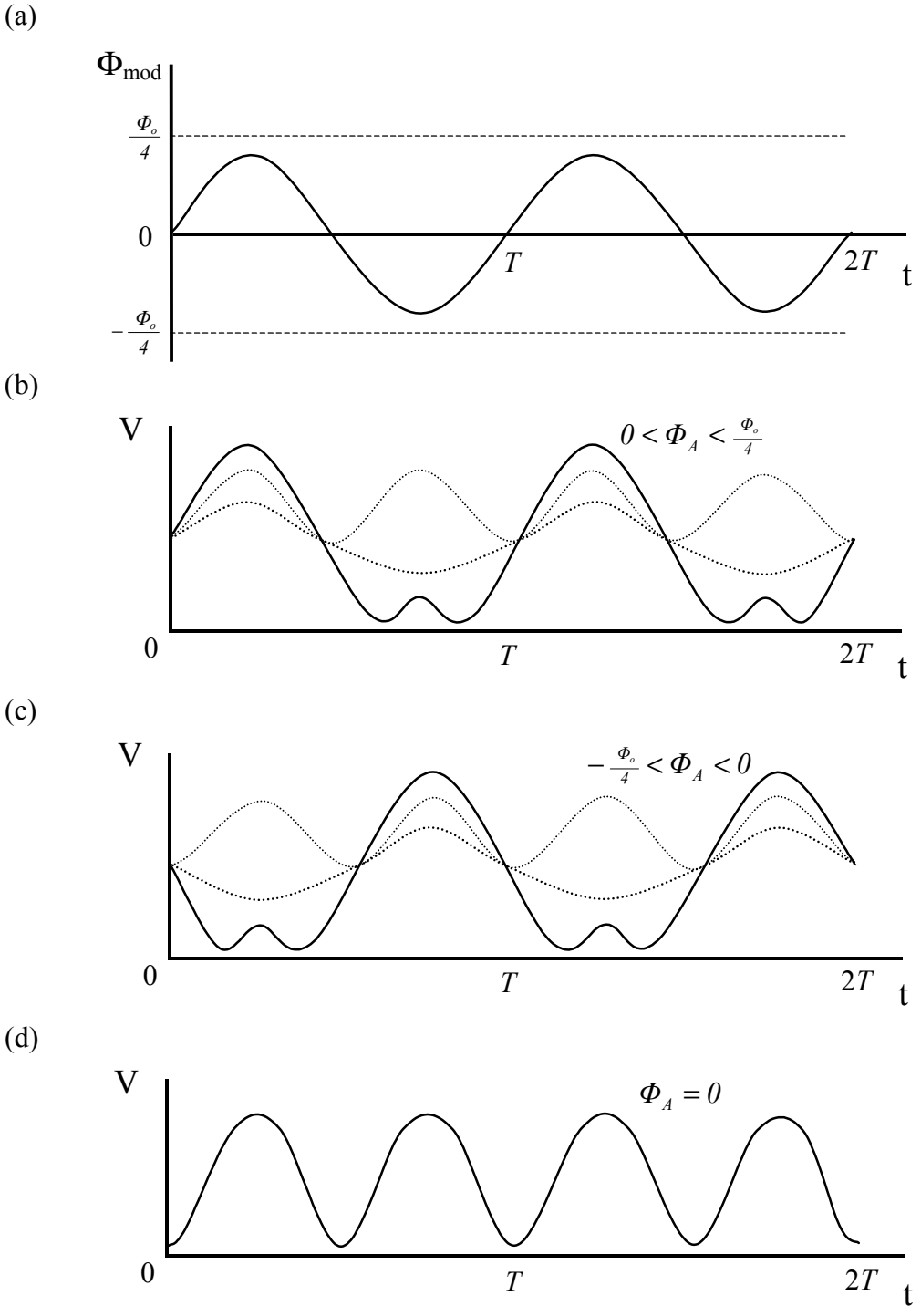

FIG. 4.9. Response of a nonhysteretic dc SQUID with optimally set constant bias. A modulating flux $\Phi_{mod} \approx \pm\Phi_o/4$ is applied on top of a quasi static external magnetic flux Φ_A. (a) AC modulation flux of period T versus time. Voltage across the dc SQUID for (b) $\Phi_A > 0$, (c) $\Phi_A < 0$, and (d) $\Phi_A = 0$. In graphs (b) and (c), the solid line is the full voltage and the dotted lines represent the first and second harmonic Fourier components of the voltage. Note the relations between the first harmonic components and graph (a).

The output of the phase detector is then fed back to the SQUID loop so as to cancel out the externally applied flux. When the system is locked, the value of this negative feedback current is a direct measure of the magnetic flux applied to the SQUID. The main output of the FLL electronics is the voltage produced when the feedback current flows through a feedback resistor R_f. However, due to the periodicity of the SQUID voltage versus flux relation, the FLL electronics does not necessarily lock on to the zero flux state. In fact, it can lock to any state that is an integer multiple of Φ_o. As a result, only relative flux changes are reflected in the output. I note that despite the intrinsic nonlinear and periodic response of the nonhysteretic dc SQUID to magnetic flux, the use of negative feedback linearizes the response of the electronics and allows it to follow magnetic flux changes that are greater than Φ_o.

Figure 4.10 shows a block diagram of the FLL. In addition to the SQUID, amplifier stage, phase detector, oscillator, and resistor R_f, an integrator and a transformer circuit are included in the electronics. The integrator acts as a stabilizing element in the negative feedback circuit. Due to finite signal propagation speeds through the electronics, at some frequency a 180° phase lag develops between the measurement of the signal and the reaction to it. The stability criterion states that for the feedback loop to be stable, the open loop gain of the amplifying circuit must fall faster than $1/\omega$ at the frequency where the phase lag is 180° [137]. The integrator ensures that the high frequency roll off of the amplifier's open loop gain satisfies this criterion.

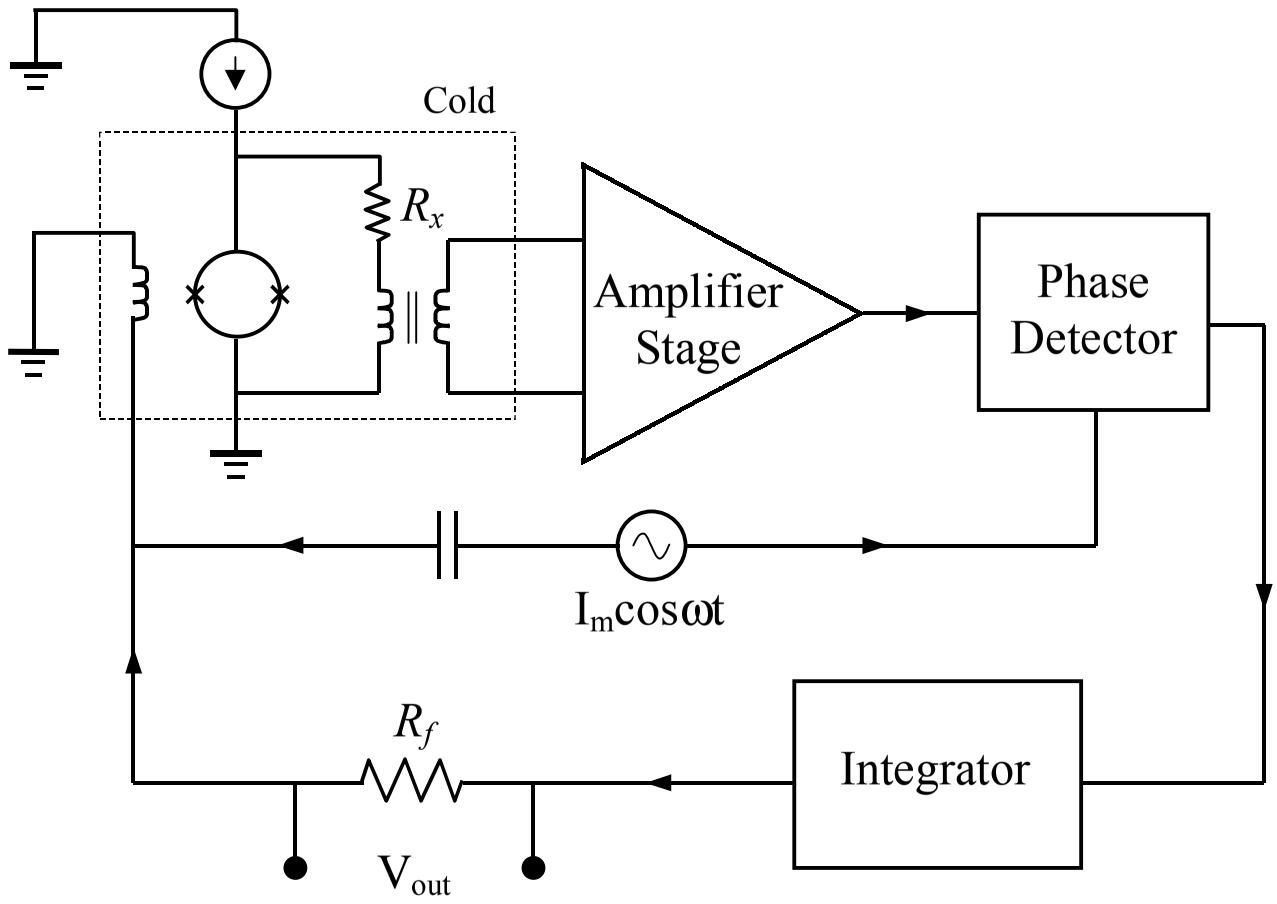

FIG. 4.10. Block diagram of modulated Flux-Locked-Loop (FLL) SQUID electronics. Elements within the dotted box are at cryogenic temperatures. The modulating current from the oscillator and the feedback current from the integrator are added to produce the total current through the feedback coil. The magnetic flux produced by the feedback coil is directed through the hole of the dc SQUID.

4.5.2 Matching Transformer Circuit

The purpose of the transformer circuit at the SQUID's output was discussed in section 3.2. I made transformers by wrapping small diameter copper magnet wire wrapped around small toroidal cores. The primary stages had only a few turns while the secondary stages had between 60 and 100 turns. Construction of a transformer was very time consuming, and its performance depended on the quality of the wrapped coils as well as on the number of turns. Ideally, the impedance of the transformer primary stage should be greater than the dynamic resistance of the nonhysteretic dc SQUID. In practice, it is a matter of trial and error to match the impedance of the primary coil to the normal resistance of the SQUID, especially when the coils are prepared before the SQUID characteristics are known.

Once completed, I tested the transformers using inductance meters and by measuring the frequency response with a signal generator and oscilloscope. Measurements using a meter gave significantly different values, depending on the specific instrument used. Consequently, I tended to trust my direct measurements more (see Fig. 4.11).

Figure 4.11 shows the voltage amplitude versus frequency for the primary stages of three different transformers. Dividing the voltage amplitude by the input current amplitude provides the impedances of the primary stages, which at 100 kHz range from 1.8 Ω to 9.0 Ω. This corresponds to 2.9 μH and 14 μH in terms of coil inductance. I note that the inductances do not follow the expected dependence on the number of turns. In fact, the coils are better modeled by an inductor and capacitor in parallel, where the capacitances for the 3 and 5 turn coils are on the order of 0.2 μF

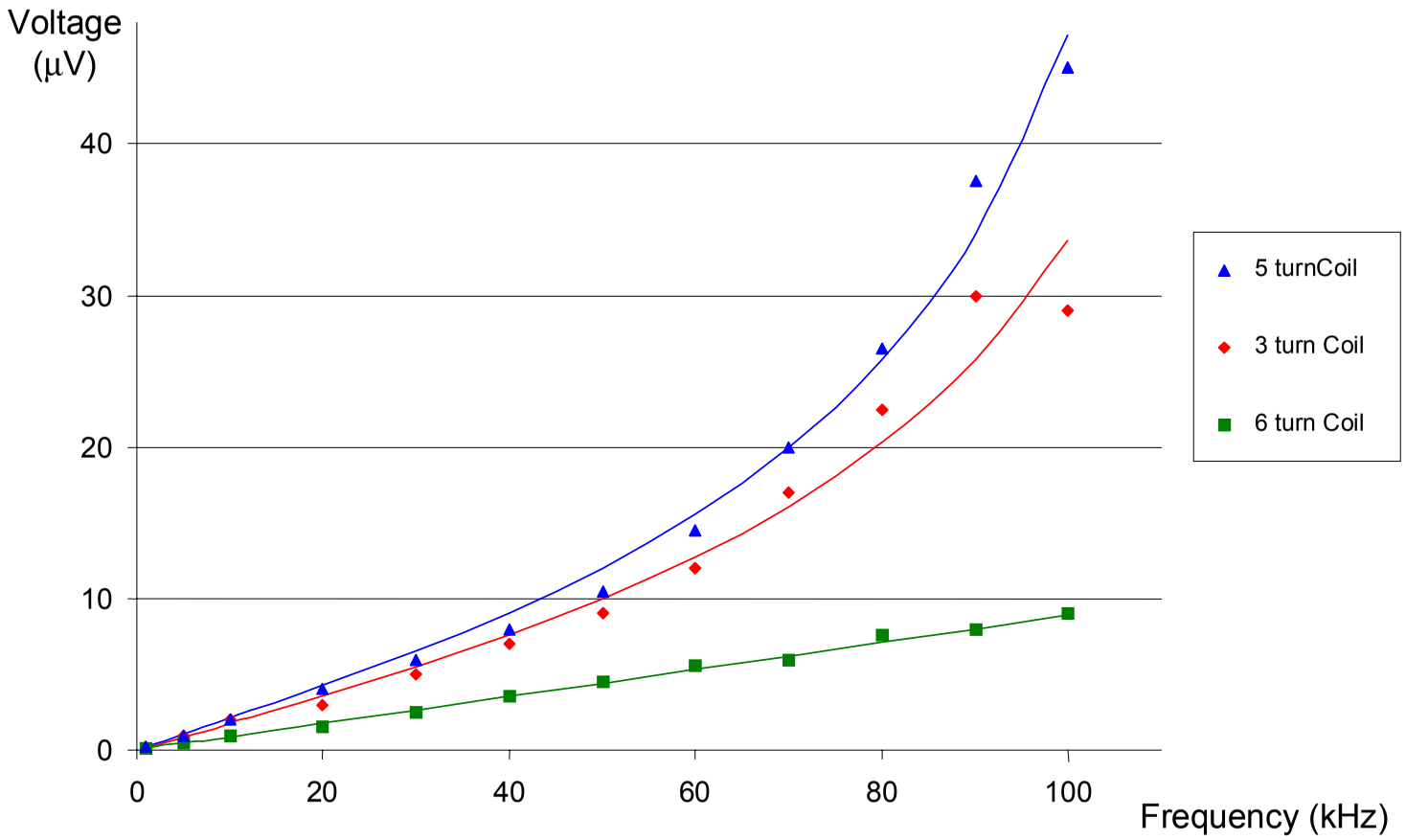

FIG. 4.11. Voltage amplitude versus frequency of the primary stages of three different SQUID output transformer coils. The voltages across the primary stages were measured while sending a sinusoidal current through them. The output voltage amplitudes are normalized to an input current amplitude of 5 μA. The transformer coils were made with small diameter (38 gauge) copper magnet wire with 3, 6, and 5 turns on the primary. The respective impedances of the primary stage coils at 100 kHz are approximately 5.8 Ω (3 turn coil), 1.8 Ω (6 turn coil), and 9.0 Ω (5 turn coil). The solid lines represent the best curve fits to an inductor in parallel with a capacitor.

and negligible for the 6 turn coil. The 6 turn coil, which has the smallest inductance, has coils that were not as tightly wound. Furthermore, the transformer was encased in epoxy to hold its form and provide better thermal conductance. However, the coil had poor noise characteristics compared with the other coils, so I decided not to encase coils in epoxy again.

To enable the dc SQUID to be biased with sufficient current, I placed a resistor R_x in series with the transformer primary to limit the flow of current through the transformer (see Fig. 4.10). As I noted in section 3.2, R_x should be much less than the impedance of the primary stage in order for most of the SQUID voltage to appear across the transformer, which is satisfied if $R_x \leq 1\ \Omega$. For the prototype microscope, I made R_x from a 1 cm long section of manganin wire whose calibrated resistivity was 15 Ω/ft. This resulted in $R_x \approx 0.5\ \Omega$.

Unfortunately, the impedances of all of the transformer coil primary stages were less than the dynamic resistance of SQUID AN (see Fig. 3.6). This resulted in a relatively weak signal being detected by the FLL electronics and lead to some problems during microscope operation. These problems are discussed in Chapter 5.

4.5.3 Signal Processing and the Integrated Computer System

Most of the instrumentation and control systems for the 4 K prototype SQUID microscope are installed in a rack next to the cryocooler and vacuum chamber chassis (see Fig. 4.2). The microscope's control system can be separated into either integrated or stand alone components. The integrated components are the translation system, the SQUID data acquisition system, and the magnetic field image processor

running in an IBM PC compatible computer. The stand alone components are the vacuum system, the cryocooler, the SQUID controller, and the temperature monitors.

The dc SQUID and FLL electronics were operated by the iMC-303 SQUID controller which interfaces to the computer system through the data acquisition controller (see Fig. 4.8). The SQUID controller was not integrated into the computer system but was instead operated manually. Nevertheless, it provided the computer with continuous magnetic field data while providing power and instructions to the iFL-301 FLL electronics.

The SQUID controller's output signal was split into ac and dc signals before it reached the computer. The dc signal was the controller output that went directly to the data acquisition controller. On the other hand, the ac signal first went through a bandpass filter to reduce low and high frequency noise and then through a lock-in amplifier where the signal at a particular frequency was detected and sent to the data acquisition controller. For electric circuit diagnostic applications, the ac signal information was more useful as the input current to the circuit could be set to a desired frequency that was distinct from background noise.

4.5.4 Temperature and Pressure Monitoring

The SQUID microscope required a number of diagnostic checks to ensure proper operation. The temperatures of the cryocooler and cold finger were monitored to determine whether the cryocooler was operating correctly and whether the SQUID chip had reached its operating temperature. Furthermore, changes in temperature affected the characteristics of the SQUID, such as the maximum critical current.

Also, excessive temperature drift was an indication of accumulating contamination in the vacuum chamber.

There were two temperature sensors in the SQUID microscope. The number of sensors was limited by the wiring. One was placed inside the top part of the cold finger which holds the sapphire rod and SQUID tip. The other was on the radiation shield which was thermally anchored to the cryocooler's first stage heat exchanger. Space was not available for a sensor right next to the SQUID chip.

The resistance temperature detector (RTD) thermometers used in the microscope have resistances that change as a function of temperature. Four point resistance measurements were made, requiring two sets of twisted pair 37 gauge copper magnet wire for each sensor. These wires broke easily, requiring care in design and handling. The wires were also thermally anchored to the cryocooler heat exchangers to prevent heating of the sensors from room temperature due to thermal conductance in the leads. The cryocooler manufacturer, Cryomech, recommends 2 in to 4 in of lead be thermally anchored [27]. Thermally conducting vacuum grease could have been used to eliminate gaps within the anchoring points for the wires, but epoxy was used instead making the attachments semi-permanent. The RTD sensors themselves were also anchored to surfaces with either epoxy or silver paint.

Temperature measurements were made using a LTC-21 low temperature controller from Neocera [138]. Different RTDs were used for different temperature ranges. For temperatures between 20 K and 100 K, such as for the microscope's radiation shield, a platinum RTD was used. For temperatures below 20 K like the cold finger, a ruthenium oxide RTD was used.

The pressure monitor was an integral part of the control system for the turbo vacuum pump. A Balzers-Pfeiffer TPR 250 compact pirani pressure gauge was used to measure the chamber pressure and determine whether the vacuum level was low enough for the cryocooler to operate. The gauge was located at the top of the vacuum chamber and can be seen next to the cryocooler cold head in Fig. 4.2. The operating range of the gauge was limited to values above 6.4×10^{-5} mbar. As a result, if the vacuum was starting to fail, the first indication was not an increase in the pressure gauge reading but an increase in base temperature due to increased thermal conductance or convection within the chamber.

The pump controller operated completely independently from other systems and incorporated its own internal safety mechanisms to shutdown the turbo pump in case of vacuum failure. If the pressure rose above a set limit, the turbo fans could not spin at the required frequency and the pump would shut itself down. An automated vacuum valve was available to isolate the chamber from the turbo pump when such situations occurred, though it was often disabled due to control problems. When a shutdown occurred, the turbo pump had to be manually restarted after a rough vacuum was recovered.

4.6 Operation and Maintenance

4.6.1 Cool Down Procedure

To start the prototype SQUID microscope, I used the following procedure. After assembling the microscope, I first used the roughing pump to reduce the pressure inside the vacuum chamber. During normal operation, the roughing pump

was kept constantly running, either roughing out the chamber or backing the turbo pump. After a few hours of pumping, the vacuum level bottomed out and the turbo pump could be engaged. The amount of time required to pump out the chamber depended on whether the chamber was left open for an extended period of time and the environmental conditions the chamber was exposed to. When the turbo pump was engaged, a fan forced air around the pump to keep it from over heating due to the amount of current that flowed through the turbo pump.

In principle, the system should be checked for vacuum leaks at this point, i.e. before starting the cryocooler, but a leak detector was not available on site. Instead, the only indicators of leaks I had was when the pressure gauge would not drop to prior levels during roughing and when the turbo pump fans were unable to reach their minimum rotation frequency. The steady state operating frequency of the pump was 1500 Hz, and a safety mechanism isolated the pump from the vacuum chamber when the frequency dropped below 1200 Hz. On the other hand, the turbo pump was able to operate at lower frequencies, or start at higher pressures. However, this risked the possibility of excessive heating and damage to the pump if the pressure did not drop.

After the chamber pressure decreased to the maximum allowed level for cryocooler operation, the temperature controller was turned on, and preparations were made to start the cryocooler. Although the recommended maximum pressure for operation is 5×10^{-4} torr or 6.7×10^{-4} mbar, on occasion the cryocooler was started with the pressure as high as 5×10^{-3} mbar. Under optimal conditions, the pressure would reach as low as 7.7×10^{-5} mbar prior to starting the cryocooler.

Before starting the cryocooler, I checked the electrical lines, high pressure gas hoses and water cooling lines to the helium compressor. It was also prudent to ensure that the vacuum chamber's thin sapphire window was located away from the SQUID tip. I then turned on the cold water supply to the helium compressor. The temperature and flow rate must meet the requirements specified by Cryomech. However, a simple check was performed; if the temperature of the outflowing water seemed too warm to the touch after about half an hour of cryocooler operation, the flow rate was increased and the temperature was tested again after several minutes.

After starting the water supply, I switched on the helium compressor. The cryocooler began to operate in conjunction with the compressor which makes a distinctive sound. At first, the temperature readings fluctuated but then stabilized and began to steadily decrease. I also found that the initial temperature readings of the heat shield and cold finger were unphysical; the temperature values beyond the calibrated ranges of the RTDs should not be trusted. Furthermore, with the cryocooler started, the pressure inside the vacuum chamber drops suddenly as gas particles inside the chamber begin to freeze out, particularly the residual water vapor.

The cooling time is typically between one and two hours. In that time, the cryocooler first stage and radiation shield cool below 70 K and gradually bottom out to a limiting temperature of around 32 K. The cold finger should reach its minimum temperature of around 3.9 K after about two hours of cryocooler operation. However, I found that this temperature tended to slowly drift upwards, probably due to a slow vacuum leak discussed earlier.

On some occasions, the temperature of the cold finger would not reach 4 K. Physical contact between the SQUID tip and radiation shield or some other component at a higher temperature was the likely cause. In such cases, I suspected large temperature differences between the SQUID chip and cold finger. To correct the problem, I had to shutdown the cryocooler, warm up the entire system, open the vacuum chamber, and adjust the height of the sapphire rod in the cold finger.

4.6.2 Preparations and Procedures for Scanning

Once the cold finger reaches 4 K, the sapphire window is brought close to the SQUID tip prior to scanning. This tends to increase the temperature of the SQUID chip by less than 1 K, which is not very significant. To bring the sapphire window close to the SQUID, I use an optical microscope and a right angle prism on the translation stage to look through the window and guide it to the SQUID tip [see Fig. 4.12(a)]. Positioning screws on the bellows allow fine adjustments of the window position. The idea is to bring the window as close as possible to the SQUID tip without touching it. I also used a small fiber optic light source placed against the fiberglass cone section to illuminate the SQUID tip inside the vacuum chamber.

Next, I connected the cable from the SQUID electronics to the dc SQUID before turning on the SQUID controller. Caution should be taken to discharge any static electricity before connecting the cable directly to the SQUID leads. Once the electronics were connected and turned on, the iMAG-303 SQUID controller went through a series of diagnostic checks then set the SQUID electronics' parameters and began measuring the ambient field [29].

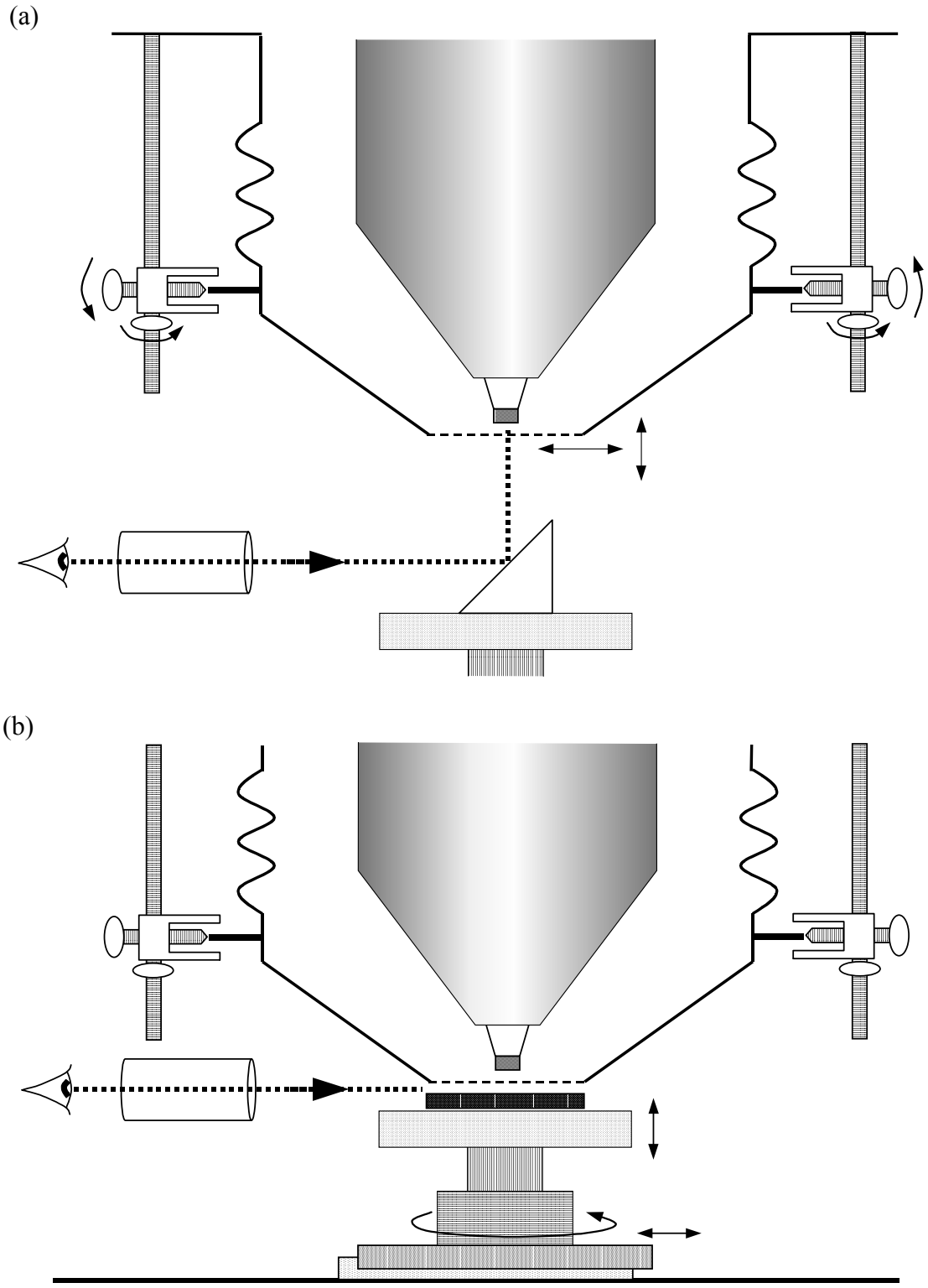

FIG. 4.12. (a) Bringing the SQUID microscope sapphire window close to the SQUID tip. The operator observes the window through an optical microscope and prism while positioning the window. (b) Positioning an object close to the sapphire window prior to scanning it.

Adjustments to the automatic controller settings can be made. The main parameters to adjust are the bias current and modulation amplitude. However, I found it difficult to determine whether modifying the settings actually resulted in better performance. Ideally, the values on the controller indicator should be away from the low and high extremes. Whether the parameters are adequate is ultimately determined by operating the microscope, for example by disturbing the ambient magnetic field and observing whether the controller reversibly follows the change. A small magnet or any magnetic object can be used for a quick test.

If operating correctly, the SQUID electronics should hold lock and follow changes in magnetic field. Sudden large changes could cause the output to "jump lock". Otherwise, the electronics should be stable and its output signal constant when the magnetic field is constant. If the output frequently jumped, a phenomenon referred to as "losing lock", or if the electronics did not faithfully follow changes in magnetic field, the SQUID bias and modulation parameters needed adjustment. With the iMAG-303 SQUID controller, the main sign of lost lock was that the output indicator would be at maximum and not follow field changes. If parameter adjustments did not result in better performance, the SQUID or its connections was likely defective.

After starting the SQUID controller and checking the SQUID's response, I started the computer scanning system's hardware and software. To perform scanning, I mounted a sample on the translation stage and brought it close to the sapphire window. There should be enough space between the sample and the window over the full x-y scanning range, and the horizontal plane of the sample should be parallel with

the plane of translation. If not, the distance between the sample and the SQUID will gradually change giving rise to an artificial gradient in the measured flux. Furthermore, if the distance is too small, the sample will crash into the window quite possibly causing damage to both window and sample. To check the spacing, I used an optical microscope to look at the gap while moving the translation stages [see Fig. 4.12(b)]. Any obstructions on the surface of the sample or near the translation stages should be removed.

Finally, I enter scanning parameters into the scanning software and the translation stages move the sample to the initial position. Before initiating the scan, I check the SQUID controller and verify that the SQUID and its electronics are operating properly. I also note the SQUID cold finger temperature for comparison after scanning. A significant temperature drift can change SQUID characteristics and result in distortion of the magnetic field image.

While scanning, the field image is displayed and updated in real time on the computer. If there is any problem with the operation of the electronics, such as losing lock, the field image will typically show only low level noise or no features at all. If the SQUID electronics jumps or loses lock during the middle of a scan, there will be a sudden change in the output, which persists for the remainder of the scan. Image distortion of this kind cannot be corrected, so the scan must be repeated after the SQUID electronics is reset. Once the scan is complete, I save the data for processing at a later time. Two separate images, one from the ac signal line and the other from the dc signal line, are available.

4.6.3 Servicing the Microscope

To service the SQUID microscope, the cryocooler has to be shutdown and the system warmed to room temperature. As a precaution, the sapphire window should first be moved away from the SQUID tip. Warming up to room temperature takes several hours. Monitors can be left on to observe the change in temperature and pressure. At the same time, vacuum pumps should be kept operating to prevent condensation from forming inside and outside the chamber. Cooling water for the cryocooler compressor should be left running until the temperature of the outflowing water matches the incoming water temperature. For safety, the compressor hoses must be left connected to the cryocooler, as recommended by Cryomech, to depressurize helium gas accumulated in the cold head [27].

The time to warm up the cryocooler would be less if the vacuum chamber were vented or filled with inert gas, but condensation would also occur on the outside of the vacuum chamber and possibly damage components such as the sapphire window, pressure gauges, or room temperature electronics. After the cryocooler reaches room temperature, vacuum pumps and other systems can be turned off and electronics and sensors disconnected from the vacuum chamber. Venting the chamber can be performed by slowly removing the pirani pressure gauge. After that, the chamber is unbolted and opened to expose the SQUID tip and radiation shield.

In order to access the cold finger and heat exchangers inside the vacuum chamber, the radiation shield has to be removed. This in turn requires removing the cryocooler and cold finger assembly from the vacuum chamber. This provides full access. Alternatively, part of the shield can be removed while the cryocooler is in

place, though this only provides partial access. In general, with the current design, I recommend complete removal of the cryocooler assembly for any significant servicing work.

When opening up the vacuum chamber, disassembly of the microscope goes from bottom to top, beginning with the fiberglass nose cone section that has the sapphire window. Reassembly is in the reverse order. This is done as a precaution to avoid damaging the SQUID tip, sapphire window, and radiation shield during cryocooler removal and insertion. It is best to have at least two people working together to remove the cryocooler. The basic cold head alone weighs 14 kg and has to be lifted straight up to avoid hitting the chamber walls and consequently damaging components.

The most common damage to the microscope during servicing was breaking wire connections. Broken wire was a major nuisance requiring frequent maintenance. Some of the wire had more durable insulating coating to help prevent breakage, but it was only available later and not installed everywhere. To help secure the wires and their connectors, I attached them to the cryocooler with vacuum compliant adhesive tape.

In any case, the risk of damage was always present and was greatest during cryocooler removal and insertion. Therefore, removal of the cryocooler should be limited and performed as infrequently as possible until the system is redesigned to allow easier access.

CHAPTER 5 Magnetic Field Image of a Test Circuit

5.1 Microscope and Test Circuit Preparations

To verify the correct operation of the prototype 4 K Scanning SQUID Microscope, I performed a scan of an electrical test circuit. The circuit was developed by Neocera for calibrating and testing their commercial scanning SQUID microscopes. The test circuit consisted of conductive leads made of gold on a flat circuit board with precisely determined features, including lines with different widths, parallel lines with different spacing, and meshed or webbed leads [see Fig. 5.1(a)]. Between two terminals on the circuit board, more current flows through the lesser resistive paths with the larger currents contributing stronger magnetic field components over the circuit. The paths of the current between the two terminals is reflected in the magnetic field image measured by the SQUID microscope and can be compared with the expected result.

To drive a current through the test circuit, I connected it to a function generator through two terminals on the circuit board. The test circuit contained no current limiting resistors. To adjust the current level, I placed a simple resistor divider network between the function generator and test circuit [see Fig. 5.2(a)]. Using the resistor network, the function generator could supply up to 100 mA to the circuit, though much lower current levels were used during testing. There was another resistor network I had prepared that provided more linearly varying current

(a)

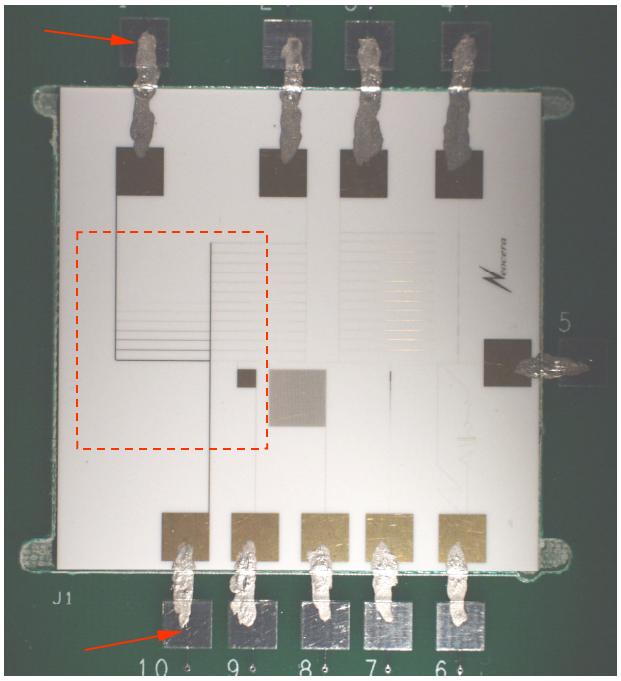

(b)

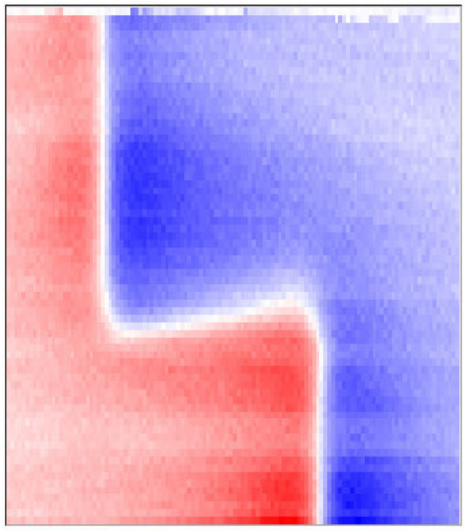

FIG. 5.1. (a) Test circuit developed by Neocera, Inc. for testing scanning SQUID microscopes. An ac current of 1.61 mA rms at 6 kHz was supplied between the two terminals indicated by arrows. (b) Magnetic field image of area indicated by dashed box in (a) obtained using prototype SQUID microscope. The image is 120×69 pixels and shows the normal component of the ac magnetic field (B_z) approximately 1 mm above the board. Relative field values are represented by color with extreme values indicated by saturated red and saturated blue. The average value is indicated by white. The FLL electronics lost lock near the top of the image.

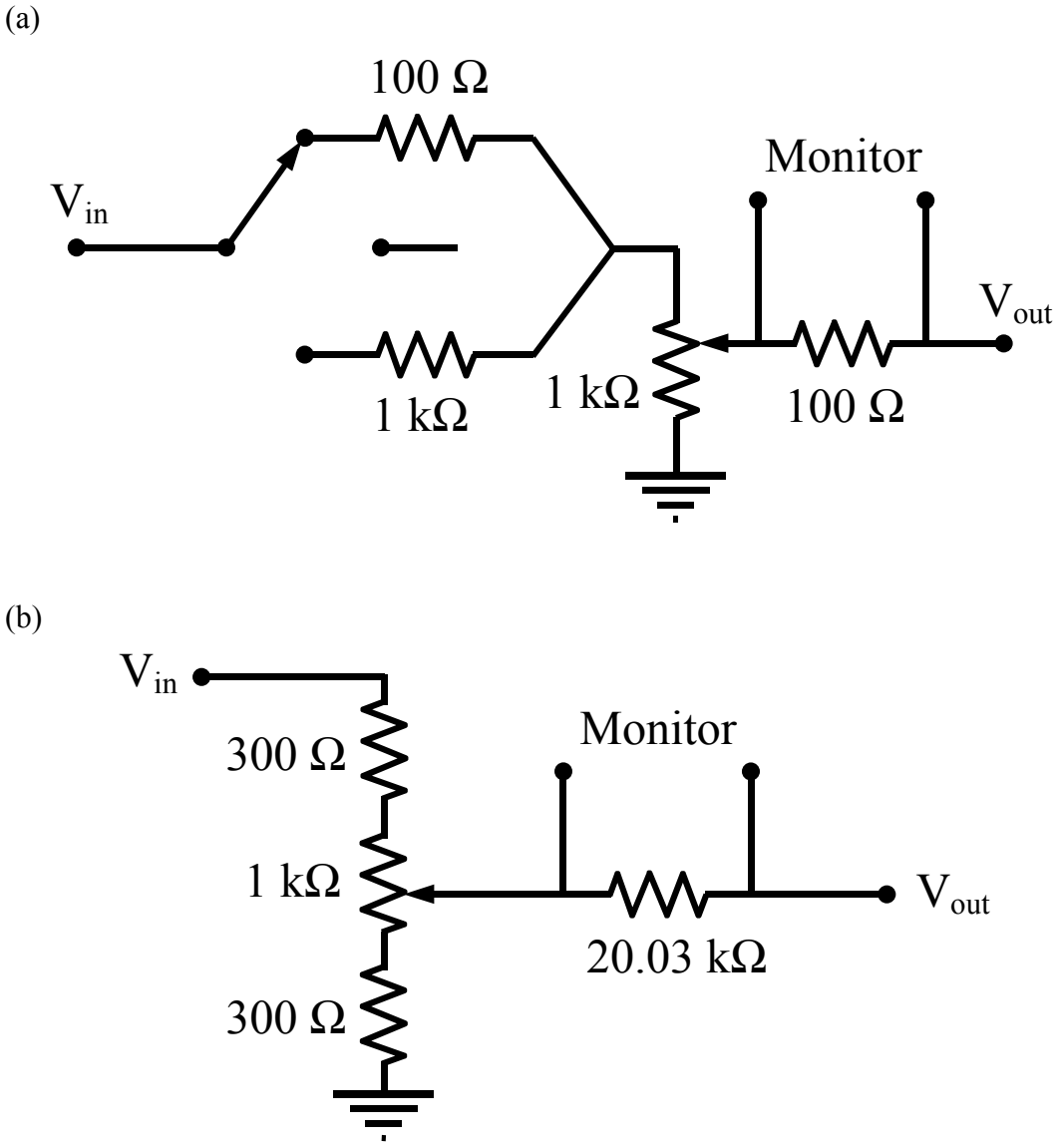

FIG. 5.2. Circuit diagrams of resistor networks used for limiting the current from a function generator. (a) Resistor network that was used with the Neocera test circuit when the prototype SQUID microscope was tested. (b) Resistor network that was used mostly for dc SQUID I-V measurements.

with changes in a potentiometer [see Fig. 5.2(b)]. It was mostly used for I-V measurements of nonhysteretic dc SQUIDs.

I set the function generator to send an ac current of 1.61 mA rms to the test circuit at 6 kHz. The frequency was chosen so that the signal did not overlap with any interfering sources within the bandwidth of the FLL SQUID electronics. I used a SR830 DSP lock-in amplifier from Stanford Research Systems to detect the 6 kHz signal from the SQUID controller output [139]. The output of the lock-in amplifier was recorded to create a magnetic field image of the scanned area. The lock-in amplifier took into account the phase of the ac signal so that the field image represented an instantaneous picture of the field.

When bringing the test circuit close to the microscope's sapphire window, I left a gap such that the distance between the SQUID and test circuit was approximately 1 mm, though I could have brought the test circuit closer with more precise adjustment of the translation stages. Furthermore, I did not employ any filtering or shielding other than what was already part of the microscope's electronics. Consequently, the magnetic field image did not show as much detail as was possible, and the field measurements including the generated field itself were subject to noise. However, these were not major issues for the test scan, as the purpose of the scan was to determine whether the prototype SQUID microscope was operating correctly.

5.2 Obtained Magnetic Field Image

The area of the Neocera test circuit that I scanned is indicated in Fig. 5.1(a). In that area, there are two terminal lines that are bridged by other lines with different

line widths. These bridges are spaced about 1.5 mm apart and have widths that decrease by approximately one half the previous width as one goes up in Fig. 5.1(a). Basic resistor network analysis shows that about half of the current from one terminal line flows through the connecting bridge that has the largest width, and about half of the remaining current flows through the connecting lead with the next largest width, etc. Therefore, the vast majority of the current flows through the lowest two bridges.

The grid size of the 21.6 mm by 24.8 mm scanned area was 120×69 pixels. This resulted in step sizes that were 180 μm in the x direction and 359 μm in the y direction. With a z-SQUID installed in the prototype microscope, the magnetic field component normal to the circuit board (B_z) was measured by the SQUID. Each flux value in the field image was the average of 15 measurements, and a successful scan took about 80 minutes.

Due to problems with the translation system, discussed in the next section, I only obtained a few successful magnetic field images. Out of many attempts, Fig. 5.1(b) shows an example of a complete field image. In the image, the output from the SQUID controller is color coded with the maximum value of 0.20 mV represented by saturated red and the minimum value of –0.18 mV represented by saturated blue. The mean value of 0.01 mV is represented by white. As the maximum and minimum values are of opposite polarity but of similar magnitude, the average value is a good indicator of the path of the current following arguments presented in section 1.1.

Comparing the field image with the scanned area, it can be seen that the path of the current is concentrated in a narrow region near the wider bridges, as expected. The slant in the white average field region between terminal lines has been observed

in other scans and is also expected [140]. The distance between adjacent lines bridging the two terminal lines is less than 5 pixels in the y direction, and the white average field region broadens out between the terminal lines. Consequently, the pixel size and the distance between the SQUID and the circuit surface were not small enough for one to distinguish adjacent current carrying lines directly from the field image (see section 1.1).

Finally, I note that the field image also shows a "jump" in the FLL electronics toward the end of the scan. This can be seen at the top of the image where the colored pixels stop following a continuous pattern. Jumps were also common during scans with the prototype microscope due to the problems with SQUID AN, as discussed in section 3.3 and in the following section.

5.3 Problems with the SQUID Microscope

5.3.1 SQUID Controller Problems

Although I was successful in obtaining an image, I had some difficulties in using the iMC-303 SQUID controller. The primary difficulty was in not being able to identify or directly control various electronics parameters such as the SQUID bias current and feedback modulation current amplitude. The controller was fully automatic and did not provide direct values of these parameters. Once the controller was turned on, it performed diagnostics and automatically set parameter values according to the results. The settings were provided to the operator in terms of some internally normalized units which had to be interpreted. Automatic recalibration of the electronics and SQUID meant losing the previous settings which were often very

different from the new settings. Moreover, it was difficult to assess whether the new settings would result in better performance, as I discussed in section 4.6.

For example, if the FLL electronics was not able to provide sufficient bias current to the SQUID, there was no indication of this from the SQUID controller. What had to be done was that after determining the characteristics of each dc SQUID, a resistor or resistors in the iFL-301 FLL electronics was replaced to match the appropriate range in current, so that the output voltage avoided the high or low extremes. Knowledge of which resistor to replace was proprietary information, and so the replacement was performed by a designated technician at Neocera.

Even after calibration and modification of the electronics, the FLL often did not keep lock. Part of the cause could be traced back to problems with the nonhysteretic dc SQUID (SQUID AN) used. SQUID AN had a large dynamic resistance compared to expectation, and the modulation was occurring well within the resistive range of the I-V curve, as discussed in section 3.3. These irregularities may not have been anticipated by the SQUID controller during automatic diagnostics and calibration and may have caused the electronics to set the parameters inappropriately. Contact resistance and failure of the electrical connection to the SQUID chip would only compound the problem, resulting in sudden changes in the SQUID response and loss of lock.

5.3.2 Scanning Problems

The other common problem I encountered was that scanning would halt in the middle of a scan with the control software immobilized. Specifically, the actuator

controlling the x direction motion would suddenly stop functioning. When that happened, the computer system waited for the actuator to move again, not recognizing a problem occurred until an instruction was entered into the computer to abort the scan, and that would not be recognized until the actuator was manually set to the end of scan position. It was unpredictable when or under what circumstances the scan would halt, though the larger and longer the scan, the more likely it was that a problem would occur. These problems were compounded by difficulties with the SQUID electronics described earlier. To take back control, the microscope's computer system had to be shutdown and reinitialized each time the problem occurred.

I had made attempts to remedy the situation by seeking the advice of the translation system developers. One suggestion was that the load on the actuator motors may have been excessive, so that pressure on the translation stages should be eased. Weakening of mechanical pressure on the actuators, however, did not solve the problem. Another suggestion was that a position error checking mechanism was halting the scan when the accumulated error exceeded some limit. Such a problem could be corrected through modifying the software or hardware. However, when it was determined that it was not practical to reengineer either the software or hardware, I had to leave the scanning system in an unreliable state. Instead, I modified the operating procedures of the scanning software to circumvent problems as much as possible.

My remedy to the scanning problem was mainly to minimize the scan area and scan time and reinitialize the computer just before the scan without letting the

software perform certain routines. By resetting the computer, the possibility of accumulated error in position or actuator control would be minimized. On the other hand, it was not known whether the self diagnosing or testing routines that were skipped did not override safety or other mechanisms that should have been in place. Regardless, this did not eliminate the scanning problem. And with the causes still unidentified, a complete upgrade of the scanning system is required.

It is perhaps worth pointing out that one of the main reasons why I was performing these tests was to run the prototype SQUID microscope through realistic operations and identify problems that occurred. Discovered problems and related issues would then be addressed before replacing the FLL with large bandwidth electronics.

CHAPTER 6 Design of Large Bandwidth SQUID Electronics

6.1 Limitations of the FLL Technique

The fastest SQUID Flux-Locked-Loop (FLL) electronics have achieved bandwidths up to around 2.5 MHz [20]. As discussed in section 3.1, the ultimate bandwidth of a hysteretic dc SQUID is set by Eqs. (3.5) and (3.9), and typically ranges between 10 GHz and 100 GHz. Thus, the bandwidth of SQUID microscopes that use FLL electronics is limited by the readout electronics and not the SQUID. To visualize the bandwidth limit, it is helpful to first look at the characteristic spectrum of the FLL output signal. For FLL electronics with zero applied flux to the SQUID, the response of the loop is flat from 0 Hz up to a fraction (between 1/10 and 1/2) of the oscillator frequency. At higher frequencies, the response falls off rapidly. The flat regime defines the working frequency range of the SQUID microscope, i.e. the bandwidth. In addition to intrinsic limitations set by the bandwidth of the closed loop gain described later, the output may also be filtered to eliminate artifacts introduced by the electronics outside the bandwidth.

For example, Fig. 6.1 shows the noise spectrum between 10 Hz and 100 kHz produced by the prototype SQUID microscope using the TRISTAN iFL-301 FLL electronics with a nonhysteretic niobium dc SQUID at around 5 K. The spectrum was taken in an unshielded lab at Neocera and shows both noise from the SQUID and external interference from equipment in the lab. The low frequency region of the

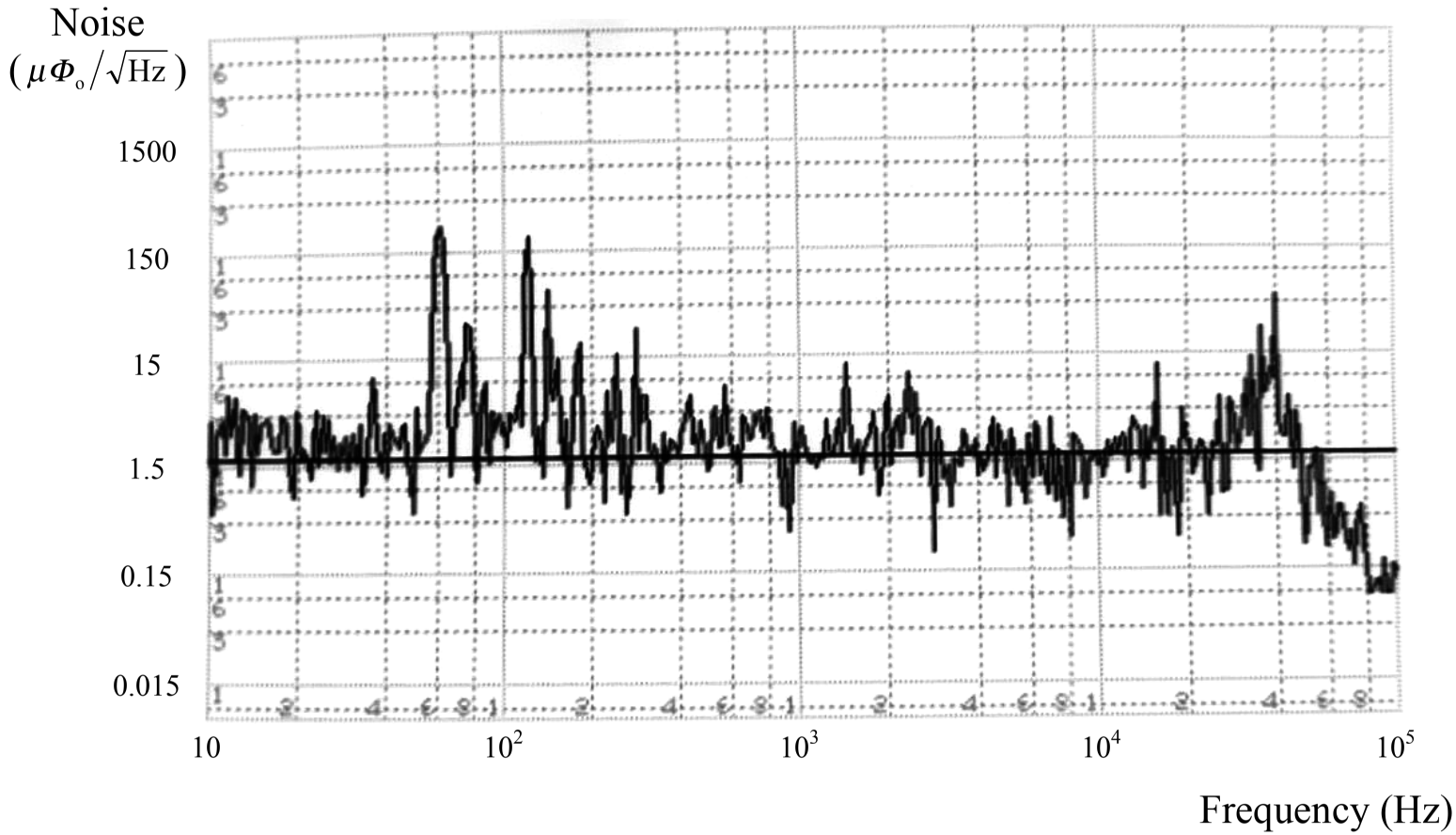

FIG. 6.1. Background flux noise spectrum measured by the prototype SQUID microscope using TRISTAN iMAG FLL electronics with a nonhysteretic dc SQUID at around 5 K. Several peaks are seen including 60 Hz noise and its harmonics. Peaks around 250 Hz correspond to noise generated by the microscope itself, particularly the helium compressor.

spectrum with 1/f noise and the high frequency region around and above the 250 kHz oscillator frequency are not shown. Peaks for ac line noise are seen at 60 Hz and its harmonics. Noise peaks due to the cryocooler and compressor are at around 250 Hz. There are also a number of other peaks from undetermined sources. The broad peak around 40 kHz is due to the closed loop gain of the FLL electronics and along with the rapid decrease in response beyond 50 kHz is characteristic of electronics of this type [19,20].

For FLL electronics to work, the Nyquist sampling criterion requires that the oscillator frequency must be at least twice the bandwidth [141]. For the iFL-301 FLL electronics, this limits the bandwidth to less than 125 kHz, with the actual bandwidth being about 20 kHz (see Fig. 6.1). In general, the response of the amplifier stages must be good to frequencies up to an order of magnitude higher than the oscillator frequency for the loop to be stable. Thus, to extend the bandwidth to 1 GHz, the FLL oscillator would have to operate at frequencies higher than 2 GHz with the amplifier stages good through 20 GHz.

As reported by Koch *et al*., the main difficulty in increasing the bandwidth of the FLL technique is the difficulty of using microwave carrier frequencies and matching them to electronic components with wide frequency response and low noise [20]. The technical limit is determined by the phase shifts in the amplifiers, which must operate from dc to frequencies an order of magnitude higher than the oscillator. In other words, the electronics still has to be able to react to slowly varying signals as well as the high frequency feedback. For example, the 2.5 MHz bandwidth system Koch *et al*. built is the state of the art in FLL electronics and uses a 16 MHz

oscillator. The system is very sensitive to small changes in its wiring and needs to be tuned very accurately [142]. In practice, it has proven very difficult to build systems with the desired phase response beyond a few megahertz, and requiring amplifier stages to have bandwidths in the tens of gigahertz is beyond current technology.

6.2 Increasing SQUID Microscope Bandwidth using a Hysteretic SQUID with Pulsed Bias Current

6.2.1 Basic Principle and Requirements

In order to go beyond the limitations of the FLL technique, an alternate technique is required that bypasses the need for conventional large bandwidth FLL circuits. The goal of my research presented in this thesis is to improve on the fastest FLL electronics ever built by about three orders of magnitude. The idea is to sample the unknown magnetic field at regular time intervals instead of attempting to follow the field continuously. The technique is analogous to stroboscopy in which the filming of fast moving objects is achieved by flashing light on the object [143]. In SQUID signal sampling, instead of flashes of light, short bias current pulses are sent through a hysteretic dc SQUID. During a current pulse, the dc SQUID will either be in the zero voltage state or in the resistive state depending on the bias current pulse and the magnetic flux modulated critical current. If the critical current of the SQUID is lower than the pulse height, a voltage will appear across the SQUID. If the modulated critical current is higher, then no voltage will be observed. This is graphically represented in Fig. 6.2.

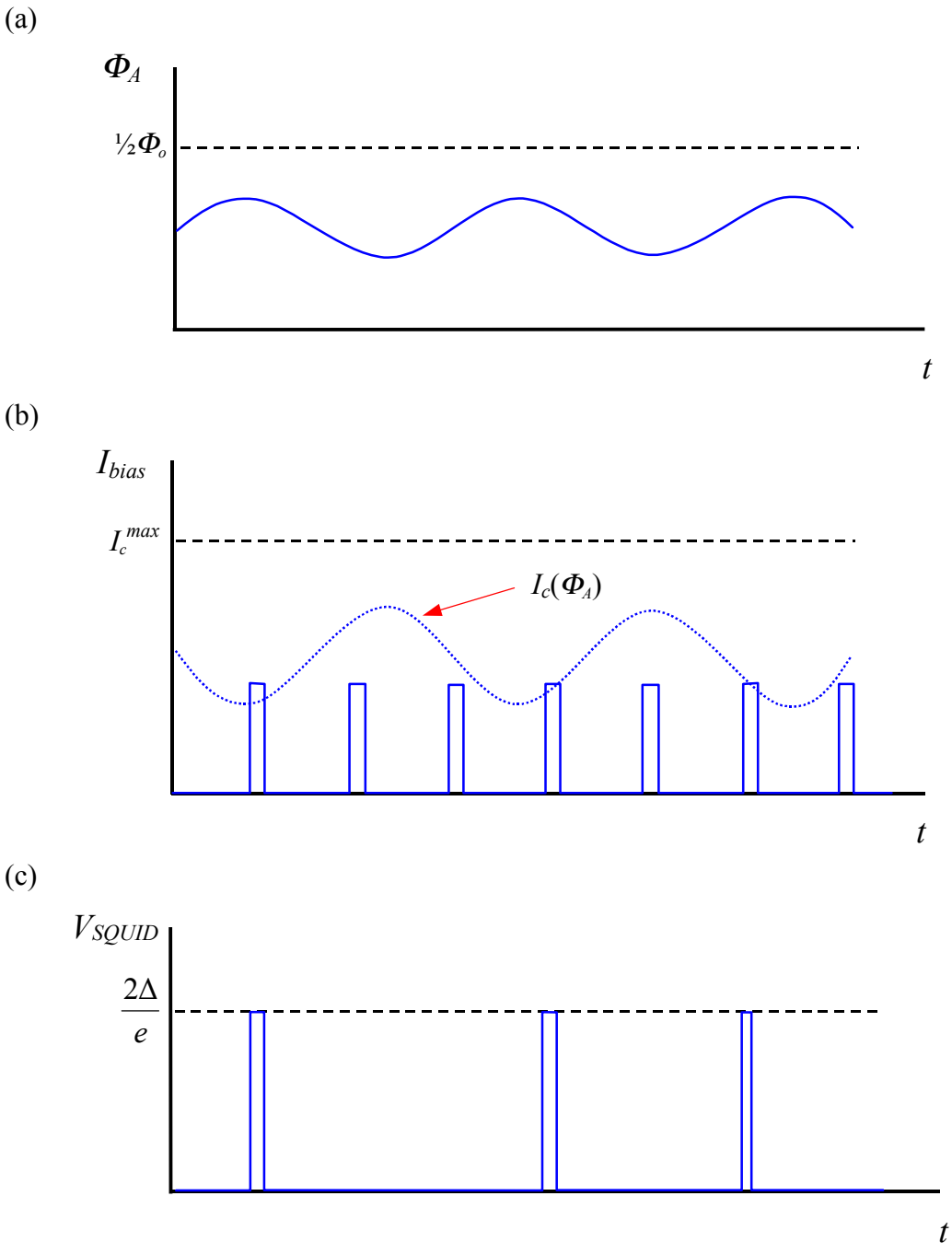

FIG. 6.2. Response of a hysteretic dc SQUID to bias current pulses with an external magnetic flux signal modulating the critical current. (a) A time varying applied magnetic flux Φ_A through the SQUID. (b) Solid line shows pulsed bias current through the dc SQUID. Dotted curve shows SQUID critical current I_c which is modulated by Φ_A of graph (a). (c) Voltage across the dc SQUID as Φ_A evolves in time.

With this scheme, information on the value of the unknown external magnetic flux can be determined from whether or not a voltage across the SQUID is seen during the pulse. If the pulse length is shorter than one half the characteristic time of variations in the magnetic field, the SQUID will faithfully sample the field with successive pulses. Furthermore, if the applied flux is centered at $\Phi = \pm\Phi_o/4$ and varies by no more than $\pm\Phi_o/4$, then modulation of the critical current will occur in a nonlinear but nevertheless well defined one-to-one relation with respect to the total flux. Thus, by following when a current pulse triggers a voltage, the critical current of the SQUID and consequently the external magnetic flux through the SQUID hole can be followed.

To make the technique work for large bandwidth applications, bias current pulses must be very short, on the order of the resolved time or inverse of the bandwidth. This means that for 1 GHz bandwidth, the pulse length should be a fraction of a nanosecond. The minimum pulse length is limited only by the restrictions imposed by the generating circuit, the wiring, and the SQUID bandwidth. These short current pulses must be delivered to the SQUID, and the SQUID must be able to react quickly with a measurable difference between the triggered and untriggered states. The former condition requires that the leads delivering the bias current pulse have sufficient bandwidth and not be too dispersive up to the desired bandwidth of 1 GHz. The latter condition can be satisfied by employing a hysteretic SQUID instead of a nonhysteretic SQUID used in FLL electronics. The reaction time of a hysteretic SQUID is given by the SQUID's voltage rise time expressed in Eq.

(3.9). For the hysteretic niobium dc SQUID shown in Figs. 2.2(b) and 3.9, Eq. (3.9) gives a rise time $\tau_{rise} \approx 12$ ps.

To understand why this technique works better with a hysteretic SQUID, consider what would happen if a nonhysteretic dc SQUID were used instead. For a nonhysteretic SQUID, there is only a gradual transition from zero voltage to the resistive state, which near the transition results in a voltage change of around I_cR [see Figs. 3.4(a) and 3.6]. For hysteretic SQUIDs at the transition, the change in SQUID voltage not only appears within the short voltage rise time τ_{rise}, the voltage change of $2\Delta/e$ is quite large and persists until the bias current decreases below the retrapping current. Thus, for the same change in applied magnetic flux, the voltage response of hysteretic SQUIDs is larger. As an example, for SQUID BH which is a hysteretic niobium dc SQUID, $2\Delta/e = 2.7 \pm 0.02$ mV at LHe temperatures (see Figs. 3.9 and 3.10). For the nonhysteretic SQUID AN, the voltage modulation is around 80 μV.

6.2.2 Pulse vs. Alternative Schemes

In addition to the pulse technique I outlined above, there were at least two other techniques that I considered to use for fast measurement or readout. One scheme was to use the fast triggering of a hysteretic SQUID as a precision switch while the bias current is ramped. Figure 6.3 depicts the idea; the bias current is steadily ramped up from zero as one measures the time from the start of the ramp to the moment the SQUID transitions to the resistive state. In this scheme, the ramped current must have a rise time significantly longer than that of the SQUID voltage rise time and should preferably increase linearly. When the current reaches the maximum

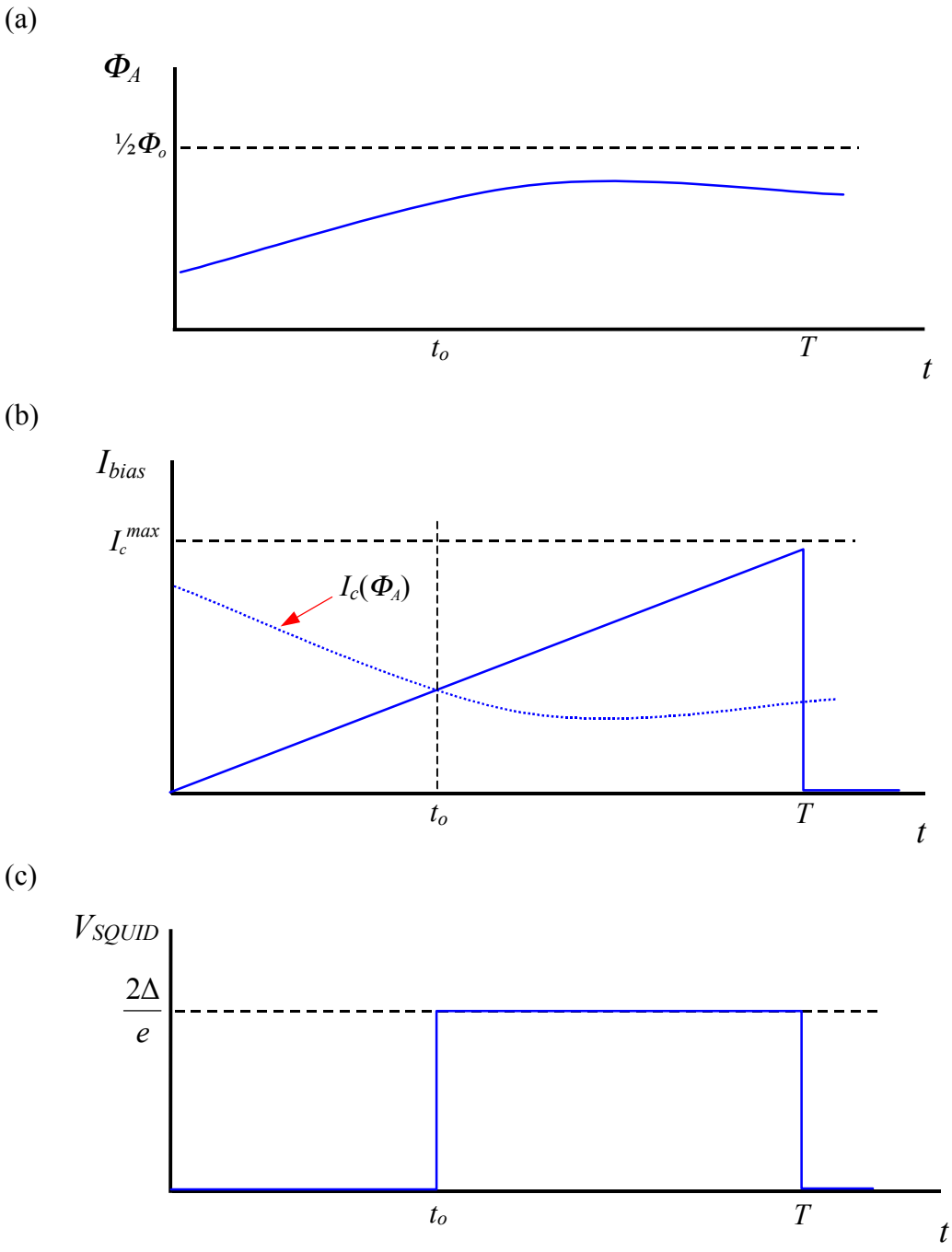

FIG. 6.3. Response of an ideal hysteretic dc SQUID to a bias current ramp with an external magnetic flux signal. (a) A time varying applied magnetic flux Φ_A through the SQUID. (b) Solid line shows bias current through the dc SQUID. Dotted curve shows SQUID critical current I_c modulated by Φ_A of graph (a). The bias current matches the modulated critical current at time t_o after the beginning of the ramp which is of duration T. (c) Voltage across the dc SQUID versus time.

supercurrent, the bias current is reset, and the process is repeated. Essentially, the dc SQUID acts as a Schmitt trigger with the applied magnetic flux controlling the threshold current level [144].

When the bias current exceeds the critical current, a voltage suddenly appears across the SQUID due to the transition. If the relation between SQUID magnetic flux and critical current is well mapped out, the magnetic flux at the moment of transition can be determined from the time it took to trigger the SQUID using the current ramp. This scheme relies on the time interval being determined extremely well and that the corresponding bias current is consistent and stable. Noise in the current ramp must be extremely low.

This scheme is exactly analogous to the technique developed in the 1980s by Martinis and others for investigating Macroscopic Quantum Tunneling (MQT) in Josephson junctions and used by Berkley *et al*. for Quantum Computing (QC) applications [44-50]. The technique works extraordinarily well for that application. However, for large bandwidth applications, the ramping would have to be very fast. For a 1 GHz bandwidth, the ramp duration would have to be less than a nanosecond, with enough critical current resolution to differentiate small changes in magnetic flux. This is quite fast compared to the few millisecond to tens of microsecond ramps typically used for MQT and QC experiments. Furthermore, function generators capable of producing sawtooth waves or pulses at microwave frequencies are difficult to obtain. Moreover, the detailed relation between critical current and flux is nonlinear and different for different SQUIDs. So, each SQUID has to be calibrated

individually and the useable dynamic range of the critical current could be small compared to the full range in bias current due to magnetic hysteresis or other factors.

An alternate readout technique involved sending a sinusoidal bias current with period T through the dc SQUID while observing the voltage response across it. This scheme was implemented in another experiment, but only at lower frequencies [145]. If the dc SQUID behaves ideally as described in Chapter 2, the SQUID voltage will trigger at a time δT determined by the critical current and bias current then return to zero when the bias current decreases and retrapping occurs at rT. On the opposite swing of the bias current, the SQUID will respond likewise but with the opposite polarity. Note that δ and r satisfy the relation $0 < \delta < r < 1$ and that retrapping will always occur near $T/2$ for a hysteretic SQUID with large β_c.

If the SQUID voltage response is sent through a low pass filter, the lowest harmonic components can be selected. If the Fourier series of the SQUID voltage response is calculated, the components will have a relative phase shift $\Delta\varphi$ given by

$$\Delta\varphi = 2\pi\left(\frac{\delta}{2}+\frac{r}{2}-\frac{1}{4}\right)=\pi\left(\delta+r-\frac{1}{2}\right) \tag{6.1}$$

with respect to the bias current (see Fig. 6.4). By measuring this phase shift and knowing when retrapping occurs, the trigger time δT can be determined. The critical current and consequently the applied magnetic flux can be deduced from this information as in the current ramp scheme.

This idea was not implemented for several reasons. First, the dynamic range in the phase shift is limited. Triggering occurs within the rising edge of the bias current, which is only a quarter period $T/4$. Second, the limited dynamic range of the

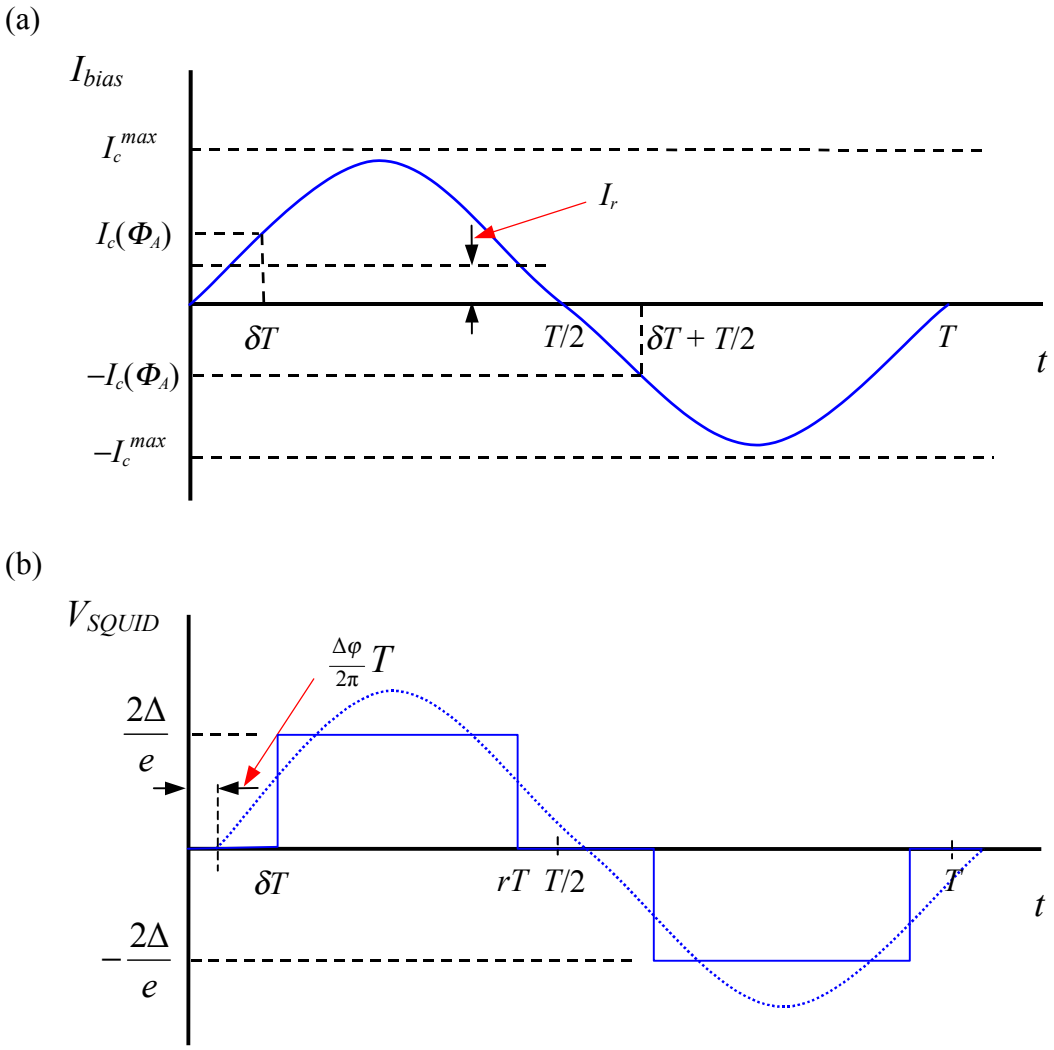

FIG. 6.4. Response of an ideal hysteretic dc SQUID to a sinusoidal bias current with period T. The dc SQUID experiences retrapping from the gap voltage $2\Delta/e$ to zero when $I_{bias} = I_r$ at rT after triggering. The amplitude of the bias current is set to a value smaller than the maximum SQUID critical current I_c^{max}. Graph (a) represents the sinusoidal bias current. Graph (b) shows a triggering event which occurs at δT after the start of the bias current signal. Dotted curve shows the primary Fourier component of the voltage signal. The Fourier component lags the bias current signal with a phase shift of $\Delta\varphi$.

phase shift places more emphasis on precision measurement while the type of measurement is shifted from time measurements to phase shift measurements. Although the phase shift can be measured with the aid of a lock-in amplifier, such an amplifier working at microwave frequencies is not available and would require a repetitive signal demanding that the bias current frequency be even higher than the target bandwidth. Third, irregularities or asymmetries in the characteristics of actual physical SQUIDs could cause undetermined phase shifts of their own. This is in addition to phase shifts from electronics and wiring.

The shortcomings of these two alternate readout techniques highlight the strengths of the pulsed current scheme. The current pulse technique avoids having to perform a timing measurement. With square pulses, it does not matter when during a pulse the SQUID triggers. It only matters whether or not a pulse triggered the SQUID into the resistive state. At the same time, it produces a large, easily measured, output voltage pulse that requires minimal electronics for detection.

6.2.3 Feedback Field Follower

The pulsed sampling technique is made possible in practice by using a hysteretic SQUID. However, to accurately follow the change in critical current and accurately determine the magnetic field from this result, some additional features are required. One such feature is the need to detect the critical current level or transition and another is to be able to follow it. There are at least two ways of detecting the critical current of a dc SQUID with pulsed sampling. One is to adjust the current pulse height until a voltage transition is found. The other way is to hold the current

pulse height to a fixed value between I_c^{min} and I_c^{max} and apply a feedback flux that will induce the transition. A feedback flux could also be used to cancel flux from an externally applied signal.

Comparing the two methods, the former method has a number of disadvantages compared to the latter. First, the critical current versus flux relation is not linear. So, as the pulse height increases the corresponding flux does not increase linearly and can even decrease. Second, the former technique cannot follow flux changes that are greater than $\Phi_o/2$. If the externally applied flux gradually changes by more than this amount, there is ambiguity as to the value of the external flux due to the periodicity between flux and critical current as discussed in section 2.3. And third, current pulses sent to the dc SQUID must be well defined and reproducible. It is far easier to produce such pulses if their characteristics are kept constant. From these considerations, it should be clear that it would be advantageous to apply feedback flux to the SQUID rather than adjust the pulse height.

Applying feedback flux also leads to a straightforward way of following the change in the critical current and external flux. When the externally applied flux varies, the feedback flux can be adjusted to compensate for the change, ideally nulling the total flux through the SQUID. The change in feedback flux then follows the change in the external flux. This is much like conventional FLL electronics.

To properly compensate the changes in external flux, one needs to know first whether the external flux increased or decreased. The information required to determine this can be obtained during the initial critical current detection stage. Adjusting the feedback flux so as to trigger the SQUID will determine whether the

flux is on an increasing edge or on a decreasing edge of the critical current versus flux curve (see Fig. 2.4). If increasing the feedback flux causes the SQUID to trigger, this means that the critical current is suppressed and the SQUID is on a decreasing edge of the curve. If decreasing the flux causes triggering, the SQUID is on an increasing edge. With this information, it is simple to determine whether the external flux increased or decreased by determining whether the critical current increased or decreased.

Given the periodicity of the critical current with respect to flux, it is possible to increase the feedback flux in one direction and locate the critical current on either an increasing or decreasing edge. This fact could be used to simplify the electronics by always locating the SQUID on one type of slope. Then, the choice of whether to increase or decrease the flux to compensate for the change in external flux becomes fixed.

The second piece of information needed for compensating the change in external flux is knowing how much the flux changed. This, however, is impossible to know without searching for the new critical current. Assuming that the change is small compared to $\Phi_o/4$, the search can be performed by programming the feedback flux to either increase or decrease in small discrete steps depending on the direction of change in the critical current. Eventually, the flux will induce a voltage transition thus revealing the new critical current. The discrete steps should be large enough to quickly compensate for the change in external flux but not too large that it over compensates. This condition should be satisfied by limiting the step size such that the change in flux through the SQUID hole is less than $\Phi_o/4$. On the other hand, if

the steps were too small, the electronics may not be able to keep up with the changing external flux.

The maximum rate of flux change that can be handled by the electronics is its slew rate. As mentioned above, the slew rate is limited by the speed of the electronics and the step size. Another limit on the slew rate can come from the need to perform multiple measurements or averaging. Usually, one averages to reduce the effects of noise. So, instead of reacting immediately to a single pulse measurement, multiple pulse measurements can be performed before adjusting the feedback flux. This adds to the time needed to react to the changing external flux. The external flux then has more time to change and may increase faster than the feedback flux can adjust. It may be possible to address rapidly varying fluxes with adaptive step sizes. However, if one follows this approach, the need for large closed loop bandwidth that limited conventional FLL electronics reappears.

Fortunately, the closed loop feedback limitation can be circumvented for a certain class of magnetic field signals, especially those that can be repeated, such as from computer circuits that are cycled through the same series of operations. For such signals, speed limitations set by the slew rate due to multiple measurements are also circumvented.

The next section includes descriptions of two signal following schemes, one of which circumvents the closed loop problem. I also present specific implementations of how the SQUID critical current can be initially determined and how to search for the new critical current after the applied external flux changes.

6.3 New SQUID Control Algorithm

6.3.1 Critical Current Detection

To implement the basic idea behind the pulsed SQUID sampling technique described in the previous section, one needs an efficient way to follow the applied external magnetic field. The question then becomes: what is the best way of determining and following changes in SQUID critical current? Clearly, in the pulsed sampling approach, one needs to make multiple measurements, as a single measurement can only determine whether the critical current is larger or smaller than the current pulse. That is, the SQUID only indicates whether its critical current is higher or lower than the bias current pulse height.

Figure 6.5 shows an example of one scheme. In this scheme, current pulses are set to some average height $I_p \approx I_c(\Phi_o/4)$. The electronics then adjusts the feedback field at regular intervals in the same direction until the voltage across the SQUID changes by the gap voltage $2\Delta/e$ between pulses. After detecting this voltage variation, the feedback field is adjusted in the opposite direction and the process is repeated. After, the initial SQUID critical current level is determined, the feedback field is switched back and forth, modulating the critical current just above and below the average value. When the applied external flux stays constant, the SQUID continuously alternates between the zero voltage and the resistive state with each bias current pulse. As the external flux changes, the feedback field will follow the change in critical current.

As long as the change in the applied external flux, and consequently the critical current, is not too large, the feedback field should be able to keep up with the

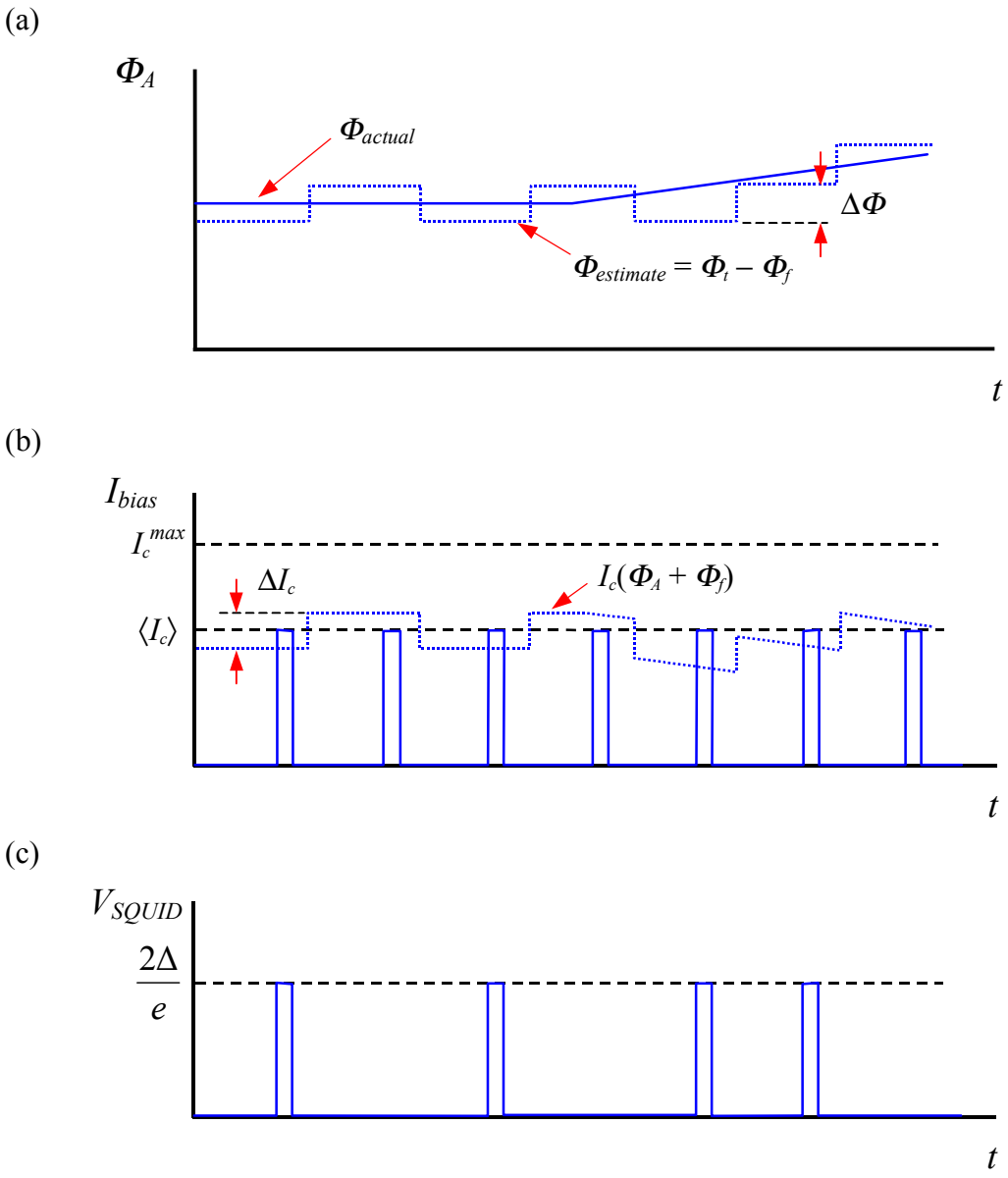

FIG. 6.5. Oscillating feedback scheme for critical current detection. This scheme uses identical bias current pulses and a feedback flux Φ_f which changes after every pulse by $\Delta\Phi$. The direction of the change in Φ_f is such that when the SQUID critical current I_c is lower than the bias current pulse height, Φ_f increases I_c by ΔI_c. When I_c is higher than the bias current pulse, Φ_f decreases I_c. Consequently, even when the external flux Φ_A is constant, Φ_f changes such that the dc SQUID alternates between the zero voltage state and the resistive state. However, an average flux $\Phi_t \approx \Phi_o/4$ and a corresponding $< I_c >$ is maintained. (a) Φ_A that is initially constant then increases. The change in Φ_f follows Φ_A and is used to produce $\Phi_{estimate}$. (b) Solid line shows pulsed bias current. Dotted curve shows I_c in response to $\Phi_A + \Phi_f$. (c) Voltage across the dc SQUID, which is used to determine whether I_c is higher or lower than the bias current pulse.

external flux. Under pseudo-dc conditions, the external flux through the SQUID hole will correspond to a level somewhere in between the modulated high and low flux levels. The difference between the high and low magnetic flux levels should be large enough that noise does not influence the triggering of the SQUID. The discrete incremental change in feedback flux then corresponds to the "one shot" flux resolution of the electronics, and the average feedback field corresponds to the SQUID critical current.

Matthews *et al*. have investigated a variation on this technique that instead of searching for the new critical current, just maps out the triggering frequency at different feedback field values [31,120]. One obtains a histogram of triggering events versus flux. The technique makes use of noise and the distribution of triggering events to determine the critical current level. In this scheme, the feedback field is adjusted such that some of the pulses trigger the SQUID into the resistive state and the rest leave it in the zero voltage state. If the feedback field exactly corresponds to the critical current, noise in the signal and system will cause only half of the pulses to trigger the SQUID. This scheme has the drawback of requiring more measurements than the scheme described in Fig. 6.5.

Figure 6.6 shows an alternative scheme which needs as few measurements as that of Fig. 6.5 but does not require the feedback field to be constantly adjusted. The technique involves using bias current pulses of two sizes that alternate. First, a small pulse is sent to the SQUID followed by a large pulse. If neither pulse triggers the SQUID into the resistive state, the critical current is larger than both pulse heights. If both pulses cause triggering, the critical current is smaller than both pulses. When

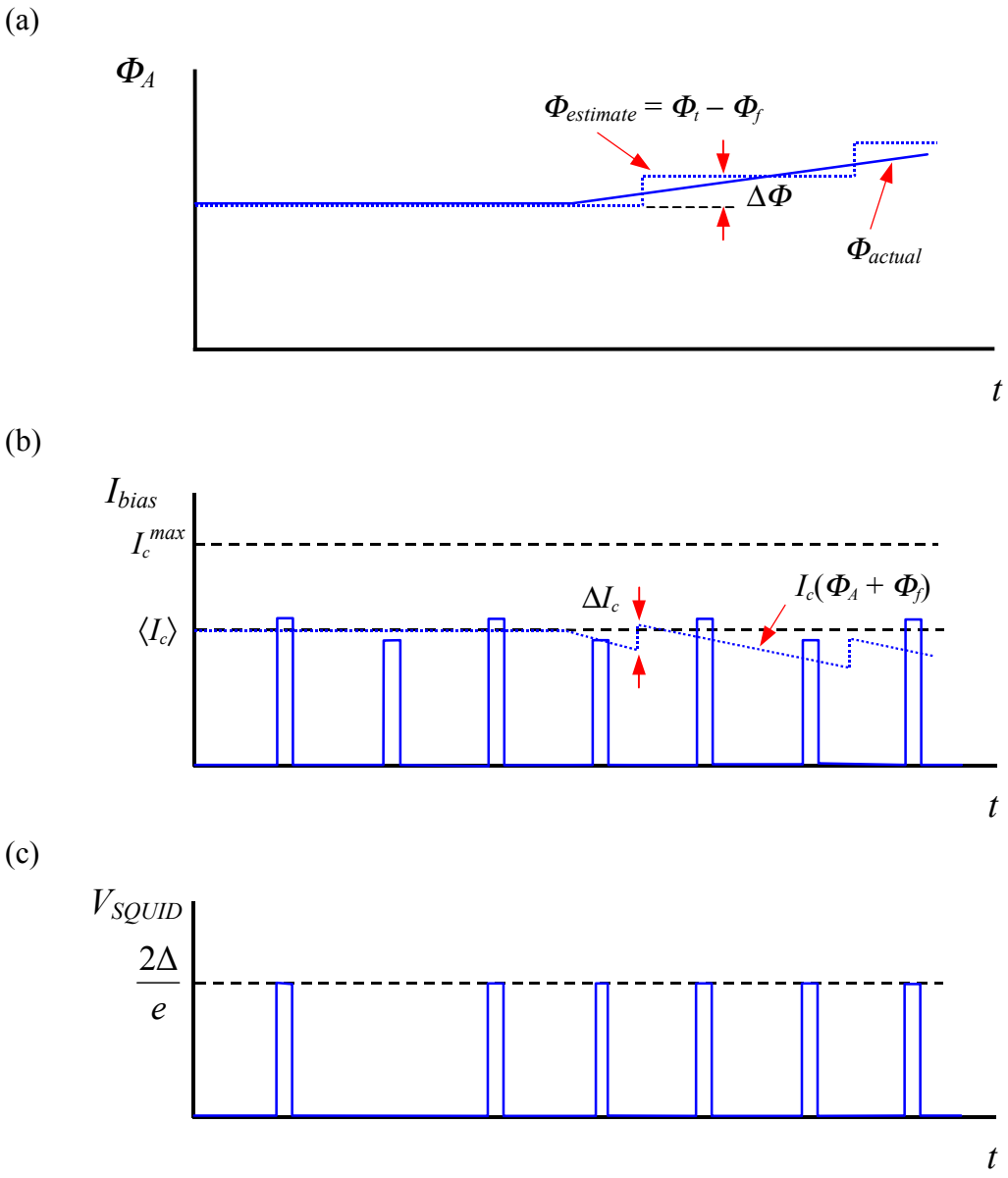

FIG. 6.6. Alternating pulse scheme for critical current detection. This scheme uses bias current pulses of alternating height and a feedback flux Φ_f which maintains the SQUID critical current I_c between the heights of the alternating pulses. (a) External flux Φ_A that is initially constant then increases. The change in Φ_f follows Φ_A and is used to produce $\Phi_{estimate}$. (b) Solid line shows pulsed bias current through dc SQUID. Dotted curve shows I_c in response to $\Phi_A + \Phi_f$. If I_c stays between the two pulse heights, Φ_f remains constant. When Φ_A changes causing I_c to drop below the shorter pulse, Φ_f changes by $\Delta\Phi$ to raise I_c by ΔI_c. If Φ_A causes I_c to increase above the higher pulse, Φ_f changes to decrease I_c. Consequently, an average flux $\Phi_t \approx \Phi_o/4$ and a corresponding $< I_c >$ is maintained. (c) Voltage across the dc SQUID, which is used to determine whether I_c has moved outside the range between the alternating pulses.

the SQUID is triggered only by the larger pulse but not by the smaller pulse, the critical current is between the two pulses. This identifies the critical current.

When the critical current is outside the upper and lower limits of the two pulses, the electronics adjusts the feedback field in the way described in section 6.2, restoring the total magnetic flux through the SQUID hole and bringing the critical current back between the two pulses. The difference in the two bias current pulses corresponds to a SQUID dependent magnetic flux difference. Unlike the oscillating feedback scheme of Fig. 6.5, the "one shot" flux resolution in the alternating pulse scheme of Fig. 6.6 is the larger of this flux difference and the discrete incremental step size of the feedback flux. Setting the difference between the two pulse heights just a little bit larger than the corresponding difference in feedback field step size optimizes the step size value. The pulse height difference should be chosen so that its somewhat larger than the rms current noise in the SQUID.

6.3.2 Pulse Rate Dependent Signal Following Schemes

Given the means of determining and following the change in critical current, detecting changes in the applied external flux on a SQUID is straightforward. However, applying feedback is more involved. Depending on the relative timing of the measured signal, the bias current pulses, and the adjustment of the feedback field, feedback can be implemented in pulsed SQUID sampling in two very different ways: "synchronous mode" or "asynchronous mode". Asynchronous mode feedback requires pulsing the current at rates that are large compared to the inverse of the characteristic time of magnetic field variations. It can be used with nonrepetitive

signals that are sufficiently slow with respect to the pulse rate. Synchronous mode feedback requires repetitive signals, generally under conditions where time variations in the measured field occur much more rapidly than the maximum possible pulse rate. Synchronous mode is well suited for measurements of chips and microcircuits, since they can be put through the same set of operations repeatedly.

Figure 6.7 summarizes the idea behind asynchronous mode. This mode can be used for both repetitive and nonrepetitive signals and involves pulsing the dc SQUID at the maximum reliable constant rate. Each pulse in Fig. 6.7 represents a determination of the critical current level and so can correspond to multiple measurements. For the oscillating feedback scheme of Fig. 6.5, it corresponds to one or more pulses determining whether the SQUID is triggering. In the case of the alternating pulse scheme of Fig. 6.6, it corresponds to one or more pulse pairs determining whether the critical current is between, above, or below both pulse heights.

The voltage across the dc SQUID must be detected at the pulse rate. After observing how many times the SQUID triggers, the electronics follows the output signal and adjusts the feedback field accordingly. In asynchronous mode, the sampled values will represent the entire evolution of the measured signal, provided that during the dead time between measurements, there are no significant variation in the signal. In particular, the variation in applied external flux should be smaller than $\Phi_o/4$, as mentioned earlier in this chapter. This is much like conventional FLL electronics except that any signal averaging is performed before adjusting the feedback field.

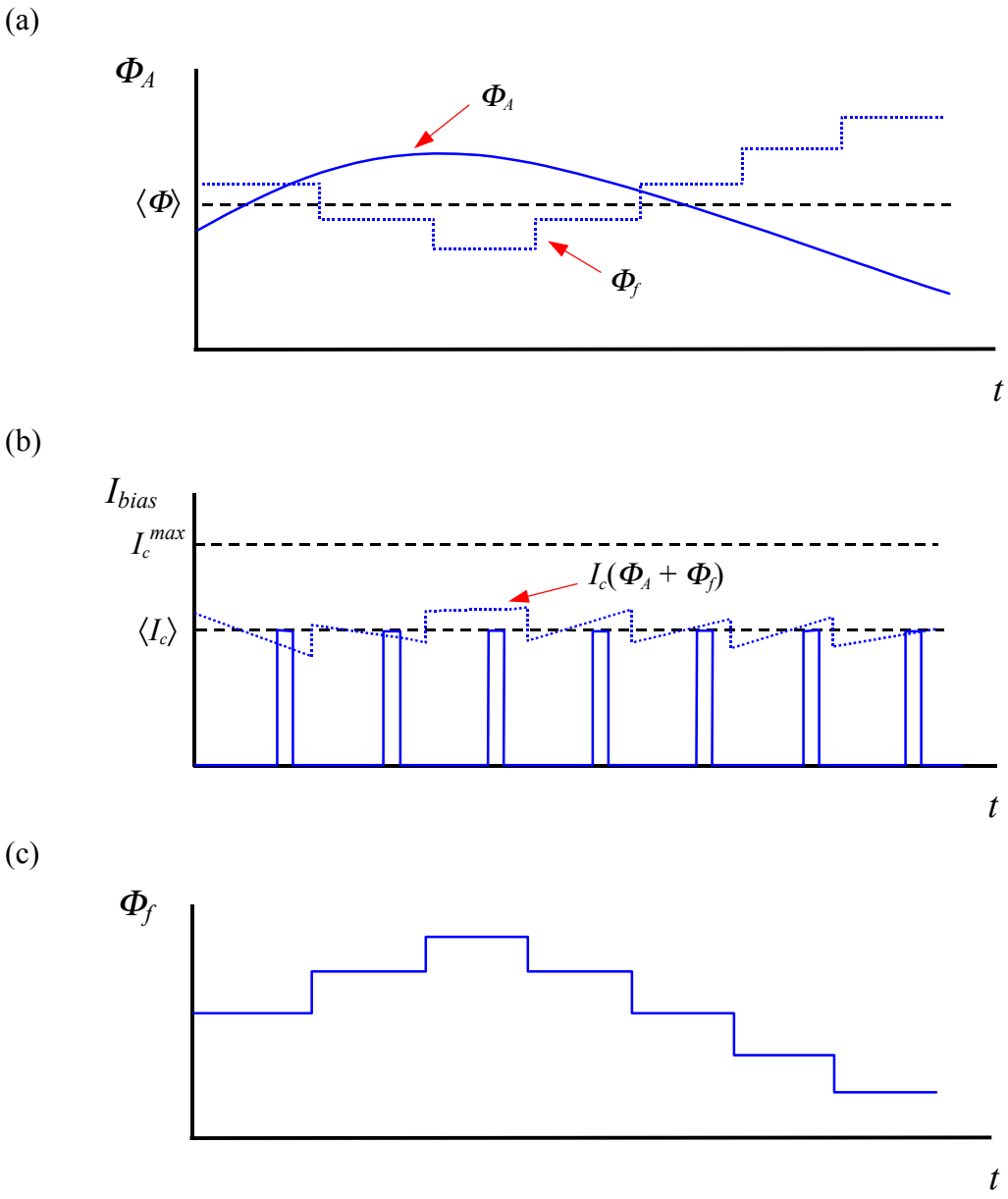

FIG. 6.7. Asynchronous pulsed SQUID sampling technique. (a) Solid curve shows the evolution of an external magnetic flux Φ_A through the dc SQUID. The dotted curve shows the evolution of a feedback flux Φ_f responding to and following Φ_A such that $\Phi_A + \Phi_f \approx <\Phi>$. (b) Solid line represents current pulsing events that determine the SQUID critical current at the indicated times which are at regular intervals. Dotted curve shows change in I_c in response to $\Phi_A + \Phi_f$. After determining I_c, Φ_f is adjusted as necessary, maintaining $I_c \approx < I_c >$. Note that changes in Φ_A are relatively small between pulsing events compared to its overall evolution. (c) Feedback flux Φ_f versus time, which can be used as the output signal.

The asynchronous pulsed sampling technique is limited by the maximum pulse frequency, minimum pulse length, the time it takes to readout the SQUID voltage, and the time it takes to integrate the feedback signal for stability purposes. All of these factors cause phase lags just as in conventional FLL electronics. Consequently, asynchronous mode operation will encounter the same limits that prevent large bandwidth measurement. Even within the bandwidth limit, the pulse period cannot be shorter than the pulse length and is usually much longer, dependent on the time required for the electronics to register the SQUID voltage, adjust the feedback field, and reset itself for the next measurement.

As an example, given a current pulse rise time of 12 ps, the minimum pulse length must be twice that or 24 ps. The maximum possible pulse rate is then around 40 GHz. However, pulse generators with repetition rates that high are not readily available. To follow a 1 GHz signal in asynchronous mode, a repetition rate that is greater and preferably much greater than 2 GHz is needed. Furthermore, the electronics must be able to read out the SQUID voltage at this rate as well. These are very serious limitations and suggest asynchronous mode operation is not viable as a large bandwidth technique. These limitations are circumvented in synchronous mode operation, described below.

In synchronous pulsed sampling, the onset of pulses is synchronized to the start of the repetitive signal. Only a single measurement is made per period, thus the pulse rate need not be fast, though multiple periods have to be sampled. In each subsequent period, an additional measurement can be made with the same synchronization and delay with respect to the start of the signal until the critical

current level at that specific delay is determined. After determining the critical current, the electronics adjusts the feedback field so as to compensate for any changes in the external flux at the specific delay time.

For successive measurements, a new delay time is chosen, and the signal is sampled repeatedly at the new delay time with respect to the start of the signal until the new critical current level is determined. After adjusting the feedback field again, the entire process is repeated at another delay time until the entire signal period is covered.

The delay should be small compared to the period of the signal in order to see the entire signal evolution within a period. On the other hand, if signal variations are small between successive delays, the offsets do not have to equal the pulse lengths and can be significantly longer, so long as the sampled values capture all the features of the signal.

As an example, suppose the pulse length is 1 ns and the signal period is 1 μs. At the first measurement, the delay time can be set to zero, so the signal at $t = 0$ ns is sampled. When measurements are finished at $t = 0$ ns, the feedback field is adjusted appropriately, and the next measurements are made with a 1 ns offset from the beginning of the signal period. Once the signal is measured at $t = 1$ ns, the feedback field is adjusted to compensate the field at $t = 1$ ns, and then the system samples the signal at $t = 2$ ns, and so on. This process is shown in Fig. 6.8. Eventually, the signal values over the 1 μs period will be sampled, and the measurements can be combined to reconstruct the entire signal over its period.

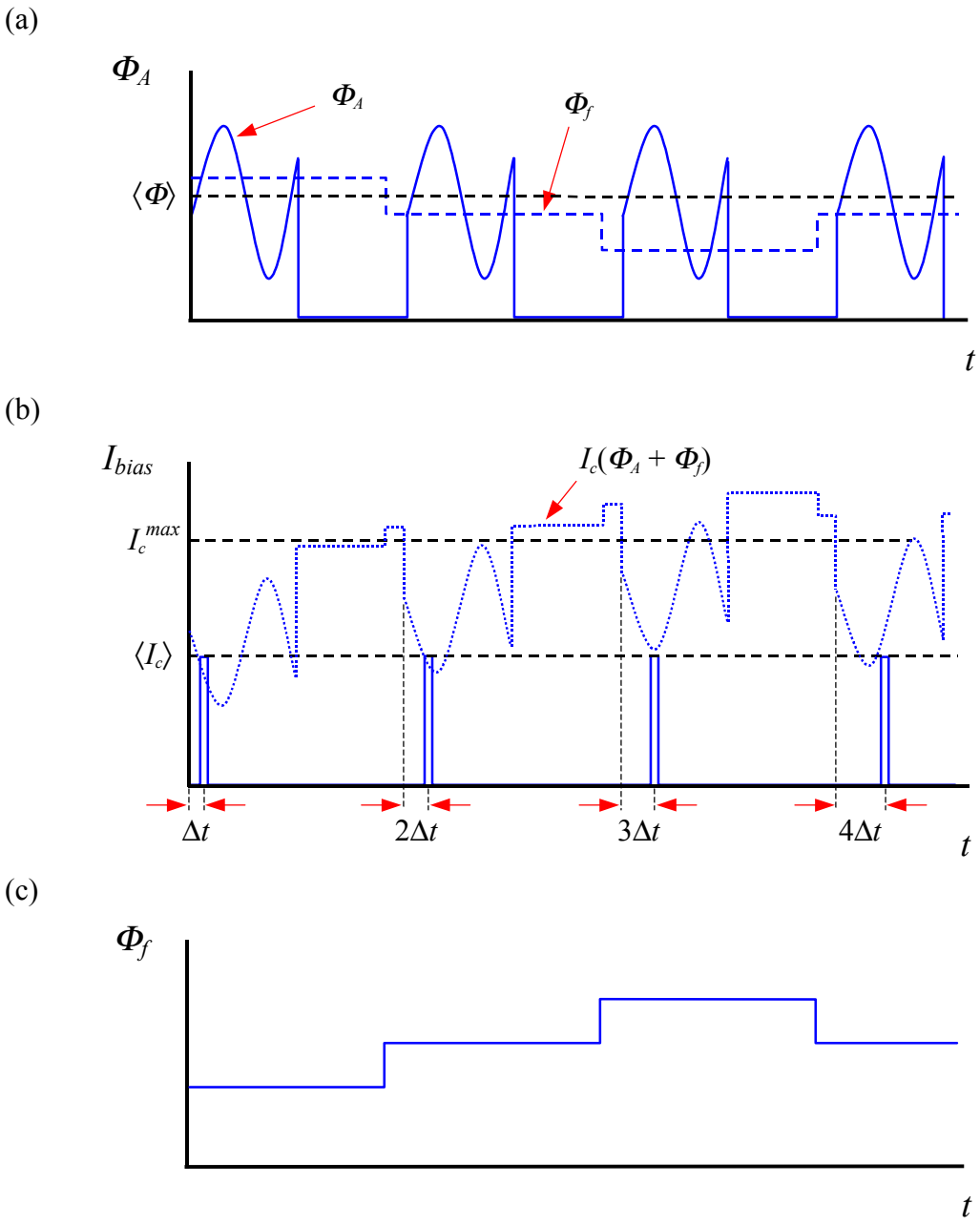

FIG. 6.8. Synchronous pulsed SQUID sampling technique. (a) Solid curve shows the evolution of a fast repeating external magnetic flux Φ_A. Dotted curve shows the evolution of a feedback flux Φ_f in response to measurements on Φ_A. (b) Solid line represents pulsed current measurements that determine the SQUID critical current I_c at the indicated delay times. Dotted curve shows change in I_c in response to $\Phi_A + \Phi_f$. After determining I_c, Φ_f is adjusted so that $\Phi_A + \Phi_f \approx <\Phi>$ and $I_c \approx < I_c >$ at the time of the pulsed measurement. The following measurement is delayed by an interval $n \cdot \Delta t$ with respect to the start of Φ_A where n represents an integer sequence. As a result, Φ_f follows Φ_A but stretched out in time. (c) Feedback flux Φ_f versus time, which can be used as the output signal.

In practice, many measurements will be needed at each delay time. Using the oscillating feedback scheme of Fig. 6.5, the SQUID voltage is repeatedly checked at the same delay until the voltage across the SQUID changes by the gap voltage $2\Delta/e$ between pulses. With the alternating pulse scheme of Fig. 6.6, one or more pulse pairs at the same delay, still one pulse per period, are needed to determine whether the critical current is between, above, or below both pulse heights.

Averaging to decrease the effects of noise will further increase the number of measurements at the same time offset. But, unlike in asynchronous mode sampling, this does not affect the slew rate; for repetitive or periodic signals that can be generated on command, synchronous mode operation allows for an arbitrary amount of time to determine the flux change.

A form of synchronous pulsed sampling of a sinusoidal signal was successfully used by Matthews *et al*. in conjunction with their technique of mapping the triggering events of a hysteretic dc SQUID at different feedback field values [31,120]. They achieved the goal of following high frequency magnetic field signals with the technique. A sample result is presented in Chapter 7.

6.4 Implementation into Electronics

6.4.1 Synchronous Alternating Pulse Scheme

Many variations on the pulsed sampling technique with different signal detecting and following schemes are possible. In this section, I discuss the design of electronics for the alternating pulse scheme of Fig. 6.6 using synchronous pulsed sampling.

To summarize the basic idea of the synchronous alternating pulse scheme, the externally applied flux is determined by adjusting the feedback flux so that the SQUID only triggers when the critical current level is between the two bias current pulses of differing height. The difference in pulse height should be larger than the current noise or corresponding flux noise to avoid random SQUID triggering. If adjustments of the feedback field are performed in discrete steps, the step size will limit the flux resolution in addition to the pulse height difference. Adaptive step sizes could make adjusting the feedback more efficient. But, in any case, the smallest increment in feedback flux should change the critical current by no more than the pulse height difference. And finally, a precision master clock must coordinate the relative timings of the pulses with respect to the signal being measured for synchronization.

The choice of the two current pulse heights is very important. For fixed step size, the optimum height difference is determined by the flux noise [see Eq. (3.18)]. For SQUID BH used in this study, this corresponds to about 5.5 mΦ_o in 25 ps at 5 K. In this estimate, I have ignored 1/f noise in the critical current, which will have a small effect in comparison [4,6,12]. Clearly, the pulse heights must be adjusted to where the slope in the critical current versus external flux curve is maximum, i.e. near $\Phi = \Phi_o/4$ where $\partial I_c/\partial \Phi$ is large. This maximizes the pulse height difference for the same difference in flux, thus, minimizing effects from bias current noise in the pulse height while maximizing flux sensitivity.

I note that the absolute maximum useful difference in pulse height is from the bottom of the critical current versus external flux curve to the top, which corresponds

to $\Phi_o/2$. For SQUID BH, this implies that the minimum pulse height difference is about 10^{-2} of the maximum critical current. More experimental details are presented in Chapter 7.

6.4.2 Pulse Counting and Averaging

Figure 6.9 shows a block diagram of the electronics for implementing the synchronous alternating pulse technique. In this implementation, instead of directly determining whether the larger and smaller pulses each trigger the SQUID, I present an indirect method which simply counts the number of pulses and compares. Other variations are clearly possible.

If the feedback field cancels the effects of the applied external flux, only the larger pulse will place the SQUID in the resistive state. So, of the N_i pulses sent by the signal generator, only $N_v = N_i/2$ should cause a triggering event. The electronics can then compare $N_i/2$ with N_v, and if they are the same, the feedback field is canceling the external flux. On the other hand, if $N_i/2 < N_v$, then the external flux changed to suppress the critical current causing too many triggering events. And, if $N_i/2 > N_v$, then the external flux changed to augment the critical current allowing too few triggering events.

The feedback field works to restore the equality $N_v = N_i/2$ by compensating for the change in applied external flux. Assuming the dc SQUID is on a decreasing edge of the critical current versus flux curve, this means decreasing the feedback field when $N_i/2 < N_v$ and increasing the field when $N_i/2 > N_v$.

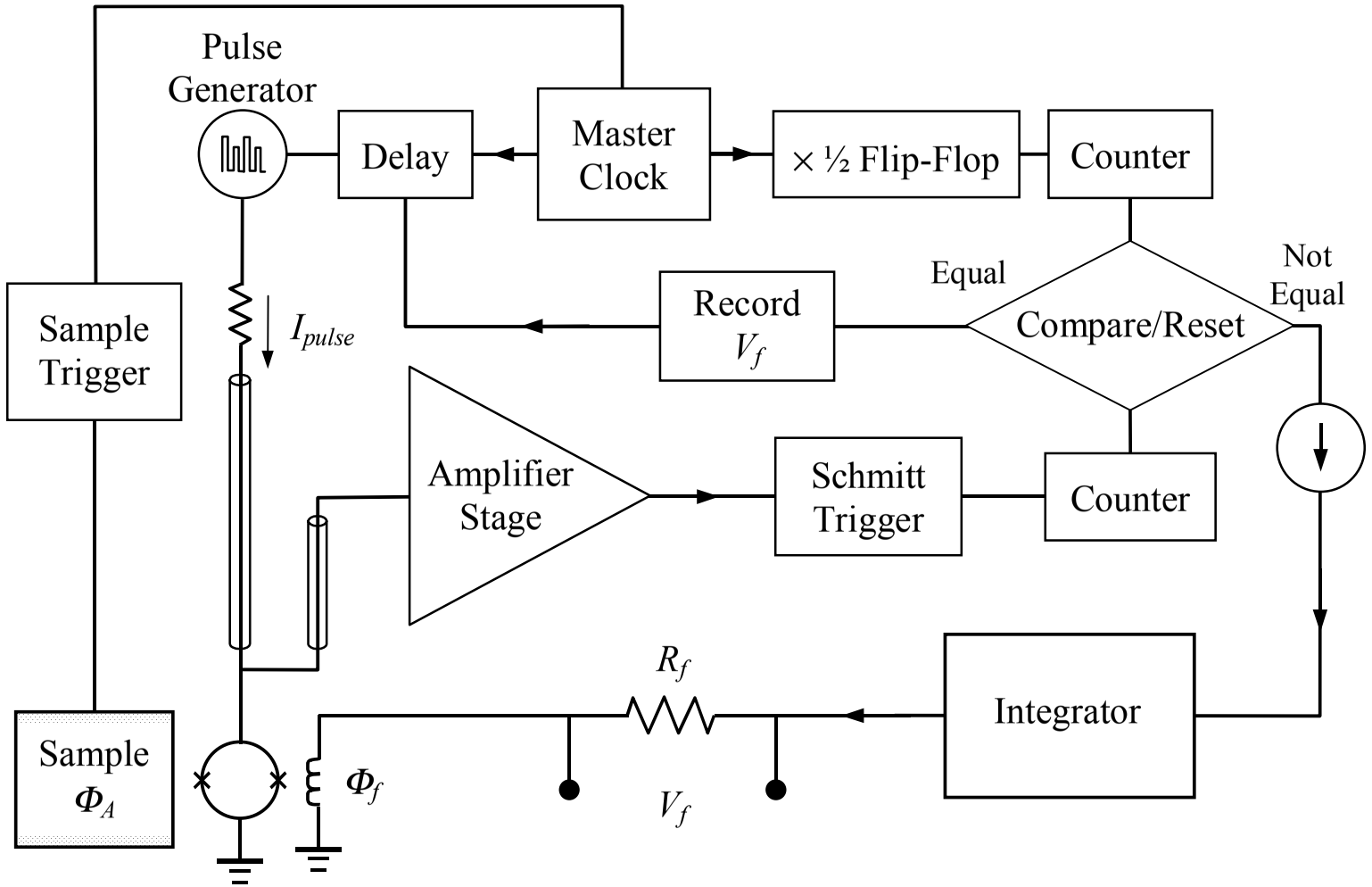

FIG. 6.9. Schematic diagram of pulsed SQUID sampling electronics using a hysteretic dc SQUID and implementing the synchronous alternating pulse technique for large bandwidth magnetic field detection applications.

The physical implementation of the above is as follows. A signal generator produces 1 ns or shorter voltage pulses with alternating height. The generator is timed or triggered by a master clock. The voltage signal from the generator is converted into a current pulse and fed to the hysteretic dc SQUID via a matched 50 Ω coaxial cable. If the SQUID is driven into the resistive state, a voltage will appear across the SQUID. An amplifier detects this voltage and sends it to a Schmitt trigger which converts the analog signal into a digital pulse [144]. This pulse is sent to a counter. At the same time, pulses from the signal generator are also sent to a counter through a divide by 2 flip-flop [146]. The results of each counter are compared with one another using digital logic.

Depending on the three possible outcomes comparing $N_i/2$ with N_v, the output voltage of the feedback flux line is adjusted. Adjustments in the voltage can be performed in unit steps or adaptively depending on the comparative difference between $N_i/2$ and N_v. The voltage drives an integrator (for feedback stability) which in turn drives current through the feedback coil that generates a magnetic field to compensate the change in externally applied flux through the SQUID hole.

After the feedback stabilizes, the pulse counters are reset, and the process is repeated for another measurement. Measurements are repeated at the same delay with respect to the measured signal until the condition $N_v = N_i/2$ is satisfied. When this condition is met, the voltage V_f across the feedback resistor R_f is stored as the quantity corresponding to the applied external flux Φ_A, just like in conventional FLL, but only at the specified delay. The external flux Φ_A can be expressed as

$$V_f = I_f R_f = \frac{R_f}{M_f}\Phi_f = \frac{R_f}{M_f}(\Phi_t - \Phi_A) \tag{6.2}$$

where M_f is the mutual inductance between the feedback coil and the SQUID loop, Φ_f is the feedback flux, and Φ_t is the total magnetic flux that the electronics attempts to conserve. Finally, a computer gathering data and controlling the system adjusts for the next delay, and the whole process is repeated.

If a single generator capable of producing pulses with alternating heights is unavailable, then two pulse generators synchronized together could be used in which one generates regular pulses of constant height and the other generates positive then negative pulses of small amplitude (see Fig.6.10). If the difference in pulse height is smaller than the retrapping current of the hysteretic dc SQUID, the second pulse generator could be replaced by a sine wave source. The difference in pulse heights would be twice the wave amplitude.

If noise in the SQUID bias current is significant, the dc SQUID could trigger without a current pulse being received. I observed such events when I performed initial I-V measurements on SQUID BH. Bias current to the dc SQUID was controlled through a resistor network [see Fig. 5.2(b)]. Observations of the resulting I-V curve included fast oscillatory transitions from the zero voltage state to the resistive state and back that were unexplainable from basic SQUID characteristics alone. When the resistor network was replaced with a single resistor, the phenomenon disappeared suggesting that it was due to pickup of interference signals.

In principle, one could address current noise problems by including coincidence checking circuitry between the pulse generator and the dc SQUID into

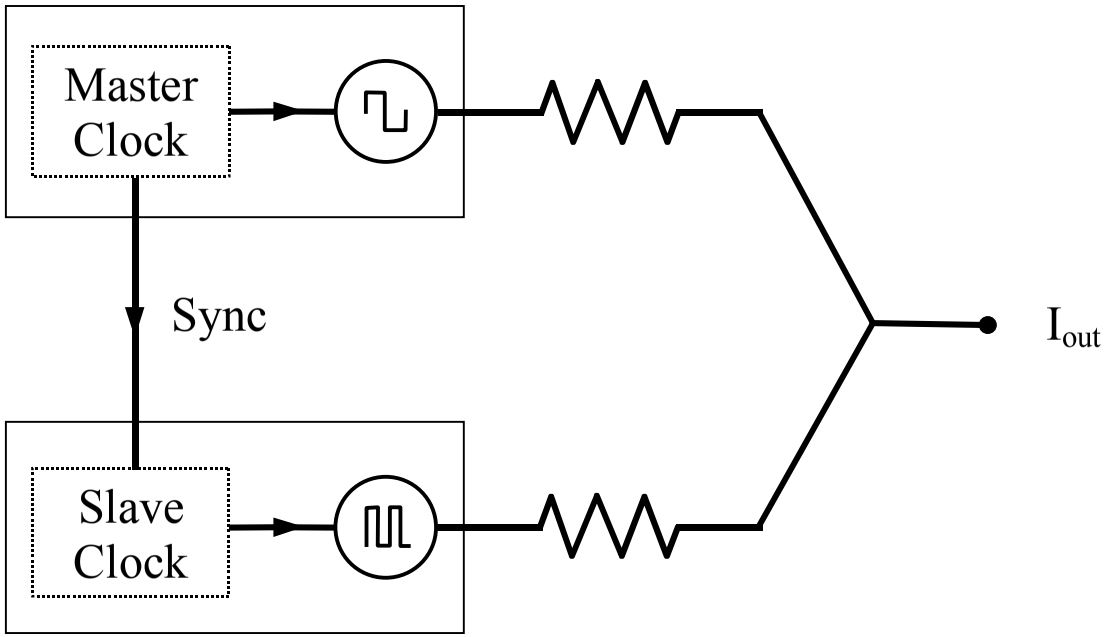

FIG. 6.10. Schematic diagram of electronics to generate alternating height current pulses using two signal generators. In this implementation, a small amplitude square wave generator and a constant height pulse generator are synchronized together. Impedance matching and proper termination is assumed.

the electronics. A pulse from the signal generator can be combined with a pulse signal from the dc SQUID through the equivalent of a logic AND-gate, which must also compensate for the short pulse lengths and timing delays in the two signals. Then, only when both the signal generator sends a pulse and the SQUID triggers is the event recognized and fed to the counter. If, on the other hand, false triggering is negligible or avoided by other means, the added circuitry should be unnecessary.

6.4.3 Superconducting Circuitry

Other than the SQUID, the key element in the electronics of Fig. 6.9 that makes pulsed SQUID sampling work is the short pulse signal generator. For 1 GHz bandwidth electronics, the pulse length has to be 500 ps or shorter. Signal generators capable of producing such short pulse lengths are available. However, they are expensive, and when pushed to produce even shorter pulse lengths their performance starts to degrade in terms of reduced pulse height and distortions in the pulse profile.

There is an alternative possibility of producing short pulses and achieving even larger bandwidth. This involves creating the required short pulses with superconducting electronics. Based on the work by Faris, Tuckerman, and Whiteley *et al*., superconducting circuits can produce very short pulse signals that have rise times of 10 ps or less [22-24,147,148]. Furthermore, superconducting electronics based on Josephson junctions or Rapid Single Flux Quantum (RSFQ) techniques have demonstrated the possibility of very fast electronics that can outperform conventional techniques [149-151]. In principle, such electronics could be accommodated on the

same superconducting chip as the SQUID, so there also would not be much additional cost once there is a working design.

Figure 6.11 shows superconducting circuitry that uses SQUIDs to produce short pulse signals. The hysteretic dc SQUID that measures the externally applied magnetic flux is SQ_3. Conventional pulse generators are still used but only for synchronizing pulses with the measured signal. In particular, the conventional generators' pulse length is not limited by bandwidth requirements but by the pulse repetition rate. An amplifier does not measure the voltage across the dc SQUID directly but the voltage signal V_{out} from a Josephson junction Schmitt trigger that reacts to the dc SQUID.

The circuit of Fig. 6.11 works as follows. The nonhysteretic dc SQUID SQ_1 is biased with dc current such that maximum voltage modulation occurs across it. The effective minimum resistance across SQ_1 should be much smaller than 1 Ω and the maximum resistance much larger than 1 Ω. The effective resistance of SQ_1 is controlled by the input signal from a conventional pulse generator. When SQ_1 is in the low resistive state, most of the bias current flows through SQ_1. When a square pulse is received through the input signal coil, SQ_1 goes into the high resistive state. The inductance L_1 is large, so initially current mostly flows through L_2. When that current reaches a maximum value determined by the Josephson junction I_{c1}, the junction transitions into the resistive state and the current then mostly flows through L_1. This results in a short current pulse through L_2. Faris suggests values of 300 pH and 20 pH for L_1 and L_2, respectively [147]. When the square pulse through the signal input disappears, current flows back mostly through SQ_1.

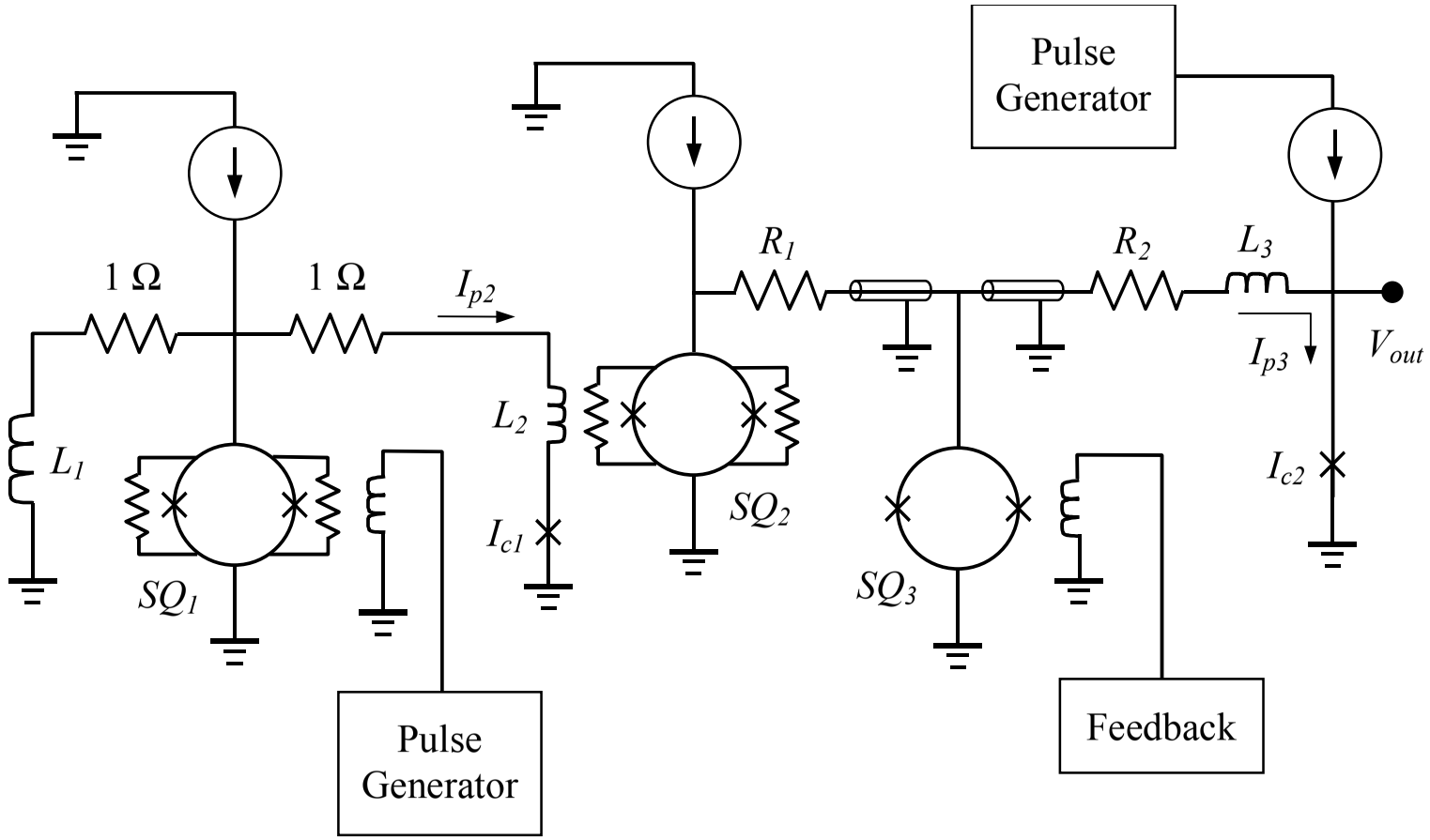

FIG. 6.11. Schematic diagram of superconducting electronics to generate very short current pulses to bias a hysteretic dc SQUID for large bandwidth pulsed SQUID sampling. All elements except for SQ_3 and its feedback coil reside on top of a superconducting ground plane.

The pulse through L_2 can be very short, as short as 26 ps, but computer simulation by Faris on a similar circuit indicates that it can have noisy features [147]. The circuit could also behave differently if instead of L_2, the load was variable like a dc SQUID. Therefore, instead of using the current pulse through L_2 as the bias current pulse to SQ_3, the current pulse through L_2 produces a magnetic field pulse into SQUID SQ_2.

Like SQ_1, SQ_2 is nonhysteretic and is also current biased to maximize voltage modulation. Coupling between L_2 and SQ_2 is set so that the maximum flux Φ_{max} through SQ_2 is

$$\Phi_{max} = M_2 I_{p2} \approx \frac{\Phi_o}{2} \tag{6.3}$$

where M_2 is the mutual inductance between L_2 and SQ_2, and I_{p2} is the height of the current pulse through L_2. SQ_2 is initially in the low resistive state, so most of the current flows through SQ_2 rather than through R_1. However, when the magnetic field pulse from L_2 triggers SQ_2 into the high resistive state, more of the current is channeled through R_1, driving a current pulse through SQ_3 with the same duration as the original short pulse through L_2. Furthermore, an additional nonhysteretic dc SQUID in series with R_1 can be used to vary the total output impedance to SQ_3, and consequently modulate the current pulse height.

This analysis assumes lump circuit behavior. So, for signal rise times of around 10 ps, the analysis would be valid for circuit lengths that are much less than 3×10^8 m/s $\cdot$ 10 ps = 3×10^{-3} m = 3 mm. This is acceptable for most of the circuit in Fig. 6.11, except near SQ_3. To minimize external field noise, the circuit elements

should be placed on top of a superconducting ground plane. However, SQ_3 must be exposed to external field and placed away from the ground plane. This requires relatively long leads between R_1, R_2, and SQ_3. Planar transmission line theory is then required to determine the optimal values of R_1 and R_2 to match SQ_3 and its leads [152].

Finally, the voltage signal across SQ_3 can be too fast to read out with conventional electronics. A technique adapted from RSFQ electronics can address this problem with the equivalent of a superconducting Schmitt trigger using a hysteretic Josephson junction I_{c2} and inductor L_3 [150]. I_{c2} is current biased below its critical current. If SQ_3 does not trigger, the current pulse I_{p3} through L_3 will be small and not enough to trigger I_{c2} into the resistive state. On the other hand, if SQ_3 does trigger, I_{p3} will be large enough to trigger I_{c2}, and a voltage will appear at V_{out}. This voltage will be maintained until the bias current to I_{c2} is reset. Mukhanov *et al*. suggest that L_3 = 1.65 pH for I_{c2} = 1 mA with a bias current of 0.63 mA [150]. The bias current is set and reset synchronously with the master pulse generator in Fig. 6.9.

I have not determined the optimal parameter values for all of the elements in the superconducting circuit described above. Even with determined values, deviations during manufacturing may render the circuit inoperable, and therefore a complete design would need to take such variations into account. Implementation of superconducting elements and the construction of the large bandwidth SQUID electronics are left as future work.

CHAPTER 7 Response of Hysteretic Niobium dc SQUIDs to Pulsed Bias Current

7.1 Background

The pulsed current SQUID readout technique described in Chapter 6 is partly based on a series of experiments I performed on hysteretic niobium dc SQUIDs. The purpose of the experiments was to test the general idea of pulsed SQUID sampling, specifically using short bias current pulses on dc SQUIDs to perform flux detection. The experiments provided insight into the design of the electronics and checked some aspects of the overall scheme.

The experiments involve sending short bias current pulses to a hysteretic dc SQUID while observing its voltage response. One expects that a voltage will be observed across the dc SQUID for the duration of the current pulse, depending on the height of the pulse and the magnetic flux through the SQUID hole. If the pulse height I_p and the range in SQUID critical current I_c is such that $I_c^{min} < I_p < I_c^{max}$, the voltage signal should appear and disappear as external magnetic flux through the SQUID hole varies.

Key questions that these experiments needed to answer were: does the pulsed SQUID sampling technique work as expected, and what limitations are there with the available apparatus? Those limitations included how short the current pulses could be, how large the signal was compared to background, how easy it was to defeat the

response, and how fast the pulses could be repeated. A question that I was not able to answer experimentally was what was the ultimate limit of the technique, especially how short the sampling time or pulse length could be. This was simply beyond the capability of the pulse generator I used. On the other hand, an integral part of the experiments was determining what type of system or apparatus would be required for the technique to work.

The first step in my experiments was to assemble hysteretic dc SQUIDs and prepare an apparatus. As mentioned in section 3.3, I obtained hysteretic SQUIDs from Hypres based on designs carried over from resistively shunted niobium dc SQUIDs used in a LHe cooled SQUID microscope [11,95,118]. The characteristics of the main SQUID I used in these experiments (SQUID BH) were summarized in Table I. Although in retrospect I could have improved on its design, SQUID BH had adequate characteristics and was very durable. Other hysteretic SQUIDs used for experiments were damaged or failed during the course of my experiments.

7.2 Large Bandwidth Dip Probe Design and Construction

7.2.1 Required Specifications

Many prior experiments had been done on resistively shunted niobium dc SQUIDs using a LHe dip probe. The probes could be inserted into LHe dewars which provide a relatively stable environment for SQUID measurements. Figures 3.6, 3.7, and 3.8 show examples of such measurements. Noise in Figs. 3.7 and 3.8 is due to noise in the external field as the probe was not magnetically shielded. Compared to configuring a cryocooler, it was relatively simple to reconfigure a dip

probe and repeat measurements. Considering these advantages, I decided it was preferable to continue using a dip probe apparatus, rather than the cryocooler, to perform experiments on the pulsed sampling technique.

However, the existing dip probe was designed for low frequency measurements and used twisted pair copper magnet wire. This would not be adequate for my purposes since twisted pair wiring has relatively poor uniformity and low impedance ($Z_c \approx 2\ \Omega$). The pulsed SQUID sampling technique required designing apparatus for bandwidths exceeding 1 GHz. Since there were no cryogenic probes with the right capability available to me, I constructed a new dip probe.

I considered two options for replacing the twisted pair cable dip probe. One involved generating and detecting short pulse signals locally, especially near or on the SQUID chip using microwave integrated circuit designs. In principle, superconducting electronics such as high frequency Josephson junction or Rapid Single Flux Quantum (RSFQ) circuits could be used [22-24,147-151]. The required design effort, however, was not compatible with the given constraints on time and resources. A simpler and quicker option was to change the wiring and connectors in the dip probe so that they matched measuring instrumentation.

The obvious choice was to substitute the twisted pair wiring with 50 Ω coaxial cable with a bandwidth exceeding 1 GHz. Micro coaxial cable with bandwidths exceeding 100 GHz had already been successfully used in other large bandwidth cryogenic applications [47,48]. So, despite space requirements and thermal conductance concerns installing it later in the cryocooled 4 K SQUID microscope, I expected the coaxial wiring to work well in the LHe dip probe.

After reviewing various choices, I selected UT-34-SS, a small diameter 50 Ω coaxial cable from Micro-Coax, Inc. [153]. The outer diameter is 0.034 in and the inner conductor diameter is 0.008 in. The dielectric material is polytetrafluoroethylene (PTFE), and the outer conductor is made of stainless steel; stainless steel has low thermal conductivity, and this would limit heat flow. The use of stainless steel for the inner conductor as well would have limited thermal heating even further. However, attenuation in the signal would have been significant, so the inner conductor was silver-plated copper-clad steel (SPCW). UT-34-SS is a semi-rigid cable, which means that it could be deformed to a certain extent and would hold its shape. The minimum allowed inside bend radius is 1.3 mm, which meant that it would be relatively easy to work with.

UT-34-SS is a nonstandard cable. Some of its specifications were not readily available from the manufacturer but appeared to be comparable to other small diameter coaxial cable. For example, I estimated the capacitance of the cable to be about 95.1 pF/m and the bandwidth approximately 155 GHz from the specifications of UT-34, which has an outer conductor made of copper but is otherwise identical in construction [153]. I expected the attenuation to be less than 1.91 dB/ft at 1 GHz based on the specifications of UT-20-SS which is similar to UT-34-SS except that it has an outer diameter of 0.020 in and an inner conductor diameter of 0.0045 in. Comparing specifications, I found that the attenuation is mainly affected by the choice of conductor material, but that there is a marginal increase in attenuation with smaller conductor diameter.

The choice of UT-34-SS was a compromise between cable diameter, thermal conductivity, attenuation, and cost. Further, an important factor was that suitable SMA connectors were available [154]. Matching converters were also available to connect to BNC cable and printed circuit board. The connectors had a much smaller bandwidth than the cable, typically about 18 GHz versus 155 GHz for the cable. The SMA-to-BNC converters had bandwidths of only 4 GHz [154]. Despite the reduced bandwidth, there was little impact on my experiments because the pulse generator I used had a more restricted bandwidth based on the shortest pulse it could produce.

Besides the wiring, making connections to the SQUID chip was also a concern. In the dip probe I used for making I-V measurements, I connected the SQUID to wiring using silver paint [see Figs. 4.7 and 7.1(a)]. These silver paint contacts were not very reliable as I discussed in sections 3.3 and 4.3. My I-V measurements of dc SQUIDs with silver painted contacts tended to show noise and much larger contact resistance compared to SQUIDs with wire bonded contacts.

In order to make the connections more robust, I decided to replace the silver paint contacts with wire bonding. This was performed by epoxying the SQUID chip to a chip holder and then wire bonding the SQUID to the holder [see Fig. 7.1(b)]. The holder was designed for the twisted pair wire dip probe. For the coaxial cable, I had decided to construct a new dip probe rather than modify the existing one, so I also designed and constructed a new chip holder and circuit board (see Fig. 7.2). The SQUID chip was epoxied directly onto the circuit board and then wire bonded to various connectors which were attached to the board as well (see Fig. 7.3).

(a)

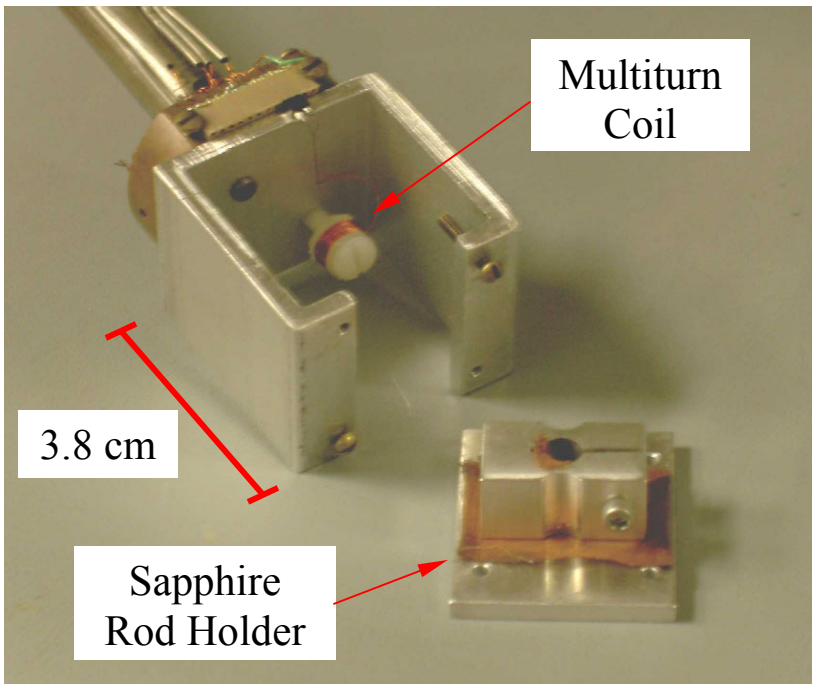

(b)

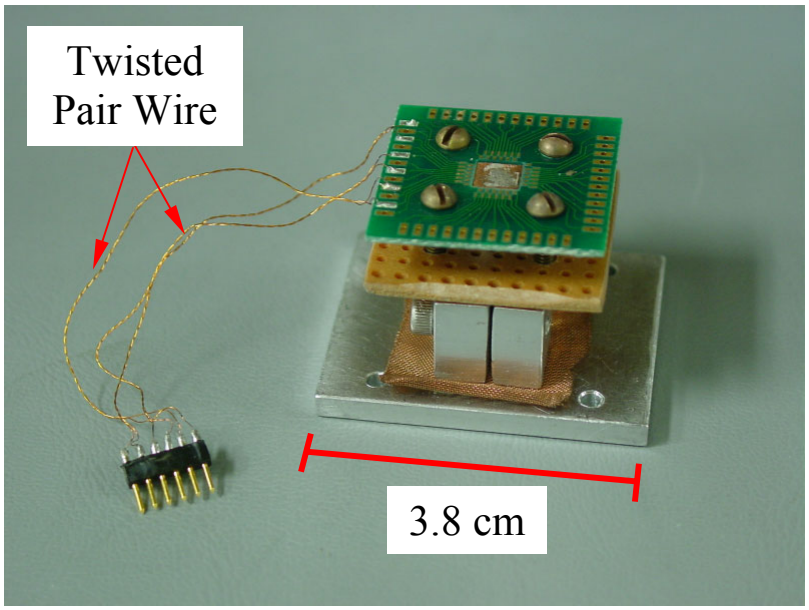

FIG. 7.1. (a) Bottom portion of twisted pair wire LHe dip probe. A multiturn coil for producing a magnetic field is seen inside the probe housing. A sapphire rod holder for testing SQUID tips and which attaches to the probe housing is also seen at bottom right. (b) Chip holder which attaches to the probe housing on the twisted pair wire dip probe. SQUID chips are glued to the center of the PC board with either silver paint or photoresist. Electrical connections to the chip are made by wire bonding.

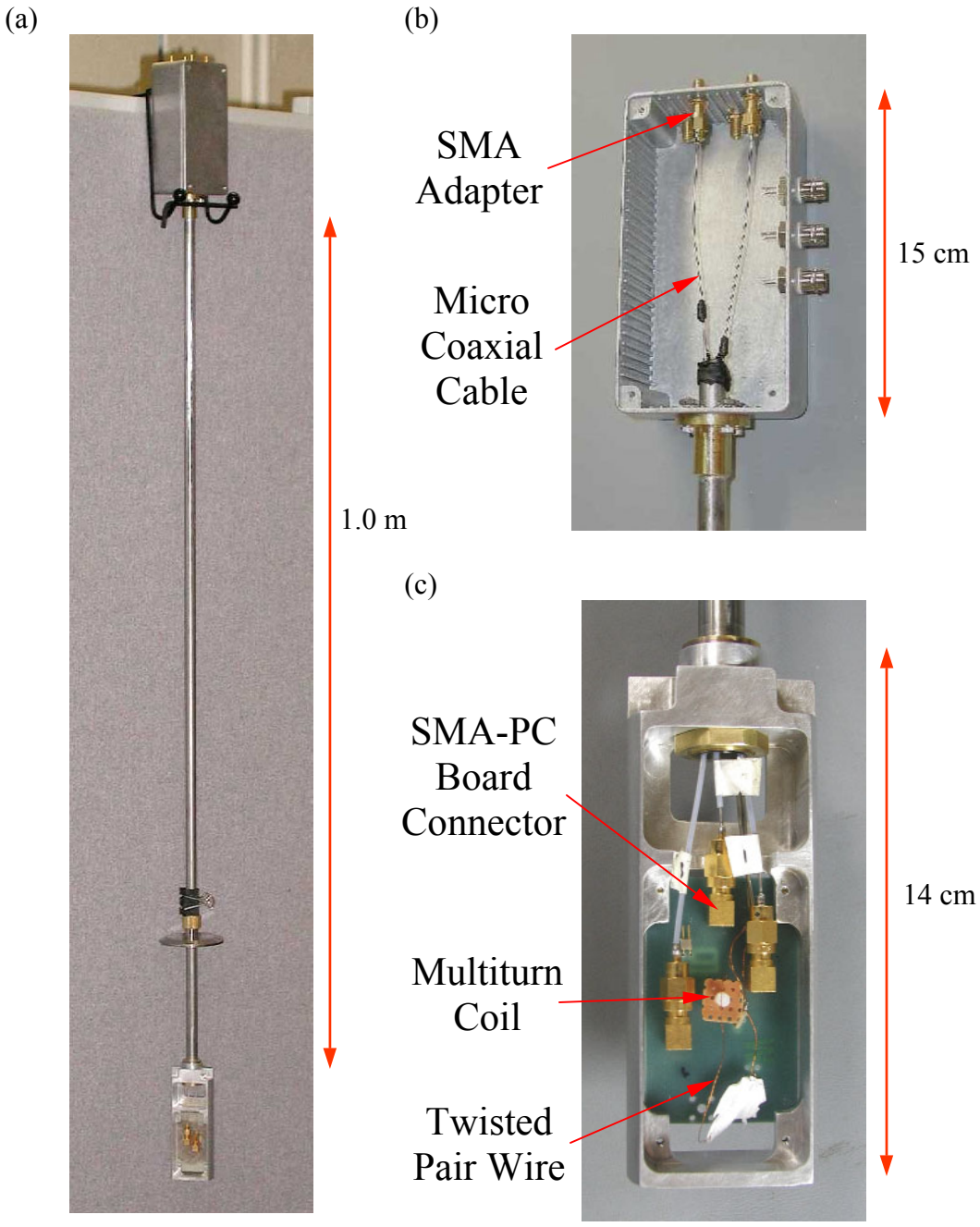

FIG. 7.2. Large bandwidth dip probe. (a) Full length view of dip probe. (b) Inside view of connector box with 2 micro coaxial cables. (c) Front view of chip holder. Micro coaxial cables and twisted pair wires are attached to PC board connectors. A multiturn magnet wire coil can be seen glued on to the middle of the PC board.

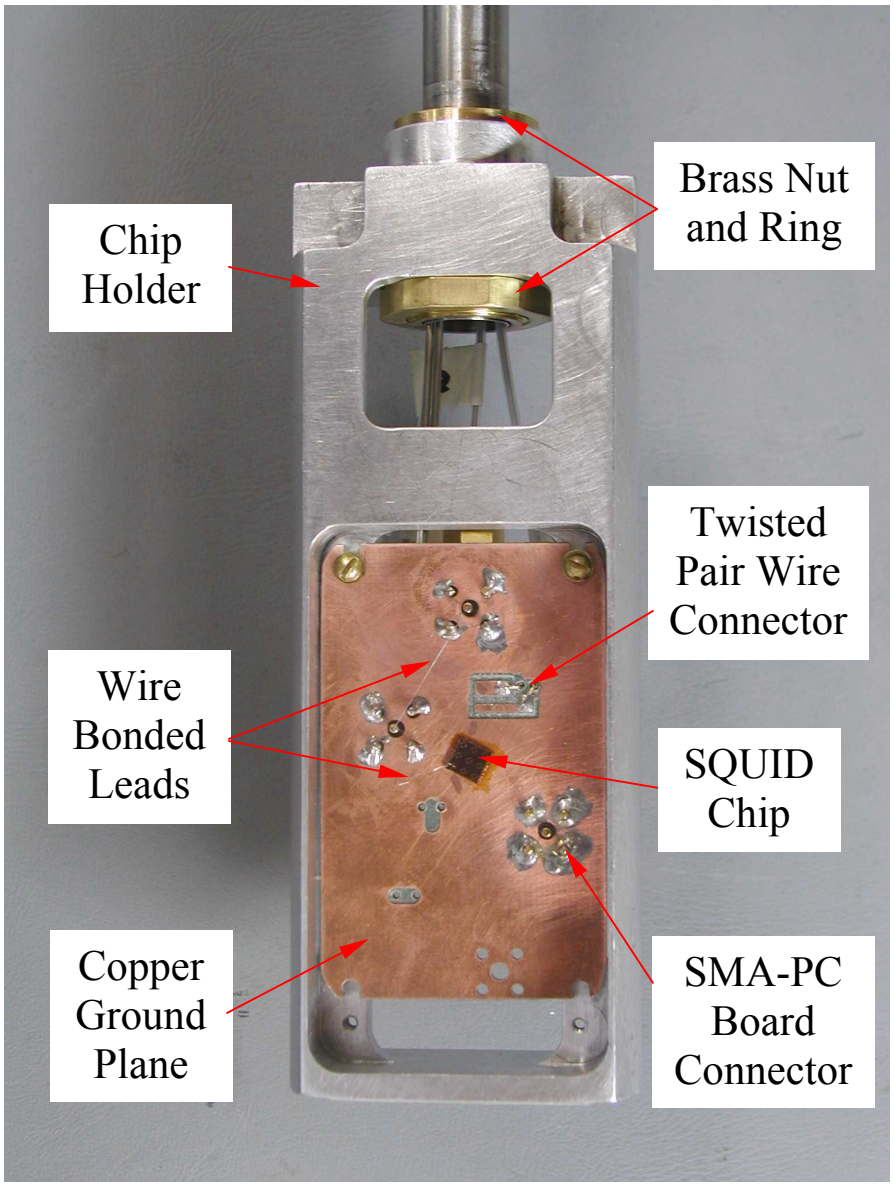

FIG. 7.3. Back side view of aluminium chip supporting holder in large bandwidth dip probe. Square shaped SQUID chip is seen attached to the PC board with photoresist. Wire bonded leads to and from connectors, the copper ground plane and SQUID chip are visible.

7.2.2 Final Design

The chip holder was constructed from a piece of aluminium and a piece of copper plated fiberglass board [see Figs. 7.2(c) and 7.3]. The coaxial cables were insulated from each other with Teflon tubing and shielded by housing them inside a 0.02 in thick stainless steel tube that also supported the chip holder. Thin stainless steel tubing was chosen to minimize thermal conductance. Thinner tubing was available but was not strong enough to withstand damage during ordinary handling. The 1.0 m length of the dip probe's stainless steel tube was determined by the depth of the CMSH-60 LHe dewar (with optional larger neck opening) into which the dip probe is inserted for cooling [155]. The depth of the chip holder inside the dewar was locked in place using a quick coupler attached to a ladish cap around the tube.

The aluminium chip holder and stainless steel tube were held together by hard soldering a brass screw ring to the end of the tube and then screwing the holder to the brass ring. I used 4% silver solder and a propane torch for soldering. Acid flux was needed to help the solder flow between the brass and stainless steel. A small brass nut was also made to help secure the holder to the ring. This design permitted the removal and exchange of holders attached to the end of the dip probe.

The circuit board inside the aluminium chip holder had copper plating on one side, which acted as a ground plane (see Fig. 7.3). I attached SMA-PC board connectors to the circuit board by soldering the ground leads to the ground plane [see Figs. 7.2(c) and 7.3]. Inside the holder, there was not enough space to house many SMA-PC board connectors. Space was limited because the entire holder had to fit

through the 2 in diameter neck of the LHe dewar, and I had to reserve some space inside the holder to facilitate the connection and disconnection of the coaxial cable to the SMA connectors. Fortunately, I only needed three coaxial cables for my experiments: one for the SQUID bias current pulses, another for the output voltage signals, and a third for high frequency signals to the one turn coil. The outer conductors of the coaxial cables were all connected to a common ground. Smaller twisted pair wiring was added for low frequency signals without taking up much additional space inside the holder.

A connector box was attached to the top of the dip probe by means of a brass flange that was hard soldered to the tube [see Fig. 7.2(b)]. The box was not hermetically sealed, so openings around the tube inside the box were covered with some plastic sealant to minimize moisture from going down the tubing. To minimize the possibility of reflections from mismatched impedances, the coaxial cable was kept in one continuous straight piece until it connected with adapters attached to the box.

To provide a controlled dc magnetic field, I prepared a small multiturn coil from copper magnet wire and attached it to the circuit board on the opposite side of the ground plane. Current to the multiturn coil was supplied by a Hewlett Packard 33120A function generator and sent down the probe to the coil through twisted pair wiring in the dip probe [156]. This coil was inadequate for producing high frequency magnetic fields due to the shielding from the ground plane, and I only used it occasionally for applying low frequency magnetic fields to the SQUID [157]. More often, I usually just rotated the dip probe in the ambient field to change the static magnetic flux through the SQUID.

To test a SQUID chip, I attached it to the circuit board using photoresist and then wire bonded gold leads directly between the SQUID chip and the circuit board SMA connectors. A ground connection was also made between the chip and the copper ground plane (see Fig. 7.3). The connections were stable, resilient to repeated thermal cycling, and did not show any noise or aging problems.

After wiring the SQUID chip and installing the circuit board inside the holder, I wrapped the holder with aluminium foil to provide some rf shielding. I also placed 50 Ω terminating resistors to the lines on the connector box at room temperature to protect the SQUID from possible damage due to electrostatic discharge. Finally, the dip probe is inserted into the CMSH-60 LHe dewar. Insertion of the dip probe was best performed slowly to allow the SQUID and dip probe to reach equilibrium with the temperature inside the dewar, thereby saving LHe and reducing thermal stress and breakage.

7.3 External Feedback Flux Control

As mentioned earlier, one of the three coaxial cables in the dip probe was connected to the one turn coil around the dc SQUID. For most of the experiments, the coil was used to apply microwave signals to the SQUID, while an "adjustable" quasi static flux was provided by rotating the dip probe in the ambient magnetic field. Rotations of the dip probe were mechanically stable enough to be performed by hand. On the other hand, if the LHe dewar was disturbed, the change in flux by rotating the dip probe would not be reversible. So, care was taken to not touch or move the dewar during experiments.

The probe and LHe dewar did not provide magnetic shielding, so the SQUID was tested in the Earth's magnetic field of about 5×10^{-5} T. For SQUID BH, which has outer dimensions of 30 μm × 30 μm with a 10 μm × 10 μm hole, the effective area is approximately the geometric mean of the outer area and the area of the hole, i.e. 30 μm × 10 μm [4,13,94]. The maximum possible flux change by rotating the dip probe should then be $\Delta\Phi \approx \pm1.5\times10^{-14}$ T·m^2 = $\pm7.3\Phi_o$, which is sufficient to generate multiple oscillations of the SQUID critical current, but not too much as to require overly fine control of the angle.

In practice, I observed between 3 and 4 full oscillations of the SQUID critical current when I rotated the SQUID by 90°, suggesting that the local field orientation was not perpendicular to the SQUID. Using this information, I can estimate the change in flux $\delta\Phi$ due to a rotation of the dip probe. The smallest rotation $\delta\theta$ of the dip probe I was able to perform was a fraction of a degree. For $\delta\theta \approx 0.5°$, one finds $0.03\Phi_o < \delta\Phi < 0.06\Phi_o$. As $\delta\Phi$ corresponded to the minimum step size of an adjustable pseudo static flux, $\delta\Phi$ also corresponded to the "one shot" flux resolution of a critical current detection scheme, described in section 6.3, for pulsed SQUID sampling.

7.4 SQUID and Pulse Signal Characterization

After cooling the SQUID, I proceeded by measuring its quasi static I-V characteristics. These measurements also revealed whether the SQUID was operating correctly, how much critical current modulation was occurring, what the mutual

inductance of the one turn coil was, and how much external magnetic flux there was through the SQUID.

Next, I configured the SQUID and dip probe for measurements with short bias current pulses. For this, I used the circuit shown in Fig. 7.4. The circuit is similar to the one I used for I-V measurements, except that 50 Ω terminators were added to all the coaxial lines at room temperature.

Current pulses were produced by a Stanford Research DG535 digital pulse generator which was connected in series with a 10 kΩ resistor [158]. The resistor, housed in an aluminium box separate from the dip probe, converted the voltage signal into a current signal, before feeding it to the dc SQUID through coaxial cable. The generator had a specified pulse rise time between 2 ns and 3 ns, limiting the minimum pulse length to around 4 ns. If the pulse length was set to shorter than 4 ns, the pulse height did not reach the generator set value and distortions occurred in its profile.

I measured the pulse profile from the generator by observing the output from the pulse generator across a 50 Ω terminator; this signal traveled about 2 m to the dip probe and back (see Fig. 7.4). A Tektronix 2465B oscilloscope with 400 MHz bandwidth was used to observe the signal [159].

Figure 7.5 shows the general profile of a 0.1 μs to 1 μs long pulse. The pulse shows some ringing, a positive peak at the front, a negative peak at the tail, and a rise time that is significantly longer than 3 ns. This profile changes if the measuring circuit changes. For example, with the addition of 50 Ω terminators, peaks disappear and the rise time decreases significantly. This suggests that the effective pulse height is affected by the circuit and can be significantly higher than the height set on the

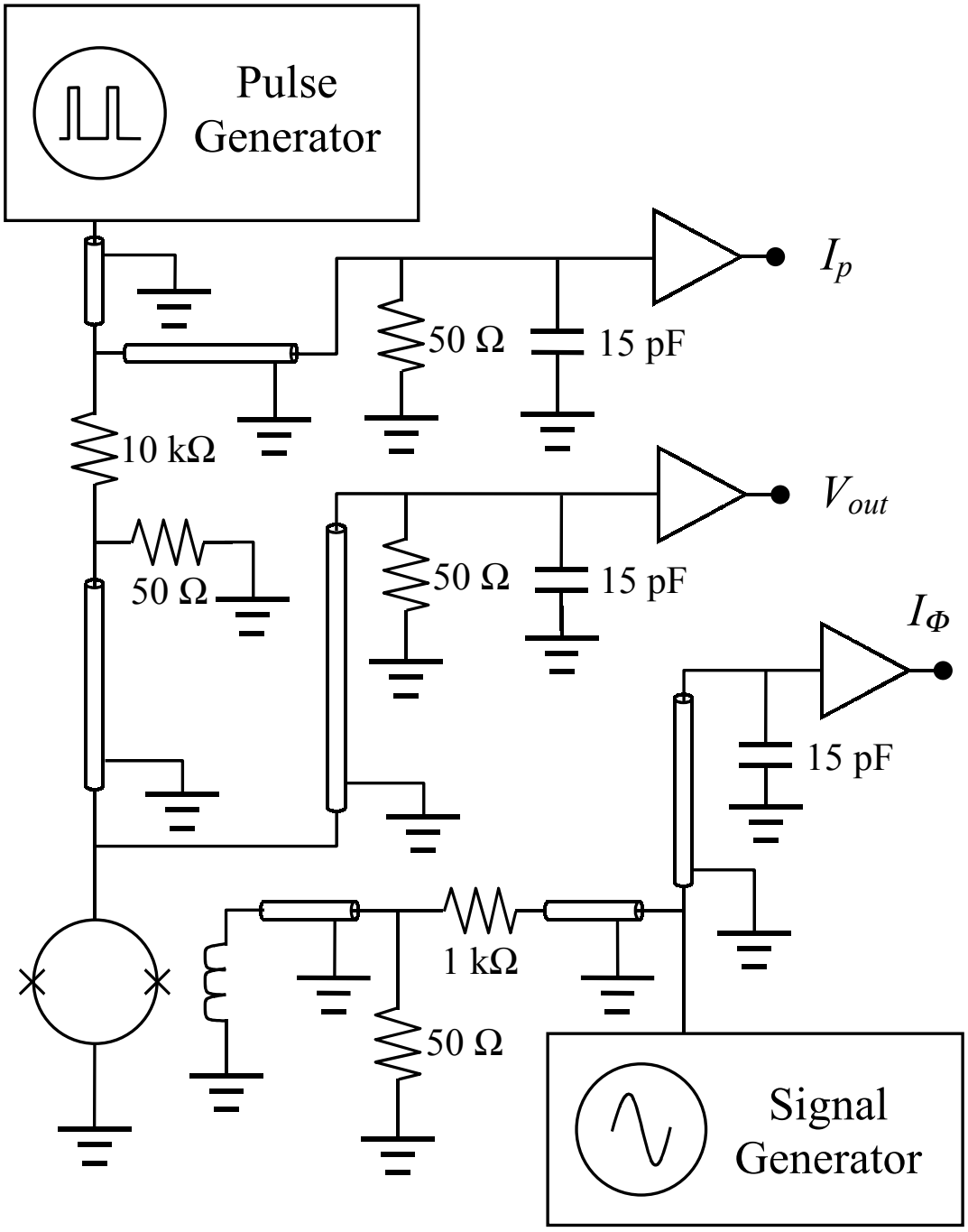

FIG. 7.4. Configuration of the experimental apparatus for testing pulsed SQUID sampling with a hysteretic dc SQUID. The dc SQUID at bottom left is electrically connected to the pulse generator and oscilloscope through a 50 Ω coaxial cable and a 10 kΩ current limiting resistor. The magnetic field generating coil is connected to a signal generator and oscilloscope through a 50 Ω coaxial cable and a 1 kΩ current limiting resistor. The 50 Ω terminators are used to minimize reflections.

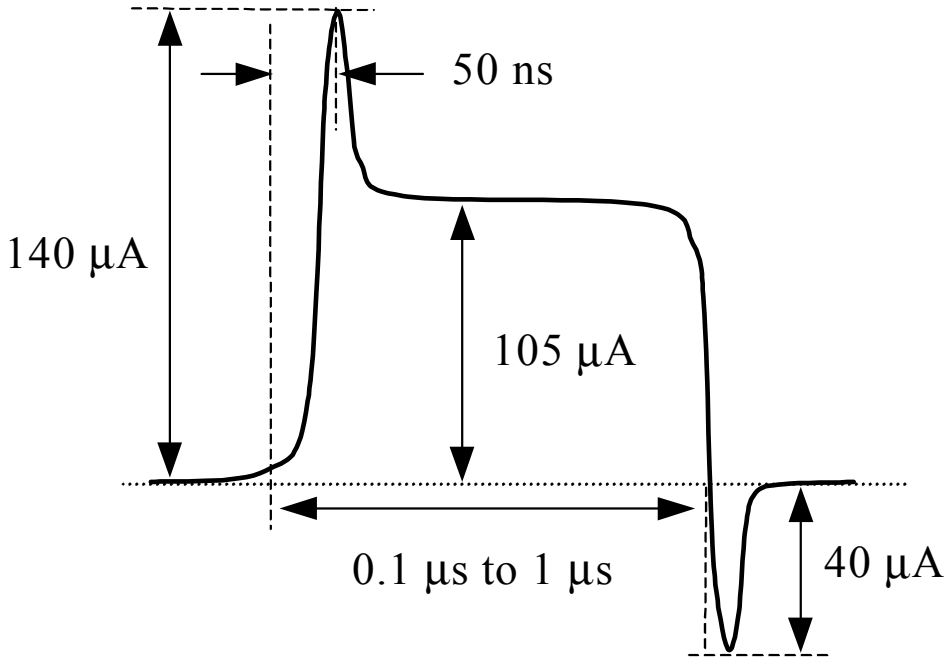

FIG. 7.5. Profile of 0.1 µs to 1 µs long, 100 µA high current pulses from a DG535 pulse generator measured through the large bandwidth dip probe. The middle section of the pulse is elongated depending on the length of the pulse.

pulse generator. Consequently, there could be discrepancies between the optimum pulse height that triggers the dc SQUID and the expected value determined from I-V characteristics. Furthermore, if triggering was caused by the brief peak in the pulse, this could produce a much shorter effective sampling time for the SQUID than the nominal pulse length would indicate. Moreover, due to the limited bandwidth of the oscilloscope, there could be additional structure in the pulse profile that is not discernible.

Figures 7.6 and 7.7 show the voltage response of a hysteretic dc SQUID to bias current pulses with different pulse lengths. The applied magnetic flux is set such that pulses always trigger the SQUID. The SQUID voltage response suggests that the effective pulse lengths are the same as the generator set values, despite a possible shorter sampling time due to a peak in the profile. This result could be understood based on retrapping. A narrow peak at the front of a current pulse may have caused the SQUID to trigger, but if the equilibrium pulse height stays above the retrapping current, a voltage signal will continue to be observed. On the other hand, other results that I present later suggest that the effective pulse length is decreased under certain circumstances.

The voltage responses show a rise time on the order of 5 ns. This is about the same as the rise time of the pulse generator, though it should be much shorter since it is based on the SQUID voltage rise time τ_{rise}. The bandwidth of the 2465B oscilloscope may be limiting the measurement. Additionally, a relatively flat pulse profile at maximum height is seen for pulses longer than 10 ns. As pulses shorten below 5 ns, the shape of the voltage response changes noticeably. In particular, the

(a)

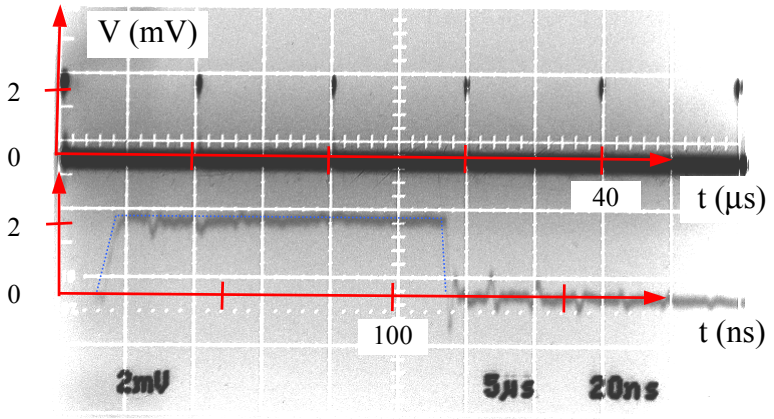

(b)

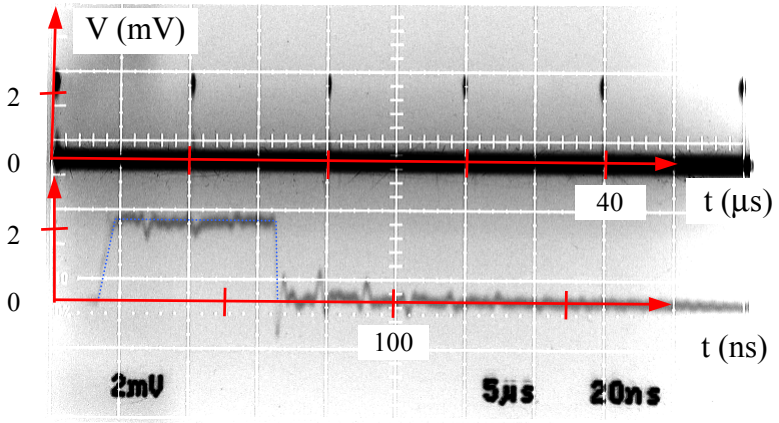

(c)

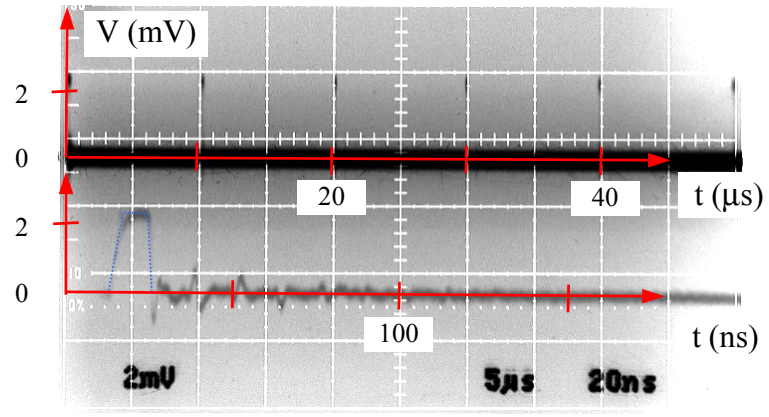

FIG. 7.6. Oscilloscope trace of the voltage response of a hysteretic dc SQUID circuit to bias current pulses. The applied magnetic flux and pulse height were set so that the SQUID triggered at every pulse. Upper curves show train of pulses 10 µs apart, and bottom curves show a single pulse with expanded time scale. Dotted curves trace out the main pulse. Traces show the responses to (a) 100 ns, (b) 50 ns, and (c) 10 ns pulses.

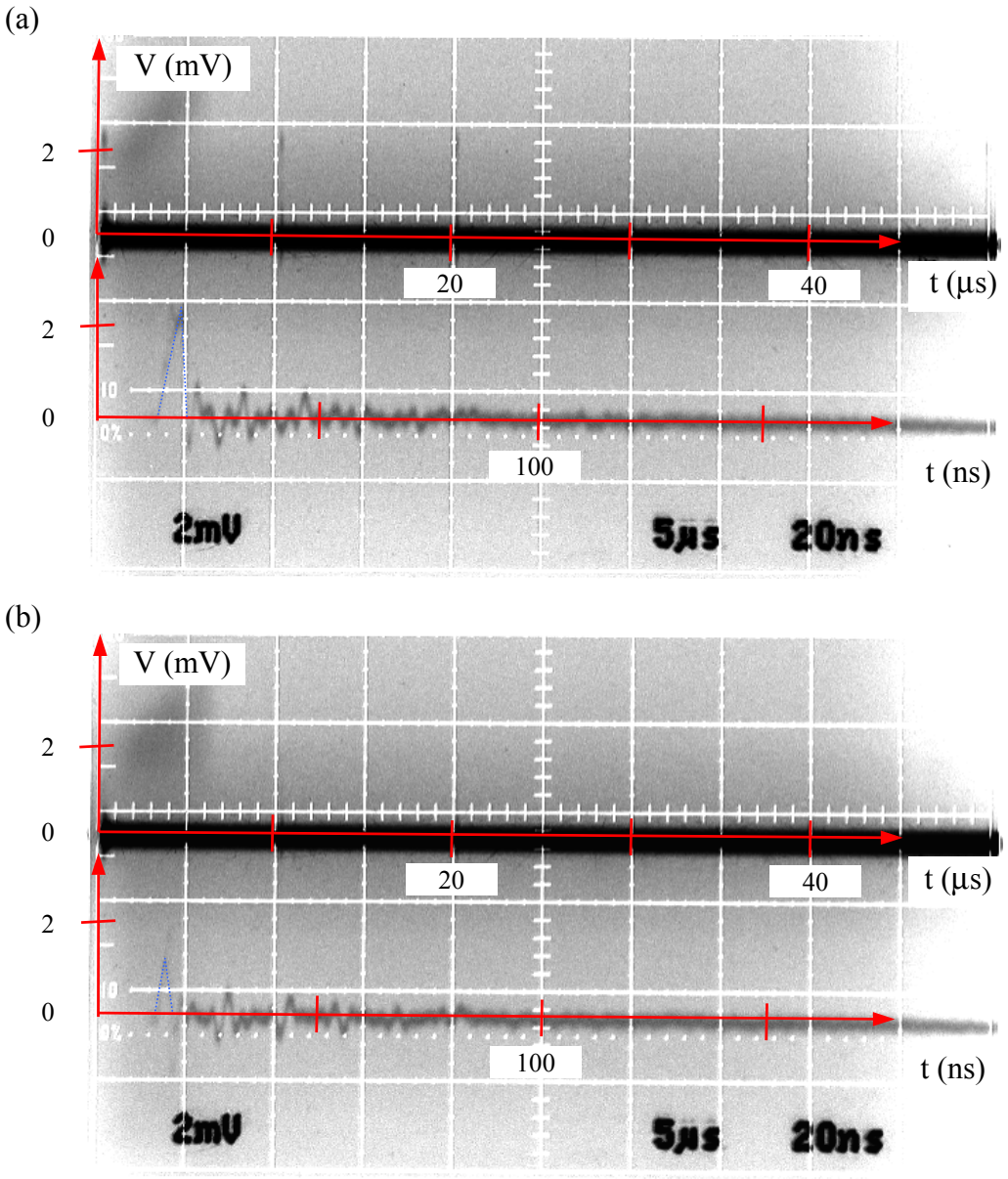

FIG. 7.7. Oscilloscope trace of the voltage response of a hysteretic dc SQUID circuit to bias current pulses shorter than 10 ns. To the best of my knowledge, the applied magnetic flux and pulse height were set so that the SQUID triggered at every pulse. Upper curves show train of pulses 10 μs apart, and bottom curves show a single pulse with expanded time scale. Dotted curves trace out the main pulse. Traces show the responses to (a) 5 ns and (b) 2.5 ns pulses. The 2.5 ns pulse response is barely visible.

pulse shape becomes more triangular and the height decreases significantly for lengths shorter than 4 ns. For example, Fig. 7.7(b) shows the SQUID voltage response to a current pulse that was set to 2.5 ns on the generator. In this case, a roughly triangular output voltage signal with a significantly decreased amplitude is barely noticeable. Voltage responses to pulses set shorter than 1 ns on the pulse generator were indistinguishable from noise.

Given that the voltage response signals are all due to triggering of the SQUID to the gap voltage $2\Delta/e$, the output pulse heights should be the same regardless of pulse length. This may naively seem to be in contradiction with the observed results for the 4 ns and shorter pulses. If, on the other hand, the 2.5 ns pulse is being filtered by the wiring, cutoff by the limited rise time, or rolled off by the oscilloscope's response, the voltage response may not be visible on the oscilloscope. In addition, there is also the possibility that the bias current pulse at the SQUID was not high enough to cause triggering, and some of the voltage response observed at the oscilloscope was due to direct pickup of the current pulse by the voltage leads.

7.5 Circuit Model of Dip Probe and dc SQUID

7.5.1 Transmission Line Model with SQUID as Voltage Source

In order to better understand the characteristics of the pulse signals, I analyzed a circuit model of the electrical setup [see Fig. 7.8(a)]. In the model, the dip probe and connecting coaxial cable are represented as one continuous transmission line. I have also included parasitic inductance between the coaxial cables and the dc SQUID; the approximately 1 cm long wire bonded leads to the SQUID have

(a)

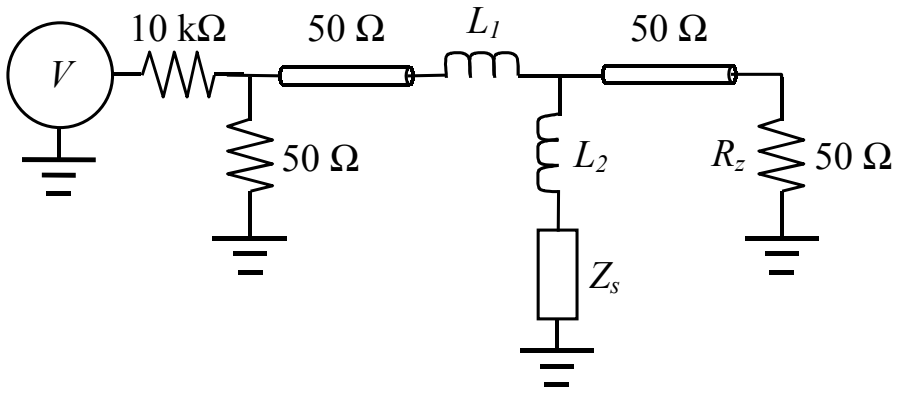

(b)

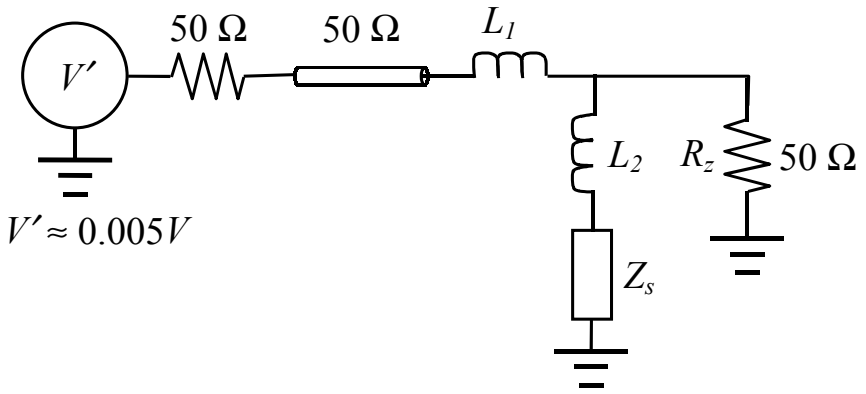

(c)

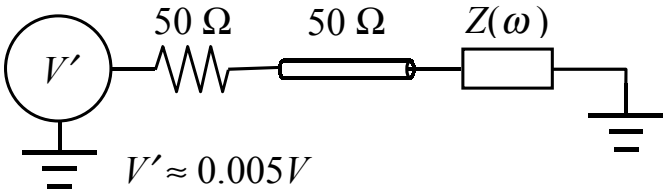

(d)

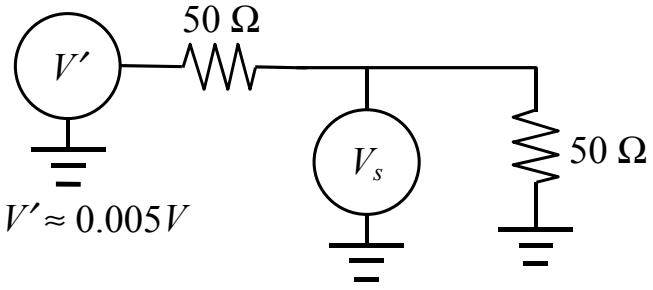

FIG. 7.8. (a) Circuit model of hysteretic dc SQUID and large bandwidth dip probe. (b) Simplified circuit of (a) using Thévenin equivalent voltage source and input impedance. Output signal coaxial cable is reduced to matched load R_z. (c) Circuit (b) with equivalent output impedance $Z(\omega)$ seen by the coaxial cable. (d) Equivalent dc circuit of (b) with SQUID modeled as a voltage source V_s.

inductance, and the high frequency Fourier components in the pulse signals make the impedance of the leads significant.

For a 1 cm lead, the inductance is $L \sim \mu_o l \approx 13$ nH using dimensional analysis. Another order of magnitude estimation comes from the expression for the impedance of a transmission line,

$$Z_c = \sqrt{\frac{L}{C}} \tag{7.1}$$

where Z_c and C are, for example, those of a coaxial cable with inner conductor dimensions similar to the wire bonded leads [160]. Using values for UT-34-SS cable, $L = 2.38\times10^{-7}$ H/m, so for a 1 cm lead at 1 GHz, the impedance $Z_l = 14.9$ Ω. These values are very rough but much more significant than the contact resistance of the leads, which can now be safely ignored for high frequencies.

The coaxial cable in Fig. 7.8(a) was assumed lossless with a uniform impedance of 50 Ω. Despite terminators, there were still some reflections due to impedance mismatch in the real circuit. Thus, I expect some discrepancies between the experimentally observed output and the results from the circuit model. The largest impedance mismatch is between the coaxial cable and the SQUID chip. Since the dc SQUID can go from a virtual short to a high impedance, this is unavoidable. Clearly, better impedance matching could further increase the bandwidth.

To model the dc SQUID, I treated it as a short when in the zero voltage state and as a voltage source when in the resistive state. The voltage source approximation can be used because when the SQUID is in the resistive state, its voltage is almost constant at the gap voltage $2\Delta/e$ (see Figs. 2.10, 3.9, and 3.10). This holds as long as

the bias current stays above the retrapping current but below the region of Ohmic behavior.

7.5.2 Frequency Domain Analysis of Circuit and Current Pulse

To analyze the circuit of Fig. 7.8(a) with the SQUID in the zero voltage state, I first reduce it to its Thévenin equivalent circuit in the frequency domain [161,162]. Near the pulse generator, the 50 Ω terminator connected to the 10 kΩ resistor results in a generator with a reduced output voltage $V' \approx 0.005V$ and an output impedance of about 50 Ω. The result is an output impedance that is practically matched at the generator end. Near the oscilloscope, the line is terminated with a matching 50 Ω resistor R_z, which results in no reflection and the line looking like a 50 Ω resistor [see Fig. 7.8(b)].

This result can then be used to simplify the load impedance presented to the cold end of the coaxial cable that delivers the current pulse. Treating the dc SQUID as a short, the load impedance Z is given by

$$Z = j\omega L_1 + \frac{j\omega L_2 Z_c}{Z_c + j\omega L_2} \tag{7.2}$$

where Z_c = 50 Ω is the cable impedance [see Fig. 7.8(c)]. The impedance Z' seen from the generator end is given by

$$Z' = Z_c \frac{Z + jZ_c \tan\theta}{Z_c + jZ \tan\theta} = Z_c \frac{Z + jZ_c \tan \omega l Z_c C}{Z_c + jZ \tan \omega l Z_c C} \tag{7.3}$$

where C is the capacitance per unit length of the coaxial cable, and l is the total length of the cable that delivers the current pulse to the SQUID [163].

The transmitted voltage V_t across Z is given by

$$V_t = TV^+ = (1+\Gamma)V^+ = \frac{2Z}{Z+Z_c}V^+ \tag{7.4}$$

where the incident voltage V^+ is given by

$$V^+ = \frac{Z'(Z+Z_c)}{2(Z'+Z_c)(Z\cos\theta + jZ_c\sin\theta)}V'. \tag{7.5}$$

So,

$$V_t = \frac{ZZ'}{(Z'+Z_c)(Z\cos\theta + jZ_c\sin\theta)}V' = \frac{Ze^{-j\theta}}{Z+Z_c}V'. \tag{7.6}$$

Now, the output voltage V_{out} on the oscilloscope is the voltage across the 50 Ω resistor R_z given by

$$\begin{aligned} V_{out} &= \left(1-\frac{j\omega L_1}{Z}\right)V_t = \left(\frac{Z-j\omega L_1}{Z}\right)\left(\frac{Ze^{-j\theta}}{Z+Z_c}\right)V' = \frac{Z-j\omega L_1}{Z+Z_c}e^{-j\theta}V' \\ &= \left(\frac{j\omega L_2 Z_c}{Z_c+j\omega L_2}\right)\left\{\frac{Z_c+j\omega L_2}{(Z_c+j\omega L_1)(Z_c+j\omega L_2)+j\omega L_2 Z_c}\right\}e^{-j\theta}V' \\ &= \frac{\omega L_2 Z_c}{\omega(L_1+2L_2)Z_c + j\left(\omega^2 L_1 L_2 - Z_c^{\,2}\right)}e^{-j\theta}V' \end{aligned} \tag{7.7}$$

Using the approximation $L = L_1 \approx L_2$,

$$V_{out} \approx \frac{\omega L Z_c}{3\omega L Z_c + j\left(\omega^2 L^2 - Z_c^{\,2}\right)}e^{-j\theta}V' = \frac{e^{-j\theta}V'}{3+j\left(\frac{\omega L}{Z_c}-\frac{Z_c}{\omega L}\right)}. \tag{7.8}$$

The magnitude and phase ϕ of V_{out} are given by

$$\begin{cases} |V_{out}| = V'\left\{9+\left(\frac{\omega L}{Z_c}-\frac{Z_c}{\omega L}\right)^2\right\}^{-\frac{1}{2}} = V'\left\{7+\left(\frac{\omega L}{Z_c}\right)^2+\left(\frac{Z_c}{\omega L}\right)^2\right\}^{-\frac{1}{2}} \\ \phi = Arg\,(V_{out}) = -\omega l Z_c C - \tan^{-1}\frac{1}{3}\left(\frac{\omega L}{Z_c}-\frac{Z_c}{\omega L}\right) \end{cases}. \tag{7.9}$$

This frequency dependent output can be applied to the Fourier components of an input voltage signal. In other words, the output response to a square input pulse is obtained by first calculating the Fourier components of an input pulse using the Fourier transform, then applying the components to Eq. (7.8), and finally recombining the results in a sum. The Fourier integral can be written as

$$V(\omega) = \frac{1}{2\pi} \int_{-\infty}^{\infty} V(t) e^{j\omega t} dt \tag{7.10}$$

where $V(t)$ is the input signal [164]. For a square pulse with a pulse length of τ and pulse height V_{in} centered around $t = 0$, $V(t)$ is given by

$$V(t) = \begin{cases} V_{in} & \text{for } -\frac{\tau}{2} \le t \le \frac{\tau}{2} \\ 0 & \text{otherwise} \end{cases}. \tag{7.11}$$

Thus,

$$V(\omega) = \frac{1}{2\pi} \int_{-\frac{\tau}{2}}^{\frac{\tau}{2}} V_{in} e^{j\omega t} dt = \frac{V_{in}}{2\pi} \frac{e^{j\frac{\omega\tau}{2}} - e^{-j\frac{\omega\tau}{2}}}{j\omega} = \frac{V_{in}}{\pi\omega} \sin\frac{\omega\tau}{2}. \tag{7.12}$$

To calculate the voltage response V_{out} using $V(\omega)$, I make a discrete approximation of $V(\omega)$, as in a Fourier series [165]. The even symmetry in $V(\omega)$ allows the discrete Fourier components to be written as

$$V_{\omega}(t) = V(\omega) e^{j\omega t} + V(-\omega) e^{-j\omega t} = 2V(\omega) \cos\omega t = \frac{2V_{in}}{\pi\omega} \sin\frac{\omega\tau}{2} \cos\omega t. \tag{7.13}$$

Combining Eq. (7.13) in complex number form with Eq. (7.8), the output signal Fourier components can be expressed as

$$V_{out} = \frac{0.005\, e^{-j\theta}}{3 + j\left(\frac{\omega L}{Z_c} - \frac{Z_c}{\omega L}\right)} \frac{2V_{in}}{\pi\omega} \sin\frac{\omega\tau}{2} e^{j\omega t}$$
$$= \frac{0.01V_{in}}{\pi\omega} \frac{\sin\frac{\omega\tau}{2}}{3 + j\left(\frac{\omega L}{Z_c} - \frac{Z_c}{\omega L}\right)} e^{j\omega(t - lZ_cC)} . \quad (7.14)$$

Recognizing that $t' = t - lZ_cC$ is just the delay in time of the output voltage signal with respect to the input signal, I sum the results $V_{out}(t')$ of Eq. (7.14) at different frequencies to determine the total output voltage signal. The sum is given by

$$\sum V_{out}(t') = \frac{2\pi}{T} \sum_n^N \frac{0.01V_{in}}{\pi\omega} \frac{\sin\frac{\omega\tau}{2}}{\sqrt{7 + \left(\frac{\omega L}{Z_c}\right)^2 + \left(\frac{Z_c}{\omega L}\right)^2}} \cos(\omega t' - \phi_\omega) \quad (7.15)$$

where $T = 2\pi N/\omega_{max}$, $\omega = \omega_{max} n/N$, ω_{max} is the maximum angular frequency in the sum, N is the number of components summed, and ϕ_ω is the frequency dependent phase shift given by

$$\phi_\omega = \tan^{-1}\frac{1}{3}\left(\frac{\omega L}{Z_c} - \frac{Z_c}{\omega L}\right). \quad (7.16)$$

Simplifying Eq. (7.15), I find

$$\sum V_{out}(t') = \frac{0.01V_{in}}{\pi} \sum_n^N \frac{\sin\frac{n\omega_{max}\tau}{2N} \cos\left(\frac{n\omega_{max}}{N} t' - \phi_\omega\right)}{\sqrt{\left(\frac{\omega_{max} L}{NZ_c}\right)^2 n^4 + 7n^2 + \left(\frac{NZ_c}{\omega_{max} L}\right)^2}} \quad (7.17)$$

where $-T/2 < t' < T/2$ due to the discrete bandwidth limited approximation of the Fourier transform. However, the time range of interest is $-\tau < t' < \tau$ which is when the input voltage signal reaches the SQUID.

The bandwidth of the input pulse Fourier spectrum was chosen by plotting the magnitude of Eq. (7.14) with respect to frequency and then determining which frequencies produce the largest signal magnitudes and consequently the majority of the output response [see Fig. 7.9(a)]. Figure 7.9(a) shows that the output response is concentrated between 1 MHz and 1 GHz for $\tau = 5$ ns and $L = 11.9$ nH. Taking into consideration the number of Fourier components to sum and the need for high frequency detail, I chose 200 discrete components between 10 MHz to 2 GHz in intervals of 10 MHz for the analysis of Eq. (7.17).

Regarding the dc component of V_{out}, the circuit of Fig. 7.8(b) reduces to that of Fig. 7.8(d) where the SQUID voltage V_s is given by

$$V_s = \begin{cases} \dfrac{2\Delta}{e} & \text{when SQUID is in resistive state with positive current} \\ 0 & \text{when SQUID is in zero voltage state} \\ -\dfrac{2\Delta}{e} & \text{when SQUID is in resistive state with negative current} \end{cases} . \quad (7.18)$$

From Eq. (7.18) and Fig. 7.8(d), it can be deduced that while the SQUID is in the zero voltage state, the dc component of $V_{out} = 0$. So, the dc component does not contribute any signal when the SQUID does not trigger.

7.5.3 Simulated Zero Voltage and Resistive State Responses

Figure 7.9(b) shows the output voltage for $t' = -6$ ns to 6 ns when the SQUID does not trigger for different values of L/L_o where $L_o = 2.38$ nH with $\tau = 5$ ns. Voltages are plotted at 0.5 ns intervals and show a positive peak at the onset of the pulse and a negative peak at its tail. Variations in L/L_o from 1 to 9 show changes in

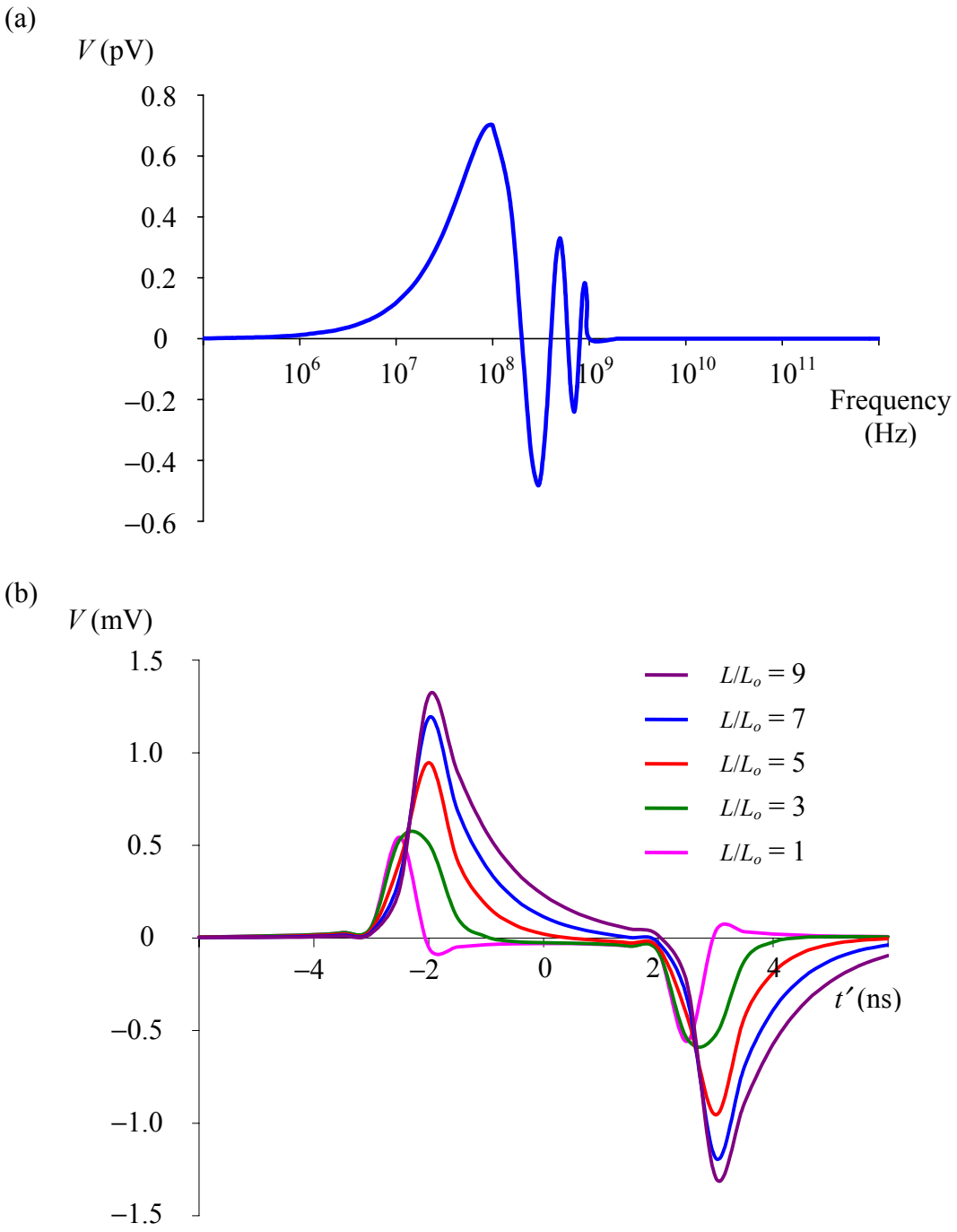

FIG. 7.9. (a) Plot of calculated spectrum of the output voltage response of the SQUID circuit using the large bandwidth dip probe. The input voltage is a 1 V, 5 ns square pulse. The inductors in the SQUID circuit are $L_1 = L_2 = L = 11.9$ nH. (b) Plots of the output voltage response of the SQUID circuit with different parasitic inductance L. The input voltage is a 1 V, 5 ns square pulse. $L_o = 2.38$ nH. Results are shown for the dc SQUID remaining in the zero voltage state. The voltage response appears after a delay Δt with respect to the input pulse centered around $t = 0$, where $t' = t - \Delta t$.

the pulse shape as well as an increase in the peaks. Increases in the pulse length τ only separate the time between the peaks. The peaks are just a back emf reaction of the inductors L_1 and L_2 to the current pulse.

To model the output voltage response for the case when the SQUID triggers into the resistive state, I replace the SQUID with a voltage source and include the dc component of V_{out} in Eq. (7.15). To accomplish this, the dc component in the frequency domain must be properly calculated from Eq. (7.12):

$$V(\omega = 0) = \lim_{\omega \to 0} \frac{V_{in}}{\pi\omega} \sin\frac{\omega\tau}{2} = \frac{V_{in}}{\pi\omega} \cdot \frac{\omega\tau}{2} = \frac{\tau}{2\pi} V_{in} . \tag{7.19}$$

This component is added to the summation inside Eq. (7.15) with the multiplication factor of about 0.005 to compensate for the reduced output voltage due to the 50 Ω terminator near the pulse generator. The current through the SQUID due to this dc voltage is added to the SQUID current resulting from the ac components. The latter current is

$$\begin{aligned} \sum I_s(t') &= \frac{2\pi}{T} \sum_n^N \frac{0.01 V_{in}}{\pi\omega^2 L} \frac{\sin\frac{\omega\tau}{2}}{\sqrt{7 + \left(\frac{\omega L}{Z_c}\right)^2 + \left(\frac{Z_c}{\omega L}\right)^2}} \sin(\omega t' - \phi_\omega) \\ &= \frac{0.01 V_{in}}{\pi L} \sum_n^N \frac{\frac{N}{n\omega_{max}} \sin\frac{n\omega_{max}\tau}{2N} \sin\left(\frac{n\omega_{max}}{N} t' - \phi_\omega\right)}{\sqrt{\left(\frac{\omega_{max} L}{N Z_c}\right)^2 n^4 + 7n^2 + \left(\frac{N Z_c}{\omega_{max} L}\right)^2}} \end{aligned} . \tag{7.20}$$

The current due to the dc component is given by

$$I_s = \frac{V'(\omega = 0) - 2V_s}{Z_c} = \frac{\frac{2\pi}{T} 0.005 \frac{\tau}{2\pi} V_{in} - 2V_s}{Z_c} = \frac{0.005 \frac{\tau}{T} V_{in} - 2V_s}{Z_c} . \tag{7.21}$$

Whether the SQUID triggers into the resistive state is determined by comparing the current through the SQUID with $V_s = 0$ to the SQUID critical current I_c. If the bias current is larger, then the SQUID triggers into the resistive state and the gap voltage $V_s = 2\Delta/e = 2.7$ mV appears. This gap voltage is maintained as long as the SQUID bias current stays above the retrapping current I_r. In turn, the output voltage response of the circuit is modified by the addition of the SQUID voltage V_s to ΣV_{out} of Eq. (7.15) and (7.17).

Once the SQUID triggers into the resistive state, the dc current through the SQUID changes according to Eq. (7.21). The new bias current and SQUID voltage state need to be self consistent. Triggering and the appearance of $V_s \neq 0$ are simulated conditionally in the analysis of the SQUID circuit. This is performed by first calculating the output voltage response and the SQUID bias current for both cases, i.e. when the SQUID is in the zero voltage state and when it is in the resistive state, at each time step in the simulation. Then, with the SQUID initially in the zero voltage state, I compare the SQUID bias current with the critical current and retrapping current I_r at each subsequent time step to determine which state the SQUID is in, taking into account which state the SQUID was during the previous time step.

Figure 7.10(a) shows the calculated output voltage responses to a 1.7 V, 5 ns pulse from the generator with $L = 11.9$ nH. The different curves show what happens when the SQUID critical current varies from 120 μA to 170 μA, which is the range of currents for which SQUID BH was observed to trigger (see Fig. 3.9 or Table I). For comparison, Fig. 7.10(b) shows the 1.7 V, 5 ns input voltage pulse used.

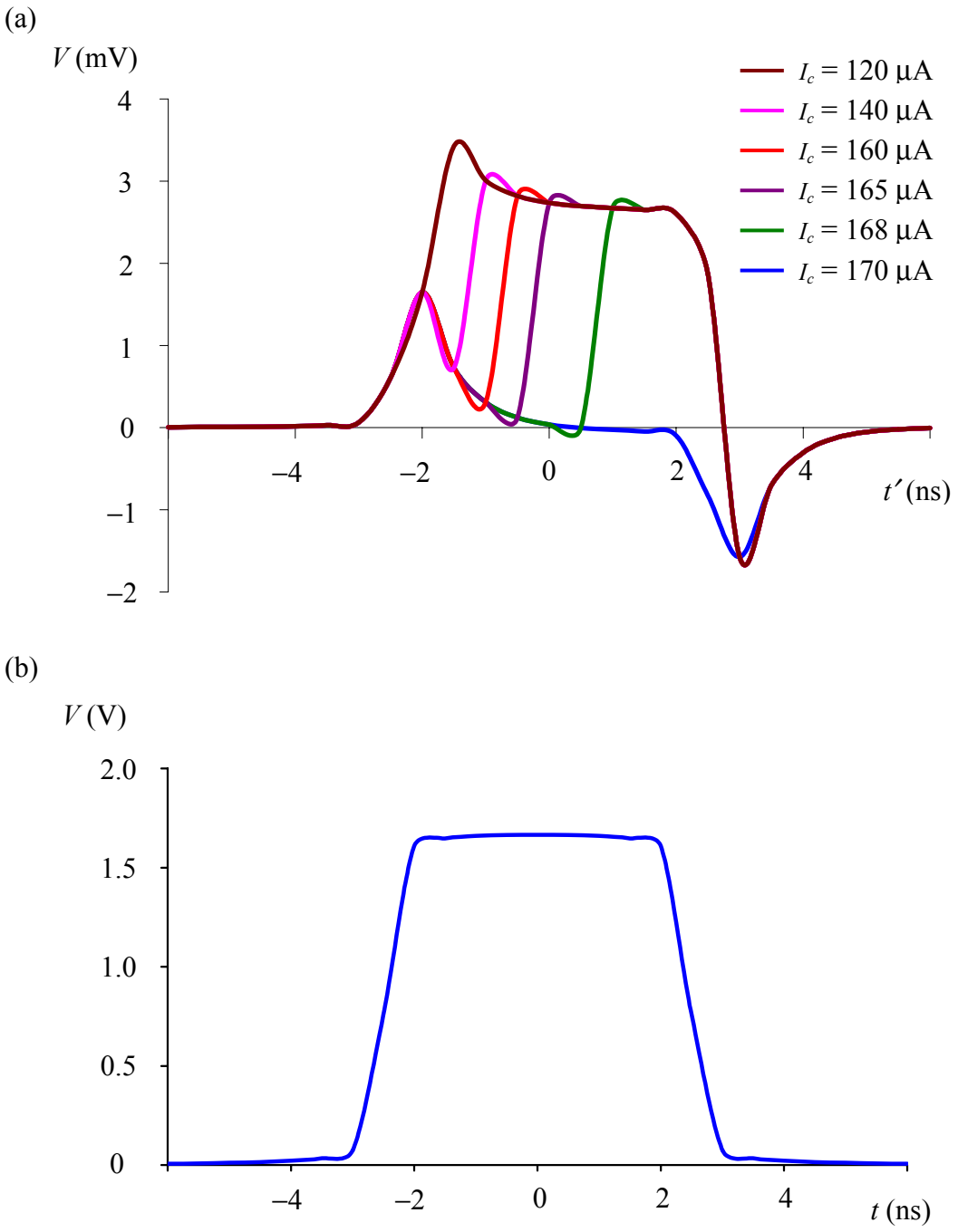

FIG. 7.10. (a) Plots of the calculated output voltage responses of the SQUID circuit using the large bandwidth dip probe for different SQUID critical currents. The dc SQUID is modeled as a bias current dependent voltage source. The inductors in the SQUID circuit are $L_1 = L_2 = L = 11.9$ nH. (b) Plot of the 1.7 V, 5 ns input voltage pulse to the SQUID circuit that generated the voltage responses calculated in (a). The voltage response appears after a delay Δt with respect to the input pulse centered around $t = 0$, where $t' = t - \Delta t$.

The calculated voltage response shows that after a delay time of $lZ_cC \sim 10$ ns, the onset of triggering occurs earlier and earlier as the critical current decreases below $I_c = 170$ μA. In particular, for $I_c = 170$ μA, the SQUID does not trigger and the response is just that found previously when the SQUID was modeled as a short. The plots also show that the onset of triggering is very sensitive to the critical current near $I_c = 170$ μA but becomes less sensitive as I_c approaches 120 μA.

I also found that in order to observe triggering behavior for critical currents between $I_c = 120$ μA and 170 μA, the pulse amplitude has to be between 1.2 V and 1.7 V, which averages to 1.45 V. I note that from Fig. 7.5, the peak of the observed input current pulse corresponds to about 140 μA for a pulse set at 100 μA. This suggests that if a pulse structure similar to that of Fig. 7.5 continues to persist for pulses as short as 5 ns, the optimal input voltage pulse height setting should be around 1.04 V instead of 1.45 V.

A significant assumption made in my model is that the SQUID voltage and current change instantaneously to the new settings at the onset of triggering. Considering the short voltage rise time across the SQUID, the approximation can be justified for the voltage. However, the sudden change in bias current could be in question. As long as the change in bias current is small, the assumption could still be justified. Yet, this condition is not assured and is the main flaw in the model.

In section 7.7, I will compare the results of this model directly to the measured response. Other models of the dc SQUID were also investigated. See for example Appendix E.

7.6 Setting Short Bias Current Pulses

After installing SQUID BH in the large bandwidth dip probe and performing an I-V measurement, I investigated what the optimal input pulse height was for pulsed SQUID sampling with the given circuit. I proceeded to do this by first finding the lowest bias current pulse that would still trigger the SQUID and then the highest pulse that would sometimes not. I found the lower limit by sending current pulses to the SQUID while rotating the dip probe in the ambient magnetic field, which changed the critical current of the SQUID. If no voltage signal was observed during the rotation, this meant that the current pulse height was less than the minimum SQUID critical current and would not trigger the SQUID into the resistive state. I then increased the pulse height and again checked for any voltage response as the dip probe was rotated. The lowest current pulse height I_p^{min} when a voltage signal began to appear while rotating the dip probe identified the lower limit. Similarly, I found the maximum pulse height I_p^{max} by identifying the minimum pulse height for which the current pulses always triggered the SQUID despite rotating the dip probe.

The optimal pulse height I_p^* corresponds to the SQUID critical current which produces the largest sensitivity in critical current per change in flux. For example, on the critical current versus flux curve in Fig. 2.4(b), it corresponds to the points with the steepest slope on the curve. Assuming a smooth transition of the critical current from I_p^{min} to I_p^{max}, the average between I_p^{min} and I_p^{max} should be near the optimal value, i.e. $I_p^* \approx (I_p^{min} + I_p^{max})/2$.

For SQUID BH, I_p^{min} = 62 μA, I_p^{max} = 122 μA, and thus I_p^* = 92 μA. These current values were determined from $I_p = V_{in}/R_g$ where V_{in} is the voltage setting of the

pulse generator and R_g = 10 kΩ. In contrast, from I-V curve measurements, the critical current for SQUID BH ranged between 123 μA and 172 μA. Thus, the actual critical current minimum and maximum were larger than I_p^{min} and I_p^{max} by 55±5 μA or 40±10%. The likely explanation is that the effective current pulse height at the SQUID is higher than the pseudo-dc level inferred from the generator setting. This is consistent with my observations of the signal pulse height, discussed earlier. In any case, for flux sensing measurements using SQUID BH, I set pulses to the average pulse height I_p^* = 92 μA by setting 0.92 V at the pulse generator.

I also note that if the pulse profile has peaks similar to those shown in Fig. 7.5, the average pulse height would be around 1.04 V rather than around 1.45 V. The experimentally obtained result of 0.92 V is closer to the 1.04 V prediction expected if ringing is present. This also suggests that there will be fine structure peaks in the pulse profile that are shorter than the pulse length itself. Thus, if there are peaks, they should have durations on the order of 1 ns or less, which would not be resolved by the 400 MHz Tektronix 2465B oscilloscope.

7.7 Detection of Microwave Frequency Magnetic Fields using Pulsed SQUIDs

7.7.1 SQUID Response to Low Frequency Signals

Finally, to test the pulsed SQUID sampling technique, I applied a time varying magnetic field on the hysteretic dc SQUID while continually pulsing its bias current. If a current pulse did not result in a voltage across the SQUID, this indicated that the modulated critical current was higher than the current pulse height I_p^*. By

augmenting the magnetic field, the critical current will eventually drop below I_p^* and trigger a voltage signal across the dc SQUID.

I began tests by applying a low frequency triangular wave field. The signals were produced by a Hewlett Packard 33120A function generator in series with a 1 kΩ current limiting resistor which sent current down the dip probe to the one turn coil on the SQUID chip [156]. I chose a triangular wave as it generates piecewise linear variations in magnetic flux. The frequency of the waves was 1 kHz to 10 kHz. For the current pulses, I set the DG535 pulse generator to apply 92 μA, 100 ns bias current pulses with a pulse repetition rate between 100 kHz and 1 MHz [158].

Figure 7.11 shows the SQUID response to a 1 kHz triangular wave magnetic field. The top part of the oscilloscope picture shows the voltage response from the SQUID circuit. The bottom part represents the magnetic field produced by the one turn coil. Each period of the magnetic field produces a clustered region of triggering events in the SQUID output. This is consistent with the ambient magnetic field producing an offset in the applied magnetic field. The correlation between the magnetic flux signal and the voltage response signal indicates that the SQUID is triggering on the applied flux.

Figures 7.12 and 7.13 show the SQUID response to a 10 kHz triangular wave magnetic field with increasing magnitude. One expects that as the wave magnitude increases from zero, a voltage response from SQUID triggering would emerge with the same periodicity as the wave. Then with further increases in amplitude, the clustered triggering regions in the oscilloscope picture should expand linearly as more pulses per wave period trigger the SQUID. In addition, individual triggering

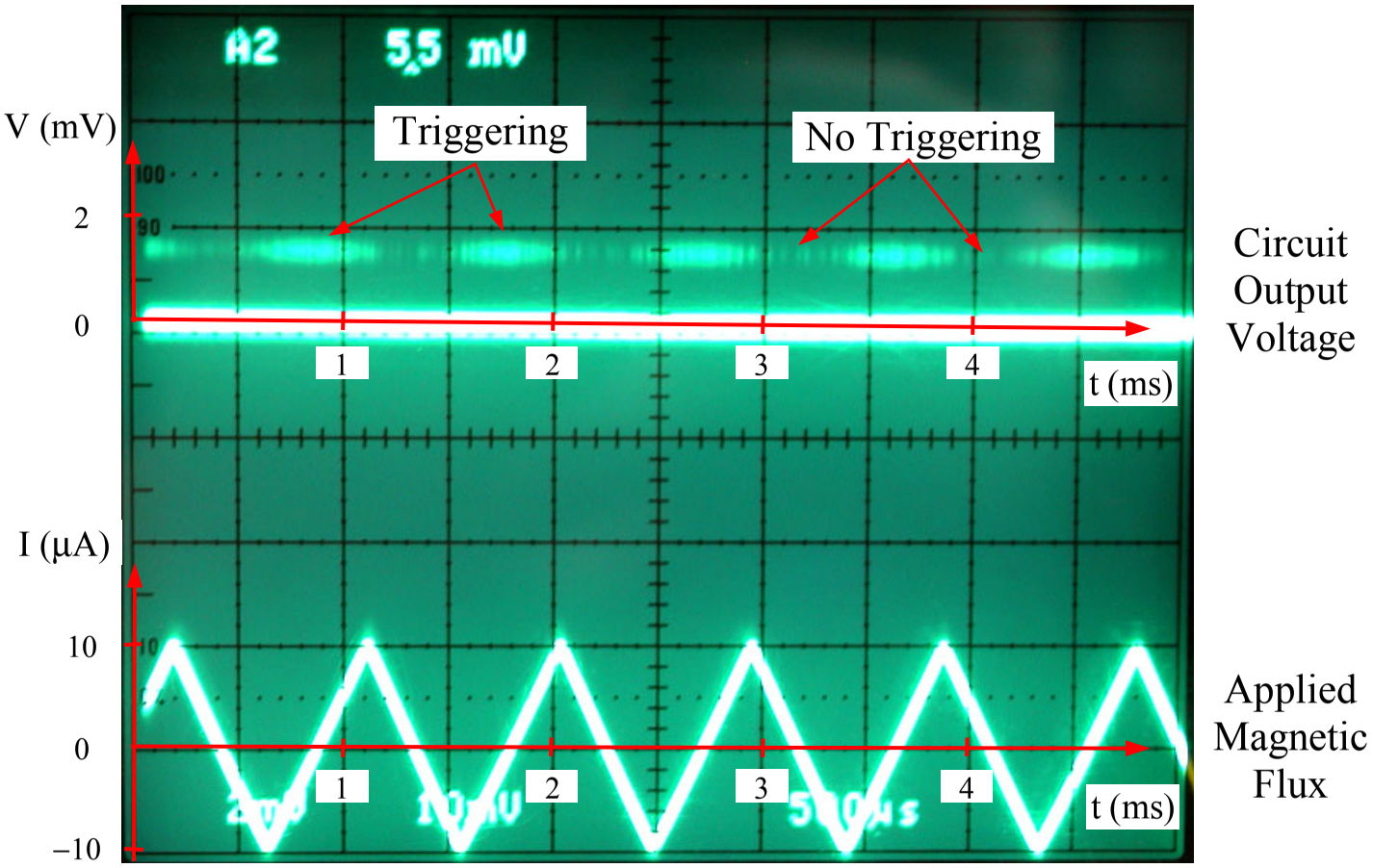

FIG. 7.11. Voltage response of a hysteretic dc SQUID to pulsed bias current and triangular wave flux signal. Current pulses were 100 ns long with a 100 kHz pulse repetition rate. A triangular wave current signal with an amplitude of 10 μA and an approximate frequency of 1 kHz was sent through an external coil to produce the applied magnetic flux. Clustered regions where the SQUID is triggering in step with the flux wave are visible.

(a)

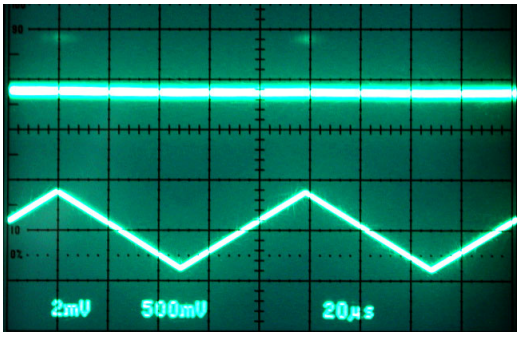

(b)

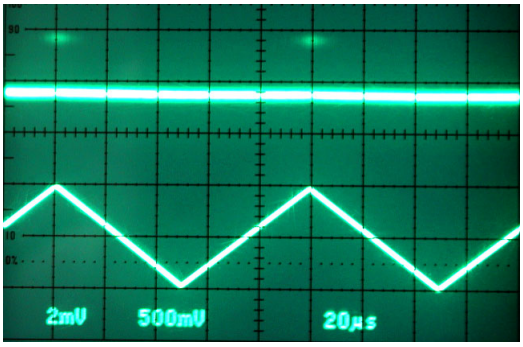

(c)

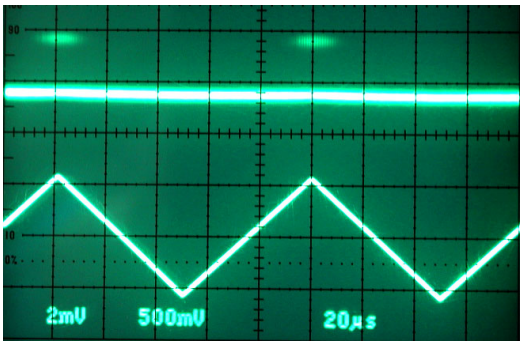

(d)

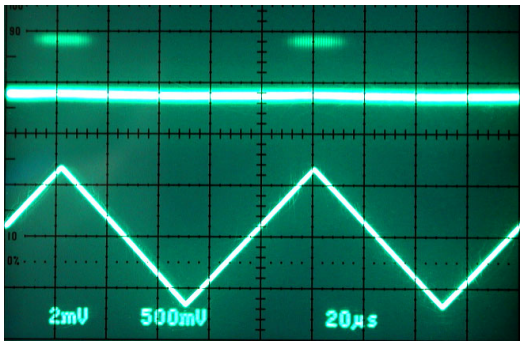

FIG. 7.12. Voltage response of SQUID BH to modulating flux with increasing amplitude. The 92 µA input current pulses were 100 ns long and had a pulse repetition rate of 1 MHz. The applied 10 kHz triangular wave magnetic field was produced by sending current through the one turn coil with amplitudes of (a) 400µA, (b) 500µA, (c) 600µA, and (d) 700µA.

(a)

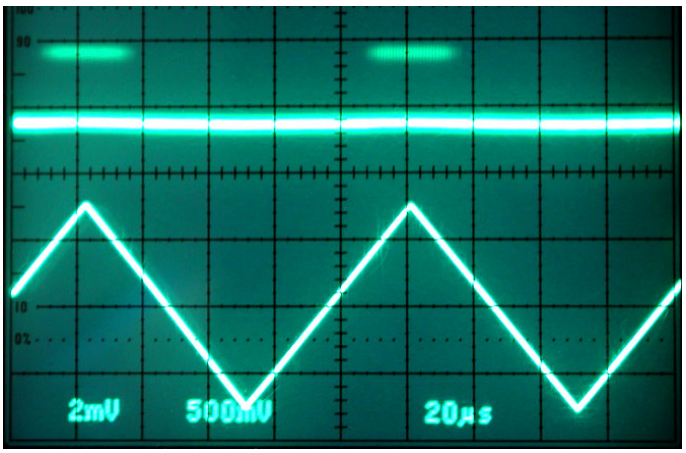

(b)

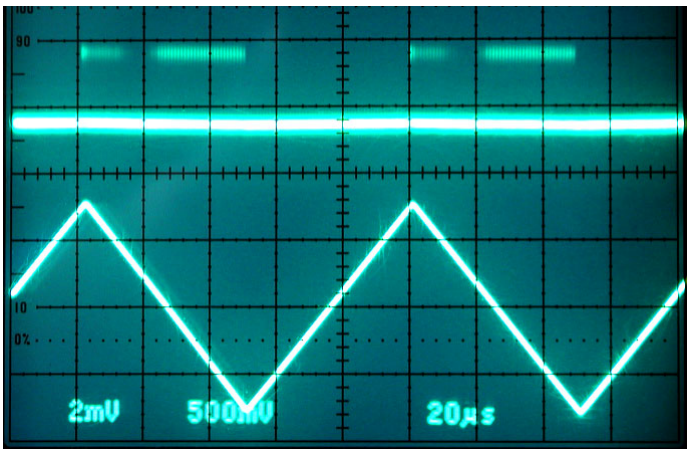

(c)

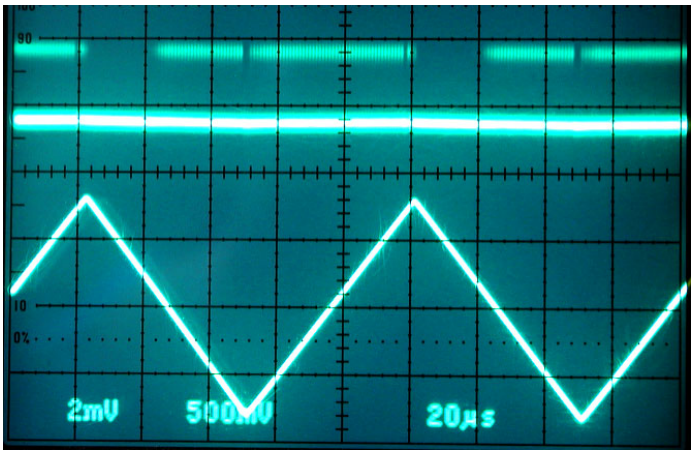

FIG. 7.13. Voltage response of SQUID BH showing irregularities to modulating flux with increasing amplitude. The 92 µA input current pulses were 100 ns long and had a pulse repetition rate of 1 MHz. The applied 10 kHz triangular wave magnetic field was produced by sending current through the one turn coil with current amplitudes of (a) 800µA, (b) 818µA, and (c) 850µA. Onset of irregularities seen in (b).

regions would be symmetric about some point due to the symmetry of the triangular wave. This is seen in Fig. 7.12 which shows the symmetric SQUID triggering regions centered around the peaks of the triangular wave, as expected in the low frequency limit.

It was also expected that as the flux wave amplitude increases by more than $3\Phi_o/4$, "holes" in the clustered SQUID triggering region would appear and grow linearly. That is, the SQUID stops triggering when the critical current exceeds the current pulse height, again due to the Φ_o periodicity of the response to applied flux. If the wave amplitude increased further, a small voltage triggering region should appear inside the holes and evolve like the larger clusters. Subsequent features in the SQUID voltage response would be a repeat of this pattern as the flux wave amplitude continued to increase.

However, the SQUID voltage response did not exactly follow the expected behavior. The first hole in the triggering response appeared when the current through the one turn coil was 818 μA [see Fig. 7.13(b)]. On the other hand, the position and symmetry of the response suddenly and dramatically changed at the same time. A sudden change in the response occurred again at an even higher wave amplitude [see Fig. 7.13(c)].

For comparison, I substituted the triangular wave flux signal with a sinusoidal signal. Figure 7.14 shows the resulting SQUID response, which was much more stable. Abrupt changes in the response disappeared, and the triggering regions continued to be symmetric and centered around the wave peaks. In Fig. 7.14(a), the sinusoidal current through the SQUID chip's one turn coil, seen in the bottom half of

(a)

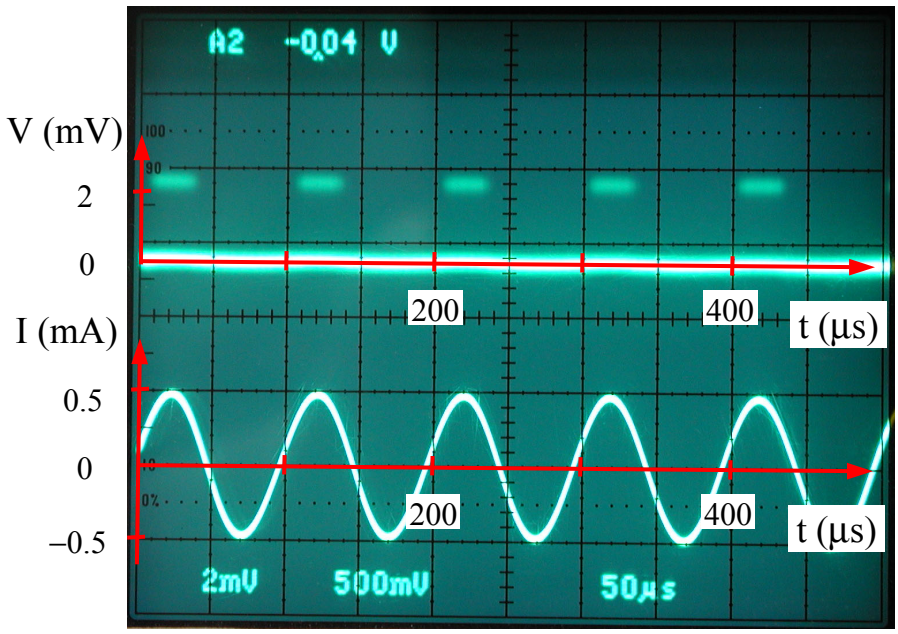

(b)

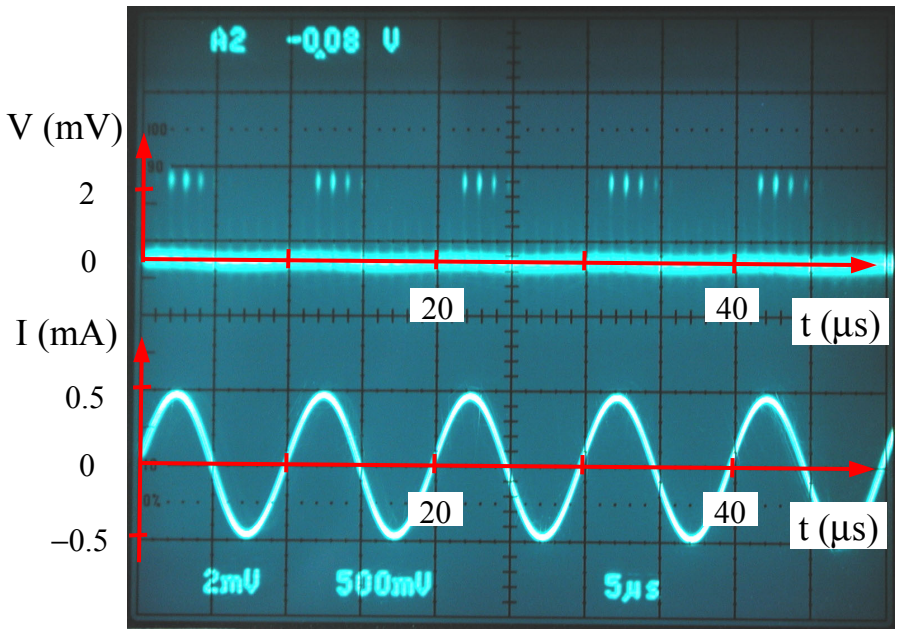

FIG. 7.14. Voltage response of SQUID BH triggering to a sinusoidally modulating flux. The output voltage responses are seen in the upper portions of the oscilloscope pictures. The lower portions show the 500 µA amplitude sinusoidal current through the one turn coil on the SQUID chip used to generate the magnetic flux. The 92 µA input current pulses for the bias current were 10 ns long and had a pulse repetition rate of 1 MHz. The frequencies of the current generating the applied magnetic flux were (a) 10 kHz and (b) 100 kHz.

the oscilloscope picture, had an amplitude of 500 μA and a frequency of 10 kHz. The frequency of the sinusoidal current in Fig. 7.14(b) was 100 kHz. Bias current pulses for these measurements were only 10 ns long with a pulse repetition rate of 1 MHz. The 1 μs intervals between current pulses can be seen in the circuit voltage response in the top half of Fig. 7.14(b). Individual pulses are too tightly clustered to be distinguished in Fig. 7.14(a).

Although abrupt changes in the voltage response did not occur, neither did I observe growing "holes" in the SQUID triggering region even with sinusoidal waves. In fact, the voltage response stopped changing altogether beyond a certain flux amplitude. There are several possible causes of this nonideal behavior. One possible explanation is that magnetic flux is being trapped in the SQUID Josephson junctions at high field, and this is blocking further modulation from occurring. Another possibility could be due to magnetic hysteresis in the SQUID, as the value of its modulation parameter $\beta \approx 1.3$ is larger than $2/\pi$. With increasing flux amplitude, the total magnetic flux through the SQUID hole could have gone through changes that include discontinuity in critical current modulation. This last possibility, however, is not supported by other related observations.

More likely, the current in the one turn coil started affecting the superconductivity of the SQUID when the current level became too high. The close proximity of the coil with the SQUID loop may have caused part of the loop to go normal, either by heating or by exceeding the critical field. It is also likely that there was some noise or irregularity in the current from the function generator.

Another simple explanation could be that the expected holes are too small and are thus masked by noise. The change in magnetic flux through the SQUID hole can be estimated from the mutual inductance of 12 pH, obtained in section 3.3, between the on chip one turn coil and the SQUID. A change of 100 μA in the current through the one turn coil should result in an approximate change of $0.6\Phi_o$ through the SQUID. A change of about $3\Phi_o/4$ should have already brought about the appearance of a hole in the clustered triggering regions. However, I did not observe the emergence of holes during a change of 400 μA in the current through the one turn coil (see Fig. 7.12). Noise in the pulsing frequency combined with insufficient temporal resolution in the oscilloscope could have masked the appearance of holes.

Without more investigation and simulation, the cause of why there are no growing "holes" in the clustered triggering regions and of other irregularities remains undetermined. In any case, despite the limit to small flux values at low frequencies, the test results clearly demonstrate the feasibility of the pulsed SQUID sampling technique.

7.7.2 100 MHz Signal Response

Figure 7.14(b) shows the possibility of detecting signals with frequencies as high as 100 kHz using the pulsed SQUID sampling technique. This corresponds to a bandwidth that is already higher than what is found in commercially available SQUID microscopes. To test the technique with even higher frequency magnetic fields, I used a microwave generator to supply current to the one turn coil on the SQUID chip. The microwave generator was a Hewlett Packard 83732B signal

generator that could produce 10 MHz to 20 GHz microwaves [166]. For bias current pulses, I selected the shortest reliable pulse length of 5 ns using the DG535 pulse generator. With shorter pulses, the pulse profile was very distorted as discussed in section 7.4. These current pulses were sent to SQUID BH at the maximum pulse rate of 1 MHz.

Elementary considerations shows that with 5 ns pulses, the highest frequency signal that can be followed is one with a period of 10 ns, which corresponds to a frequency of 100 MHz. Accordingly, I sent microwave signals with frequencies up to 100 MHz to the one turn coil. In order to observe the conditional triggering of the dc SQUID at different delays with respect to the signal, I employed a variation of the synchronous mode signal following scheme of section 6.3. The idea was to pulse the SQUID at different time delays with respect to the microwave signal.

First, the oscilloscope was synchronized, i.e. triggered with respect to the bias current pulses. The microwave flux signal was sent to the one turn coil without any synchronization, neither with the current pulses nor with the oscilloscope. When a current pulse arrived at the SQUID, it would be at some arbitrary phase with respect to the flux signal. If subsequent pulses arrived at slightly different relative phases, the SQUID's response to the flux signal could be mapped out.

To ensure that pulses arrived at a phase that was shifted with respect to the previous phase between the pulse and flux signal, I incorporated a very small difference in frequency between the 100 MHz microwave signal and an integer multiple of the 1 MHz pulse repetition rate. A difference of one part in 10^8 was sufficient. Due to the frequency difference, the relative phase between the pulses and

microwave signal slipped by a small fixed phase after every pulse. Therefore, each successive pulse polled the flux signal at a different relative phase with time, which was the desired result.

Figures 7.15, 7.16, and 7.17 show the response of SQUID BH to the 100 MHz flux signal. The top parts of the oscilloscope pictures show the flux signal. The middle part shows the SQUID circuit's output voltage response. The bottom part shows the input voltage pulse signal. The delay between the input voltage pulse and the output voltage response is partly due to a short (1 m) coaxial cable between the pulse generator and oscilloscope and a long (5 m) coaxial cable between the dip probe and the oscilloscope. Figure 7.15(a) shows SQUID BH triggering near the onset of the bias current pulse, and Fig. 7.15(b) shows the response when SQUID BH is not triggering. Figure 7.16 shows the intermediary case when the current pulse arrives at the SQUID at a relative phase between the two phases of Fig. 7.15.

In Fig. 7.15, simulation results presented in section 7.5 are superimposed on the oscilloscope traces of the voltage responses for comparison. The height of the simulated voltage responses are scaled to that of a V_{in} = 1.7 V input voltage pulse, whereas the actual pulse was set to 0.92 V. The simulated pulse length was τ = 5 ns, and the circuit model inductors were set to $L_1 = L_2$ = 11.9 nH. The discrepancies between the simulation and experimental results are due to distortions in the input voltage pulse as well as reflections from impedance mismatches.

Figure 7.16 shows multiple transitions from the zero voltage state to the resistive state, similar to the simulated results of Fig. 7.10(a). Noise in either the applied flux or the pulse frequency, in conjunction with the limited temporal

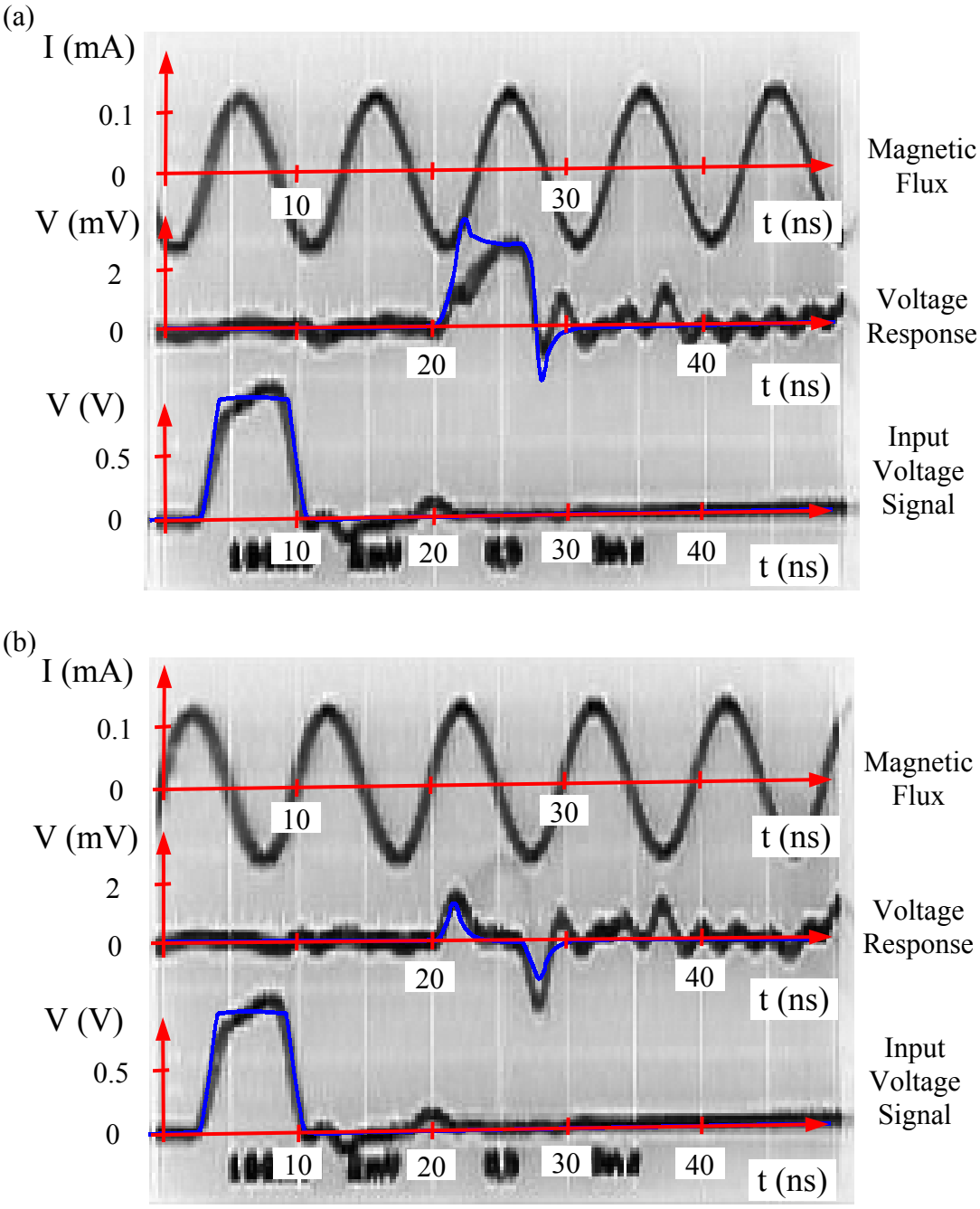

FIG. 7.15. Voltage responses of SQUID BH to 0.92 V, 5ns input voltage pulses and an applied magnetic flux signal at different delays, in the large bandwidth dip probe. The applied flux is produced by a 100 μA amplitude, 100 MHz current signal through the one turn coil of the SQUID chip. The responses show SQUID BH (a) triggering near the onset of the bias current pulse and (b) not triggering. For comparison, simulation results for a 1.7 V input pulse are superimposed over the voltage response traces, while the input voltage height is scaled to 0.92 V. The voltage response is delayed with respect to the input pulse by sending it through a long coaxial cable.

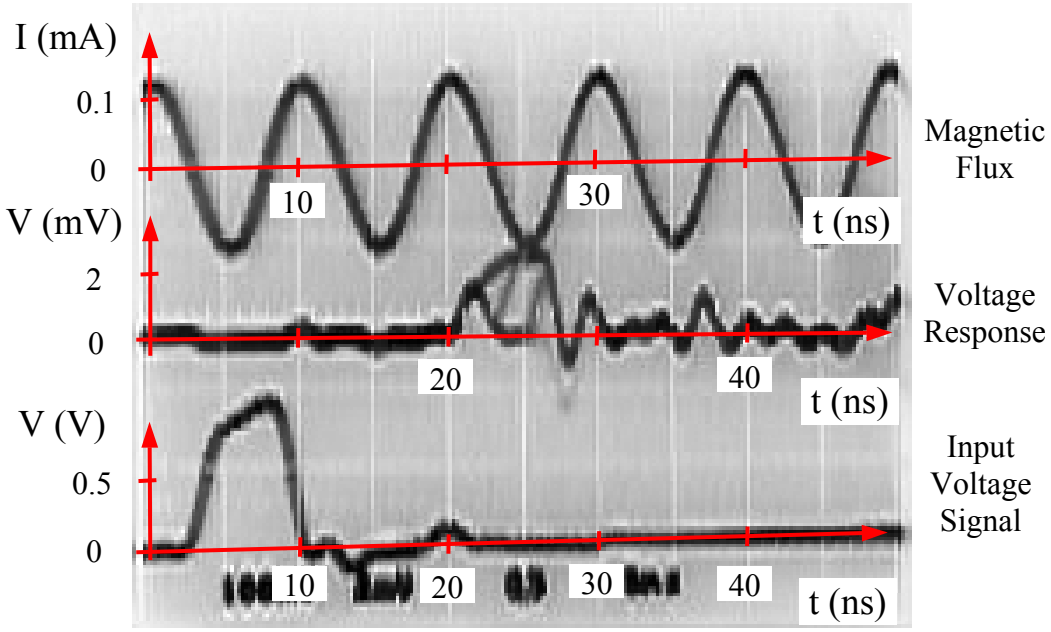

FIG. 7.16. Voltage response of SQUID BH to 0.92 V, 5ns input voltage pulses and an applied magnetic flux signal at different delays showing multiple transitions from the zero voltage state to the resistive state, in the large bandwidth dip probe. The applied flux is produced by a 100 μA amplitude, 100 MHz current signal through the one turn coil of the SQUID chip. The voltage response shows SQUID BH triggering at different relative delays due to noise in either the applied flux or the pulse frequency. The voltage response is delayed with respect to the input pulse by sending it through a long coaxial cable.

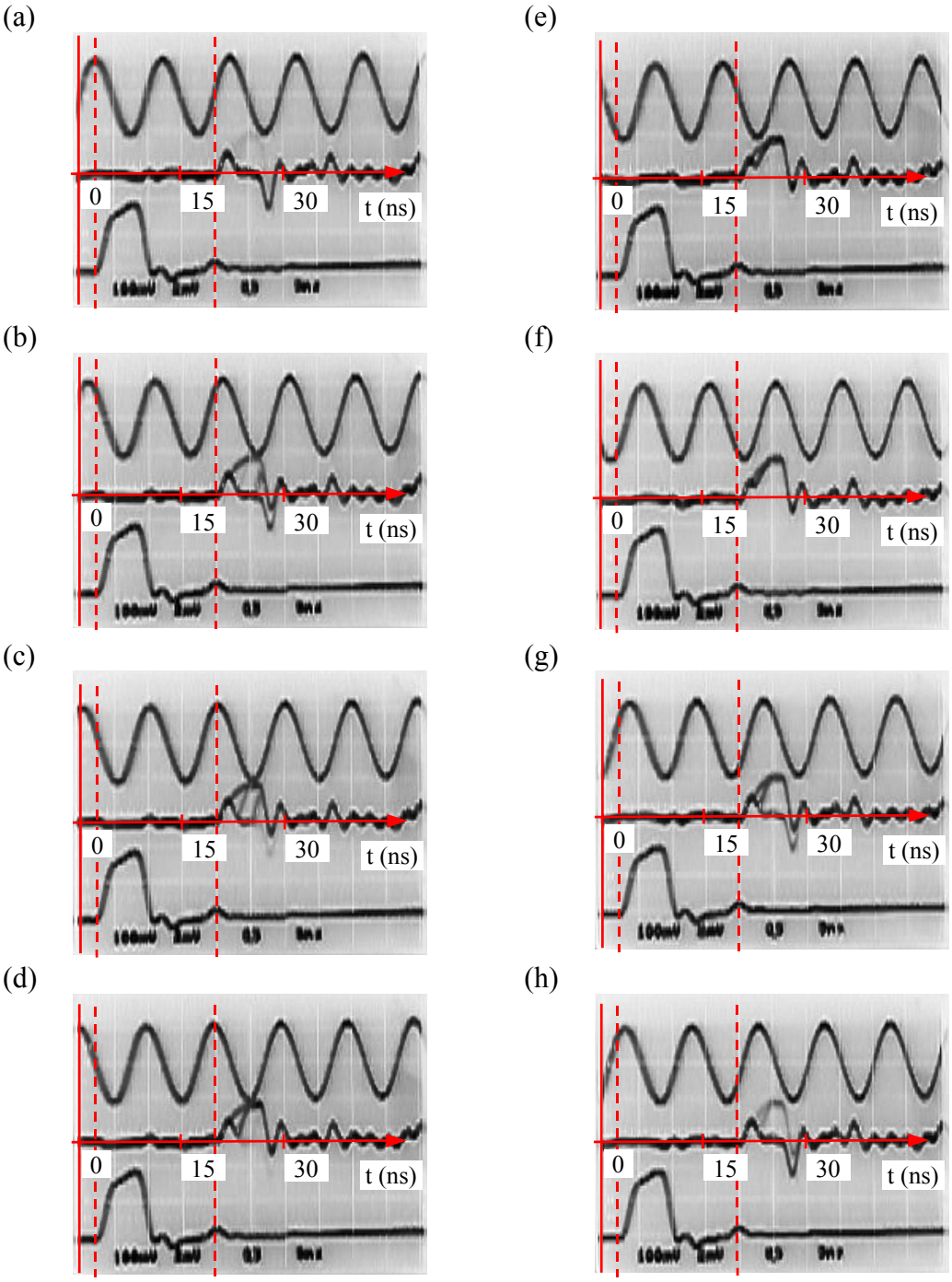

FIG. 7.17. Series of oscilloscope traces showing the progression of the voltage response of SQUID BH to 0.92 V, 5 ns input voltage pulses and an applied 100 MHz magnetic flux signal with varying delay, in the large bandwidth dip probe. Vertical markers indicate the onset of the input voltage pulse and the voltage response. The relative delay between the applied flux signal and the onset of the input voltage pulse can be tracked by noting the points at which the flux signal crosses the markers. The relative delays are approximately (a) 0 ns, (b) 1.5 ns, (c) 2.5 ns, (d) 3.0 ns, (e) 4.5 ns, (f) 6.5 ns, (g) 8.5 ns, and (h) 9 ns.

resolution of the oscilloscope image capturing system, caused triggering at different delay times to be observed in the same oscilloscope picture.

Figure 7.17 shows the progress of the voltage response as the current pulse arrives with successively later delays. A gradual change in the output voltage response is seen going from Fig. 7.17(a) to Fig. 7.17(f) as the relative phase between the bias current pulse and flux signal changes. The progression of the voltage response resembles the change in output voltage response obtained from simulations, especially when the SQUID critical current increases in Fig. 7.10(a). As the relative phase between the bias current pulse and flux signal increases, the output voltage response progresses from Fig. 7.17(f) to Fig. 7.17(h), eventually returning to the original no-triggering state shown in Fig. 7.17(a). The total shift in the flux signal from Fig. 7.17(a) to Fig. 7.17(h) corresponds to one full period of 10 ns. I can conclude that the progression of the output voltage response in Fig. 7.17 is due to the gradual change in SQUID critical current caused by the 100 MHz flux signal.

Figure 7.17(a) shows SQUID BH not triggering to bias current pulses due to high critical current. Figure 7.17(f) shows triggering of SQUID BH near the onset of the bias current pulse due to low critical current. Between these points, the intensities of the voltage response curves suggest that the SQUID triggers only part of the time. This behavior is understood as the SQUID being triggered for only a fraction of the times it is pulsed and at different delays with respect to the onset of the pulse. Noise and other factors can trigger the SQUID into the resistive state if the difference between current pulse height and modulated critical current is sufficiently small. As the difference between the pulse height and critical current increases above the noise

level, it becomes more likely that the SQUID will be in one state rather than the other.

In order to obtain the results shown in Figs. 7.15, 7.16, and 7.17, I had to adjust the ac and dc magnetic fluxes applied to SQUID BH. To perform this, I first set the microwave signal generator to a signal amplitude of 100 mV. The pseudo-dc current amplitude corresponded to 100 μA with a flux amplitude of about $0.6\Phi_o$ applied to the SQUID. I calculated the flux amplitude using the mutual inductance of 12 pH, obtained in section 3.3 with measurements on SQUID AN. However, this did not take into account possible attenuation of the current before it reached the coil. So, the flux value was only roughly known and could have been and probably was somewhat smaller.

The applied dc magnetic flux had to be adjusted so that the ac flux from the one turn coil would modulate the SQUID critical current such that the SQUID would trigger about half of the time it was pulsed and not the rest. With an ac flux amplitude of $0.6\Phi_o$, this should have automatically been satisfied. However, this was not the case suggesting that the current to the one turn coil was indeed attenuated. I adjusted the dc flux by rotating the dip probe, as discussed in section 7.3. Conditional triggering in response to the ac flux was found easily, needing only a small rotation of the dip probe.

7.7.3 Unexpected Phenomena in the Voltage Response

On a minor point, if I applied large flux signals to the one turn coil, I noticed significant inductive effects in the system. Figure 7.18 shows the result when instead

(a)

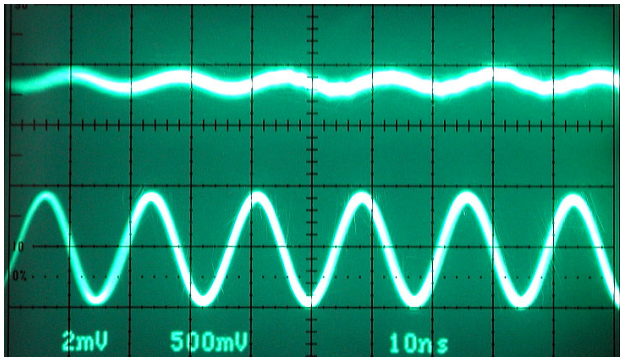

Voltage Response

Magnetic Flux

(b)

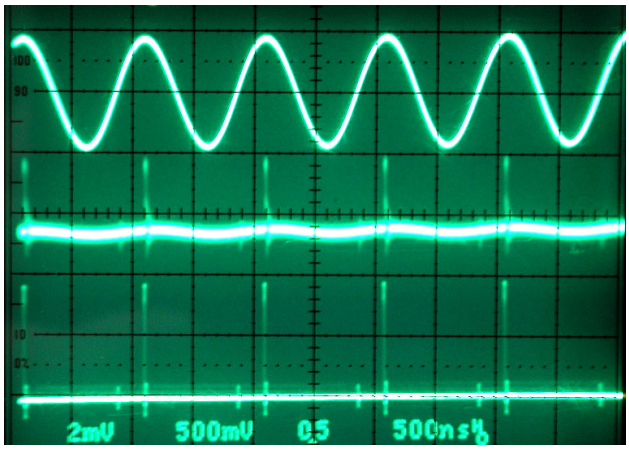

Magnetic Flux

Voltage Response

Input Voltage Signal

(c)

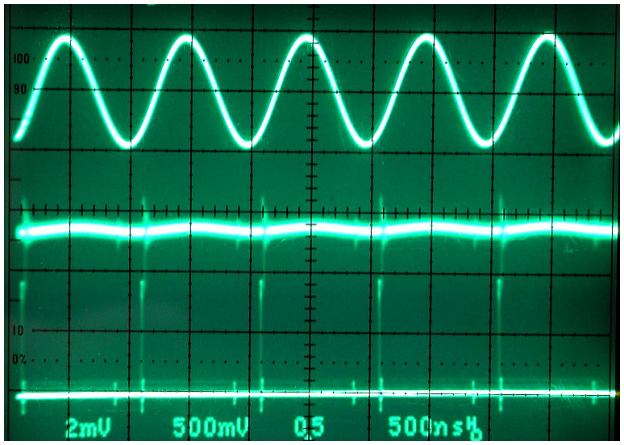

Magnetic Flux

Voltage Response

Input Voltage Signal

FIG. 7.18. Oscilloscope traces showing coupling between the current to the one turn coil for the applied magnetic flux and the output voltage response signal of the SQUID circuit. The frequency of the applied flux is 56 MHz for (a) and 1 MHz for (b) and (c). Undulations in the voltage response are induced at the same frequency as the flux signal. As the flux frequency increases, there is an increase in undulation amplitude accompanied by a change in relative phase between the voltage response and the flux signal. Conditional triggering of SQUID BH by bias current pulses and applied flux is seen in (b) and (c). The triggering is not affected by the coupling.

of 100 mV, the microwave signal amplitude was set to 500 mV; I observed a small amplitude ac voltage signal with the same frequency as the microwave signal at the SQUID circuit's output voltage. When the frequency of the microwave was increased from 1 MHz to around 56 MHz, the amplitude of the ac voltage signal increased and was accompanied by a phase shift [see Fig. 7.18(a)]. Since the SQUID was not triggering for most of the cycle, this was a definite sign of inductive pickup between the flux lines or one turn coil and the bias current or SQUID voltage lines. Reducing the flux amplitude reduced the effect on the output voltage.

Although undesirable and like the thermoelectric emf effect described in section 3.3, inductive pickup had minimal impact on magnetic flux detection. In particular, the response of the dc SQUID to bias current pulses appeared to be unaffected. Figures 7.18(b) and 7.18(c) show the voltage responses to a 1 MHz flux signal inducing an ac voltage in the output voltage signal while SQUID triggering and no SQUID triggering were being observed, respectively. It is interesting to note that this result is inconsistent with the ac bias voltage phenomena mentioned in section 3.1, and suggests that nonlinear effects in the SQUID circuit may not be very detrimental.

A more interesting phenomenon was observed when currents with frequencies higher than 100 MHz were sent through the one turn coil. Despite the nominal 5 ns pulse length of the bias current, when higher frequency signals were sent through the coil, SQUID BH continued to respond to the flux with conditional triggering. Beyond some limiting frequency, the SQUID should have been triggering continuously as during every current pulse, the modulated critical current will at

some point be below the pulse height. However, this did not occur. Instead, the SQUID continued to trigger in correlation with the flux signal well beyond the expected limiting frequency of 100 MHz. Due to the limited bandwidth of the Tektronix 2465B oscilloscope, the correlation between the flux signal and the voltage response could not be verified beyond 380 MHz, though the voltage response continued to show signs of conditional triggering.

This unexpected phenomenon could be due to an effective pulse length that is shorter than the generator set value. The ability of the SQUID to clearly follow significantly higher frequency signals strongly suggests a shorter pulse length. The result is also consistent with a pulse profile with peaked structures produced by the pulse generator, as mentioned in sections 7.4 and 7.6. If I had found a limiting frequency above 100 MHz where conditional triggering failed, this would have confirmed the hypothesis. But, I was unable to find such a limiting frequency up to the 400 MHz bandwidth of the oscilloscope. If the hypothesis is correct, this null result suggests that the effective pulse length is shorter than 1.3 ns. Further investigation with better diagnostic equipment would be helpful in resolving the issue.

7.8 1 GHz Measurements and Extensions to Larger Bandwidth

Using my apparatus, Matthews and Vlahacos also performed experiments on SQUID BH and detected magnetic fields with frequencies higher than 100 MHz using a variation of my pulsed SQUID sampling technique [31]. The technique they used is described in section 6.3 and involves finding the distribution of SQUID

triggering events from multiple measurements. By identifying the transitional point where half of the bias current pulses results in triggering and the other half does not, they could follow magnetic flux signals applied to the SQUID. Ultimately, they were successful in following a 1 GHz microwave magnetic flux signal applied on SQUID BH (see Fig. 7.19).

The 1 GHz measurement is remarkable because Matthews and Vlahacos used 10 ns bias current pulses for the measurement. That is, within the duration of a pulse, the flux signal would have caused 10 oscillations of the SQUID critical current. Naively, the SQUID should have triggered with every pulse and thus not be able to follow the flux signal. Given that the 1 GHz signal was observed, Matthews *et al*. also concluded that the effective bias current pulse is much shorter than the generator set value of 10 ns.

A hint to the cause and understanding of the 1 GHz result may lie in the behavior of the noise in the measurement. Examination of Fig. 7.19 shows that decreasing edges of the 1 GHz signal contain more noise, particularly a broader distribution of triggering events, than the increasing edges. Naively, one would expect the noise to be more evenly distributed between both edges if it were due to noise in the microwave flux signal or in the 10 ps delays used to synchronize the current pulses [12]. On the other hand, if there were significant subnanosecond structure to the pulses, the distribution of triggering events would reflect the actual pulse shape.

In any case, these experiments clearly demonstrate that the technique of pulsed SQUID sampling can be implemented and extended to 1 GHz bandwidth. The

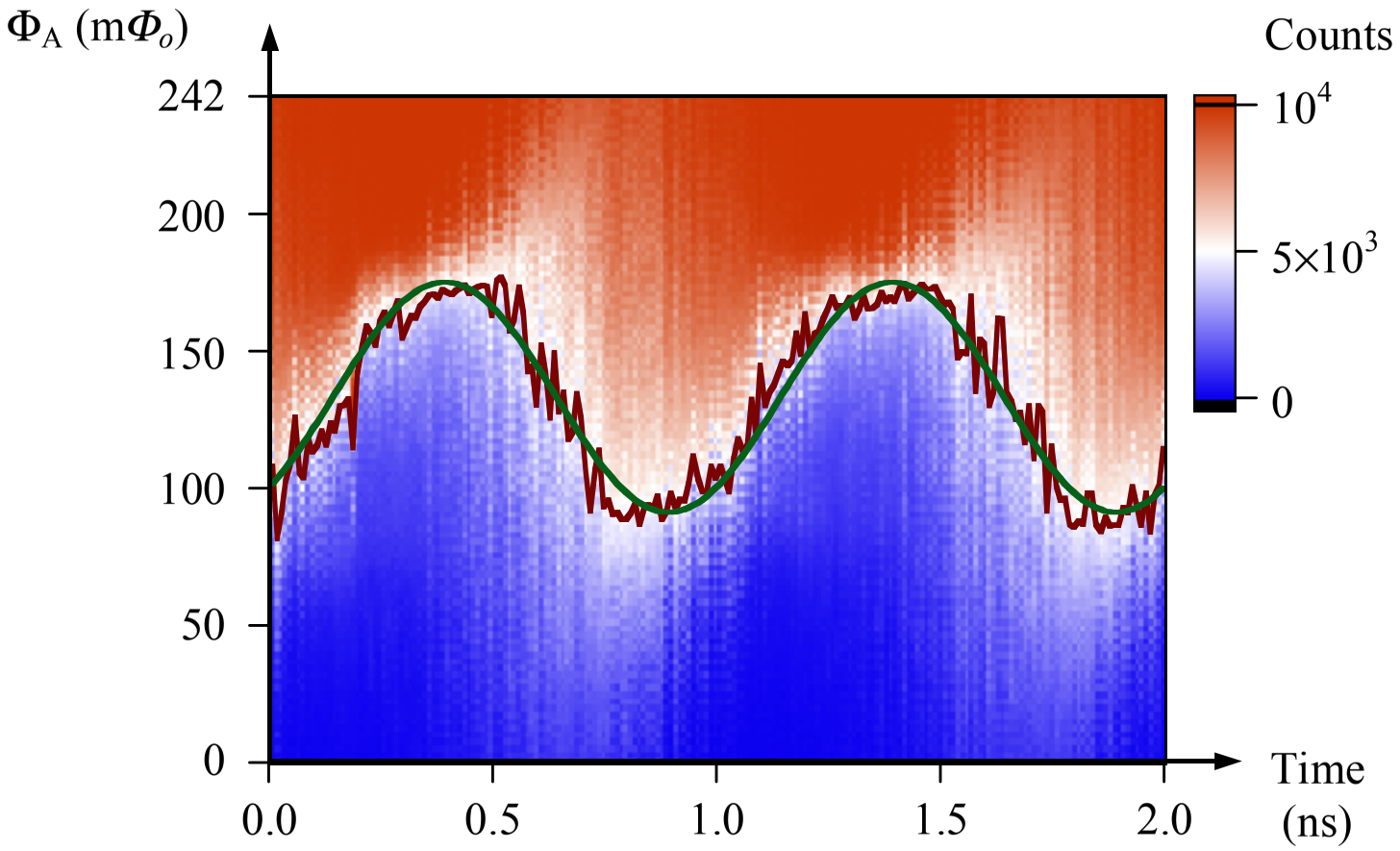

FIG. 7.19. Two dimensional histogram of SQUID BH triggering events in the presence of a 1 GHz magnetic field. There were 10^4 triggering events per data point. The SQUID bias current was pulsed with 10 ns pulses. A dc feedback field was applied to the SQUID and incremented after each data point at the same delay. The vertical axis is the applied flux through the SQUID. The horizontal axis is the time delay in 10 ps steps. The purple curve shows where half of the pulses resulted in triggering. The green curve represents the best sinusoidal fit to the purple curve. (Plot courtesy of J. Matthews.)

technique requires the reliable generation of short current pulses. I note that generators capable of producing very short pulses are commercially available and some have pulse rise times as short as 50 ps. Yet, even with the DG535 pulse generator with a minimum reliable pulse length of 5 ns, limited mostly by its rise time, small magnetic flux signals with frequencies above 100 MHz can still be followed.

An interesting alternative approach is to use superconducting electronics to produce picosecond scale pulses, as I discussed in section 6.4 [22-24,147-151,167]. This may be a practical option as the needed cryogenic components are already in place. Superconducting electronics may also have better noise characteristics and could be placed near the SQUID itself making connections to the SQUID easier. The main difficulty would be in designing the circuits and adjusting or tuning circuit parameters after fabrication. One can also envision more integrated circuits incorporating synchronization of current pulses to the flux signal, precise control of pulse delays and amplitude, and other features required for fully implementing synchronous mode pulsed SQUID sampling [22-24].

The point of controlling pulse parameters deserves some additional discussion. For the technique to work, pulses must be adjustable. As long as the pulse length is longer than the voltage rise time of the dc SQUID, the length can be fixed for all measurements. But, the height and the relative timing of the pulses need to be adjustable. For the alternating pulse height technique presented in section 6.3, the pulse height difference in particular will determine the flux resolution and so should be adjusted for the characteristics of the particular SQUID being used. The

pulse generator must also be connected to other components of the electronics, such as the generator for the magnetic feedback flux, the pulse counter, and the comparison logic. In the case of asynchronous mode sampling, the speed at which these components interact will partly determine the maximum slew rate of the electronics, as discussed in section 6.3.

Lastly, as the 1 GHz measurements show significant noise, the question can be raised whether low noise can be achieved with the larger bandwidth. I do not have much data on this question, but there are still some conclusions that can be drawn. The flux resolution of SQUID BH using the dip probe and the ambient magnetic field was obtained for the pulsed SQUID sampling technique and found to be no more than $0.06\Phi_o$ for one shot (see section 7.3). This flux resolution or uncertainty is for a single measurement and can be reduced by averaging multiple measurements. If measurements are made at 10 MHz for 10 μs, there are 10^2 measurements, which reduces the uncertainty by its square root or 10. The result then for a 10 μs measurement is an uncertainty of 6 mΦ_o, which is a relatively small flux.

The flux uncertainty can be translated into an upper limit for the flux noise in the system. This upper limit can then be compared to the performance of commercially available SQUID microscopes. A typical commercial microscope has a base noise level on the order of 10 $\mu\Phi_o/\sqrt{\text{Hz}}$ and a bandwidth of 100 kHz or less. Therefore, if it could make one measurement in 10 μs, its rms flux noise would be around 3 mΦ_o. In conclusion, the pulsed SQUID sampling technique using SQUID BH has the potential to perform equally well in terms of reducing noise or increasing flux resolution, if the sampling rate is high enough. Even with comparable or slightly

higher noise levels, the larger bandwidth of pulsed SQUID sampling would have much broader usefulness in high speed applications. Furthermore, better electronics and feedback control should be able to reduce the extrinsic noise factors for pulsed SQUID sampling than what has been demonstrated so far.

CHAPTER 8 Conclusions

8.1 Summary of Work

In the previous chapters, I described my work on all of the major components that are needed to construct a large bandwidth scanning SQUID microscope. First, I assembled and tested a closed cycle pulse tube cryocooler for a prototype microscope, which can maintain a SQUID attached to a cold finger at temperatures around 5 K [27]. There were some minor vacuum and temperature stability problems, but these should be readily solvable with improvements in the cold finger and ceramic material surrounding the sapphire window. I also discovered vibrations and mechanical motion in the system that are significant and require more extensive redesign of the cold finger including modifications in the radiation heat shield and vacuum chamber. Here, there is a technical solution to the problem derived from work performed by Kenyon *et al*., so this difficulty is surmountable [131,132].

Next, in conjunction with coworkers, I assembled the prototype scanning SQUID microscope and made modifications for some design flaws. With the microscope, I was able to obtain a scanned image of the magnetic field produced by a current driven test circuit despite problems with subsystem components.

Regarding the SQUIDs themselves, I designed dc SQUIDs for near field magnetic field sensing in scanning microscopes and determined the criteria needed for optimal performance. Designs were made for both nonhysteretic resistively

shunted niobium dc SQUIDs and unshunted hysteretic dc SQUIDs. I used nonhysteretic SQUIDs for testing the cryogenic system and prototype microscope as a conventional SQUID microscope with standard "off the shelf" FLL electronics [29]. Hysteretic SQUIDs were used to develop and test a new large bandwidth readout technique.

I also improved on procedures for preparing SQUID chips for installation into the microscope. Through my experiments, I concluded that prior techniques for making electrical contacts to dc SQUIDs using silver paint were inadequate and that more robust connections such as wire bonding were required. This led me to redesign the prototype microscope cold finger.

To investigate techniques for large bandwidth SQUID readout, I constructed a large bandwidth coaxial cable dip probe that could carry high speed signals to a SQUID. Working from ideas used in Quantum Computing experiments, I developed a readout algorithm for a hysteretic dc SQUID using pulsed bias current [44-50]. I then proceeded to test parts of the readout algorithm with the hysteretic SQUIDs I designed. Finally, I compared results from the tests with a numerical model that showed some consistent behavior and insight into what was occurring electrically.

The experimental apparatus limited the range of signals that I could test with the SQUIDs. I was able to observe predictable responses to an applied 100 MHz magnetic field signal, i.e. a bandwidth that is two orders of magnitude higher than results reported for the best FLL electronics [20]. However, I observed evidence and structure in the bias current pulses indicating that the useful bandwidth of the apparatus was larger. In fact, coworkers Matthews *et al*. were able to achieve readout

bandwidths as large as 1 GHz using my SQUIDs and experimental apparatus [31,120].

8.2 Large Bandwidth SQUID Microscopy

Essential to my approach to increasing the bandwidth of SQUID electronics is the use of hysteretic dc SQUIDs. Currently, commercially available SQUIDs that can be made to order make use of niobium technology which require LHe temperature cooling [112-115,117,118]. The intrinsic bandwidth limit of these hysteretic niobium dc SQUIDs are dependent on junction characteristics, especially the ratio between the critical current and capacitance of the Josephson junctions. Based on this criterion, I calculated that my SQUIDs have an ultimate bandwidth of around 40 GHz, which is greater than that of any of the other electronics components with the exception of the coaxial cable.

Cooling technology for the SQUIDs is also available, and I found that application of 4 K cryocooler technology, which is desirable from an industrial standpoint, is feasible. Furthermore, adapting the design of a sapphire window in the vacuum chamber has allowed the temperature of measured samples to be at room temperature in atmospheric conditions, independent of cooling system requirements [8,12,17]. This is a major advantage for practical applications.

As to the readout technique of pulsed SQUID sampling, there are two main components: SQUID critical current detection and the signal following scheme. I have proposed two different detection schemes to perform critical current detection. Of the two, I developed the alternating pulse height scheme which makes use of

current pulses of two different heights corresponding to two different critical current levels. As in conventional FLL electronics, feedback magnetic flux counteracts the externally applied magnetic flux and is used to read out changes in the applied field.

Changes in the externally applied field are followed using the signal following scheme. Of the two following schemes I described, a major increase in SQUID electronics bandwidth can be achieved by synchronous pulsed sampling. This following scheme is applicable to repetitive external signals which can be synchronized to the pulse generating mechanism.

Synchronous pulsed sampling is particularly useful for high speed micro circuit diagnostics in which the evolution of current with time in a particular circuit lead has to be followed. With fully implemented electronics, one can expect to see nanosecond scale time sequences of operating circuits. There are also other applications that can benefit from the synchronous detection of very weak magnetic fields at nanosecond time scales, e.g. solid state Quantum Computing experiments.

8.3 Limits of the Pulsed SQUID Sampling Technique

To obtain bandwidths in excess of 1 GHz, the sampling time must be shorter than 0.5 ns, requiring dc SQUID bias current pulses to be of that same duration. With asynchronous pulsed sampling, this means the minimum pulse rate must be 2 GHz. However, dead time between pulses is needed to process the information, and with feedback the required time can be much more, reducing the slew rate and bandwidth. In synchronous pulsed sampling, the input signal is repeated while the electronics processes the information between repetitions. Therefore, the sampling rate

determines the effective bandwidth in asynchronous sampling, and in synchronous sampling, it is a combination of the pulse length and delay time interval.

I have not experimentally determined the ultimate maximum sampling rate. Theoretically, it should be limited by the SQUID bandwidth, which for my SQUIDs is around 40 GHz. The pulse generator I used in my experiments, however, restricted the bandwidth to a lower value. First, the minimum pulse length was limited to 4 ns with a maximum pulse rate of 1 MHz, the former implies a maximum bandwidth of 125 MHz for synchronous mode and the latter a bandwidth of 500 kHz for asynchronous mode. Given the similarities in operation between FLL electronics and asynchronous mode sampling and that the bandwidth with feedback of the best FLL electronics is a reported 2.5 MHz, one expects that the bandwidth of asynchronous mode pulsed SQUID sampling can match or exceed that of the best FLL electronics with a sampling rate greater than 5 MHz [20]. A 5 MHz sampling rate with 5 ns pulses only allows 195 ns per pulse for data processing, which is fast but probably well within current technology.

For synchronous mode sampling, the bandwidth can be orders of magnitude larger than the best FLL electronics. The pulse generator used in my experiments was capable of synchronized time delays with a precision of 5 ps [158]. So, the limiting factor in my generator was the minimum 4 ns pulse length. As there are pulse generators which can provide 100 ps scale pulses as well as superconducting electronics that can produce 10 ps scale pulses, it seems possible that the maximum bandwidth can approach that of the SQUID [147,148,150,151].

On the other hand, magnetic flux resolution with pulsed SQUID sampling for a single shot is dependent on either the minimum feedback flux step size for the oscillating feedback detection scheme or the minimum pulse height difference for the alternating pulse detection scheme. Both quantities depend on the SQUID's flux noise and bias current noise. Although I have not measured the intrinsic noise in a hysteretic dc SQUID, I have experimentally determined that the flux noise in a single shot measurement using my SQUID is less than $0.03\Phi_o$. This result is consistent with the flux noise estimate from Eq. (3.18), derived from thermal arguments, which for my SQUID is around 4.2 mΦ_o over 40 GHz at 4 K [4,6,63,64,100].

8.4 Future Work

8.4.1 Needed Microscope Components and Replacements

Work on constructing a large bandwidth Scanning SQUID Microscope continues. There are several components in the prototype 4 K Scanning SQUID microscope that need to be replaced or modified before the microscope can operate optimally. The most problematic component in the prototype microscope was the scanning system, especially the sample translation actuators and control software. Due to the tight integration of the software with specific hardware, the scanning system in the microscope should be completely replaced and the software upgraded. There are scanning systems complete with software for the user interface and field image analysis [17]. These systems come as a package, and it would be simpler to replace the entire system than attempt to fix the problems in the system installed in the prototype microscope (see section 5.3). After replacement, the interaction

between software and hardware needs to be thoroughly tested and compatibility among different subsystems, such as the SQUID data acquisition unit and the actuator motor controller, needs to be assured to avoid similar scanning problems.

When choosing new translation hardware, there may be advantages in selecting one type of actuator motor system over another, depending on the way the software controls the actuators and reads the SQUID data. The actuators move the translation stages that support the scanned object, and they usually come in two types of motors, dc motors or stepper motors [134]. DC motor actuators operate by running an electrical motor for a given time at a given current. The current in combination with the time determines the angular rotation of a shaft. The rotation of the shaft extends a screw which moves a stage. The current value determines the speed of translation. In a stepper motor, there are two sets of magnet "teeth" which are paired to each other. The strengths of the selectable magnets can be controlled causing the relative position of the two "teeth" to lock in different combinations. By sequencing the strengths of the magnets, one set of magnets can be moved along relative to the other. If the magnet "teeth" are configured in concentric circles, one set of "teeth" will rotate relative to the other and make it possible to turn a shaft as in the case of a dc motor. Other geometrical configurations are also possible.

Due to the difference in mechanism, dc motors are better at maintaining a specified speed while stepper motors are more reliable in terms of position due to the locking of their "teeth". Position with dc motors is continuous. To take advantage of their characteristics, the timing between translation and data acquisition should be programmed differently for the two different motor types. Notwithstanding, the

choice between dc motor or stepper motor actuator is not usually made based on which characteristic is more important for the application but more commonly on availability and price.

In addition to basic reliable operation, it is worth having some transparent means of calibrating or correcting position error. Lack of such capability in the scanning system caused minor damage to one of the actuators when the translation stage position was over extended. One way of implementing position error correction is for the software to constantly check the position of the stages as they move. There are features in some hardware that facilitate this function, and software should recognize and take full advantage of it. This was also the case in the scanning system of the prototype microscope, but the mechanism was not transparent and may have contributed to its unreliable performance.

If there is no built in error correction feature, corrections can be attempted through software alone by recognizing the position from field images using predetermined reference features in those images. As an example, magnetic markers of known intervals and geometry can be used as reference points on an undetermined field source. The markers can be used to correct any distortions in position, and if the field strengths of the markers are also known, then the flux magnitudes could also be calibrated.

After replacing the scanning system, an accurate determination of the microscope's spatial resolution can be made. In general, spatial resolution is limited by the dimensions of the SQUID, but other factors can worsen it. One of those is the mechanical motion of the SQUID, described in section 4.3. Vibration isolation in the

microscope could perhaps be improved by isolating the compressor and burying its compressed helium hoses in sand to prevent coupling through the floor as well as through the hoses. Oscillations of the SQUID due to the expansion of the pulse tubes, however, will require modification of the cold finger. A new cold finger design using ultra pure copper foil to decrease mechanical coupling and nylon cord to rigidly hold the SQUID is presented in Appendix B.

With regard to additional equipment, I found it useful, and sometimes necessary, to have additional diagnostic sensors in the microscope. The limiting factors were whether there was room for the sensors and whether they would unduly increase the thermal load on the cryocooler. More temperature sensors on the cryocooler, radiation heat shield, and cold finger would help diagnose operational problems involving vacuum leaks and heat transfer. A pressure gauge with a larger operating range compared to the Balzers-Pfeiffer compact pirani gauge would have been more useful, as would have been a second pressure gauge near the vacuum pumps, for diagnosing leaks and pump problems.

Finally, the microscope vacuum chamber was designed to tightly fit the pulse tube cryocooler and radiation shield. This turned out to be a problem as there was not much room for error in positioning the cryocooler during assembly. Furthermore, the lack of room hindered easy access for *in situ* maintenance which would have reduced the risk of cryocooler damage from removal and reassembly. In particular, the position of radiation shield bolts made removal of the shield very inconvenient with the cryocooler in place. Some modifications of the table top chassis had already been performed to facilitate access, but additional changes including changes in the

vacuum chamber and radiation shield would be needed to make servicing the microscope practical for regular maintenance with the cryocooler in place.

Some of these additions or upgrades can be implemented without modifications to the existing cryocooler chassis, vacuum chamber, and radiation shield. However, more wiring would be required and this would have to be thermally anchored to the cryocooler cold stages. On the other hand, in order to implement large bandwidth electronics with coaxial cable wiring and a redesigned cold finger, new thermal grounding attachments will have to be prepared and installed for the cryocooler cold stages anyway. And, this would be made easier with modifications in the radiation shield, vacuum chamber, and chassis.

8.4.2 Upgrading to Large Bandwidth

Besides replacement of basic SQUID microscope components, co-workers are currently modifying the microscope with a hysteretic dc SQUID, a new cold finger, and coaxial cable wiring. New hysteretic niobium dc SQUIDs were ordered from Hypres. These SQUIDs are being installed into a modified cold finger which orients the SQUID in the x-SQUID configuration so that electrical connections can be made by wire bonding. Furthermore, compliance with Hypres design rules will make the SQUIDs more robust, and fine tuning Josephson junction shape and size should allow better control of SQUID parameters.

The installation of a hysteretic SQUID will enable the prototype microscope to implement pulsed SQUID sampling. To improve on the previous means of generating current pulses, an Agilent Technologies 81133A 3.35 GHz pulse/pattern

generator has been obtained [168]. This generator is capable of reliably producing subnanosecond pulses needed for extending readout bandwidth to 1 GHz or more. The very short current signals will have to be carried by coaxial cable which has to be installed into the microscope. Modification of the microscope cold finger should also include changes to accommodate connections to the coaxial cable. Until then, the Agilent 81133A pulse generator can be tested with hysteretic SQUIDs using the large bandwidth dip probe.

The 81133A pulse generator is also capable of generating programmed patterns or pulses. This is ideal for implementing the alternating pulse height scheme for critical current detection. However, if this scheme turns out to be too difficult to implement, the oscillating feedback scheme using constant height current pulses should be straightforward to implement using the pulse generator. Once achieved, essential elements of the apparatus can be redesigned into a self-contained system incorporating other functions. In addition, there is the possibility of designing and using superconducting circuits to generate pulses and perhaps perform additional functions. This activity can be done concurrently with other development and could have other useful applications.

Beyond installing new electronics, a detailed and comprehensive analysis of the microscope's circuit will be needed to optimize performance. To compare with experiments and aid development, better diagnostic equipment would be useful. For example, the oscilloscope used in my experiments limited analysis of SQUID signal responses to frequencies below 400 MHz. This limited not only the range of magnetic field signals that could be represented on the oscilloscope, but more

importantly, detailed structure in the bias current pulse profile could not be observed. Along these lines, a 4 GHz Tektronix TDS7404B digital oscilloscope has been obtained, which will satisfy these needs [169]. With the oscilloscope, direct determination of correct operation of the SQUID electronics can be performed with signal frequencies well beyond 1 GHz.

APPENDIX A: Critical Current of Ideal dc SQUID with Asymmetric Junctions

In this appendix, I derive an expression for the total supercurrent of an ideal dc SQUID where the critical currents of the two Josephson junctions are not identical. I start from the Josephson equations

$$I = I_c \sin\gamma \tag{A.1}$$

$$\frac{d\gamma}{dt} = \frac{2\pi}{\Phi_o} V \tag{A.2}$$

where γ is the gauge invariant phase across a junction given by

$$\gamma = \theta_2 - \theta_1 + \frac{2e}{\hbar}\int_1^2 \boldsymbol{A}\cdot d\boldsymbol{l}\,. \tag{A.3}$$

Here, $\boldsymbol{A}$ is the vector potential and the integration is performed over the region corresponding to the change of supercurrent phase from θ_1 to θ_2, i.e. across the junction barrier.

For an ideal dc SQUID, the total supercurrent is given by

$$I = I_1 \sin\gamma_1 + I_2 \sin\gamma_2\,. \tag{A.4}$$

Expressing Eqs. (A.1) and (A.4) using complex numbers or phasors, Eq. (A.4) can be written as

$$I = I_1 e^{i\gamma_1} + I_2 e^{i\gamma_2} \tag{A.5}$$

where the imaginary part of Eq. (A.5) matches Eq. (A.4). The magnitude of the new phasor is

$$
\begin{aligned}
|I|^2 &= (I_1 \cos\gamma_1 + I_2 \cos\gamma_2)^2 + (I_1 \sin\gamma_1 + I_2 \sin\gamma_2)^2 \\
&= I_1^2 + I_2^2 + 2I_1I_2(\cos\gamma_1 \cos\gamma_2 + \sin\gamma_1 \sin\gamma_2) \\
&= (I_1 - I_2)^2 + 2I_1I_2 + 2I_1I_2 \cos(\gamma_1 - \gamma_2) \\
&= (I_1 - I_2)^2 + 2I_1I_2[1 + \cos(\gamma_1 - \gamma_2)]
\end{aligned}
\quad . \tag{A.6}
$$

Using the trigonometric identity

$$
\cos 2\theta = 2\cos^2\theta - 1 , \tag{A.7}
$$

Eq. (A.6) is transformed into

$$
|I|^2 = (I_1 - I_2)^2 + 4I_1I_2 \cos^2\frac{\gamma_1 - \gamma_2}{2} . \tag{A.8}
$$

From section 2.3, the phase difference $\Delta\gamma = \gamma_1 - \gamma_2$ can be expressed as a function of the total magnetic flux Φ through the SQUID hole,

$$
\Delta\gamma = 2\pi n + 2\pi\frac{\Phi}{\Phi_o} \tag{A.9}
$$

where n is some integer. Substituting Eq. (A.9) into Eq. (A.8) gives

$$
\begin{aligned}
|I|^2 &= (I_1 - I_2)^2 + 4I_1I_2 \cos^2\left(\pi n + \pi\frac{\Phi}{\Phi_o}\right) \\
&= (\Delta I)^2 + 4I_1I_2 \cos^2\pi\frac{\Phi}{\Phi_o}
\end{aligned}
\tag{A.10}
$$

where $\Delta I = I_1 - I_2$.

The phase φ of the new phasor representing Eq. (A.5) is given by

$$
\begin{aligned}
\tan\varphi &= \frac{I_1 \sin\gamma_1 + I_2 \sin\gamma_2}{I_1 \cos\gamma_1 + I_2 \cos\gamma_2} = \frac{\frac{I_c + \Delta I}{2}\sin\gamma_1 + \frac{I_c - \Delta I}{2}\sin\gamma_2}{\frac{I_c + \Delta I}{2}\cos\gamma_1 + \frac{I_c - \Delta I}{2}\cos\gamma_2} \\
&= \frac{I_c(\sin\gamma_1 + \sin\gamma_2) + \Delta I(\sin\gamma_1 - \sin\gamma_2)}{I_c(\cos\gamma_1 + \cos\gamma_2) + \Delta I(\cos\gamma_1 - \cos\gamma_2)}
\end{aligned}
\tag{A.11}
$$

where $I_c = I_1 + I_2$. Using an elementary trigonometric identity,

$$\tan\varphi = \frac{2I_c \sin\frac{\gamma_1+\gamma_2}{2}\cos\frac{\gamma_1-\gamma_2}{2} + 2\Delta I\cos\frac{\gamma_1+\gamma_2}{2}\sin\frac{\gamma_1-\gamma_2}{2}}{2I_c\cos\frac{\gamma_1+\gamma_2}{2}\cos\frac{\gamma_1-\gamma_2}{2} - 2\Delta I\sin\frac{\gamma_1+\gamma_2}{2}\sin\frac{\gamma_1-\gamma_2}{2}}$$
$$= \frac{I_c \sin\gamma_{av}\cos\frac{\Delta\gamma}{2} + \Delta I\cos\gamma_{av}\sin\frac{\Delta\gamma}{2}}{I_c\cos\gamma_{av}\cos\frac{\Delta\gamma}{2} - \Delta I\sin\gamma_{av}\sin\frac{\Delta\gamma}{2}} \qquad \text{(A.12)}$$

where $\gamma_{av} = (\gamma_1 + \gamma_2)/2$. If I divide the numerator and denominator of Eq. (A.12) by $I_c\cos(\gamma_{av})\cos(\Delta\gamma/2)$, the result is

$$\tan\varphi = \frac{\frac{\sin\gamma_{av}}{\cos\gamma_{av}} + \frac{\Delta I\sin\frac{\Delta\gamma}{2}}{I_c\cos\frac{\Delta\gamma}{2}}}{1 - \frac{\Delta I\sin\gamma_{av}\sin\frac{\Delta\gamma}{2}}{I_c\cos\gamma_{av}\cos\frac{\Delta\gamma}{2}}} = \frac{\tan\gamma_{av} + \frac{\Delta I}{I_c}\tan\frac{\Delta\gamma}{2}}{1 - \frac{\Delta I}{I_c}\tan\gamma_{av}\tan\frac{\Delta\gamma}{2}}. \qquad \text{(A.13)}$$

Substituting Eq. (A.9) into Eq. (A.13),

$$\tan\varphi = \frac{\tan\gamma_{av} + \frac{\Delta I}{I_c}\tan\left(\pi n + \pi\frac{\Phi}{\Phi_o}\right)}{1 - \frac{\Delta I}{I_c}\tan\gamma_{av}\tan\left(\pi n + \pi\frac{\Phi}{\Phi_o}\right)} = \frac{\tan\gamma_{av} + \frac{\Delta I}{I_c}\tan\pi\frac{\Phi}{\Phi_o}}{1 - \frac{\Delta I}{I_c}\tan\gamma_{av}\tan\pi\frac{\Phi}{\Phi_o}}. \qquad \text{(A.14)}$$

If the substitution

$$\tan\delta = \frac{\Delta I}{I_c}\tan\pi\frac{\Phi}{\Phi_o} \qquad \text{(A.15)}$$

can be made, Eq. (A.14) becomes

$$\tan\varphi = \frac{\tan\gamma_{av} + \tan\delta}{1 - \tan\gamma_{av}\tan\delta} = \tan(\gamma_{av} + \delta). \qquad \text{(A.16)}$$

So, for $-\pi/2 < \varphi < \pi/2$, the total supercurrent through the dc SQUID is given by

$$I = \left[(\Delta I)^2 + 4 I_1 I_2 \cos^2 \pi \frac{\Phi}{\Phi_o} \right]^{\frac{1}{2}} e^{i(\gamma_{av} + \delta)} \tag{A.17}$$

or taking the imaginary part of Eq. (A.17)

$$I = \left[(\Delta I)^2 + 4 I_1 I_2 \cos^2 \pi \frac{\Phi}{\Phi_o} \right]^{\frac{1}{2}} \sin(\gamma_{av} + \delta). \tag{A.18}$$

For $I_1 = I_2$, this reduces to the symmetric result

$$I = I_c \cos \pi \frac{\Phi}{\Phi_o} \sin \gamma_{av} . \tag{A.19}$$

From Eq. (A.18), I note that amplitude modulation is accompanied by a magnetic flux dependent phase shift when the critical currents are unequal. Also, the supercurrent magnitude never vanishes. By Eq. (A.2), γ_{av} is constant with time in the zero voltage state. For an ideal dc SQUID in general, the dynamic behavior of γ_{av} is the same as that of a single Josephson junction. When the SQUID loop inductance and other circuit elements are taken into account, the dynamic behavior of γ_{av} only matches that of a single junction when the dc SQUID is perfectly symmetric [63,64].

Note that when $\Delta I << I_c$, Eq. (A.15) can be approximated by

$$\delta \approx \frac{\Delta I}{I_c} \tan \pi \frac{\Phi}{\Phi_o} << 1 \tag{A.20}$$

unless $\Phi / \Phi_o = n + 1/2$ for some integer n. Then, to first order, Eq. (A.18) becomes

$$\begin{aligned} I &\approx I_c \cos \pi \frac{\Phi}{\Phi_o} (\sin \gamma_{av} + \delta \cos \gamma_{av}) \\ &\approx I_c \cos \pi \frac{\Phi}{\Phi_o} \left(\sin \gamma_{av} + \frac{\Delta I}{I_c} \tan \pi \frac{\Phi}{\Phi_o} \cos \gamma_{av} \right) \\ &\approx I_c \cos \pi \frac{\Phi}{\Phi_o} \sin \gamma_{av} + \Delta I \sin \pi \frac{\Phi}{\Phi_o} \cos \gamma_{av} \end{aligned} \tag{A.21}$$

On the other hand, if $I_1 >> I_2$, so that $\Delta I \approx I_c$, Eq. (A.15) can be approximated by

$$\begin{aligned} \tan\delta &\approx \tan\pi\frac{\Phi}{\Phi_o} \\ \delta &\approx \pi\frac{\Phi}{\Phi_o} + \pi n = \frac{\Delta\gamma}{2} \end{aligned} \tag{A.22}$$

where in the last equality, Eq. (A.9) is applied. Then, to first order, Eq. (A.18) becomes

$$\begin{aligned} I &\approx \left({I_1}^2 + 2I_1 I_2 \cos 2\pi\frac{\Phi}{\Phi_o} \right)^{\frac{1}{2}} \sin\left(\gamma_{av} + \frac{\Delta\gamma}{2} \right) \\ &\approx I_1 \left(1 + \frac{I_2}{I_1}\cos 2\pi\frac{\Phi}{\Phi_o} \right) \sin\left(\frac{\gamma_1 + \gamma_2}{2} + \frac{\gamma_1 - \gamma_2}{2} \right) \\ &\approx I_1 \sin\gamma_1 + I_2 \cos 2\pi\frac{\Phi}{\Phi_o}\sin\gamma_1 \end{aligned} \tag{A.23}$$

These results indicate that as the asymmetry in the critical currents of the Josephson junctions increases, the modulation amplitude of the SQUID supercurrent decreases, and the total supercurrent becomes dominated by the larger critical current junction in the extreme.

APPENDIX B: Design of a New SQUID Microscope Cold Finger

In this appendix, I layout the design of a new SQUID microscope cold finger using strips of ultra pure (99.999% pure) copper foil. Determination of the number of foil strips needed to cool the cold finger can be estimated by considering the heat flow. When testing the prototype SQUID microscope, I found that the cold finger with the current design reached temperatures as low as 3.9 K. Assuming that the cold finger is in thermal equilibrium at the same temperature with the second stage of the cryocooler, the heat load can be estimated from the manufacturer's nominal cooling capacity of the cryocooler, which is about 0.4 W.

A significant portion of this heat load is due to radiative heating from the room temperature environment. The power P_{in} incident on the cold finger is given by the Stefan-Boltzmann Law:

$$P_{in} = \frac{\partial Q}{\partial t} = A\varepsilon\sigma T^4 \tag{B.1}$$

where, A is the surface area of the body, ε is its emissivity, $\sigma = 5.67\times10^{-8}$ W·m^{-2}·K^{-4} is the Stefan-Boltzmann constant, and T is its temperature [170]. The net power between the emitted and absorbed heat by the cold finger is then

$$P_{net} = P_2 - P_1 = \Delta\frac{\partial Q}{\partial t} = A\varepsilon\sigma\left(T_2^4 - T_1^4\right) \tag{B.2}$$

where, T_2 = 3.9 K and T_1 = 300 K for room temperature. Because of a radiation heat shield, only the tip of a sapphire rod holding the SQUID chip is exposed to room

temperature radiation. If the tip is approximated by a hemisphere of area $A = 2\pi r^2$ with $r = 0.7$ cm, the net inward heat flow from Eq. (4.3) is 0.14 W for an ideal black body, $\varepsilon = 1$. This value is an upper limit to the heat flow as real bodies absorb and radiate with $\varepsilon < 1$. Similar calculations for heating due to the radiation shield, for which $T_1 = 32$ K, show orders of magnitude less power because of the fourth power dependence in temperature despite that the cryocooler's entire second stage area is exposed.

From this analysis, it is clear that the cold finger would not reach 4 K without a radiation shield. Furthermore, the difference between the cooling capacity of 0.4 W and maximum radiative heating of 0.14 W suggests that there were other heating sources. This may have come in the form of conductive heating through the copper wires that go from room temperature to the cold finger. Some of the leads were used for diagnostic purposes and could be removed without compromising the microscope performance.

The heat transfer by copper leads or foil strips can be estimated as follows. The heat flow through a strip of copper is given by the thermal conduction equation for solids:

$$\frac{\partial Q}{\partial t} = \frac{A}{l}\int_{T_1}^{T_2} K(T)\,dT \qquad \text{(B.3)}$$

where, A is the cross sectional area of the solid, l is its length, and $K(T)$ is the temperature dependent thermal conductivity of the solid [171]. Over the temperature range from 300 K to 4 K, the thermal conductivity of ultra high purity copper changes dramatically, particularly at low temperatures [172]. Near room temperature, the

value of $K(T)$ is around 4 $W \cdot cm^{-1} \cdot K^{-1}$. The conductivity peaks near 10 K, where it is around 200 $W \cdot cm^{-1} \cdot K^{-1}$, and then drops dramatically below 100 $W \cdot cm^{-1} \cdot K^{-1}$ as the temperature drops under 4 K. If the average thermal conductivity between 300 K and 4 K is 17 $W \cdot cm^{-1} \cdot K^{-1}$, the heat flow for a 1 cm wide, 10 cm long strip that is 0.005 cm thick is 2.5 W. However, as the temperature of the tip approaches 4 K, the heat flow decreases to less than 0.4 W.

In section 4.3, I discussed the fact that there was a 1 K temperature difference between the SQUID and the cold finger due to heating from the room temperature environment. The copper foil strips must provide at minimum the 0.4 W heat flow capacity at 4 K in the presence of the heating that causes the 1 K difference. At 4 K, the heat flow for a 1 K drop is around 0.05 W per 1 cm wide, 10 cm long strip of copper foil mentioned above. Thus, eight or more strips of foil are needed for the estimated 0.4 W load.

With use of ultra high purity copper foil, a redesign of the existing cold finger is necessary to accommodate the additional space needed for attaching the foil. For good vibration isolation, the foil should be formed into an S-shape (see Fig. B.1). This maximizes flexibility in all three dimensions. To maximize thermal conductance, the contact areas between the foil and cold finger must be maximized, though too much rigid contact will decrease flexibility. As in other designs, I expect some soldering or application of thermally conducting filler material in addition to mechanical clamping will be necessary for the contact area.

Vibration isolation of the SQUID cold finger would also improve with a better position holder than the existing fiberglass holder which fits over the cold finger. A

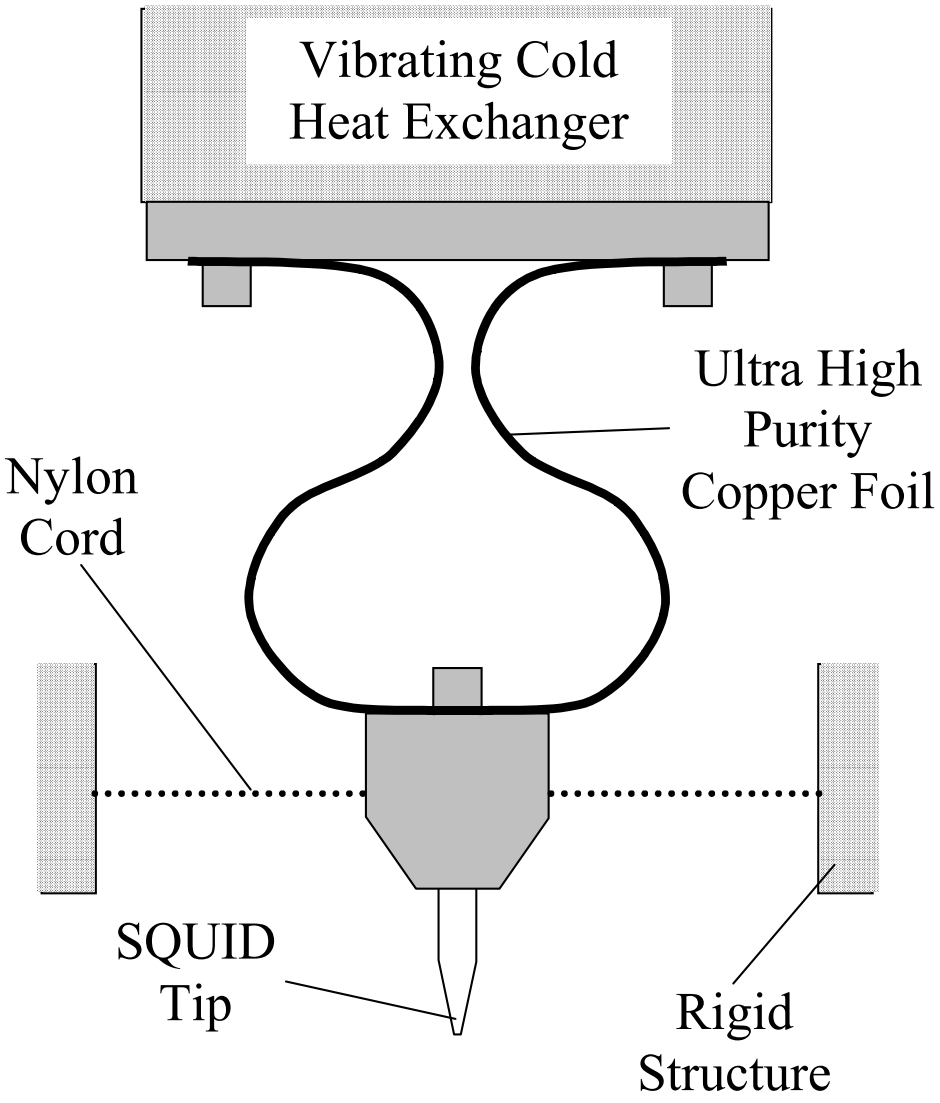

FIG. B.1. Diagram of SQUID microscope cold finger using strips of ultra high purity copper foil to connect the top and bottom parts. The foil strips shown in black are formed into an S-shape which provides vibration isolation between the two parts. Only two strips are shown, though additional strips can be added. The part of the cold finger which holds the SQUID tip is rigidly held by nylon cord with low thermal conductance.

mechanism to more rigidly hold the SQUID tip inside the prototype microscope could be adapted from the motion isolation scheme of Kenyon *et al*. for an SET system [131,132]. That system made use of thin yet strong nylon cord, such as dental-floss, which has low thermal conducting properties. The cord held the cold finger in a mesh with the ends tied to a rigid fixture in the vacuum chamber. If adapted, such a scheme would not only require changes in the cold finger but also require modifications in the radiation shield and vacuum chamber.

APPENDIX C: Characteristics and Impedance Analysis of Twisted Pair Wire Dip Probe

Prior experiments with resistively shunted niobium dc SQUIDs were performed in LHe with a dip probe. The dip probe used small diameter twisted pair magnet wire to send and receive signals to and from the SQUID chip [see Fig. 7.1(a)]. I began to see problems with the dip probe at high frequencies during tests of SQUID microscope transformers used with FLL electronics. Peaks in the voltage gain seemed to be occurring at much lower frequencies than expected. The main cause was parasitic capacitance in the transformer coil windings, but I inquired whether the dip probe I was using during low temperature testing was contributing to the effect.

I tested the dip probe's approximately 1.3 m twisted pair cable in an open circuit configuration measuring the ratio of the input current amplitude to the output voltage amplitude of sinusoidal signals at different frequencies (see Fig. C.1). Results showed an effective capacitance of 1.9±0.1 nF for frequencies up to 100 kHz, which was an order of magnitude higher than in typical coaxial cable. At higher frequencies, distortions in the sinusoidal output waveform began to appear while the output voltage continued to decrease. Basically, the driving current was leaking through the cable before it would reach the load connected at the end. If I

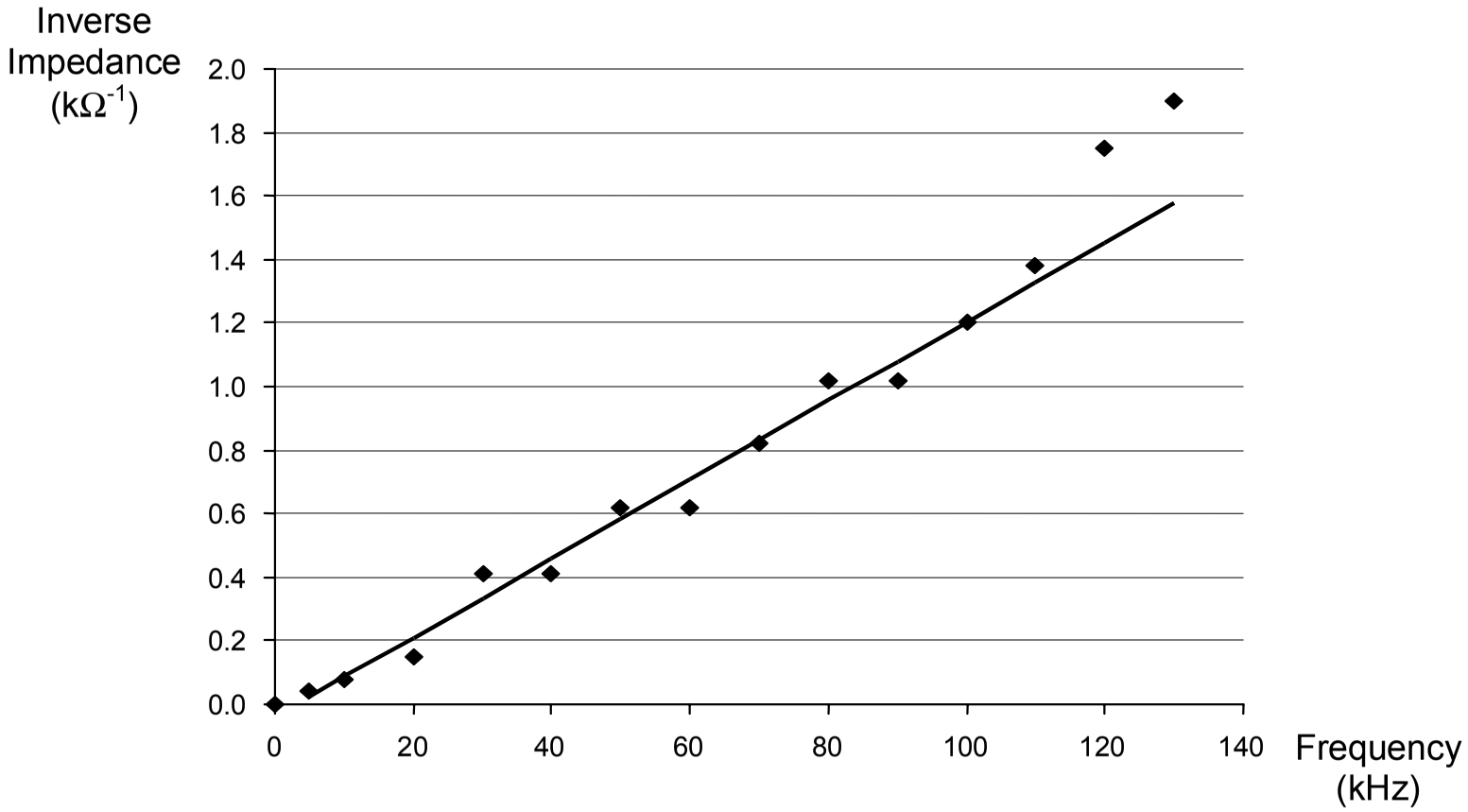

FIG. C.1. Inverse impedance versus frequency of cable in the twisted pair wire LHe dip probe. The inverse impedance values were determined by driving a sinusoidal current through the probe leads which were left open at the other end. The current amplitude was divided by the amplitude of the voltage across the leads at various frequencies. The graph shows linear behavior consistent with a capacitor. The solid line is the best linear fit through the data points and gives a capacitance $C = 1.9 \pm 0.1$ nF for the 1.3 m cable. Signals above 110 kHz were not used in the fit.

extrapolated the effect to signal frequencies 1 GHz and above, the amplitude of the impedance across the twisted pair cable would be

$$Z_c = \frac{1}{\omega C} \leq 0.08\ \Omega \tag{C.1}$$

which would short out any current sent through the dip probe. However, the testing and analysis were confined to the low frequency limit, and by 1 GHz, transmission line theory should be used to analyze the apparatus.

Approximating the twisted pair wire with two parallel cable conductors, the characteristic impedance of the wiring from field equations and transmission line theory is given by

$$Z_c = \frac{1}{\pi}\sqrt{\frac{\mu_o}{\varepsilon}}\cosh^{-1}\frac{D}{d} \tag{C.2}$$

where D is the center-to-center distance between the cables, d is the diameter of each cable, and ε is the permittivity of the medium [160]. As D is only slightly larger than d, Eq. (C.2) can be approximated by substituting

$$\frac{D}{d} = 1 + \delta \tag{C.3}$$

where $\delta << 1$. Recognizing that

$$\cosh z = \frac{e^z + e^{-z}}{2} \approx \frac{1}{2}\left(1 + z + \frac{1}{2}z^2 + 1 - z + \frac{1}{2}z^2\right) = 1 + \frac{1}{2}z^2 \tag{C.4}$$

for small z,

$$\begin{aligned} \delta &= \frac{1}{2}z^2 \\ z &= \sqrt{2\delta} \end{aligned} \quad . \tag{C.5}$$

The characteristic impedance Z_c of the cable then becomes

$$Z_c \approx \frac{1}{\pi}\sqrt{2\delta\,\frac{\mu_o}{\varepsilon}}\,. \tag{C.6}$$

As δ is small, Z_c is also small.

The value of Z_c can also be estimated from its relation with the capacitance C per unit length, which is

$$Z_c = \frac{\sqrt{\mu_o \varepsilon}}{C}. \tag{C.7}$$

Although ε is not known, a lower limit is $\varepsilon \approx \varepsilon_o$ for vacuum or air. The actual value of ε is not expected to be different by orders of magnitude. With the length of the cable at 1.3 m, Eq. (C.7) gives $Z_c \approx 2.3\ \Omega$. This result is consistent with the assumptions of Eq. (C.6), giving $\delta \sim 2\times10^{-4}$.

The value of Z_c results in an impedance mismatch between the twisted pair cable, pulse generator, and dc SQUID. Most high frequency apparatus are matched to 50 Ω. Consequently, most of the high frequency signals sent to the dip probe are reflected back. From transmission line theory, the coefficient of reflection Γ is given by

$$\Gamma = \frac{Z_l - Z_c}{Z_l + Z_c} \tag{C.8}$$

where Z_l is the characteristic impedance of the load connected to the cable [163]. In this case, the load is the twisted pair cable with Z_l = 2.3 Ω, and Z_c = 50 Ω. Thus, using Eq. (C.8), $\Gamma \approx -0.91$ so most of the signal is reflected back with opposite polarity. The coefficient of transmission T is given by

$$T = 1 + \Gamma = \frac{2Z_l}{Z_l + Z_c} \approx 0.09 \tag{C.9}$$

for the twisted pair cable.

Figure C.2 shows a simple model of the dip probe and dc SQUID configured with a driving signal generator at one end and measuring instrumentation with 50 Ω termination at the other. All of the cable is assumed to be loss-less. When the dc SQUID remains in the zero voltage state, $Z_s = 0$ and $\Gamma = -1$ between the twisted pair cable and the SQUID, so no current flows either to the SQUID nor to the other cable resulting in no voltage signal detected at the other end.

On the other hand, if the dc SQUID triggers into the resistive state, a voltage appears across the SQUID, and a signal is transmitted to the detector end. For simplicity, the dc SQUID can be modeled as a resistive load connected across the twisted pair cable. For SQUID BH, $Z_s = 16.9\ \Omega$. The load impedance seen by the twisted pair cable then becomes $Z_l = (Z_s^{-1} + Z_{o2}^{-1})^{-1} \approx 2.0\ \Omega$, and $\Gamma \approx -0.06$. More importantly, the voltage across the SQUID, which is the signal that I attempt to observe in my experiments, must travel through another twisted pair cable to the measuring instrumentation. When the impedance of that cable transitions from 2.3 Ω to 50 Ω, reflections occur with $\Gamma \approx 0.91$, which create more signals as they get reflected back at the other end.

What this demonstrates is that the mismatch in impedances will result in "ringing" of pulse signals between the twisted pair cables, regardless of whether the outside 50 Ω cables are matched at the ends. If the cables are not long enough, the ringing will overlap with the original pulse and make it difficult to identify the triggering of the SQUID from the voltage signal. Attempts to match impedances by shunting a $(Z_{o2}^{-1} - Z_{o1}^{-1})^{-1} \approx 2.4\ \Omega$ resistor between the twisted pair and coaxial cable

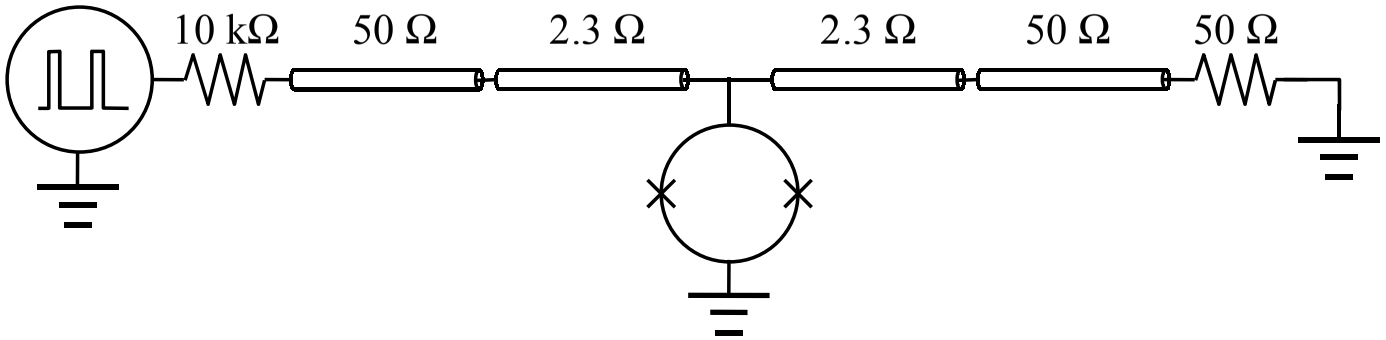

FIG. C.2. Simple model of SQUID circuit using the LHe dip probe with twisted pair wire and coaxial cable at the ends. The measuring instrumentation detects the voltage across the 50 Ω resistor on the right. This circuit configuration is inadequate for high speed large bandwidth applications due to reflections between the 2.3 Ω cable.

reduces the current and consequently the signal to the measuring instrumentation to less than 5% of the original signal. With my measuring equipment, this would bring the overall signal level to the limit of uncertainty.

APPENDIX D: Change in Magnetic Flux due to a Rotation

Assuming a uniform magnetic field, the magnetic flux Φ and the change in flux $\delta\Phi$ over an area A due to a rotation of the area by an angle $\delta\theta$ are given by

$$\Phi = BA\cos(\theta) \tag{D.1}$$

$$\delta\Phi = -BA\sin(\theta)\,\delta\theta \tag{D.2}$$

where θ is the angle between the direction of the uniform field $\boldsymbol{B}$ and the normal direction to the area. The magnitude of $\delta\Phi$ is bound by the upper limit

$$\delta\Phi \approx BA\,\delta\theta \tag{D.3}$$

which can be used as an approximation of Eq. (D.2).

For a rotation of 90°, there can be an apparent change in flux $\Delta\Phi$ that is given by $n\Phi_o < \Delta\Phi < m\Phi_o$ where n and m are some constants. Now, $\Delta\Phi$ depends on the range of angles with respect to the magnetic field and can vary between a minimum and maximum given by

$$\begin{cases} \Delta\Phi_{min} = BA - BA\cos\dfrac{\pi}{4} = BA\left(1 - \dfrac{1}{\sqrt{2}}\right). \\ \Delta\Phi_{max} = BA \end{cases} \tag{D.4}$$

This is demonstrated in Fig. D.1 which shows the SQUID orientations for $\Delta\Phi_{min}$ and $\Delta\Phi_{max}$. In the case of $\Delta\Phi_{min}$, only half of the change $\Delta\Phi$ is due to a continuous increase or decrease of the magnetic flux due to symmetry with respect to the angle θ.

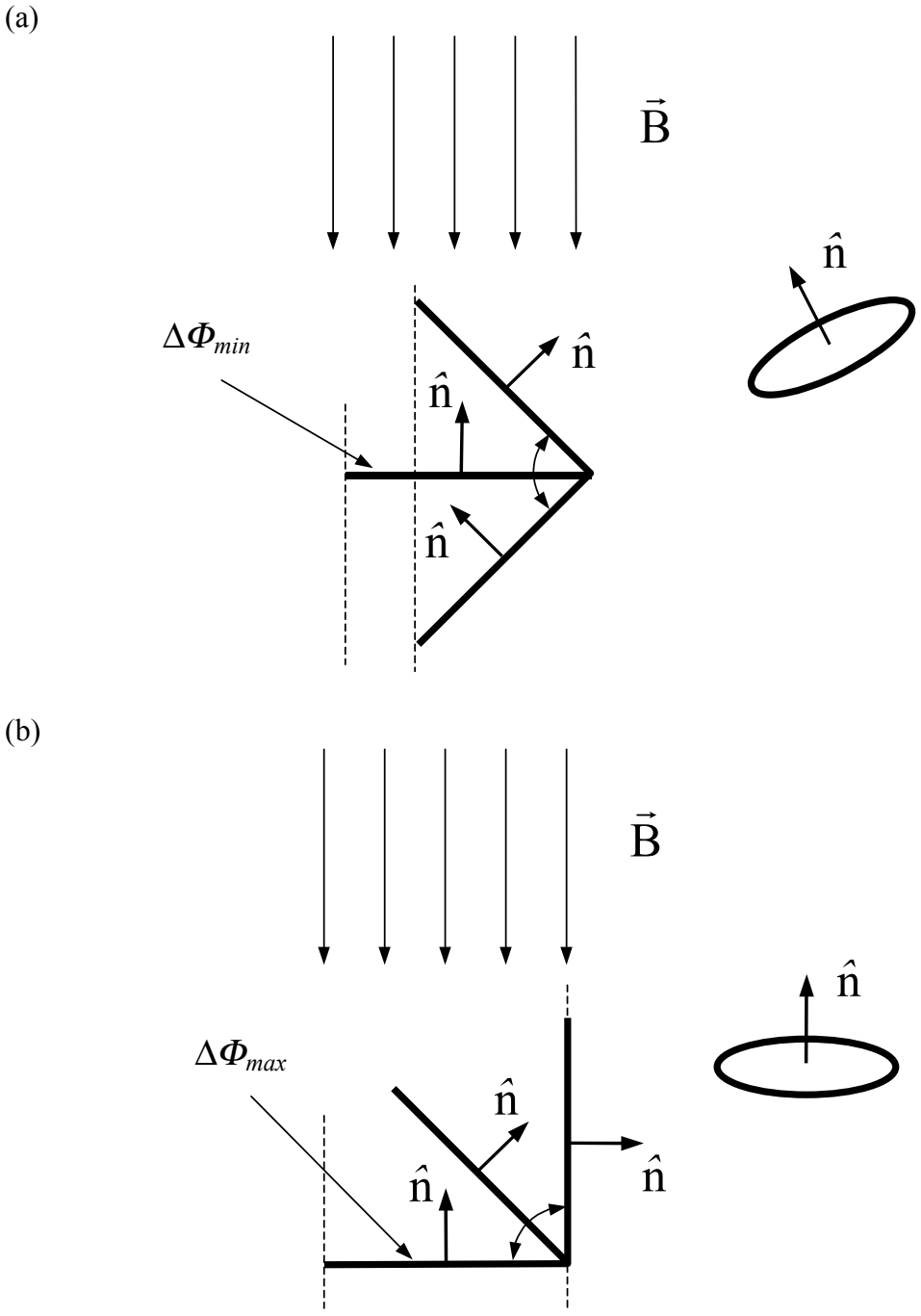

FIG. D.1. Diagrams showing the orientations of an area ***n*** with respect to a uniform magnetic field ***B***, as the area goes through a 90° rotation about an axis normal to the direction of the field. The two diagrams show when the change in magnetic flux through the area is (a) a minimum and (b) a maximum as the area is rotated.

The apparent change $\Delta\Phi$ can be a result of either the orientation producing $\Delta\Phi_{min}$ or $\Delta\Phi_{max}$. Substituting for $\Delta\Phi$, the two cases give

$$\frac{n}{2}\Phi_o < BA\left(1-\frac{1}{\sqrt{2}}\right) < \frac{m}{2}\Phi_o \tag{D.5}$$

$$n\Phi_o < BA < m\Phi_o \tag{D.6}$$

for $\Delta\Phi_{min}$ and $\Delta\Phi_{max}$, respectively. Combining Eqs. (D.5) and (D.6), the full range of BA is given by

$$n\Phi_o < BA < m\left(1+\frac{1}{\sqrt{2}}\right)\Phi_o\,. \tag{D.7}$$

Using Eqs. (D.3) and (D.7), I can estimate the small change in flux due to the rotation $\delta\theta$ of the area. For $n = 3$ and $m = 4$, this results in

$$3\Phi_o\delta\theta < \delta\Phi < \left(4+2\sqrt{2}\right)\Phi_o\delta\theta\ . \tag{D.8}$$

For $\delta\theta$ = 0.5°, Eq. (D.8) gives $0.03\Phi_o < \delta\Phi < 0.06\Phi_o$. Given that Eq. (D.3) is an upper bound limit, I believe $\delta\Phi$ is closer to the lower limit of $0.03\Phi_o$.

APPENDIX E: Modeling the dc SQUID as a Resistor in the Large Bandwidth Dip Probe

Following the approach of section 7.5, the dc SQUID is modeled as a resistor in the large bandwidth dip probe. This involves replacing Z_s in Figs. 7.8(a) and 7.8(b) with a resistor R_s such that the new impedance for the segment is $R_s + j\omega L_2$. Analysis is performed on the resulting circuit in the frequency domain. The output signal Fourier components in complex number form are then given by

$$V_{out} = \frac{\frac{0.01V_{in}}{\pi\omega}\left\{\left(\frac{R_s}{Z_c}\right)^2 + \left(\frac{\omega L}{Z_c}\right)^2\right\} sin\frac{\omega\tau}{2} e^{j\omega(t-lZ_cC)}}{\left\{2\left(\frac{R_s}{Z_c}\right)^2 + \left(\frac{R_s}{Z_c}\right) + 3\left(\frac{\omega L}{Z_c}\right)^2\right\} + j\left(\frac{\omega L}{Z_c}\right)\left\{\left(\frac{R_s}{Z_c}\right)^2 + \left(\frac{R_s}{Z_c}\right) + \left(\frac{\omega L}{Z_c}\right)^2 - 1\right\}} \qquad \text{(E.1)}$$

again with the approximation $L = L_1 \approx L_2$. The dc component of V_{out} is given by

$$V_{out} = \frac{R_s}{2R_s + Z_c}\frac{0.005\tau}{2\pi}V_{in}. \qquad \text{(E.2)}$$

Taking the sum over the same frequencies as in section 7.5, the resulting output voltage responses after the delay time $lZ_cC \sim 10$ ns are plotted in Fig. E.1(a) for the parameter values $\tau = 5$ ns, $V_{in} = 1.7$ V, and $L = 11.9$ nH. The different curves show what happens when the resistance R_s varies from 0 Ω to 160 Ω, which encompasses the estimated resistances of SQUID BH (see Fig. 3.9 or Table I). The current through R_s is plotted in Fig. E.1(b).

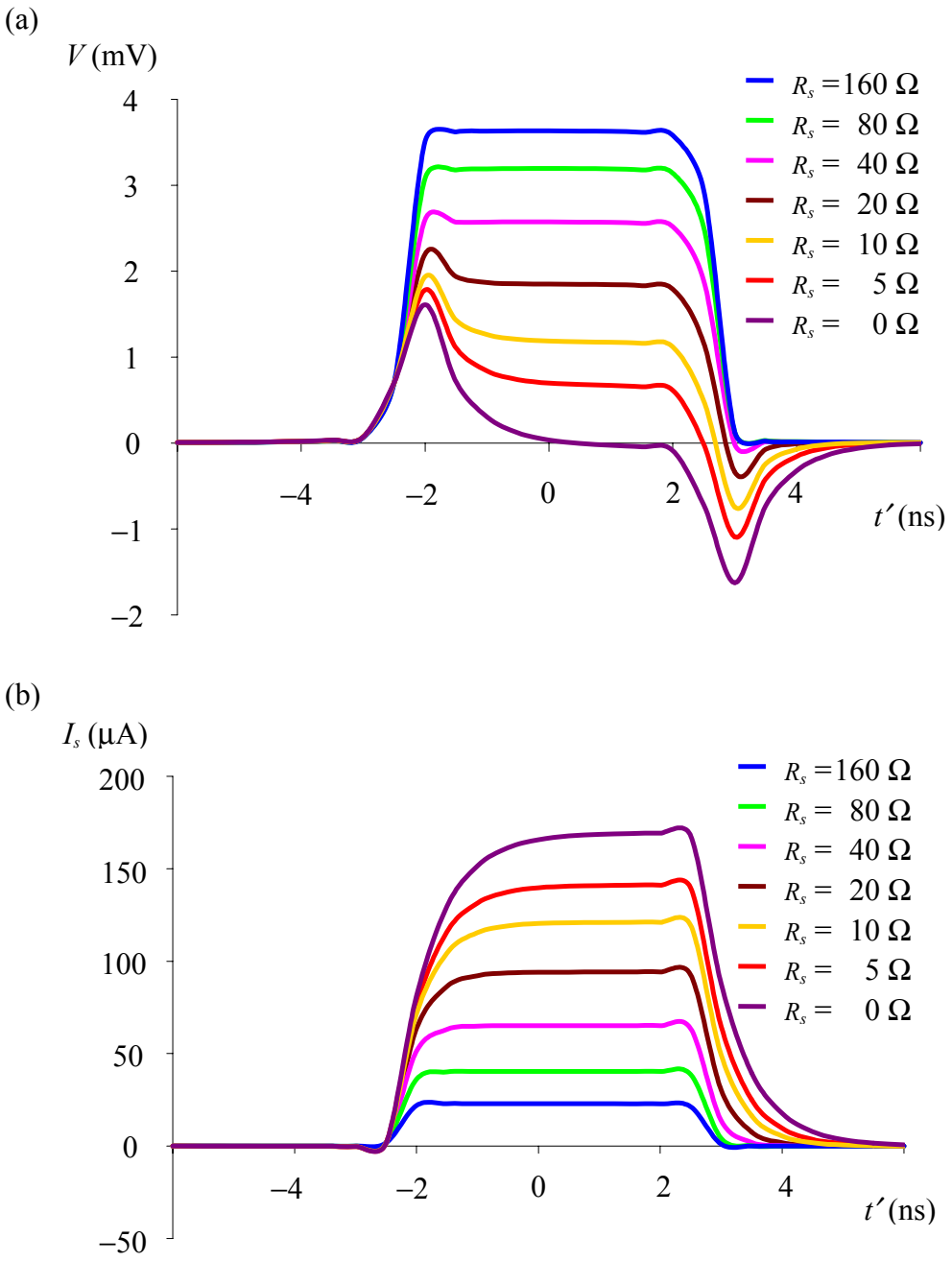

FIG. E.1. (a) Plots of the calculated output voltage response of the SQUID circuit using the large bandwidth dip probe with $L = 11.9$ nH and modeling the dc SQUID as a resistor. The input voltage is the 1.7 V, 5 ns pulse seen in Fig. 7.10(b). The voltage response appears after a delay Δt with respect to the input pulse centered around $t = 0$, where $t' = t - \Delta t$. (b) Plots of the calculated current through the dc SQUID modeled as a resistor, corresponding to voltage responses in (a).

Initially, the system is in the R_s = 0 Ω state. As the current through R_s increases and exceeds the SQUID critical current I_c, the system jumps to the state with the appropriate resistance $R_s = 2\Delta/eI_c$. When the current decreases below the retrapping current I_r, the system should return to the R_s = 0 Ω state. The plots show that the voltage amplitudes vary logarithmically with R_s and that there is an initial rapid rise in the current through R_s, which levels off at a height dependent on R_s. This helps explain the high sensitivity of the onset of triggering when I_c is large, as seen in the analysis of section 7.5 where the dc SQUID is modeled as a voltage source. Furthermore, large changes in the voltage response diminish as the value of R_s increases. The maximum current through R_s also decreases logarithmically with R_s. So, as the critical current decreases, the effective resistance R_s increases and overall sensitivity to the critical current decreases.

Although modeling the dc SQUID as a resistor sheds additional light on the SQUID circuit's behavior, the model possesses the same flaw as when the SQUID is modeled as a voltage source. In particular, sudden changes in the current through R_s cannot be accounted for. The problem is most significant for small R_s including the range R_s = 10 Ω to 40 Ω which are the resistances corresponding to the critical currents of SQUID BH.

Finally, comparing the input current pulse profile of Fig. 7.5 with the output voltage response in the resistor model, similarities can be seen in the plots for small R_s. This suggests that there is a significant reactive element in the transport of current pulses through the dip probe and connected elements. The result is the observed large range of signal rise times and peak heights in the profile of current pulses

applied to the SQUID, which depend on the specific circuit configuration. A consequence of this is that the optimal input voltage pulse height becomes difficult to predict and will need to be determined experimentally.

REFERENCES

[1] R. C. Jaklevic, J. Lambe, A. H. Silver, and J. E. Mercereau, Phys. Rev. Lett. **12**, 159 (1964).

[2] R. C. Jaklevic, J. J. Lambe, A. H. Silver, and J. E. Mercereau, Phys. Rev. Lett. **12**, 274 (1964).

[3] R. C. Jaklevic, J. Lambe, J. E. Mercereau, and A. H. Silver, Phys. Rev. **140**, 1628 (1965).

[4] D. Koelle, R. Kleiner, F. Ludwig, E. Dantsker, and J. Clarke, Rev. Mod. Phys. **71**, 631 (1999).

[5] M. B. Ketchen, W. M. Goubau, J. Clarke, and G. B. Donaldson, J. Appl. Phys. **49**, 4111 (1978).

[6] J. Clarke and R. H. Koch, Science **242**, 217 (1988).

[7] J. Clarke, Science **184**, 1235 (1974).

[8] R. C. Black, Ph.D. thesis, University of Maryland, College Park, 1995.

[9] A. Mathai, Ph.D. thesis, University of Maryland, College Park, 1995.

[10] E. F. Fleet, S. Chatraphorn, F. C. Wellstood, L. A. Knauss, and S. M. Green, Rev. Sci. Instrum. **72**, 3281 (2001).

[11] A. P. Nielsen, Ph.D. thesis, University of Maryland, College Park, 2001.

[12] S.-Y. Lee, Ph.D. thesis, University of Maryland, College Park, 2004.

[13] F. Baudenbacher, L. E. Fong, J. R. Holzer, and M. Radparvar, Appl. Phys. Lett. **82**, 3487 (2003).

[14] S. Chatraphorn, E. F. Fleet, F. C. Wellstood, L. A. Knauss, and T. M. Eiles, Appl. Phys. Lett. **76**, 2304 (2000).

[15] B. J. Roth, N. G. Sepulveda, and J. P. Wikswo Jr., J. Appl. Phys. **65**, 361 (1989).

[16] J. O. Gaudestad, L. A. Knauss, A. Orozco, and S. I. Woods, Solid State Technol. **47**, 55 (2004).

[17] Magma C20, Neocera Inc., Beltsville, MD.

[18] R. L. Forgacs and A. Warnick, Rev. Sci. Instrum. **38**, 214 (1967).

[19] F. Wellstood, C. Heiden, and J. Clarke, Rev. Sci. Instrum. **55**, 952 (1984).

[20] R. H. Koch, J. R. Rozen, P. Wöltgens, T. Picunko, W. J. Goss, D. Gambrel, D. Lathrop, R. Wiegert, and D. Overway, Rev. Sci. Instrum. **67**, 2968 (1996).

[21] P. A. Moskowitz, S. M. Faris, and A. Davidson, IEEE Trans. Magn. **19**, 503 (1983).

[22] S. R. Whiteley, G. K. G. Hohenwarter, and S. M. Faris, IEEE Trans. Magn. **23**, 899 (1987).

[23] E. R. Hanson, G. K. G. Hohenwarter, S. R. Whiteley, and S. M. Faris, Proc. SPIE **795**, 143 (1987).

[24] S. R. Whiteley, E. R. Hanson, G. K. G. Hohenwarter, F. Kuo, and S. M. Faris, Proc. SPIE **947**, 138 (1988).

[25] W. C. Stewart, Appl. Phys. Lett. **14**, 392 (1969).

[26] S. M. Faris and N. F. Pedersen, Physica B **108**, 1087 (1981).

[27] Cryomech, *Model PT405 Cryogenic Refrigerator – Operation and Service Manual* (Syracuse, 2000).

[28] S. P. Kwon, L. A. Knauss, N. Lettsome, A. B. Cawthorne III, C. J. Lobb, and F. C. Wellstood, Bull. Am. Phys. Soc. **48**, 573 (2003).

[29] TRISTAN Technologies Inc., *User's Manual for iMAG HTS Multi-channel dc SQUID System* (San Diego, 1998).

[30] S. P. Kwon, C. P. Vlahacos, A. J. Berkley, M. A. Gubrud, F. C. Wellstood, and A. B. Cawthorne III, Bull. Am. Phys. Soc. **49**, 135 (2004).

[31] J. Matthews, C. P. Vlahacos, S. P. Kwon, and F. C. Wellstood, IEEE Trans. Appl. Supercond. **15**, 688 (2005).

[32] C. J. Gorter, Rev. Mod. Phys. **36**, 3 (1964).

[33] J. Bardeen, L. N. Cooper, and J. R. Schrieffer, Phys. Rev. **106**, 162 (1957).

[34] J. Bardeen, L. N. Cooper, and J. R. Schrieffer, Phys. Rev. **108**, 1175 (1957).

[35] M. Tinkham, *Introduction to Superconductivity* 2nd. ed. (McGraw-Hill, New York, 1996), Chap. 1, p. 9-11.

[36] L. N. Cooper, Phys. Rev. **104**, 1189 (1956).

[37] L. N. Cooper and B. Stölan, Phys. Rev. B **4**, 863 (1971).

[38] B. D. Josephson, Rev. Mod. Phys. **36**, 216 (1964).

[39] B. D. Josephson, Rev. Mod. Phys. **46**, 251 (1974).

[40] V. Ambegaokar and A. Baratoff, Phys. Rev. Lett. **10**, 486 (1963).

[41] V. Ambegaokar and A. Baratoff, Phys. Rev. Lett. **11**, 104(E) (1963).

[42] P. W. Anderson and J. M. Rowell, Phys. Rev. Lett. **10**, 230 (1963).

[43] S. Washburn, R. A. Webb, R. F. Voss, and S. M. Faris, Phys. Rev. Lett. **54**, 2712 (1985).

[44] M. H. Devoret, J. M. Martinis, D. Esteve, and J. Clarke, Phys. Rev. Lett. **53**, 1260 (1984).

[45] J. M. Martinis, M. H. Devoret, and J. Clarke, Phys. Rev. Lett. **55**, 1543 (1985).

[46] M. H. Devoret, J. M. Martinis, and J. Clarke, Phys. Rev. Lett. **55**, 1908 (1985).

[47] A. J. Berkley, Ph.D. thesis, University of Maryland, College Park, 2003.

[48] H. Xu, Ph.D. thesis, University of Maryland, College Park, 2004.

[49] J. R. Anderson, A. J. Berkley, A. J. Dragt, M. A. Gubrud, P. R. Johnson, C. J. Lobb, R. C. Ramos, F. W. Strauch, F. C. Wellstood, and H. Xu, Superlattices and Microstructures **32**, 231 (2003).

[50] H. Xu, A. J. Berkley, M. A. Gubrud, R. C. Ramos, J. R. Anderson, C. J. Lobb, and F. C. Wellstood, IEEE Trans. Appl. Supercond. **13**, 956 (2003).

[51] P. R. Johnson, F. W. Strauch, A. J. Dragt, R. C. Ramos, C. J. Lobb, J. R. Anderson, and F. C. Wellstood, Phys. Rev. B **67**, 020509(R) (2003).

[52] T. P. Orlando and K. A. Delin, *Foundations of Applied Superconductivity* (Addison-Wesley, Reading Massachusetts, 1991), Chap. 8, p. 398-405.

[53] C. Kittel, *Introduction to Solid State Physics* 7th. ed. (John Wiley & Sons, New York, 1996), Chap. 12, p. 366-369.

[54] J. J. Winter, H. A. Leupold, and J. T. Breslin, J. Appl. Phys. **43**, 631 (1972).

[55] N. Uchida, K. Enpuku, Y. Matsugaki, S. Tomita, F. Irie, and K. Yoshida, J. Appl. Phys. **54**, 5287 (1983).

[56] T. P. Orlando and K. A. Delin, *Foundations of Applied Superconductivity* (Addison-Wesley, Reading Massachusetts, 1991), Chap. 8, p. 420-431.

[57] M. Tinkham, *Introduction to Superconductivity* 2nd. ed. (McGraw-Hill, New York, 1996), Chap. 6, p. 215-217.

[58] T. P. Orlando and K. A. Delin, *Foundations of Applied Superconductivity* (Addison-Wesley, Reading Massachusetts, 1991), Chap. 8, p. 406-407.

[59] M. Tinkham, *Introduction to Superconductivity* 2nd. ed. (McGraw-Hill, New York, 1996), Chap. 6, p. 198.

[60] T. P. Orlando and K. A. Delin, *Foundations of Applied Superconductivity* (Addison-Wesley, Reading Massachusetts, 1991), Chap. 8, p. 410-420.

[61] M. Tinkham, *Introduction to Superconductivity* 2nd. ed. (McGraw-Hill, New York, 1996), Chap. 1, p. 4-6; Chap. 3, p. 100-108.

[62] T. P. Orlando and K. A. Delin, *Foundations of Applied Superconductivity* (Addison-Wesley, Reading Massachusetts, 1991), Chap. 10, p. 528-544.

[63] C. D. Tesche and J. Clarke, J. Low Temp. Phys. **29**, 301 (1977).

[64] V. J. de Waal, P. Schrijner, and R. Llurba, J. Low Temp. Phys. **54**, 215 (1984).

[65] M. Tinkham, *Introduction to Superconductivity* 2nd. ed. (McGraw-Hill, New York, 1996), Chap. 6, p. 225-229.

[66] W. C. Stewart, Appl. Phys. Lett. **12**, 277 (1968).

[67] D. E. McCumber, J. Appl. Phys. **39**, 3113 (1968).

[68] S. H. Strogatz, *Nonlinear Dynamics and Chaos* (Perseus, Cambridge Massachusetts, 1994), Chap. 4, p. 106-113.

[69] T. P. Orlando and K. A. Delin, *Foundations of Applied Superconductivity* (Addison-Wesley, Reading Massachusetts, 1991), Chap. 9, p. 458-466.

[70] M. Tinkham, *Introduction to Superconductivity* 2nd. ed. (McGraw-Hill, New York, 1996), Chap. 6, p. 202-210.

[71] D. E. Prober, S. E. G. Slusky, R. W. Henry, and L. D. Jackel, J. Appl. Phys. **52**, 4145 (1981).

[72] S. L. Wipf, J. Appl. Phys. **39**, 2538 (1968).

[73] J. M. Victor and W. H. Hartwig, J. Appl. Phys. **39**, 2539 (1968).

[74] M. Tinkham, *Introduction to Superconductivity* 2nd. ed. (McGraw-Hill, New York, 1996), Chap. 3, p. 77.

[75] T. P. Orlando and K. A. Delin, *Foundations of Applied Superconductivity* (Addison-Wesley, Reading Massachusetts, 1991), Chap. 3, p. 94-104.

[76] M. Tinkham, *Introduction to Superconductivity* 2nd. ed. (McGraw-Hill, New York, 1996), Chap. 8, p. 288-293.

[77] T. P. Orlando and K. A. Delin, *Foundations of Applied Superconductivity* (Addison-Wesley, Reading Massachusetts, 1991), Chap. 7, p. 353-368.

[78] M. Tinkham, *Introduction to Superconductivity* 2nd. ed. (McGraw-Hill, New York, 1996), Chap. 5, p. 162-170.

[79] T. P. Orlando and K. A. Delin, *Foundations of Applied Superconductivity* (Addison-Wesley, Reading Massachusetts, 1991), Chap. 9, p. 450-458.

[80] M. Tinkham, *Introduction to Superconductivity* 2nd. ed. (McGraw-Hill, New York, 1996), Chap. 6, p. 198-202.

[81] S. H. Strogatz, *Nonlinear Dynamics and Chaos* (Perseus, Cambridge Massachusetts, 1994), Chap. 8, p. 265-273.

[82] S. H. Strogatz, *Nonlinear Dynamics and Chaos* (Perseus, Cambridge Massachusetts, 1994), Chap. 4, p. 101-103; Chap. 6, p. 168-174.

[83] E. Ben-Jacob, D. J. Bergman, B. J. Matkowsky, and Z. Schuss, Phys. Rev. A **26**, 2805 (1982).

[84] J. B. Marion and S. T. Thornton, *Classical Dynamics of Particles & Systems* 3rd. ed. (Harcourt Brace Jovanovich, Orlando, 1988), Chap. 3, p. 98-151.

[85] K. T. Alligood, T. D. Sauer, and J. A.Yorke, *Chaos - An Introduction to Dynamical Systems* (Springer-Verlag, New York, 1996), Chap. 2, p. 52-57; Chap. 2, p. 84-85; Chap. 5, p 228-230.

[86] M. Tinkham, *Introduction to Superconductivity* 2nd. ed. (McGraw-Hill, New York, 1996), Chap. 3, p. 62-64.

[87] M. Tinkham, *Introduction to Superconductivity* 2nd. ed. (McGraw-Hill, New York, 1996), Chap. 9, p. 331-334.

[88] V. Ambegaokar and B. I. Halperin, Phys. Rev. Lett. **22**, 1364 (1969); **23**, 274(E) (1969).

[89] B. A. Huberman, J. P. Crutchfield, and N. H. Packard, Appl. Phys. Lett. **37**, 750 (1980).

[90] N. F. Pedersen and A. Davidson, Appl. Phys. Lett. **39**, 830 (1981).

[91] R. L. Kautz, J. Appl. Phys. **52**, 6241 (1981).

[92] R. F. Miracky, J. Clarke and R. H. Koch, Phys. Rev. Lett. **50**, 856 (1983).

[93] R. L. Kautz, J. Appl. Phys. **52**, 3528 (1981).

[94] A. H. Miklich, D. Koelle, E. Dantsker, D. T. Nemeth, J. J. Kingston, R. F. Kromann, and J. Clarke, IEEE Trans. Appl. Supercond. **3**, 2434 (1993).

[95] A. B. Cawthorne III, Ph.D. thesis, University of Maryland, College Park, 1998.

[96] J. M. Jaycox and M. B. Ketchen, IEEE Trans. Magn. **17**, 400 (1981).

[97] S. S. Mohan, M. M. Hershenson, S. P. Boyd, and T. H. Lee, IEEE J. Solid-State Circuits **34**, 1419 (1999).

[98] J. D. Jackson, *Classical Electrodynamics* 3rd. ed. (John Wiley & Sons, New York, 1999), Chap. 5, p. 216-218.

[99] T. P. Orlando and K. A. Delin, *Foundations of Applied Superconductivity* (Addison-Wesley, Reading Massachusetts, 1991), Chap. 9, p. 474-483.

[100] J. J. P. Bruines, V. J. de Waal, and J. E. Mooij, J. Low Temp. Phys. **46**, 383 (1982).

[101] H. Nyquist, Phys. Rev. **32**, 110 (1928).

[102] A. H. Silver, R. C. Jaklevic, and J. Lambe, Phys. Rev. **141**, 362 (1966).

[103] T. P. Orlando and K. A. Delin, *Foundations of Applied Superconductivity* (Addison-Wesley, Reading Massachusetts, 1991), Chap. 9, p. 470.

[104] C. Grebogi, E. Ott, and J. A. Yorke, Science **238**, 632 (1987).

[105] T. P. Orlando and K. A. Delin, *Foundations of Applied Superconductivity* (Addison-Wesley, Reading Massachusetts, 1991), Chap. 8, p. 408-410; Chap. 9, p. 466-469.

[106] M. Tinkham, *Introduction to Superconductivity* 2nd. ed. (McGraw-Hill, New York, 1996), Chap. 6, p. 211-214.

[107] S. Shapiro, Phys. Rev. Lett. **11**, 80 (1963).

[108] P. Russer, J. Appl. Phys. **43**, 2008 (1972).

[109] P. K. Tien and J. P. Gordon, Phys. Rev. **129**, 647 (1963).

[110] C. D. Tesche and J. Clarke, J. Low Temp. Phys. **37**, 397 (1979).

[111] P. Horowitz and W. Hill, *The Art of Electronics* 2nd. ed. (Cambridge University Press, Cambridge, 1989), Chap. 7, p. 440-443.

[112] B. T. Matthias, T. H. Geballe, and V. B. Compton, Rev. Mod. Phys. **35**, 1 (1963).

[113] T. P. Sheahen, Phys. Rev. **149**, 370 (1966).

[114] C. Kittel, *Introduction to Solid State Physics* 7th. ed. (John Wiley & Sons, New York, 1996), Chap. 12, p. 344.

[115] T. P. Sheahen, Phys. Rev. **149**, 368 (1966).

[116] D. Brandshaft and M. Stegall, *ICED – Graphics Editor for IC Design* (IC Editors Inc., Santa Clara, 1990).

[117] Hypres, *Niobium Design Rules* rev. 017 (Elmsford NY, 1997).

[118] Hypres, *HYPRES Niobium Integrated Circuit Fabrication – Design Rules* rev. 019 (Elmsford NY, 2003).

[119] M. P. Marder, *Condensed Matter Physics* (John Wiley & Sons, New York, 2000).

[120] C. Vlahacos, S. P. Kwon, J. Matthews, and F. C. Wellstood, Bull. Am. Phys. Soc. **50**, 298 (2005).

[121] P. Kittel, world wide web URL http://irtek.arc.nasa.gov/CryoPTHist.html

[122] P. R. Roach and A. Kashani, Adv. in Cryogenic Eng., **43**, 1895 (1998).

[123] P. Kittel, Cryogenics **32**, 843 (1992).

[124] A. T. A. M. de Waele, P. P. Steijaert, and J. Gijzen, Cryogenics **37**, 313 (1997).

[125] A. T. A. M. de Waele, P. P. Steijaert, and J. J. Koning, Cryogenics **38**, 329 (1998).

[126] G. K. White, *Experimental Techniques in Low-Temperature Physics* 2nd. ed. (Oxford University Press, London, 1968), Chap. 1, p. 14-15.

[127] R. A. Haefer, *Cryopumping - Theory and Practice* (Oxford University Press, Oxford, 1989), Chap. 9, p. 198-201.

[128] MVP 015, Pfeiffer Vacuum Technology AG, Asslar, Germany.

[129] STYCAST 2850FT, Emerson and Cuming, Billerica, MA.

[130] P. E. Gifford (private communication).

[131] M. Kenyon, Ph.D. thesis, University of Maryland, College Park, 2001.

[132] H. Paik, Center for Superconductivity Research Seminar, University of Maryland, College Park, 2002.

[133] 850G Series, Newport Corporation, Irvine, CA.

[134] Newport, *ESP6000 PC-Based High-Performance Motion Controller – User's Manual* (Irvine, 2000).

[135] ESP6000DCIB, Newport Corporation, Irvine, CA.

[136] 100 kHz SQUID Electronics, Electronic Development Group, University of Maryland Physics Department, College Park, MD.

[137] P. Horowitz and W. Hill, *The Art of Electronics* 2nd. ed. (Cambridge University Press, Cambridge, 1989), Chap. 4, p. 242-248.

[138] LTC-21, Neocera Inc., Beltsville, MD.

[139] Stanford Research Systems, *MODEL SR830 DSP Lock-In Amplifier* rev. 2.0 (Sunnyvale CA, 2002).

[140] L. A. Knauss (private communication).

[141] P. Horowitz and W. Hill, *The Art of Electronics* 2nd. ed. (Cambridge University Press, Cambridge, 1989), Chap. 11, p. 775-776.

[142] S. I. Woods (private communication).

[143] P. W. W. Fuller, in *High Speed Photography and Photonics*, edited by S. F. Ray (Focal Press, Oxford, 1997), Chap. 2, p. 36.

[144] P. Horowitz and W. Hill, *The Art of Electronics* 2nd. ed. (Cambridge University Press, Cambridge, 1989), Chap. 4, p. 229-232.

[145] M. A. Gubrud (private communication).

[146] P. Horowitz and W. Hill, *The Art of Electronics* 2nd. ed. (Cambridge University Press, Cambridge, 1989), Chap. 8, p. 504-512.

[147] S. M. Faris, Appl. Phys. Lett. **36**, 1005 (1980).

[148] D. B. Tuckerman, Appl. Phys. Lett. **36**, 1008 (1980).

[149] H. H. Zappe, IEEE Trans. Magn. **13**, 41 (1977).

[150] O. A. Mukhanov, V. K. Semenov, and K. K. Likharev, IEEE Trans. Magn. **23**, 759 (1987).

[151] O. A. Mukhanov, S. Sarwana, D. Gupta, A. F. Kirichenko, and S. V. Rylov, Physica C **368**, 196 (2002).

[152] R. E. Collin, *Foundations for Microwave Engineering* 2nd. ed. (McGraw-Hill, New York, 1992), Chap. 3, p. 125-180.

[153] Micro-Coax, *Semi-Rigid Coaxial Cable* (Pottstown PA, 2003).

[154] Huber+Suhner, *Suhner Coaxial Connectors General Catalogue* (Herisau Switzerland, 2001).

[155] CMSH-60, Cryofab, Kenilworth, NJ.

[156] HP 33120A, Agilent Technologies, Palo Alto, CA.

[157] J. Matthews and C. P. Vlahacos (private communication).

[158] Stanford Research Systems, *MODEL DG535 Digital Delay / Pulse Generator* rev. 2.6 (Sunnyvale CA, 2000).

[159] 2465B, Tektronix, Beaverton, OR.

[160] R. E. Collin, *Foundations for Microwave Engineering* 2nd. ed. (McGraw-Hill, New York, 1992), Chap. 3, p. 112-117.

[161] P. Horowitz and W. Hill, *The Art of Electronics* 2nd. ed. (Cambridge University Press, Cambridge, 1989), Chap. 1, p. 11-44.

[162] G. Arfken, Mathematical Methods for Physicists 3rd. ed. (Academic Press, San Diego, 1985), Chap. 15, p. 820-823.

[163] R. E. Collin, *Foundations for Microwave Engineering* 2nd. ed. (McGraw-Hill, New York, 1992), Chap. 3, p. 72-96.

[164] G. Arfken, Mathematical Methods for Physicists 3rd. ed. (Academic Press, San Diego, 1985), Chap. 15, p. 794-807.

[165] G. Arfken, Mathematical Methods for Physicists 3rd. ed. (Academic Press, San Diego, 1985), Chap. 14, p. 787-791.

[166] HP 83732B, Hewlett-Packard, Rohnert Park, CA.

[167] S. M. Faris, IBM Tech. Disclos. Bull. **26**, 1338 (1983).

[168] 81133A, Agilent Technologies, Palo Alto, CA.

[169] Tektronix, *User Manual CSA7404B Communications Signal Analyzers, TDS7704B, TDS7404B, TDS7254B & TDS7154B Digital Phosphor Oscilloscopes – 071-1226-03* (Beaverton OR, 2005).

[170] G. K. White, *Experimental Techniques in Low-Temperature Physics* 2nd. ed. (Oxford University Press, London, 1968), Chap. 7, p. 217-221.

[171] G. K. White, *Experimental Techniques in Low-Temperature Physics* 2nd. ed. (Oxford University Press, London, 1968), Chap. 7, p. 213-217.

[172] R. W. Powell, C. Y. Ho, and P. E. Liley, in *Handbook of Chemistry and Physics* 52nd. ed., edited by R. C. West (The Chemical Rubber Company, Cleveland, 1971), Sec. E, p. E-10.